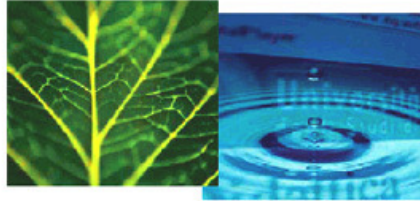**PhD Dissertation**

**International Doctorate School in Information and
Communication Technologies**

DISI - University of Trento

Novel Methods based on the Fusion of Multisensor Remote Sensing Data for Accurate Forest Parameter Estimation

Claudia Paris

Advisor:

Prof. Lorenzo Bruzzone

University of Trento

April 2016

A mia sorella Simona,
che ci vede sempre a lungo

"Logic will get you from A to B.
Imagination will take you everywhere."

Albert Einstein

Abstract

In the last decade the increasing availability of high resolution remote sensing data enabled precision forestry, which aims to obtain a precise reconstruction of the forest at stand, sub-stand or individual tree level. This calls for the need of developing techniques tailored on such new data that can achieve accurate forest parameters estimations. Moreover, in this context the integration of multiple remote sensing data brings to a more comprehensive representation of the forest structure. Accordingly, the goal of this thesis is the development of novel methods for the automatic estimation of forest parameters that can exploit the different properties of multiple remote sensing data sources. The thesis provides five main novel contributions to the state-of-the-art.

The first contribution of the thesis addresses the problem of the single tree crowns segmentation in multilayered forest by using very high-density multireturn LiDAR data. The aim of the proposed method is to fully exploit the potential of these data to detect and delineate the single tree crowns of both dominant and sub-dominant trees by a hierarchical 3-D segmentation technique applied directly in the point cloud space. The second contribution of the thesis regards the estimation of the diameter at breast height (DBH) of each individual tree by using high-density LiDAR data. The proposed data-driven method extensively exploits the information provided by the high resolution data to model the main environmental variables that can affect the stems growth in terms of crown structure, topography and forest density. The third contribution of the thesis proposes a 3-D model based approach to the reconstruction of the tree top height by fusing low-density LiDAR data and high resolution optical images. The geometrical structure of the tree is reconstructed via a properly defined parametric model which drives the fusion of the data. Indeed, when high resolution LiDAR data is not available, the integration of different remote sensing data sources represents a valid solution to improve the parameter estimation. In this context, the fourth contribution of the thesis addresses the fusion of low-density airborne LiDAR data and terrestrial LiDAR data to perform localized forest analysis. The proposed technique automatically registers the two LiDAR point clouds by using the spatial pattern of the forest in order to integrate the data and to automatically estimate the crown parameters. The fusion of the LiDAR point clouds leads to a more comprehensive representation of the 3-D structure of the crowns. Finally, we introduce a sensor-driven domain adaptation method for the classification of forest areas sharing similar properties but located in different areas. The proposed method takes advantage from the availability of multiple remote sensing data to detect features subspaces where data manifolds are partially (or completely) aligned.

Qualitative and quantitative experimental results obtained on large forest areas confirm the effectiveness of the methods developed in this thesis, which allow an improvement in terms of accuracies when compared to other state-of-the-art methods.

Acknowledgements

At the beginning of my PhD experience I wouldn't have expected to grow up so fast from the professional and the personal view point. During these three years I got the possibility of living abroad, attending international conferences, writing scientific papers and presenting my work in front of the most important scientists in my field. For all of that, my deepest gratitude goes to my advisor Lorenzo, who has always believed in me since the beginning. I would like to thank him for guiding and motivating me over this experience and for all he has taught me. Thank you for your dedication to both my personal and academic growth. More than a leader, you were a mentor for me.

I would like to thank Francesca just for standing by me with her sensitivity and for being there every time I needed to talk to her. Thank you for supporting me, for encouraging me when I felt inadequate and for sharing your experience. Above all I want to thank you for being brutally honest when I was making a mistake!!

I would like to thank my RsLab colleagues Massimo Zanetti who made my PhD much more funny as soon as he joined us, Silvia Demetri for her kindness and Davide Castelletti for making me laugh with his proverbial cynicism. A special thanks goes to Leonardo Carrer and Andrea Stenico: guys, life is better when you are with me! Leo, I am missing your noise in the lab and our worthy discussions at 7 p.m. on radar sounder while I was driving back home! Thank you for forcing me to go out when I was too lazy to move and for pushing me to play squash. I am waiting for you to come back in Trento. Andrea, there are many things I have to thank you for, but basically I just want to thank you for your true valuable friendship.

For my US experience I would like to thank my hosting advisor Jan, who did everything he could to make me feel at home as soon as I arrived in Rochester. I want to thank my American brother Mr. Kelbe that was taking care of me during the 3 months spent there. Thank you for involving me in the parties, in the camp fires and to make me eat my first marshmallow! Last but not least I would like to thank Anton, Javier and Yana. You guys were my family in the US. We had a great friendship and I would never forget my last crazy weekend with you in NY city. I am glad I met you and even though we are far I hope we will meet again all together sooner or later.

I would like to thank Michele for making me forgetting all the negative thoughts every time he smiles and for making me so happy when we are close. I am glad I have you in my life and I wish us to keep collecting beautiful memories all over the world.

Finally, I would like to thank Caterina, Francesco, Simona and Pierpaolo that supported me in all my decisions. Thank you for celebrating all the exciting moments and for fighting all of life's battles with me. In particular, I dedicated this thesis to my sister because she is my lighthouse. Simona, you are the best gift I have ever had. I am not worried for the future because I know you will be always by my side.

Contents

List of Tables

List of Figures

List of Abbreviations

AL	Active Learning
ALS	Airborne Laser Scanning
ALTM	Airborne Laser Terrain Mapper
ALI	Advanced Land Imager
BHC	Binary Hierarchical Classifier
CCD	Charge Coupled Device
CHM	Canopy Height Model
COM	Commission errors
CR	Crown Radius
CRS	Canopy Reflection Sum
DA	Domain Adaptation
DBH	Diameter at Breast Height
DET	Detection accuracy
DGPS	Differential Global Positioning System
DSM	Digital Surface Model
DTM	Digital Terrain Model
ECBD	Enhanced Clustering Based Diversity
EO	Earth Observing
ETM	Enhanced Thematic Mapper
FOV	Field Of View
FWHM	Full Width at Half Maximum
GCC	Global Canopy Cover
GFOV	Ground Field Of View
GIFOV	Instantaneous Ground Field of View
GLS	Generalized Least Square
GWR	Geographically Weighted Regression
HFD	Height Frequency Distribution
IFOV	Instantaneous Field of View
INS	Inertial Navigation System
ITC	Individual Tree Crown
JM	Jeffreys-Matusita distance
k-NN	k Nearest Neighbor
LCC	Local Canopy Cover
LCS	Laser Cross Section
LiDAR	Light Detection and Ranging

LME	Linear Mixed-effect Model
LMF	Local Maxima Filtering
LMS	Laser Measurement Systems
LSM	Level Set Method
MAE	Mean Absolute Error
MCLU	Multi Class Level Uncertainty
ME	Mean Error
MSE	Mean Square Error
NDVI	Normalized Difference Vegetation Index
NEON	National Ecological Observatory Network
NRMSE	Normalized Root Mean Square Error
OA	Overall Accuracy
OAA	One Against All
OLS	Ordinary Least Square
OM	Omission errors
P^{3}SVM	Progressive Semisupervised Support Vector Machine
PA	Producer Accuracy
PCS	Point Cloud Space
PDF	Probability Density Function
PM	Proposed Method
PRF	Pulse Repetition Frequency
R^2	Coefficient of Determination
RBF	Radial Basis Function
RMSE	Root Mean Square Error
RMSE(%)	Percentage Root Mean Square Error
RS	Remote Sensing
SFFS	Sequential Forward Feature Selection
SPOT	Satellite Pour l'Observation de la Terre
SSD	Sum of Squared Differences
SSL	Semi Supervised Learning
SVM	Support Vector Machine
TCA	Transfer Component Analysis
TLS	Terrestrial Laser Scanning
TR	Training
TS	Test
UA	User Accuracy

List of Symbol

P_t	Transmitted power
P_e	Received power
R_t	Range between LiDAR and target
ϑ_{BW}	Laser beam width
σ	Laser cross section
A	Aperture of the receiving lens
O_{eff}	Optical efficiency of the TX-RX chain
D_l	Lens Diameter
λ	Laser wavelength
c	Light speed
f	Focal lenght
w	Detector width
I_a	radiance scattered by the atmosphere
I_t	radiance reflected by the target and transmitted to the sensor
I_b	radiance reflected by the background
$\mathcal{P}$	Normalized LiDAR point cloud (PCS)
$\mathcal{T}_{\mathrm{CHM}}$	Set of dominant tree-top detected in the CHM
$\mathbf{p}_i = (x_i, y_i, z_i)$	Ground coordinates of the LiDAR point
$\mathbf{t}_j = (x_j^t, y_j^t, z_j^t)$	Ground coordinates of the tree top
$\mathcal{P}_j$	Set of LiDAR points extracted around the tree top $\mathbf{t}_j$
R_s	Search radius
N_θ	Number of angular sectors used for the 3D crown segmentation
Θ_k	Angular partition between the adjacent angles θ_k and θ_{k+1}
$\mathcal{P}_{j,\Theta_k}$	LiDAR points belonging to the angular sector Θ_k
$S_{j,\Theta_k}(\rho)$	1-D discrete signal representing $\mathcal{P}_{j,\Theta_k}$
Π_c	Circular projection that maps the points into the ρz plane
ξ	Quantization step of the distance of the points from the tree-top
F	Number of horizontal quantization steps
$S'_{j,\Theta_k}(\rho)$	Discrete derivative of $S_{j,\Theta_k}(\rho)$
M_{j,Θ_k}	Closest height maximum to the tree-top $\mathbf{t}_j$ of the angular sector Θ_k
$\mathcal{T}_{\mathrm{PCS}}$	Set of dominant tree-top detected in the PCS
$\mathcal{T}^{\mathrm{sub}}$	Set of sub-dominant tree top
E_{j,Θ_k}	Closest height minimum to the tree-top $\mathbf{t}_j$ of the angular sector Θ_k
$\mathcal{C}$	Set of dominant segmented tree crowns

L	Number of angular sectors used for the detection of the sub-dominant trees, with $L \leq N$
$V_{j,\Theta_k}(z)$	1-D vertical signal representing $\Pi_c(\mathcal{C}_{j,\Theta_k})$, with $\mathbf{p}_i = (z_i, \rho_i)$
D	Number of vertical quantization steps
δ	Quantization step of the vertical profile of dominant tree
H_{j,Θ_k}	Maximum height value of the set of points $\mathcal{C}_{j,\Theta_k}$
$H_{j,\Theta_k}^{\mathrm{sub}}$	Height of the sub-dominant tree detected in the angular sector Θ_k
$\mathcal{P}_{j,\Theta_k}^{\mathrm{sub}}$	Set of LiDAR points $\mathbf{p}_i \in \mathcal{C}_{j,\Theta_k}^{sub}$ having $z_i \leq H_{j,\Theta_k}^{\mathrm{sub}}$.
$\mathcal{T}^{\mathrm{sub}}$	Set of dominant tree-top detected in the CHM
$\mathcal{P}_k^{\mathrm{sub}}$	LiDAR point sectors associated to the sub-dominant tree-top
$\mathcal{C}^{\mathrm{sub}}$	Set of sub-dominant segmented tree crowns
$\mathbf{x}^{\mathrm{Tree}}$	variables modeling the structure of the tree
$\mathbf{x}^{\mathrm{Plot}}$	variables modeling the stand density
$\mathbf{x}^{\mathrm{Dtm}}$	variables modeling the topography
$z = g(x,y)$	DTM
$g_x = \frac{\partial z}{\partial x}$	partial derivatives along x
$g_y = \frac{\partial z}{\partial y}$	partial derivatives along y
$g_{xx} = \frac{\partial^2 z}{\partial x^2}$	partial derivatives along xx
$g_{yy} = \frac{\partial^2 z}{\partial y^2}$	partial derivatives along yy
$g_{xy} = \frac{\partial^2 z}{\partial x \partial y}$	partial derivatives along xy
p	$(g_x^2 + g_y^2)$
q	$(g_x^2 + g_y^2 + 1)$
H_{max}^r	Maximum height per return, with $r =[1,4]$
H_{range}^r	Height range per return, with $r =[1,4]$
H_{av}^r	Average height per return, with $r =[1,4]$
H_{var}^r	Variance height per return, with $r =[1,2]$
H_{skw}^r	Skewness height per return, with $r =[1,2]$
H_{kurt}^r	Kurtosis height per return, with $r =[1,4]$
H_{max}^1-H_{max}^3	Max height 1st - Min height 3rd
H_{av}^1 - H_{av}^2	Average height 1st - Average height 2nd
H_{av}^1 - H_{av}^3	Average height 1st - Average height 3rd
H_{av}^1 - H_{av}^4	Average height 1st - Average height 4th
H_{av}^2 - H_{av}^3	Average height 2nd - Average height 3rd
H_{av}^2 - H_{av}^4	Average height 2nd - Average height 4th
H_{av}^3 - H_{av}^4	Average height 3rd - Average height 4th
H_p	pth height percentile, with $p =\{25,50,75,90,95\}$
C_a	Crown area
r_1	Radius of the circle circumscribed to the crown
r_2	Radius of the ellipse circumscribed to the crown
p_2/p_1	Ratio of 2nd and 1st return pulses (in a radius = 10m)
S_{west}	Slope between (x^t, y^t) and $(x^t - 10 \text{ m}, y^t)$
S_{east}	Slope between (x^t, y^t) and $(x^t + 10 \text{ m}, y^t)$
S_{south}	Slope between (x^t, y^t) and $(x^t, y^t - 10 \text{ m})$

S_{nord}	Slope between (x^t, y^t) and $(x^t, y^t + 10 \text{ m})$
γ	Aspect (degrees clockwise from north)
φ	Profile Curvature: direction of max slope
ϕ	Plan Curvature: transverse to the max slope
w	Wetness Index
A_{min}	Minimum Altitude
A_{max}	Maximum Altitude
A_{av}	Average Altitude
$\Omega_M = \{\omega_i\}_{i=1}^M$	M growth model classes
$\mathbf{x}^{Env}$	Environmental feature space
$\{v_i\}$	cluster center
B_{ht}	Bhattacharyya distance of the classes ω_h and ω_t
JM_{ht}	JM distance of the classes ω_h and ω_t
μ_h	Mean vector of class ω_h,
Σ_h	Covariance matrix of class ω_h
$\mathbf{y}_i$	vector of observed DBH values
$\mathbf{X}_i$	matrix of extracted variables
$\boldsymbol{\beta}_i$	vector of model parameter estimation
$\boldsymbol{\varepsilon}_i$	residual error
Q	Structural element chosen for dilating the CHM image
D_{CHM}	Domain of the image CHM
D_Q	Domain of the structuring element Q
th_{Height}	Height threshold
M_{sk}	Mask Image
G	Green band of the optical image
G_m	Masked green band of the optical image
$\mathcal{N}$	Number of LiDAR pulses associated to each crown
n_j	Number of LiDAR pulses associated to the crown C_j
ch	Crown height
cc	Crown curvature
cr	Crown radius
$r_i(\bar{z}_j^t)$	Residual of the ith LiDAR point
d_{ref}	distance of the LiDAR point from the center of the tree
N_m	Possible tree models
$\mathcal{P}_n^T$	Normalized nth terrestrial LiDAR scan
$\mathcal{P}^A$	Normalized airborne LiDAR data
ζ_n	Geometric affine transformation
I^A	CHM of the airborne LiDAR data
I_n^T	CHM of the nth terrestrial LiDAR scan
S^A	segmented image
$\mathcal{C}^A$	Set of airborne segmented crown
I_n^A	Portion of the airborne image having the same size of I_n^T
ϕ	Rotation angle
$[s_x, s_y]$	Scaling factor

$[t_x, t_y]$	Translation factor
$I_n^{A'}$	Registered airborne CHM
Υ	Correlation coefficient
μ_n^T	Mean value of I_n^T
μ_n^A	Mean value of $I_n^{A'}$
$\mathcal{C}_n^T$	Set of segmented LiDAR point clouds of I_n^T
Ψ_n	nth sensor
$\mathbf{x}^{\Psi_n}$	Feature vector extracted by the nth sensor
$\Omega = \{\omega_m\}_{m=1}^M$	M land-cover classes
$\mathcal{D}_S = \{\mathcal{X}_S, \mathcal{Y}_S\}$	Source domain
$\mathcal{D}_T = \{\mathcal{X}_T\}$	Target domain
$P(\omega_m)$	Prior probability of ω_m
$p(\mathbf{x}|\omega_m)$	Class conditional probability of ω_m
$p^S(\mathbf{x})$	Distribution of the source domain
$p^T(\mathbf{x})$	Distribution of the target domain
$\mathcal{C}_{all}$	Set of classes of the hierarchical tree structure
$M(c_k)$	Parent class of c_k
$F(c_k)$	Set of child classes
$\mathcal{C}_v \subseteq \mathcal{C}_{all}$	Subset of classes for which none of the sensors available can measure invariant features
$\mathcal{C}_{inv} \subseteq \mathcal{C}_{all}$	Subset of classes for which at least one sensor available is able to measure spatial invariant features
$\mathcal{X}_{c_k}^T$	Unlabeled samples of the target domain belonging to c_k
$\mathcal{T}_{c_k}^S$	Training set of $\mathcal{D}_S$ for the considered invariant classes c_k
$\mathbf{w}$	Vector normal to the separating hyperplane
b	Bias term
C	Regularization parameter
ξ_i^s	Slack variable associated with the ns_{c_k} labeled samples of the source domain for the classes c_{k_1} and c_{k_2}
α_i^s	Lagrange multipliers, with $i = 1, .., ns_{c_k}$
$\langle \mathbf{x}_i^s \cdot \mathbf{x}_j^s \rangle$	Inner product between the two feature vectors x_i^s and x_j^s
$\Phi(\mathbf{x})$	Nonlinear mapping function to project the samples into an higher dimensional space
$K(\mathbf{x}_i^s, \mathbf{x}_j^s)$	Kernel function
$\mathcal{G}$	Subset of training samples corresponding to the nonzeros Lagrange multipliers
$\mathcal{X}_{c_k}^T$	Target unlabeled samples
$f(\mathbf{x})$	SVM hyperplane
$\mathcal{T}_{c_k(0)}^T$	Initial training set of $\mathcal{D}_\mathcal{T}$
$\mathcal{T}_{c_k(1)}^T$	Training set including all the original unlabeled samples $\mathcal{X}_{c_k}^T$
$\mathcal{T}_{inf}^T$	Initial training set for all the $\mathcal{C}_{inv}$ classes of $\mathcal{D}_\mathcal{T}$

Introduction

This chapter presents an introduction to the PhD thesis work. We briefly introduce the framework where this work has been developed by providing an overview of the problem of forest parameter estimation using remote sensing data. This allows us to highlight and discuss the motivation, the objectives and the novel contributions of this thesis. Finally, the structure of the document is reported.

Background

Nowadays, the accurate estimation of forest parameters at individual tree level has become an important research topic. Precision forestry is the new direction of modern forest inventories, which aims to obtain a comprehensive representation of the tree structure for better forest management. In this framework, the integration of different remote sensing sources represents an effective solution to obtain precise analysis of the forest parameters. This calls for the development of novel methods being able to exploit the complementary information provided by the different data sources. Moreover, the new generation of high resolution sensors results in the collection of an overwhelming amount of detail of the forest. The availability of this large amount of information encourages the definition of automatic techniques being able to exploit the full potential of these data for an accurate estimation of the forest parameters. In the following a brief overview on the use of remote sensing data for forest parameter estimation is given.

Remote sensing data have been widely employed to estimate forest parameters due to the possibility of monitoring objectively and accurately large forest areas. The traditional approach, based on field observations, is constrained by lack of access to remote areas (especially in mountainous scenarios) and involves high costs related to the amount of time spent for collecting field data. Moreover, in order to obtain reliable estimates, the number of ground measurements collected should be proportional to the extension of the considered forest area. Therefore, this approach is efficient when applied to small areas, but at regional scale the data collected could be not sufficient for modelling accurately the entire investigated area. In this framework, remote sensing represents a valuable technology for providing measures useful for forestry inventories. In particular, in this thesis we focus the attention on Active Light Detection and Ranging (LiDAR) sensor and passive high spatial/spectral resolution optical sensors.

LiDAR data have been extensively used for the forest attribute estimation because of the capability of the laser scanner of directly measuring the height and the vertical structure of the trees. This technology, based on line-of-sight measurements, penetrates

the tree crowns and allows the 3-D reconstruction of the forest. The acquisition of LiDAR data can be carried out by either Airborne Laser Scanning (ALS) systems or Terrestrial Laser Scanning (TLS). ALS systems are suited for surveying and mapping large forest areas, whereas TLS data are usually employed for local forest inventories. When acquired with high laser sampling density (i.e., characterized by a number of hits per m^2 higher than 5), ALS data allow the precise estimation of different forest variables such as height, volume or basal area both at individual tree level or at stand level (group of trees). Although many approaches have been developed to estimate forest parameters by using ALS data, the new generation of high resolution LiDAR sensors acquire significantly more detail of the inner structure of the forest than the systems available some years ago. These new technologies provide a higher spatial point density as well as additional information on the reflecting characteristics of the forest structure like branches and stems. This calls for the need of developing automatic methods that can maximize the information extracted from the data to accurately estimate the forest parameters. Moreover, towards the direction of the precision forestry, the integration of airborne and terrestrial LiDAR data is gaining interest because of the possibility of using TLS to complement the weak points of ALS, and thus link ground-level structural measurements with the measures of the uppermost portion of the canopy provided by the ALS. Indeed, despite the improved capability of the new ALS systems of penetrating the vegetation, they still provide limited information on the below-canopy tree structure, especially in dense forest scenario. On the contrary, TLS systems are able to record a very high resolution profile of sub-canopy tree crown structure, while missing the uppermost part of the tree canopy. In light of this, the fusion of the LiDAR point clouds acquired by different view points allows a more comprehensive representation of the crown structure, which is useful to perform localized environmental analysis (e.g., biogeochemical cycles, fuel loading, habitat provision, etc.).

Passive sensors can acquire images of the Earth's surface measuring the energy reflected by the target at different wavelengths. In the past, satellite optical images were one of the first remote sensing data source exploited for forestry applications. In particular, these data have been mainly employed for forest species classification since plant species can be analyzed considering the reflective characteristic of the foliage in the visible and infrared bands. Depending on the spatial and the spectral resolution of the optical image it is possible to solve the classification problem at different levels. High geometrical resolution optical sensors provide more accurate geometrical representation of the horizontal structure of the forest because of their high spatial resolution. However, due to the low spectral resolution, their capability of discriminating forest species is limited. In contrast, hyperspectral images allow the distinction of different tree species and the discrimination of similar forest types due to the dense sampling of the spectral signature. Although optical images have also been used for tree volume estimation, the accuracy of the estimates declines with the increase of the forest volume as these data do not provide any information about the vertical structure of the forest. In contrast, LiDAR sensors are suited for the estimation of vertical forest parameters, whereas do not achieve accurate forest species classification since they are not able to discriminate similar tree species. Due to the different properties of the passive and active sensors, LiDAR data and optical images provide complementary information about the structure of the forest.

In this framework, the integration of these data sources represents an effective solution to obtain precise analysis of the forest parameters. However, in order to cope with this large amount of data, it is necessary to develop techniques that can automatically achieve accurate forest parameters estimations by fusing the information provided by different data sources.

Another important research topic in forestry is related to the precise land cover mapping of the forest area and the forest species. To obtain reliable classification maps, supervised classification methods are usually employed. The main drawback of these methods is the need of a sufficient number of labeled ground reference samples for training the classification algorithm. However, in many cases reference samples are expensive and difficult to collect. Therefore, in real application scenarios, it is not reasonable to assume to have groundtruth available on wide forest area. To mitigate the need of labeled samples, the classification of a remote sensing data where no ground data is available (target domain) can be performed by using ground reference data associated to a data acquired by the same sensor in a region with comparable properties (i.e., the same set of land-cover classes). However, even tough the data are similar to each other, it is necessary to face many problems. The different acquisition conditions of the two data (e.g., illumination conditions, atmosphere conditions, look/view angles, sensor parameters) affect the radiometry of the scene. Moreover, the phenological state of the vegetation or the differences in the soil moisture can lead to crucial variations in the spectral response of the same land-cover classes. In machine learning and pattern recognition literature, these problems are usually addressed by domain adaptation (DA) methods. The main idea is to model the changes between similar domains by transferring the knowledge learned on the source domain (one or more) to a target domain. DA methods address critical and challenging problems due to the fact that labeled data are assumed to be available only for the source domain, which is different from the target domain. It is clear that in such a complex scenario the accuracy of the obtained results is strongly related to the capability of modelling properly the changes occurring between the two image domains. In this framework, the availability of multiple remote sensing data sources results in the collection of complementary measurements of the classes. By exploiting the capability of each sensor of measuring different physical properties of the scene it is possible to increase the reliability of the obtained results.

Objectives and Novel Contributions of the Thesis

The work presented in this thesis is aimed at investigating and defining novel methods for the precise estimation of forest parameters by exploiting the properties of different remote sensing data sources. In particular, we focused the attention on the main gaps present in the literature towards the direction of the precision forestry. Accordingly, it is necessary to develop automatic methods capable of exploiting the full potential of the new generation of high resolution LiDAR sensors and to define data fusion techniques being able to accurately integrating the different information provided by multiple remote sensing sources. In greater detail, the novel contribution of the thesis are as follows:

1. A hierarchical 3-D crown segmentation method in multilayered forest for very high-

density LiDAR data.

2. An adaptive tree stem diameter estimation technique for high-density LiDAR data.

3. A tree top height estimation method based on the fusion low-density LiDAR data and high resolution optical images.

4. A crown structure estimation method based on the fusion of airborne and terrestrial LiDAR data.

5. A sensor-driven DA method for the classification of large forest areas with multisensor data.

In the following subsections the main objectives and novelties per contribution of the thesis will be briefly described.

Hierarchical 3-D Crown Segmentation Method

As mentioned above, the accurate estimation of forest parameters at individual tree level is becoming essential for modern forest inventories. The estimation of the tree parameters requires the segmentation of the single tree crowns including the dominant trees and the understory vegetation. Thus, in this thesis we present a novel method for the detection and delineation of the single tree crowns in multilayered forest by using very high-density LiDAR data. The proposed method performs a 3-D segmentation of both the dominant and the sub-dominant trees visible in the LiDAR point cloud. Unlike the methods present in the literature, the proposed approach does not require any prior knowledge on the crown size and forest density, but relies on the geometrical structure of the forest and the properties of the LiDAR data. Thus, it can be successfully applied to large forest areas characterized by heterogeneous 3-D crown structures. The method considers both the rasterized version of the LiDAR data (i.e., image domain) and the original point cloud domain. The main novelties of the proposed approach are: (i) the use of the LiDAR point cloud to detect the dominant trees missed in the image domain, (ii) the identification of the sub-dominant trees located in different sides of the dominant tree crowns by means of an angular analysis, and (iii) a crown delineation method for both dominant and sub-dominant trees based on the derivative analysis of the horizontal profile of the trees in the LiDAR point cloud. The effectiveness of the proposed method is demonstrated in experiments carried out in a complex dense forest scenario located in the Southern Alps of the Trentino region (Italy) by using very high-density LiDAR data (up to 50 pts/m^2) and high-density LiDAR data (up to 5 pts/m^2).

Adaptive Tree Stem Diameter Estimation Method

The Diameter at Breast Height (DBH) is a fundamental tree parameter for forest inventories. Indeed, the accurate estimation of stem diameter allows a proper representation of the 3-D forest structure. While the height of the trees is directly measured by the sensor, DBH should be retrieved by means of regression analysis. By training a unique regression model medium size tree diameter are accurately estimated, while small and large stem

DBH are usually overestimated and underestimated, respectively. These errors lead to a wrong reconstruction of the forest structure as well as a wrong estimation of the forest volume. To solve this problem, we propose an adaptive method to the accurate estimation of the DBH. First, the main tree growth model classes are detected by means of a data-driven approach. Then, for each growth model class, a tailored regression rule is defined and used to improve the estimation accuracy of small and large stem diameters. All the factors which can affect the growth of the tree stem in terms of topography and forest density are modeled. Differently from the literature, the proposed approach: (i) performs a data-driven detection of the growth model classes, (ii) allows an accurate representation of the environmental factors which affect the DBH growth, and (iii) defines different regression models for each growth model class. Experiments were carried out on high-density LiDAR data in a forest area characterized by a wide range of stem diameters. The results show that the method has a high estimation accuracy regardless of the size of the tree stem.

Tree Top Height Estimation Method

One of the most important forest parameter that needs to be accurately estimated is the height of the trees. Due to the high acquisition costs of high-density LiDAR data, when dealing with large forest areas low-density data are typically acquired. However, the reduction of the number of laser points results in: (i) an underestimation of the height of the trees, (ii) the missed detection of some trees present in the scene. To mitigate the lack information due to the low laser sampling, thus improving the estimation results, low cost high resolution optical images can be employed. Accordingly, by integrating the accurate representation of the horizontal structure of the forest provided by the optical data to the vertical height information of the LiDAR sensor, we aim to reconstruct the tree top height by means of a 3-D tree model representing the crown structure. Moreover, the heights of the missed trees are estimated by means of a k-Near Neighbours trees (k-NN trees) technique which takes advantage from the correlation between tree height and crown area. The main novelties of the proposed technique are: (i) the use of a 3-D parametric model for the reconstruction of the tree top height of those crowns hit by LiDAR points, and (ii) the estimation of the tree top height for those crowns that are missed by any LiDAR pulse with a k-NN trees technique. In this study, we concentrate our attention on coniferous forests in the Alpine scenario. In the experiments, we considered four LiDAR datasets of low laser sampling density (i.e., 1, 0.75, 0.5, and 0.25 pt/m^2) and very high resolution optical images (0.20 m). The experimental results obtained confirm the effectiveness of the proposed technique.

A Method for Crown Structure Estimation based on the Fusion of Airborne and Terrestrial LiDAR data

Although LiDAR measures are effective for estimating forest parameters, when acquired from a single view point they are not able to perform an exhaustive representation of the entire scene. Moreover, when airborne low-density LiDAR data is available, it is not possible to accurately characterize the structure of the trees. To solve these problems,

we present a method that integrates the terrestrial and low-density airborne LiDAR data for the accurate crown structure estimation for localized forest analysis. TLS data are typically acquired to replace traditional forest inventories, thus used as reference data to estimate forest parameters using ALS. However, despite the increasing availability of the two data types on the same forest area, few papers address the fusion of these data source. Moreover, to the best of our knowledge, the fusion of these data is usually performed considering the synthesis of derived parameters rather than integration of the ALS/TLS data from a real fusion view point. Based on this knowledge gap, we propose an automatic data fusion technique that aims to exploit the complementarity of these data to accurately estimate the 3-D structure of the forest stand and model the structure of the crowns. The main novel contributions of this method are: (i) the use of the ALS data for the automatic registration of the multiple terrestrial scans (without the need for reference targets), (ii) the analysis of the forest spatial pattern to perform the registration of the data, (iii) the use of the airborne segmentation results to delineate the crown in the TLS scans, and (iv) the integration of the 3-D LiDAR point clouds. The experimental results obtained in an open woodland forest scenario demonstrate the importance of fusing the two LiDAR point clouds to accurately represent the crown structure.

Classification of Large Forest Areas by a Sensor-Driven Domain Adaptation Method

As mentioned above, to obtain accurate forest land-cover maps, field data are needed to train the classification algorithm. However, it is not feasible to have ground reference samples every time that a remote sensing image is acquired. Moreover, due the different acquisition scenario a shift in the spectral responses of the land-cover classes is expected. To solve this problem, we introduce a transfer learning method which performs the adaptation by taking advantage from the availability of multisensor remote sensing data. The specific properties of the different remote sensing data sources are exploited to facilitate the transfer of knowledge in a reliable way. In particular, we propose a method for the classification of large forest areas by a sensor-driven DA based on LiDAR data, hyperspectral images and high resolution optical data. Because of the capability of each sensor of measuring different physical properties of the scene, we identify one sensor (or a combination of sensors) being able to measure spatial invariant properties for a subset of classes. The detection of these invariant feature subspaces allows us to infer labels of samples in forest areas that result aligned to the area where ground reference data are available. Then, the inferred labeled samples are re-projected into the full feature space to classify the remaining target samples of the same classes. Finally, for those classes for which none of the sensors can measure invariant features, we perform the adaptation via a standard Active Learning (AL) technique. The sensor-driven inference method allows us to: (i) accurately model the distribution of the subset of classes for which invariant feature subspaces have been detected, and (ii) introduce constraints on the general structure of the adaptation problem, thus simplifying the adaptation procedure. Experimental results confirm the effectiveness of the proposed method.

Thesis Organization

The present Chapter provided a brief overview on the use of remote sensing data for forestry application. In addition, it introduced the motivation, the objectives and the novel contributions of this thesis. The rest of this dissertation is organized in six main chapters. Chapter 1 illustrates the fundamentals and the background notions useful for understanding the thesis. Moreover, a brief analysis of the state-of-the-art on the use of remote sensing data for forest parameter estimation is presented. Chapter 2 introduces to the main problems related to the single tree crown segmentation in multilayered forest by using LiDAR data. Then, it presents the proposed novel 3-D segmentation approach to the detection and the delineation of dominant crowns and understory vegetation, which takes advantage from the properties of the very high resolution LiDAR sensor. Chapter 3 proposes an adaptive data-driven method based on the detection of growth model classes for an accurate estimation of the DBH by using high-density LiDAR data.

In the framework of the fusion of multisensor remote sensing data, Chapter 4 illustrates the proposed 3-D model based approach to the accurate tree top height estimation, which is based on the fusion of low-density LiDAR data and high resolution optical images. Chapter 5 presents the fusion of low-density airborne and terrestrial LiDAR data for an accurate 3-D canopy structure characterization, whereas Chapter 6 reports the novel sensor-driven DA method for transferring the knowledge between remote sensing data acquired on different forest areas but sharing similar properties.

In each chapter an introduction to the specific topic and a review of the related state-of-the-art is provided. Finally, in the last chapter the conclusions of the thesis are drawn and proposals for future research developments are discussed.

Chapter 1

Fundamental and Background

In this chapter we review the fundamentals of remote sensing data used in this thesis. In the first section we provide the concepts and definitions needed throughout the dissertation. In particular, we illustrate the basic principles of LiDAR sensor mounted on both airborne and terrestrial platforms, and passive high spatial/spectral resolution optical sensors. Then, a brief analysis of the state-of-the-art regarding the use of remote sensing data for forest parameter estimation is reported.

1.1 Fundamentals

In the framework of remote sensing technologies, two main classes of sensors can be distinguished: active sensors and passive sensors. Active sensors generate and direct energy toward a target and subsequently record the backscattered radiation. Most common active sensors are RADAR (radio detection and ranging) and LiDAR (light detection and ranging). In this thesis we focus the attention on LiDAR systems, which emit pulses of light by laser beams. This characteristic allows the acquisition of LiDAR data during the night, when the air is usually clearer. However, unlike RADAR systems LiDAR sensors cannot penetrate clouds, rain, or dense haze due to the working wavelengths. Passive sensors measure the electromagnetic energy radiated and reflected by the Earth surface. The radiation measured by the passive systems comes from an emitting external source of energy (typically the sun in the visible and infrared portions of the spectrum), which propagates through the atmosphere and hits the Earth's surface. The Earth's surface interacts with the incident electromagnetic wave by absorbing, transmitting and reflecting the incident energy of the transmitted component. The reflected components propagate back through the atmosphere (again with absorption), thus reaching the sensor. In this thesis, we focus on the analysis of high geometrical and high spectral resolution optical images. In the following, the basic principle of LiDAR and passive optical sensors are presented.

1.1.1 LiDAR basis

Also known as LADAR or laser altimetry, LiDAR is the acronym for light detection and ranging. This active remote sensing system is able to characterize an object by measuring

the properties of the laser light reflected by the target. The sensor transmits a short-duration pulse of laser light towards the target, while the receiver (placed in the same location of the sensor) measures the elapsed time between emission and detection of the reflected light back at the sensor (Fig. 1.1). By using the speed of light, the time measure is then converted into the distance of the point from which the light was reflected. Similar to RADAR systems, but working at smaller wavelengths, LiDAR is highly sensitive to small targets such as aerosols and cloud particles and thus, it has also been used for atmospheric research. Most of the LiDAR systems operate in the near-infrared part of the electromagnetic spectrum (i.e., for forestry application typically between 1010 $[nm]$ - 1064 $[nm]$), even though some sensors work in the green band to penetrate water and detect bathymetry features. Moreover, due to their very narrow beam, LiDAR data are characterized by a high geometrical resolution.

Let us focus the attention on the LiDAR transmission equation. The echo power P_e received is a function of the transmitted power P_t and depends on four main contributions. By assuming the laser beam larger than the target size and the source of power as a point isotropic radiator, the first contribution is the power density emitted by the source located at distance R_t over a spherical area, i.e.,:

$$\frac{P_t}{(4\pi) \ R_t^2} \tag{1.1}$$

Accordingly, the echo power is affected by the return power density scattered over the forward hemisphere, i.e.,:

$$\frac{1}{2\pi \ R_t^2} \tag{1.2}$$

The third factor that affects the power returned from the target is the directivity of the lens used to radiate the power in a given direction, which depends on the laser beam width ϑ_{BW} as follows:

$$\frac{4\pi}{\pi/4 \ \vartheta_{BW}^2} \tag{1.3}$$

Finally, the last contribution is given by the Laser Cross Section (LCS) σ, the aperture of the receiving lens A and the optical efficiency of the TX-RX chain O_{eff}. The LCS estimates how detectable the object is for the laser pulse, and depends on the size and the chemical composition of the target and the wavelength. Accordingly, the relation of the transmitted laser power P_t to the echo power of its reflections P_e is given by the following LiDAR transmission equation:

$$P_e = \frac{P_t}{4\pi R_t^2} \cdot \frac{1}{2\pi \ R_t^2} \cdot \frac{4\pi}{(\pi/4)\vartheta_{BW}^2} \cdot \sigma \cdot A \cdot O_{eff} \tag{1.4}$$

The laser beam ϑ_{BW} depends on the lens diameter D_l and the λ wavelength of the adopted light radiation, i.e.,:

$$\vartheta_{BW} = \frac{\lambda}{D_l} = \lambda \cdot \sqrt{\frac{\pi}{4A}} \tag{1.5}$$
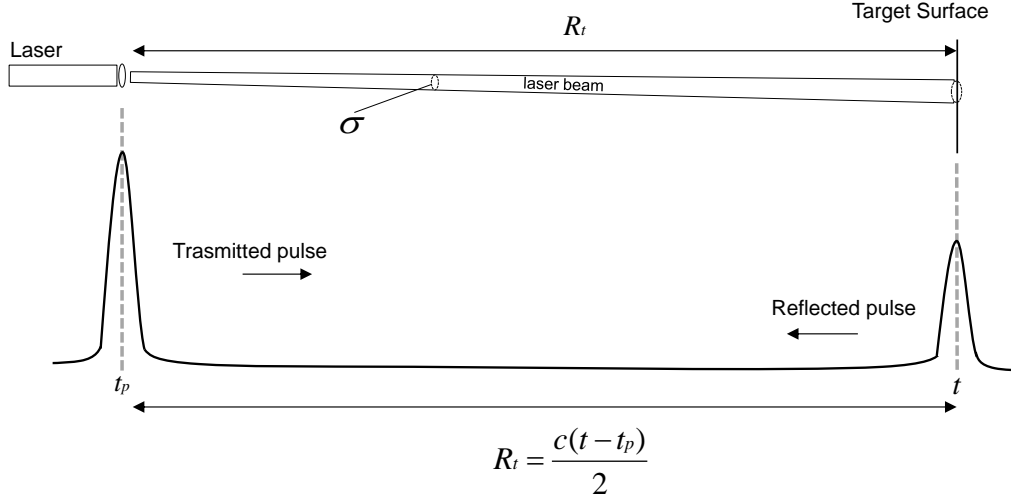
Figure 1.1: Basic principle of LiDAR sensor.

Thus, the LiDAR transmission equation can be rewritten as follows:

$$P_e = \frac{8A^2 \cdot P_t \cdot \sigma \cdot O_{eff}}{\pi^3 R_t^4 \lambda^2} \qquad (1.6)$$

In Fig. 1.1 the basic principle of the sensor is illustrated. The target surface placed at distance R_t is hit by the pulse emitted at time t_p. At time t the energy is observed back at the laser location. The distance of the target from the scanner is estimated according to the speed of light and time difference between the pulses, which is halved due to the round-trip. In real application scenario, when the laser emit the light pulse, the sensor position in terms of latitude, longitude and altitude are recorded in order to convert the position of the target in geographic coordinates (x,y,z). At the end of the acquisition phase, the outcome of the sensor is a 3-D point cloud, derived by the laser range measurements and the knowledge on the position and altitude of the instrument.

According to the LiDAR system used, the run time for submitted laser pulses or the phase shift for continuous wave (cw-LiDAR) emission can be acquired. For pulsed laser systems the reflected signal can be recorded over time (full waveform analysis) instead of just measuring the time of discrete returns (first pulse, last pulse or multiple returns) [1]. Discrete return LiDAR systems consist of a laser transmitter that emits a sequence of pulses characterized by specific pulse duration and specific Pulse Repetition Frequency (PRF), thus generating a discrete acquisition of the target. The range of the object is measured considering the time delay between transmitted and received pulses. While early version of laser transmitters were able to measure only the distance of the first contact with the target, new high resolution LiDAR sensors are able to measure from one to a few echoes for each emitted pulse (i.e., multireturn LiDAR data). Full waveform LiDAR systems record the entire return intensity for each pulse as a function of time. Although these data are computational demanding because of the huge amount of information recorded,
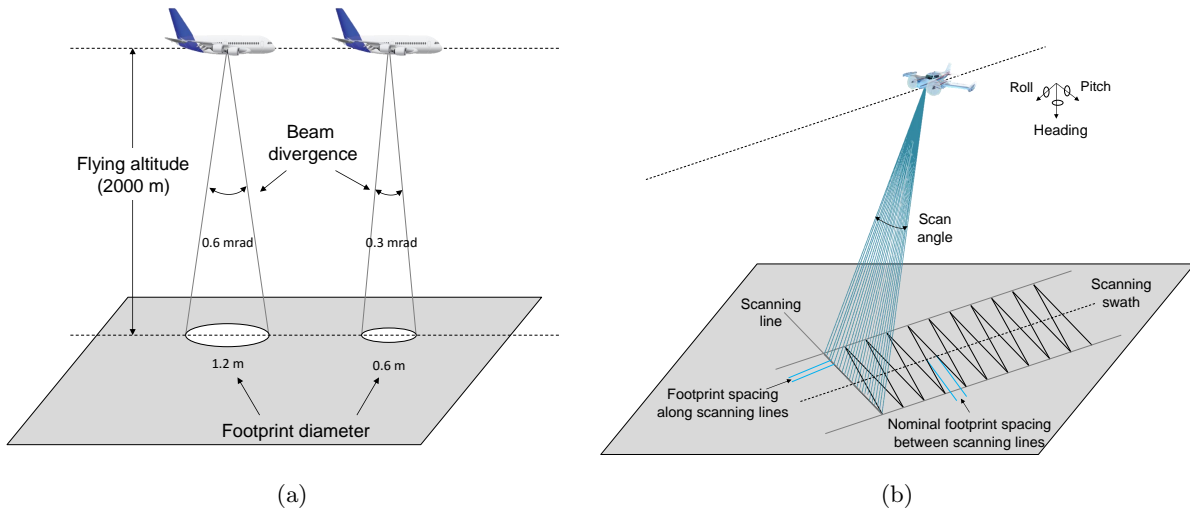
Figure 1.2: Principle of ALS system: (a) example of LiDAR beam divergence, for a given flying altitude the footprint diameter depends on the laser beam of the sensor, (b) representation of the main scanning attributes of airborne LiDAR data acquisition considering a zizag scanning pattern.

they result in an accurate representation of the 3-D shape and the inner structure of the target [2, 3].

The acquisition of LiDAR data can be performed by using different platforms according to the application. In this thesis we focus the attention on the ALS and the TLS for forestry applications. In the following sections the two systems are described in detail.

1.1.2   Airborne Laser Scanning (ALS)

ALS systems consist of a set of instruments that work independently: (i) the laser device, (ii) a Differential Global Positioning System (DGPS) which records the geographic position for each collected point, (iii) an Inertial Navigation System (INS) which monitors the flight dynamic by recording the parameters related to the rotation angles of the vehicle (pitch, roll and yaw) and the horizontal and vertical movements of the aircraft (Fig. 1.2b), and iv) a computer interface that manages communication among devices and data storage.

Although full waveform laser scanners provide very high-density LiDAR point clouds as well as additional information on the reflecting properties of the tree branches and stems, ALS discrete return systems are usually acquired for surveying and mapping large forest areas due to the limited storage capacities. While old system were able to discriminate only either the first or the first and last returns, recent sensors penetrate the structure of the vegetation thus measuring the foliage, the deepness of the canopy and even reach lower trees. Moreover, they allow the detection of multiple returns (e.g., up to five) from a single beam. According to the length of the emitted laser pulse (i.e., pulse length), it is possible to determine the range resolution of the pulse or the minimum distance between consecutive returns from a pulse. In particular, to accurately characterize the structure of the crowns, typically small footprint multireturn LiDAR data are acquired. The footprint
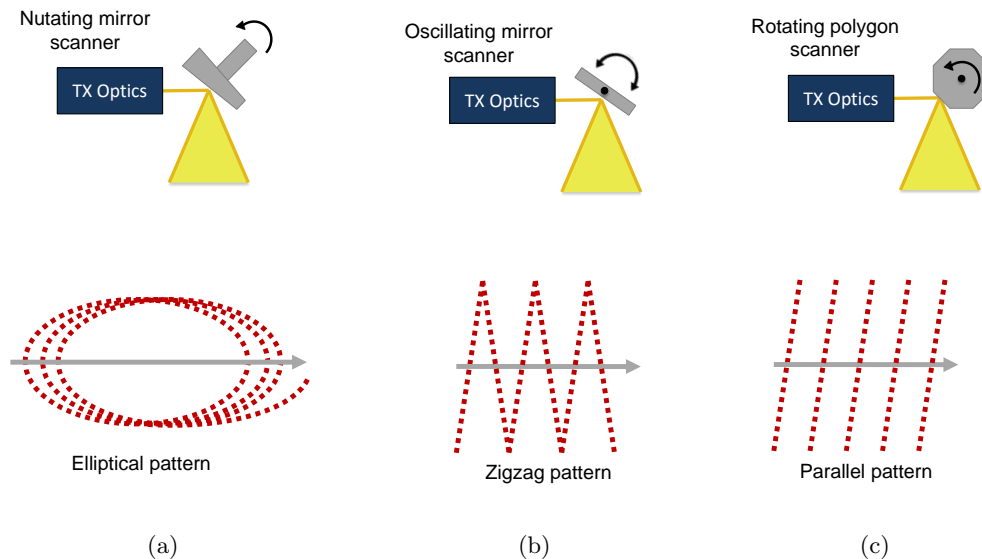
Figure 1.3: Examples of theoretical LiDAR scanning patterns: (a) elliptical pattern, (b) zigzag pattern, and (c) parallel pattern. The presented spatial arrangement of the pulse returns is the one expected in case of flat surface.

diameter depends on the beam divergence and the flying altitude. In greater detail, it is defined as the beam diameter intercepted by a plane positioned perpendicularly to the beam direction at a distance from the instrument equal to the nominal flying altitude. Fig. 1.2a presents a practical example where, for the same flying altitude (i.e., 2000 m), different footprint diameters are obtained because of the different beam divergence. Indeed, even though in a true laser system the trajectories of the photons generate a cylinder, in a beam emitted by a LiDAR instrument their trajectories slightly deviate, thus forming a narrow cone. By increasing the distance between the laser and the target, the footprint diameter increases. To obtain an accurate representation of the forest structure, small footprint (i.e., 0.1m - 2 m) are preferred because they facilitate accurate linkages between the LiDAR point cloud and the individual trees or forest stands. Indeed, the distribution of the pulse energy is not uniform within the footprint, thus it is usually approximated with 2-D Gaussian distributions since it radially decreases from the center.

Together with the footprint diameter, one of the most important ALS operational specification is the point spacing on the ground (i.e., laser point density). This parameter is affected by the flight properties such as flying altitude, flying speed and scanning pattern, and the sensor properties in terms of PRF and scan angle. The PRF (or scanning frequency) is the number of laser beams emitted by the laser per second. While old instruments were able to record few thousand pulses in 1 second, modern sensors typically operate at 100 kHz up to 400 kHz. The choice of the PRF has a significant impact in the ALS derived metrics because of the introduction of noise. In [4] the authors demonstrate that by increasing the PRF an upwards shift is visible in the canopy height distribution and the proportion of multiple echoes decreases. Accordingly, between different PRFs

(50 kHz and 100 kHz), different forest parameter estimation are obtained, especially for metrics derived from the last echoes. The scan angle is defined as the off-nadir angle at which the sensor acquires during scanning. By increasing the scan angle it is possible to reduce the acquisitions cost, because of the possibility of covering more ground in a single flight line. However, canopy penetration deteriorates at higher values of scan angles. Moreover, height measurement errors are visible with scan angles $> 10°$ off-nadir [5].

To collect the LiDAR point cloud all over the considered scene, the direction of the laser beam needs to be moved across the flight direction while the aircraft is moving since it can illuminate a single point at once. Depending on the mechanism used to direct pulses across the flight lines, multiple types of patterns are defined. Indeed, during the ALS acquisition, the laser beam is pulsed towards a mirror and projected downward from the aircraft. Moreover, the beam is scanned from side to side by a moving optics as the aircraft flies over the investigated area according to a specific scanning pattern. Fig. 1.3 presents the most common scanning patterns employed. Even though the configuration is usually designed to preserve equal spacing between returns, in real acquisition scenarios pulse density is not uniform and laser density eventually is higher at the end of the swath because of mirror deceleration. However, according to the scanning pattern, the footprint spacing along the scanning lines and the nominal footprint spacing between the scanning lines can be calculated (Fig. 1.2b).

1.1.3   Terrestrial Laser Scanning (TLS)

TLS systems refer to LiDAR acquisition performed from a static view point, typically a tripod, thus creating a 3-D point cloud of the surrounding vegetation. In the framework of forest parameter estimation, TLS is typically acquired for accurate local forest inventories. Indeed, it is a valuable tool for retrieving tree parameters because of its capability of recording high resolution profiles of the individual tree crowns. Moreover, the 3-D point cloud provided by the laser scanner solves the limitations in structural detail which can be measured by conventional forest inventory. Similarly to the airborne sensor, the basic concept of this system is the use of light to determine the target distance. TLS systems were initially developed for engineering and mining applications, with characteristics (e.g., cost, resolution, acquisition efficiency, portability) that precluded a favorable cost-benefit for forestry applications. However, in recent years the development of portable and cost-effective TLS increased the possibility of performing efficient forest structure assessment using these systems. The survey equipment used to collect TLS data include tripods, targets, tribrachs, target poles, and a laptop computer. Typically the radial survey method is used for the terrestrial data acquisition. The basic components of the TLS system are shown in Fig. 1.4.

Similarly to the airborne case, one of the most important system specification in TLS is the beam divergence. The initial beam diameter depends on the LiDAR instrument and can range from 0.1-1.0 millirads. Unlike the airborne case characterized by a constant flying altitude, in the terrestrial scanning the beam size on a target varies as a function of the initial beam diameter, the beam divergence and the target distance. Accordingly, the scan resolution is affected by this beam widening when the final spot size of the beam illuminates the target. The attributes within the illuminated area are averaged and
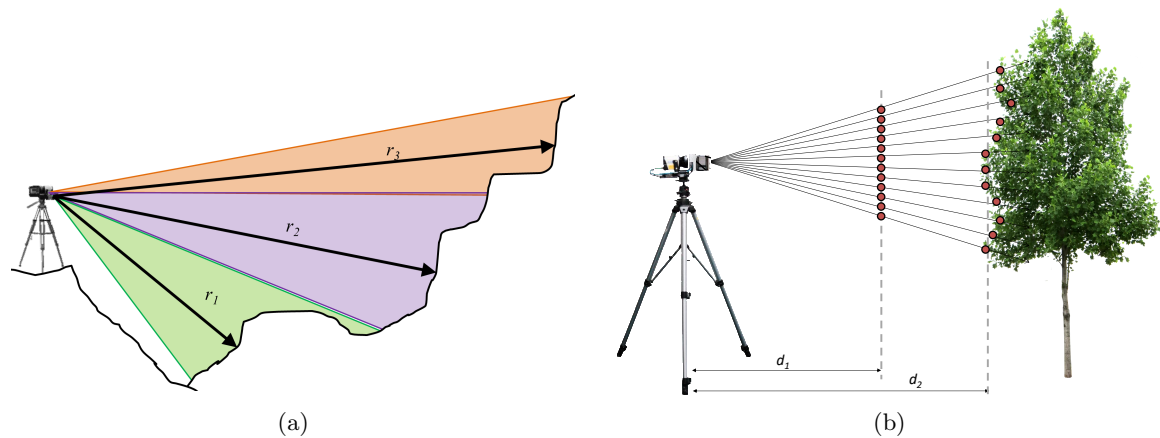
Figure 1.4: Basic components of the TLS system acquisition: (a) example of scan partitioning. For each scan, different angular steps should be considered to have the same point density in the whole acquisition, and (b) example of terrestrial LiDAR data acquisition. By increasing the distance of the scanner from the target, the point density decreases.

recorded by the receiver. Thus, the wider is the illuminated area, the less overall detail is gained on a scale smaller than the illuminated area. Together with the beam divergence, the resolution of the terrestrial LiDAR data is affected by the angular resolution, which influences the point density. The point density of the TLS systems depends on the distance of the target and the angular step. The higher is the distance of the target from the scanner, the lower is the point density acquired (Fig. 1.4b). However, by decreasing the angular step of the laser beam, the spot space decreases, improving the spatial resolution of the data. Thus, to obtain a high resolution scan at long ranges, the angular step should be tuned considering the distance from the target. In particular, this parameter can be adjusted in the vertical and the horizontal directions in order to obtain a very high points density acquisition. It is worth noting that extremely dense point clouds require more storage space and take a longer time to scan. This impacts both the time spent out in the field collecting data and the data processing computational complexity. Finally, the terrestrial LiDAR acquisitions are strongly affected by the topography of the scene because of the varying ranges of the objects measured by the sensor within the same scan. For this reason, in order to obtain a homogeneous point density acquisition in the entire scene, the scan needs to be partitioned into several scans at determined mean distance intervals (Fig. 1.4a). Then, the angular step should be adjusted as a function of that mean distance to achieve the same resolution and point density. In particular, since TLS scans along vertical and horizontal orientations, vertical and horizontal partitioning needs to be taken into consideration during a complex project.

1.1.4 Passive Optical Sensors

Passive optical sensors record the energy emitted and reflected by the Earth's surface operating at visible, near infrared, short-infrared and thermal infrared wavelengths. These systems are passive sensors, as they do not illuminate the target and thus cannot operate
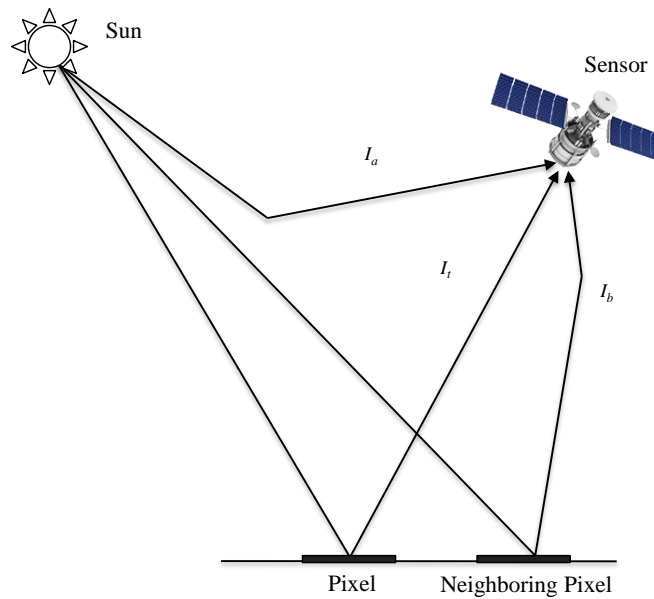
Figure 1.5: Representation of the main components that affect the radiance recorded by the sensor.

without the sun radiation. The solar radiation spectrum can be modeled by a black body with source temperature of 5900 K, with a peak radiation located at wavelength of about 500 nm. The signal measured by the sensor is mainly the radiation coming from the sun, which is reflected by the Earth's surface passing through the atmosphere. A small amount of energy is also directly emitted by the Earth's surface. The interaction between the solar radiation and the gas molecules present in the atmosphere strongly affects the solar radiation. Thus, only the wavelength regions of the electromagnetic spectrum where the atmospheric gas absorption effect is minimized can be used for remote sensing. Fig. 1.5 shows a schematic representation of the main components that affect the radiance recorded by the sensor which are: (i) the radiation scattered by the atmosphere I_a in the viewing direction, (ii) the radiance reflected by the target I_t and transmitted to the sensor, and (iii) the radiation reflected by the background I_b. The measured radiance hit the electronics detectors (i.e., the Charge Coupled Device (CCD)) placed on the focal plane. The signal focused by the optics of the imaging system is converted into electrical current to obtain the digital image and be stored.

In a real acquisition scenario, the energy emitted by a point source is spread over the finite size of the cells of the CCD sensor. This effect, due to the sensor's focal length f and the detector width w, determines the spatial resolution of the image, which is the capability of the sensor of distinguishing two spatially adjacent points on the ground. The angle subtended by a single detector element on the axis of the optical system is referred as the Instantaneous Field of View (IFOV). When dealing with remote sensing data acquisition, passive sensors are usually mounted on aircraft or spaceborne platforms. In this thesis we focus the attention on optical images acquired by airborne platform. According to the altitude of the aircraft, by projecting the IFOV on the ground we obtain the Ground-projected Instantaneous Field of View (GIFOV), which corresponds to the
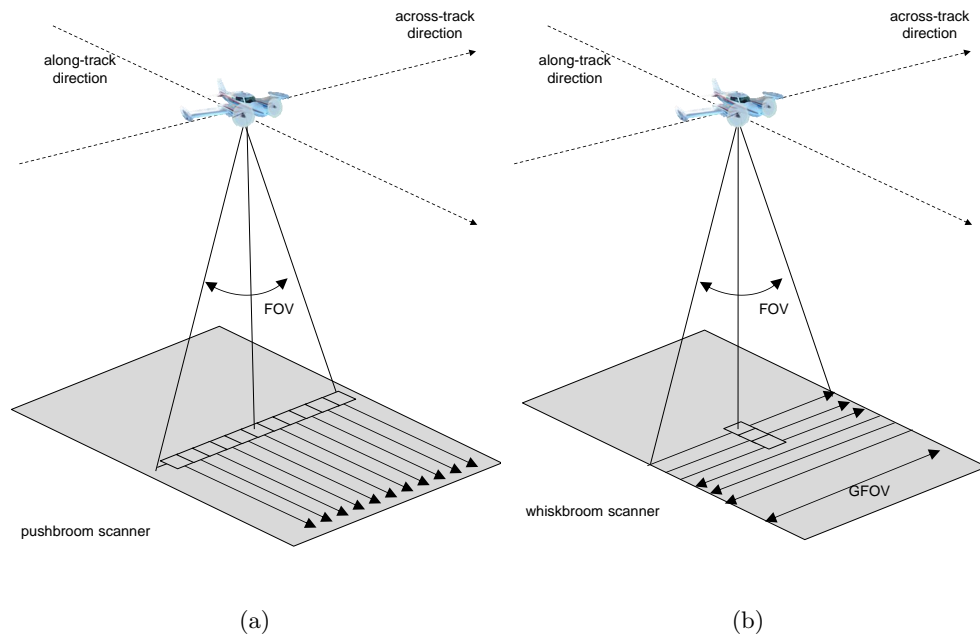
Figure 1.6: Examples of scanning methods for the acquisition of optical images: (a) pushbroom scanner, (b) whiskbroom scanner.

geometrical resolution of the optical image (i.e., pixel size). Thus, each pixel represents a portion of the investigated area enclosed in the angular cone of visibility of the sensor at a given flight altitude.

To generate the optical image, the scanning in the *across-track* direction (orthogonal to the motion of the sensor platform) is combined with the motion of the platform in the *along-track* direction. According to the number of detectors used to scan, different scanning patterns are used. Fig. 1.6 shows the main types of scanning patterns for the acquisition of optical images: the whiskbroom scanner and the pushbroom scanner. The whiskbroom scanner uses several CCD detectors aligned in track to achieve parallel scanning, thus acquiring more pixels simultaneously. However, to scan the entire scene a rotating mirror which moves back and forth across the flight direction is required. The mechanical rotating mirror limits the acquired spatial resolution due to slower data rates. The pushbroom scanner, also referred to as *across-track* scanners, is a wide-angle optical system which uses a linear array of thousand of CCD detectors arranged perpendicular to the flight direction. While the aircraft flies forward, the scanner is acquiring one line at a time of the optical image. Although the detectors need to be perfectly calibrated to avoid striping artefacts, these systems allow the fast acquisition of high data rates. Thus, this technique is suited for high resolution sensors.

In this framework, it is clear that the information content of the remote sensing images strongly depends on the amount of details recorded according to the spatial resolution of the image, which indicates the smallest distance between two objects that can be distinguished in the image. When acquired with high spatial resolution (i.e., smaller than 1 m), optical images allows the precise recognition of the shape and the geometry of the

analyzed scene. For this reason, high spatial optical images represent an important source of information for environmental monitoring. However, the energy emitted by the source is quantized both from the spatial and the spectral view point. Thus, together with the spatial resolution, one of the most important characteristic of the optical sensor is the spectral resolution, which describes the sensitivity of a sensor to the wavelength interval. The finer is the spectral resolution, the narrower is the wavelength range for a particular channel or band. To characterize the target, it is possible to analyze its reflecting behaviour at different wavelengths, i.e., its spectral signature. Indeed, depending on the chemical and physical characteristic of the object, the solar radiation can be transmitted, absorbed or reflected by the target surface in a different way in different portions of the electromagnetic spectrum. If the optical remote sensing system has a sufficient spectral resolution, the object can be identified by its spectral signature. Depending on the application, the main passive optical remote sensing sensors that can be considered are: multispectral sensors and hyperspectral sensors. Multispectral sensors are characterized by a few broad bands (< 10), whereas hyperspectral sensors have up to a few hundred of very narrow spectral bands. These data are a rich source of information for precise recognition and characterization of the material and objects on the ground, thus facilitating fine discrimination between different targets based on their spectral response in each of the narrow bands. Hyperspectral images allow the precise identification of land-cover classes and thus, they are suited for application such as detailed classification of forest areas. In this thesis high spatial resolution and high spectral resolution optical images are considered.

1.2 Related Works: Remote Sensing and Forestry

The estimation of forest attributes has been effectively improved by the use of the remote sensing technology. The traditional approach to forest inventories is based on ground measurements that are collected for some stand plots usually chosen by randomly sampling a forest area. Then, these measurements are statistically extended to the entire area in order to obtain global estimates of the forest parameters (e.g., average tree volume, average tree height, tree density). For obtaining reliable estimates, the amount of data collected should be representative of the entire forest ecosystem considered. However, field surveys are costly, time consuming and constrained by lack of access to remote areas (especially in mountainous scenarios). In this context, remote sensing represents an important tool for monitoring objectively and accurately large forest areas. In the following a brief analysis of the state-of-the-art on the use of remote sensing data for forest parameter estimation is presented. In particular, in this thesis we focus the attention on LiDAR data and optical images even though SAR data have been employed for single tree detection [6, 7]. More details on specific topics will be given in the next Chapters.

1.2.1 Forest Parameters Estimation with LiDAR Data

LiDAR is a well established active remote sensing technology widely employed for estimating forest parameters [8, 9]. As mentioned in the previous section, the sensor is

typically mounted on an airborne platform (ALS) or a terrestrial platform (TLS). Due to the capability of the ALS systems of collecting measurements on wide forest areas with high spatial resolution, in many countries it has been incorporated as tool for operational forest inventories [10, 11, 12]. Moreover, ALS data have been extensively employed in many countries to generate detailed Digital Terrain Models (DTMs) [13, 14].

Research studies on the use of ALS for modelling forest attributes began in the mid-1970s with experiments using simple profiling instruments. However, the commercial development of ALS measurements started in 1990s, when the system was integrated with the GPS and the INS instruments, thus facilitating the accurate positioning of the scanner. The very early studies addressed the estimation of the forest parameters at stand level, i.e., the area-based approaches, later refined by the more accurate individual tree approaches. The area-based approaches aim to estimate forest parameters such as stand volume or basal area by considering groups of trees [15, 16, 17, 18]. Typically, the predicted variables are the ALS height distribution attributes collected over the entire stand plot (i.e., mean height, height percentiles, return density, etc.). In [15], the authors present a method for the estimation of forest stem volume at stand level by training a multiplicative regression model based on statistical LiDAR derived variables. The paper demonstrates the importance of dividing the sample plots in homogeneous forest age classes (i.e., young forest, mature forest in good site quality and mature forest in poor site quality) to obtain accurate estimation results. Indeed, one of the main limitation of the area-based approach is that regression models used to link ALS derived metrics to the predicted variable have limited portability to other species or other study areas. This is confirmed by the results obtained in [16], where the authors evaluate the performances of a multiplicative regression method widely applied to boreal forest region when used on the alpine scenario in Vorarlberg, Austria. The results demonstrate that to obtain comparable estimation accuracy to the one obtained in a boreal forest, it is necessary to re-calibrate the regression model by using inventory data collected in the local forest. Thus, to obtain reliable estimates the stand level approach requires sample plots with similar properties.

Due to the visibility of single trees in high-density LiDAR data, to obtain more accurate estimates, the individual tree crown approach is usually considered [19, 20, 21, 22, 23, 24, 25]. For individual tree level inventories, the estimation of the forest attributes requires the tree detection and delineation, the feature extraction, and finally the regression of the considered forest variables. In this framework, the accuracy of the segmentation results strongly affect the crown parameter estimation. Not all trees can usually be detected due to the different forest condition. Indeed, the stand density and spatial pattern of the forest play a dominant role in the number of trees identified due to the problems related to both interlaced tree crowns and understory vegetation [26]. However, the performance of the tree identification is influenced by the detection algorithm and its parameterization [27]. To perform the estimation of the tree attributes, different features can be considered. Some papers address the tree parameters estimation through linear regression models based on LiDAR derived height and LiDAR derive crown radius [20, 21, 22]. In this case the crown delineation result plays a crucial role in the estimation accuracy since it is directly linked to the predictors. Although the geometry of the crown is well described

by theses two parameters, they are not sufficient to accurately model the variability of the tree attributes especially in heterogeneous forest scenario. Thus, to obtain a more detailed characterization of the canopy structure, some papers extract LiDAR point cloud metrics calculated from the area of the segmented crowns [23, 24, 25, 19]. In [25], after having segmented the single trees by means of a watershed segmentation algorithm, the authors extract a set of statistical variables from the LiDAR data to estimate forest stem volume. However, the accuracy of the results obtained was affected by the availability of first and last returns per crown. In contrast, a more detailed analysis could be performed when multiple returns per pulse are recorded. In [28] the authors extract a large set of statistical variables in order to select the pool of variables that better characterize the stem diameter. The variables extracted from the multireturn LiDAR data model the distribution of the laser pulses within the crown, thus representing the height of the tree, the horizontal and vertical shape of the crown, the crown internal structure and the forest species. In [19], the reported results show the strong correlation between the capability of the LiDAR to penetrate the crown and the precise characterization of the tree in the framework of the stem volume estimation. In particular, the authors demonstrated that the number of acquired returns is directly proportional to the crown depth and, thus linked to the volume of the tree. Few papers extended the analysis to the circular area around the tree [29, 30, 31]. Indeed, the stand density plays a fundamental role in the tree growth in terms of availability of water and sunlight and thus, in the estimation of its parameters. In [31] the authors define a competition index to evaluate the influence of the surrounding trees (i.e., competitors) on the DBH growth in old-aged forest. The height and the distance of the competitors are evaluated to quantitatively estimate their pressure on the growth of the considered tree. Results confirm the importance of modelling the forest environment.

Currently, large effort is devoted to the acquisition of TLS data because of the increasing need of having a precise estimation of the forest structure for monitoring biogeochemical cycles, fuel loading and habitat provision, as well as for forest management and planning. Although initially developed for applications in the built environment, increasing potential has been shown in the assessment of forest structure. However, this system is not suited for forest mapping but for local forest inventories. Indeed, TLS provides hemispherical scanning from a ground-based platform, and thus is tuitable for performing localized sampling of the forest structure. Most of the papers in the literature exploit the TLS data to perform accurate estimation of the 3-D structure of the crowns [32, 33], while others focus their attention on the precise reconstruction of the tree stem and branch structures [34, 35, 36]. Moreover, TLS surveys allow the automatic detection of the individual tree stems location with high accuracy [37, 38]. Indeed, due to the acquisition platform, very high resolution profile of sub-canopy tree crown structure are recorded. However, the main limitation of the TLS acquisition is the need of performing multiple scanning within the same forest to overcome occlusion. Multi-angular scans are labor-intensive and time-consuming due to the need of positioning reference targets to co-register the scans. Moreover, the geometric registration of the scans represents a complex task which often results in manual refinements.

1.2.2   Forest Parameters Estimation by Optical Images

As anticipated in the previous section, different remote sensing sources have been employed for the estimation of forest parameters. In the past, satellite optical images were one of the first remotely sensed data exploited for forestry applications. The main advantage of these data are the wide area coverage provided with a low cost acquisition, in particular when compared to the high cost related to field data collection. In regions such as Finland, Sweden or Canada, characterized by large forest areas, optical images have been employed for national forest inventories [39]. In particular, standard passive sensors have been mainly used for forest species classification. Depending on the spatial and the spectral resolution of the optical image, it is possible to solve the classification problem at different levels. While in the case of low spatial resolution multispectral images the classification analysis is limited to forest and no forest areas [40], by increasing the spatial/spectral resolution of the multispectral image is it possible to increase the capability of distinguishing different vegetation classes [41, 42, 43]. In [43] the authors demonstrate that by using Landsat Enhanced Thematic Mapper Plus (ETM+) images, they were able to distinguish eight different vegetation classes, whereas in [41] the authors classify six forest types using Quickbird images due to possibility of performing detailed geometrical analysis.

Although the use of multispectral data has a longer tradition for the species classification, when dealing with forest characterized by a high number of similar tree species the spectral resolution of these sensors is not sufficient to obtain accurate classification results. In [43] the authors were able to distinguish only three kinds of mangrove using Ikonos and Quickbird data because of relatively small number of bands with large spectral interval. In this context, hyperspectral data allow the distinction of different tree species and the analysis of similar forest types due to the dense sampling of the spectral signature [44, 45]. In particular, these data have become more popular in the recent years due to their increased availability. In [46] the authors present a comparison of the classification results obtained by using two multispectral sensors (i.e., the Landsat-7 ETM+ and the EO-1 ALI), and the EO-1 Hyperion hyperspectral sensor. The results demonstrate that with hyperspectral data it is possible to strongly improve the classification accuracy obtained with the multispectral data. In [47] the authors confirm the effectiveness of these data by accurately discriminating different coniferous species besides their similarity. Moreover, these data have been used to perform precise analysis of the forest environment such as the estimation of the chlorophyll concentration [48, 49, 50]. Just few radiance-based approaches have been developed for estimating forest biomass by exploiting the reflective characteristic of the vegetation, [51, 52, 53, 54]. However, this type of data do not provide any information about the vertical structure of the forest, thus reducing the capability of forest biomass estimation when dealing with dense forest scenario as demonstrated in [54].

Several papers have investigated the possibility of generating Digital Surface Models (DSM) by using optical images as an alternative to the laser scanner [55] or as additional information to combine with LiDAR data [56, 57, 58, 59]. In [55] the authors proposed a novel image matching technique for the reconstruction of the 3-D structure of the forest using pairs of stereo images. In the first experiment, the DSM derived from high resolution

aerial images allowed a better description of the 3-D structure of the forest with respect to the DSM obtained by using low-density LiDAR data (i.e. 0.5 pts/m^2). In particular, the authors compared the results obtained with manually measured reference points directly derived from the stereo images. In the second experiment, the best DSM is derived from a LiDAR characterized by 1.5 pts/m^2 compared to the result obtained using multitemporal satellite images. Similar results have been presented in [56], where the authors compared the estimation of plot forest variables derived from the DSM generated by using high-density LiDAR data (7 pts/m^2) and high resolution aerial images. LiDAR data achieved the best accuracy in the estimation of mean height, mean diameter and volume. In [58] the authors proposed a hybrid technique that combines photogrammetric Canopy Height Model (CHM) obtained by pairs of stereo aerial images supported by LiDAR data. LiDAR has been employed both for selecting the absolute orientation parameters of the stereo model and for deriving the ground elevation data. Results pointed out that the quality of the CHM was strongly affected by the dissimilarities of stereo images caused by the combination of view and sun angles, as well as by the complexity of the forest canopy surface. Indeed, in order to accurately match the two optical images, reference points (or edges) should be detected, which results to be difficult due to the different point of views of the images [55]. Moreover, the complex surface of the canopy could create occlusions that increase image matching uncertainty [60]. The results obtained showed an average Root Mean Square Error (RMSE) between the DSM generated by using satellite images and that produced by LiDAR data of 2.7 m, which increased to 5.3 m in the forest area. However, due to the need of more than one optical image on the same area, different illumination and atmospheric conditions or different image orientations could result to be very critical.

1.2.3   Data Fusion Approaches to the Estimation of Forest Parameters

The fusion of LiDAR data and optical images has been widely addressed in the literature since the integration of these data can lead to more accurate estimation results. Also when acquired with high laser sampling density, LiDAR data can take advantage from optical images for better describing the structure of the forest. Indeed, high spatial resolution optical images provide a detailed representation of the horizontal structure of the forest, whereas LiDAR data not always allow a precise reconstruction of the 3-D shape of the target (e.g., building corner missing) because of the irregular sampling of the LiDAR points. However, the laser scanner is able to measure the vertical dimension of the target. In [61] the complementary of these data is demonstrated for the individual tree crown segmentation. While the high resolution optical image allow a better segmentation results in dense forest area, ALS are more effective in the delineation of isolated tree crowns. Thus, the vertical information measured by the LiDAR sensor allows the correct discrimination of ground and forest areas. In contrast, due to the illumination conditions, the radiance values of bare soil and forest are similar in the optical image, but the high spatial resolution gives a geometrical detail that allows a better representation of the crown structure in dense forest areas. By fusing the information brought by the data sources, the number of the false tree detected on the optical image was strongly reduced. In [62], an approach to the detection of the single trees was applied to both LiDAR data

and high resolution aerial photo. The results confirm that optical images are suited for describing dense forest, whereas LiDAR data allow higher accuracy on lower tree density areas.

The importance of integrating the laser scanner information with the optical images is even more evident in the estimation of forest parameters mainly related to the vertical dimension. Some papers address the stem volume estimation issue by fusing low-density LiDAR data and optical images [63, 64]. In [63], the authors demonstrate the importance of a having a precise tree height estimation for accurately estimating the tree volume. They compare the results obtained by extracting the tree-top height from 3 high-density LiDAR datasets of respectively 57, 25 and 9 point/m^2 and 3 low-density LiDAR dataset of 0.25 point/m^2 from the same segmentation result obtained on a high resolution optical image in order to calculate the volume at single tree-level by means of an allometric equation. Finally, they compute the error metrics of the entire stand. In the high-density case the root mean square error (RMSE) ranges from 156.0 m^3/ha to 163.6 m^3/ha, while in the low-density case the RMSE ranges from 205.4 m^3/ha to 209.0 m^3/ha. The technique proposed in [64] combines optical data acquired by the SPOT5 satellite with tree height information provided by laser scanner. A multiple linear regression analysis is developed for both each source and the combination of the two data sources in order to perform volume estimation. The joint use of the two sources improves the volume estimation of 49% compared to the use of the only optical image, reducing the RMSE on the average volume from 31% to 16%. In [65], the authors exploit the combination of an aerial photograph and low-density LiDAR data in order to delineate the tree crowns and estimate the tree height. The optical image corresponding to the studied area is segmented for deriving the canopy shape of the trees (coconuts plantation) while LiDAR data are used to derive the tree height of each individual tree identified. In order to delineate the tree crowns a contouring technique is applied to the green band. Although the segmentation algorithm applied to the aerial photo successfully detects the crowns, the LiDAR derived height is underestimated due to the low-density LiDAR data acquisition.

The combination of ALS and multi- or hyper-spectral data provides valuable complementary information for the species classification. The integration of the two remote sensing data improves the classification accuracy of those species having similar spectral signature but different height values [66, 67, 68, 69]. In particular, two main approaches have been explored to combine optical and LiDAR data: (a) the individual tree crown approach, (b) the pixel approach. In the first case, the features extracted from the spectral and the ALS data are combined per crown area [70, 71], whereas in the latter case the features are extracted per pixel and afterwards the pixel level classification map is aggregated per tree crown extracted from ALS data. Some studies that follow the pixel based approach do no perform the crown aggregation [66, 72] to obtain a classification map that is not affected by possible crown segmentation results. However, when working at individual tree level, it is possible to reduce the effect of the shadows which strongly impact the reflectance values. In [73] and [74], the authors reduce the classification error due to self-shading by considering for each crown only the pixels from the sunny side of the tree. However, both at pixel and at individual tree level, the joint use of these data improves the classification accuracy with respect to the results obtained by using

the singular remote sensing data. In [75] the authors obtained a sharp improvement in the classification accuracy combining hyperspectral and ALS data compared to only ALS or combined ALS and multispectral data. The kappa accuracy improved from 0.56, when using only ALS data, to 0.78 by combining the two data sources. In [70] the classification results obtained using only ALS for discriminating pine, spruce and deciduous trees (i.e., 87–88 %) increased up to 95–96 % by including the spectral mean values calculated at pixel level.

In the data fusion context, the combination of ALS with TLS has been explored in the framework of collecting detailed measures at plot level. In [76] the authors extract tree stem positions and attributes from TLS scan in order to train the ALS data. Indeed, TLS is an alternative to traditional field inventories for ALS forest assessment. However, when dealing with dense forest scenarios a manual noise removal in the areas surrounding the scanner should be done for obtaining an accurate stem detection. In [77] the authors examined the voxel column percentile distributions of point returns for both ALS and TLS and demonstrated that a higher percentage of laser pulses intercept the top of the canopy for ALS, with limited returns within the canopy and understory. Likewise, TLS exhibited a higher number of returns from the lower-canopy, but had fewer returns in the upper canopy. In light of this, there is a growing research interest in using TLS to complement the ALS [78, 79], and thus link ground-level structural measurements with the top view perspective of ALS. However, there has been limited research in this area, in part due to the difficult prerequisite of registration [80].

Chapter 2

Hierarchical 3-D Crown Segmentation Method

The estimation of the forest parameters at individual tree level is based on an accurate detection and delineation of the single tree crowns. Accordingly, the first contribution[1] of this thesis presents a novel hierarchical method to the 3-D segmentation of individual tree crowns in multilayered forest. The proposed approach allows the detection and the delineation of trees belonging to the dominant and the sub-dominant layers of the forest by using both the original point cloud and the rasterized version of the LiDAR point cloud (i.e., image domain). Unlike the state-of-the-art methods, the proposed approach does not require any prior knowledge on the forest stand properties (e.g., average crown size, forest density). It relies on the geometrical structure on the tree crowns and the properties of the LiDAR data. The effectiveness of the proposed method is confirmed by experimental results obtained on two LiDAR datasets characterized by different laser point densities.

2.1   Introduction

One of the most important step in the estimation of the forest attributes is the accurate segmentation of the individual tree crowns. To this end, many methods have been proposed in the literature [81, 82, 83, 84, 85]. Most of them focus on the analysis of the Canopy Height Model (CHM), the rasterized image obtained by interpolating the normalized LiDAR point cloud. The position of the trees is identified by detecting the peaks present in the CHM image, which should correspond to the top of the trees. Typically, these peaks are identified by means of a Local Maxima Filtering (LMF) Algorithm [84] or a Level Set Method (LSM) [86] applied to smoothed version of the CHM. Indeed, a Gaussian Filtering is necessary before segmenting the trees to avoid the detection of false

---

[1]Part of this chapter appears in:
C. Paris, D. Valduga, and L. Bruzzone, "A hierarchical approach to the segmentation of single dominant and dominated trees in forest areas by using high-density lidar data," in *Geoscience and Remote Sensing Symposium (IGARSS), 2015 IEEE International.* IEEE, 2015, pp. 65-68.

C. Paris, D. Valduga, L. Bruzzone, "A Hierarchical Approach to 3-D Segmentation of LiDAR Data at Single Trees Level in Multi-Layered Forest," *Geoscience and Remote Sensing, IEEE Transactions on*, in press.

tree tops while reducing the noise.

The crowns are delineated around each detected tree top in the CHM by means of region growing algorithms [84, 87, 88], watershed or pouring techniques [89, 90, 91, 92, 93, 94], or methods based on template matching [95, 96, 97]. However, in mixed forest stands, combinations of tree groups can be segmented in one single crown due to the smoothing introduced by the filtering process, thus degrading the accuracy of the tree parameters estimation [98]. In particular, in heterogeneous forest it is not possible to find the optimal smoothing factor because of the variable crown size [92]. To reduce the over-segmentation problem, in [87] the region growing segmentation results are constrained by rules on the shape of the crowns, whereas in [94] the watershed algorithm is driven by a prior estimation of the canopy size, thus reducing the applicability of the method to wide areas forest. Moreover, even though the rasterization provides the regularized version of the LiDAR point cloud, thus facilitating the analysis of the data, the spatial resolution of the CHM and the interpolation process influence the detection and delineation results. However, there are no reliable rules to select the spatial resolution of the CHM, which is constrained by the LiDAR data properties [99]. In [91] the authors present a strategy to determine the best CHM resolution at plot level by estimating the spatial stem distribution of the forest stand. By testing a set of candidate pixel sizes, the best spatial resolution is the one that allows the detection of a number of local maxima equals to the predicted number of stems. However, the method relies on the assumptions that all the trees are visible in the CHM and that the number of trees can be accurately estimated.

By comparing the segmentation results obtained in the CHM and the LiDAR point cloud, the highest accuracy is obtained in the point cloud domain [100]. In contrast, when performing the tree detection in the LiDAR point cloud problems arises in choosing the right scale [101] and with the irregular sampling of the tree crowns by the LiDAR sensor [102]. For all these reasons, several methods perform the detection in the CHM and the segmentation in the point cloud space by k-means clustering algorithm [103, 104, 105]. In [103] the authors compare the results obtained by setting the initial clusters centroids randomly or using the set of local maxima identified in the CHM. Moreover, they investigate the possibility of scaling down the height value instead of using the original one to minimize the intra-cluster variance and fit the conical shape of the crown. The highest accuracy are obtained by initializing the algorithm with the detected tree tops and re-scaling the height value. Indeed, shape constraints should be considered to obtain a reasonable result when clustering the trees to avoid ball-shaped clusters of LiDAR points [104]. However, the main lack of the detection algorithms applied to the CHM is the missing detection of the understory vegetation not visible in the image [106]. When dealing with multilayered forest it is necessary to detect both the dominant and the sub-dominant trees present in the scene to properly estimate the forest structure, to generate accurate fire behaviour models [107] as well as the forest planning.

To solve this problem, the detection analysis is extended to the LiDAR point cloud. In [108] the authors present a segmentation method suited for full waveform LiDAR data. The segmentation of the dominant trees is performed in the CHM by means of a watershed segmentation algorithm, subsequently refined by detecting the stems of trees to recover missed crowns. By analyzing the dominant segmented crowns in the LiDAR

point cloud, understory vegetation is detected using the normalized cut segmentation approach presented in [109]. Although this technique obtains high detection rate for small trees, many false trees are identified. Moreover, the detection of the sub-dominant trees strongly depends on several parameters. In [110], the authors perform a k-means clustering algorithm to segment the crowns of both the dominant and the sub-dominant layer of the forest. While the cluster centers of the dominant trees are the local maxima detected in the CHM, for the sub-dominant trees the centroids are placed at regular horizontal distance and the height is the half of the dominant tree mean height. While the dominant trees are properly segmented, many sub-dominant crowns delineated do not correspond to any field-measured tree. The identification of sub-dominant trees has been also addressed by applying a statistical analysis of the LiDAR point cloud [111, 112, 113, 114, 115, 116]. In [115] the authors detect the understory vegetation without tuning any parameters or thresholds. For each segmented dominant crown the height frequency distribution is computed and then interpolated with a polynomial function. By analyzing the behaviour of the interpolated curve sub-dominant trees are detected. Similarly in [116] the height distribution probability function of the entire stand plot is analyzed to split the LiDAR point clouds into two layers. However, this approach assumes the vertical forest structure characterized by two layers separable by a plane.

In this chapter we propose a novel hierarchical 3-D segmentation method to the detection of both dominant and sub-dominant trees. Unlike the methods presented in the literature, the proposed approach does not require knowledge on the considered forest area and unrealistic homogeneity assumptions on the average crown size. In contrast, it relies on the geometrical structure of the crowns and the LiDAR data properties. Accordingly, the proposed method can be applied to wide are forest characterized by variable crown size. In greater detail, the proposed approach: (i) exploits the joint use of the CHM image domain and the original LiDAR point cloud to improve the detection-rate of the dominant trees, (ii) detect the sub-dominant trees by analyzing the vertical profile of the dominant trees in different angular sectors, and (iii) delineates the dominant and the sub-dominant tree crowns directly in the LiDAR point cloud by means of a derivative analysis of the horizontal profile of the trees. To assess the effectiveness of the proposed method experimental results have been carried out in a complex dense forest scenario located in the southern Italian Alps by using very high-density LiDAR data (up to 50 pts/m^2) and high-density LiDAR data (up to 5 pts/m^2).

The rest of this chapter is organized as follows. Sec. 2.2 presents the proposed method for the automatic detection and delineation of the dominant and the sub-dominant trees. Sec. 2.3 shows the experimental results obtained on two LiDAR dataset characterized by different laser densities. Finally Sec. 2.4 draws the conclusion of the chapter.

2.2 Proposed 3-D Segmentation Method

The aim of the proposed method is the accurate segmentation of all the trees visible in the LiDAR point cloud. To decompose the segmentation process, and thus facilitate the segmentation problem, we exploit a hierarchical approach which concentrates sequentially on the dominant and on the sub-dominant layers of the forest. Fig. 2.1 shows the archi-
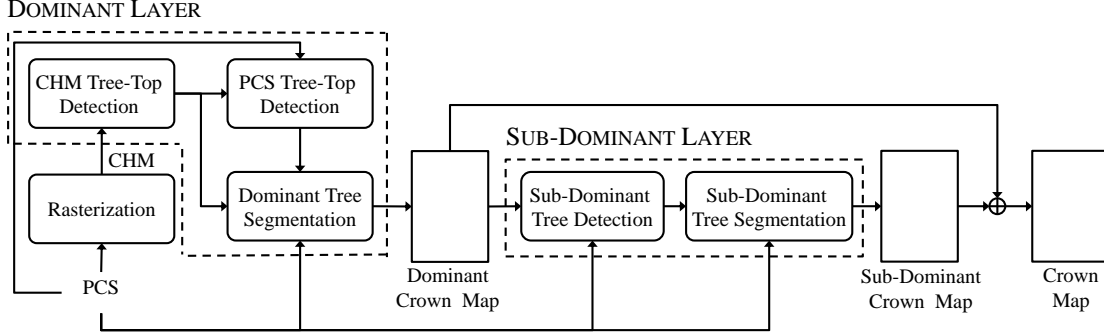
Figure 2.1: Architecture of the proposed hierarchical approach to 3-D segmentation of the dominant and the sub-dominant crowns.

tecture of the proposed method, where the Point Cloud Space (PCS) is the normalized LiDAR point cloud obtained after the subtraction of the Digital Terrain Model (DTM).

2.2.1 Dominant Trees Detection

The aim of the first step is the accurate detection of the dominant trees present in the scene. To this end, both the CHM and the PCS are considered to take advantage from the complementary of the two domains. While in the CHM it is possible to detect most of the trees present in the scene with a low computational load, the analysis of the PCS allows us to recover the missed tree tops. First, a coarse tree detection is performed in the image domain by applying a LSM [86]. Second, the analysis is refined in the PCS to detect close neighbouring trees that may not appear clearly separated in the CHM due to the smoothing filtering but are visible in the point cloud.

Let $\mathcal{P} = \{\mathbf{p}_1, \mathbf{p}_2, .., \mathbf{p}_N\}$ be PCS and let $\mathcal{T}_{\mathrm{CHM}} = \{\mathbf{t}_1, \mathbf{t}_2, .., \mathbf{t}_M\}$ be the set of tree tops detected in the CHM. Note that $\mathbf{p}_i$ and $\mathbf{t}_j$ are 3-element row vectors defined by the x, y, z coordinates, i.e., $\mathbf{p}_i = (x_i, y_i, z_i)$ and $\mathbf{t}_j = (x_j^t, y_j^t, z_j^t)$. To identify possible missed crowns, we analyze directly in the PCS the forest area around each tree top detected in the CHM. Let us define with $\mathcal{P}_j$ the set of LiDAR points extracted around the tree top $\mathbf{t}_j$ within a given search radius R_s, which is large enough to represent the surrounding crowns (e.g., three times the crown radius). The detection of the neighbouring tree tops in different directions is performed by means of an angular analysis which partitions $\mathcal{P}_j$ into N_θ angular sectors. Let Θ_k be the angular partition between the adjacent angles $\theta_k = 2\pi k/N$ and $\theta_{k+1} = 2\pi(k+1)/N$, with $k \in [0, N\text{-}1]$ (Fig. 2.2a and Fig. 2.2b). The set of LiDAR points belonging to the angular sector $\mathcal{P}_{j,\Theta_k}$ is defined as:

$$\mathcal{P}_{j,\Theta_k} = \left\{ \mathbf{p}_i \in \mathcal{P}_j \,\middle|\, \arctan\left(\frac{x_i - x_j^t}{y_i - y_j^t}\right) \in [\theta_k, \theta_{k+1}) \right\} \tag{2.1}$$

To detect the tree top of the neighbouring trees, we model the angular sector with a 1-D discrete signal $S_{j,\Theta_k}(\rho)$ composed by the coordinates z_i of the LiDAR points $\mathbf{p}_i \in \mathcal{P}_{j,\Theta_k}$
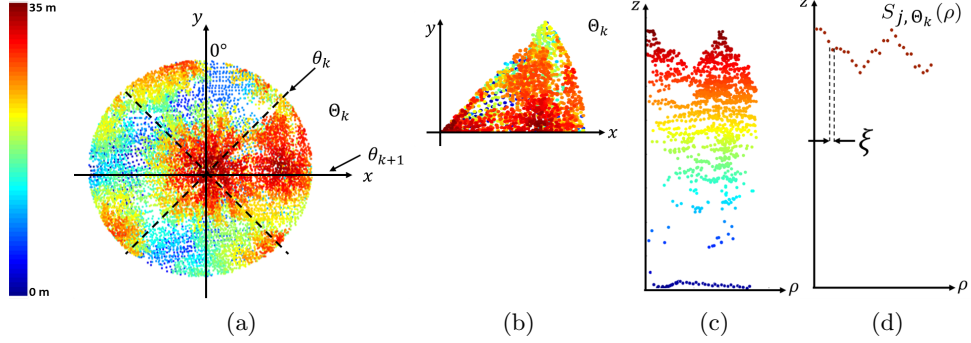
Figure 2.2: Example of angular analysis: (a) top view of the LiDAR point cloud $\mathcal{P}_j$ divided into N_θ angular sectors, with $N_\theta=8$, (b) top view of the angular sector Θ_k, (c) side view of the angular sector Θ_k after the circular projection, (d) side view of the 1-D discrete signal $S_{j,\Theta_k}(\rho)$ that approximates the shape of the crown in the sector Θ_k.

and depending on their distances from the tree top ρ_i, i.e.:

$$\rho_i = \sqrt{(x_i - x_j^t)^2 + (y_i - y_j^t)^2} \tag{2.2}$$

To this end, we first apply a circular projection to the points $\mathbf{p}_i \in \mathcal{P}_{j,\Theta_k}$ onto the ρz plane centered in the tree top coordinates (x_j^t, y_j^t). Let us define $\Pi_c : (x, y, z) \mapsto (\rho, z)$ as the circular projection that maps the points from the 3-D space $\mathbf{R}^3$ to the 2-D space $\mathbf{R}^2$ (Fig. 2.2c). Second, we keep the set of highest points belonging to the first return to represent the crowns surface. Accordingly, we quantize the distance of the points from the tree top $\rho_i \in [0, R_s]$ into F intervals $\xi = R_s/F$ and select the maximum height value in each ξ (Fig. 2.2d). Note that, the quantization step should be tuned considering the properties of the LiDAR data (i.e., footprint, point density) to guarantee that in each interval ξ the highest LiDAR point represents the crown surface. A similar angular analysis is presented in [117], where the authors refine the manual segmentation of tree crowns based on field measurements, by removing those sectors including LiDAR points of the neighbouring trees. In particular, they represent the angular sector considering the mean height values in each interval $\xi =0.5$ m. Then, by evaluating the trend of the sector profile, they determine possible over-segmentation. In contrast, we consider the maximum height value per interval to represent the shape of the crown and we aim to detect the position of the closest tree top.

A Gaussian filtering is then applied to $S_{j,\Theta_k}(\rho)$ to trim upper branches and thus avoid false local maxima. Unlike filtering applied in the image domain, we do not lose any detail while still smoothing the conical shape of the crown. Finally, for each 1-D signal $S_{j,\Theta_k}(\rho)$ we compute the discrete derivative $S'_{j,\Theta_k}(\rho)$ to detect the closest local height maximum, i.e,:

$$M_{j,\Theta_k} = S_{j,\Theta_k}(\rho_0), \text{ with } \rho_0 = \underset{\rho}{\operatorname{argmax}}\{S_{j,\Theta_k}(\rho)\} \tag{2.3}$$

To avoid false tree tops detection, a local maximum is considered a tree top when it is detected from at least two different tree apexes identified in the CHM. This is based on

the reasonable assumption that a missed apex is surrounded by more than one tree. Since we are dealing with dense forest scenarios, this cross check allows us to avoid false local maxima without losing possible tree tops. The new set of candidate tree tops $\mathcal{T}_{\mathrm{PCS}}$ is then compared with the set of tree tops $\mathcal{T}_{\mathrm{CHM}}$ to remove the redundancy. At the end of this step, we obtain the whole set of tree apexes $\mathcal{T} = \{\mathbf{t}_1, \mathbf{t}_2, .., \mathbf{t}_H\}$.

Note that the hybrid approaches presented in the literature typically refine the segmentation results obtained in the CHM by detecting the tree stems [108] or by fitting parametric models to the segmented point clouds [118]. However, tree stems are not always visible (especially in dense forest scenario). Moreover, to obtain accurate detection results it is necessary to properly tune the model parameters. In contrast, the proposed method jointly uses the CHM and PCS to improve the detection of the trees by relying only on the geometrical structure of the crown. Moreover, the proposed analysis of the PCS is not computationally demanding and thus can be easily applied to large forest areas.

2.2.2 Dominant Trees Segmentation

To avoid the drawbacks of the segmentation methods applied to the CHM, the crowns have been delineated in the PCS by means of clustering techniques [104, 103]. However, the bottleneck of these methods is the computational burden because of their need of processing the entire point cloud. Moreover, they do not consider the physical properties of the shape of the crown to perform the segmentation. In contrast, we aim to exploit the geometrical convex shape of the crowns to segment each single tree. Moreover, due to the angular analysis we are in the condition of accurately adapting the segmentation to the different portions of the crown by considering each angular sector separately. Furthermore, by focusing the attention on the set of LiDAR points $\mathcal{P}_j$ extracted around the tree top $\mathbf{t}_j \in \mathcal{T}$ within a radius R_s we can segment each crown separately and in parallel from the others, thus strongly reducing the computational effort.

By modelling the profile of angular sector $\mathcal{P}_{j,\Theta_k}$ with the discrete 1-D signal $S_{j,\Theta_k}(\rho)$, the position of the edge E_{j,Θ_k} can be associated to the first local minimum detected computing the discrete derivative $S'_{j,\Theta_k}(\rho)$, i.e.,

$$E_{j,\Theta_k} = S_{j,\Theta_k}(\rho_0), \text{ with } \rho_0 = \operatorname*{argmin}_{\rho}\{S_{j,\Theta_k}(\rho)\} \qquad (2.4)$$

By analyzing the distance ρ_i of the LiDAR points $\mathbf{p}_i \in \mathcal{P}_{j,\Theta_k}$ from the tree top $\mathbf{t}_j$, we can identify the points belonging to the crown C_j that are those having $\rho_i \leq E_{j,\Theta_k}$. At the end of this step the edge positions E_{j,Θ_k} with $k \in [0, N\text{-}1]$ within the angular sectors have been identified. Therefore, we can segment the crowns directly in the PCS thus generating the set of segmented crowns $\mathcal{C} = \{C_1, C_2, .., C_H\}$, where for each detected tree top $\mathbf{t}_j \in \mathcal{T}$ we associate the set of LiDAR points $C_j = \{\mathbf{p}_1, \mathbf{p}_2, .., \mathbf{p}_B\}$ belonging to the crown. Note that the size of the angular sectors can be the same of the one used for the detection of the tree top. However, to better delineate the crown contours it is possible to increase the number of angular sectors as long as there is a sufficient number of LiDAR points in each Θ_k to represent the shape of the crown. Finally, we check the set of trees detected by means of the derivative analysis to assess that those segmented point clouds have a
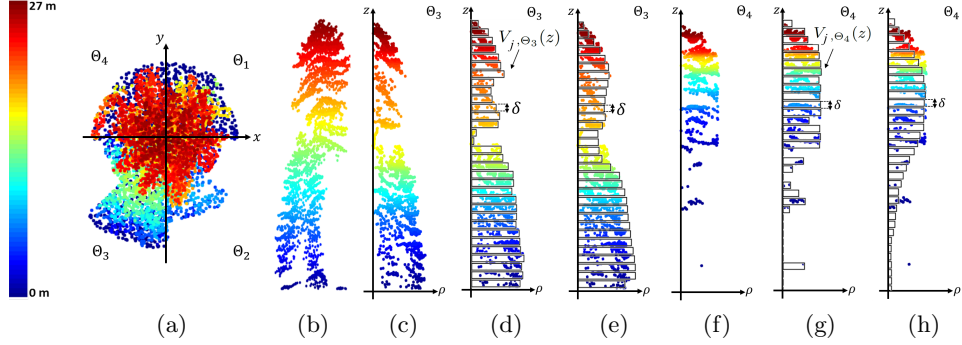
Figure 2.3: Example of sub-dominant tree crown detection: (a) top view of the dominant tree crown C_j divided into L angular sectors, with $L=4$, (b) side view of C_j, (c) vertical profile of the projected LiDAR points $\Pi_c(\mathbf{p}_i) \in C_{j,\Theta_3}$, where the sub-dominant crown is present, (d) vertical profile quantization $V_{j,\Theta_3}(z)$, (e) $V_{j,\Theta_3}(z)$ after the Gaussian filtering, (f) vertical profile of the projected LiDAR points $\Pi_c(\mathbf{p}_i) \in C_{j,\Theta_4}$, where no sub-dominant crowns are present, (g) vertical profile quantization $V_{j,\Theta_4}(z)$, (h) $V_{j,\Theta_4}(z)$ after the Gaussian filtering.

minimum number of LiDAR points. Indeed, in the case upper branches might appear as local maxima in the derivative analysis, the crowns delineated around them can be easily removed because they result in few LiDAR points.

2.2.3 Sub-Dominant Trees Detection

In this step we aim to detect all the sub-dominant trees covered by upper canopies. Therefore, we are not assuming that the forest is characterized by two layers of trees, but we can address the multilayered forest case. To automatically detect the understory vegetation, we first split each segmented crown C_j into L angular sectors (Fig. 2.3a and Fig. 2.3b), large enough to reveal the presence of sub-dominant trees. Thus, the number of angular sectors could be different from the number of sectors employed to perform the dominant tree crowns segmentation, i.e., $L \leq N$. Second, we analyze the vertical profile of each sector to detect both the presence and the height of the sub-dominant trees. Indeed, if there is a sub-canopy, it is reasonable to assume the presence of a hump in the bottom part of the vertical profile of the angular sector of the crown (Fig. 2.3c), otherwise not visible (Fig. 2.3f). Accordingly, we model the angular sector C_{j,Θ_k} with the 1-D vertical discrete signal $V_{j,\Theta_k}(z)$, composed of the distances from the tree top ρ_i of the LiDAR points $\mathbf{p}_i \in C_{j,\Theta_k}$ and depending on the height coordinates z_i. To this end, we first apply the circular projection Π_c to the LiDAR points $\mathbf{p}_i \in C_{j,\Theta_k}$. Let H_{j,Θ_k} be the maximum height value of the set of points C_{j,Θ_k}. Second, we quantize the height values $z_i \in [0, H_{j,\Theta_k}]$ into D steps $\delta = H_{j,\Theta_k}/D$ and select in each δ the LiDAR point having maximum distance ρ_i from the tree top $\mathbf{t}_j$ (Fig. 2.3d and 2.3g). Finally, a Gaussian filtering is applied to smooth the profile and reduce the noise introduced by the tree branches (Fig. 2.3e and Fig. 2.3h). It is worth noting that, unlike the 1-D discrete signal $S_{j,\Theta_k}(\rho)$ generated to perform the derivative analysis, $V_{j,\Theta_k}(z)$ depends on the variable z (instead of ρ) since we are interested in the vertical profile of the tree rather than in the horizontal one. By computing the discrete derivative $V'_{j,\Theta_k}(z)$, we aim to the detect the presence of a local
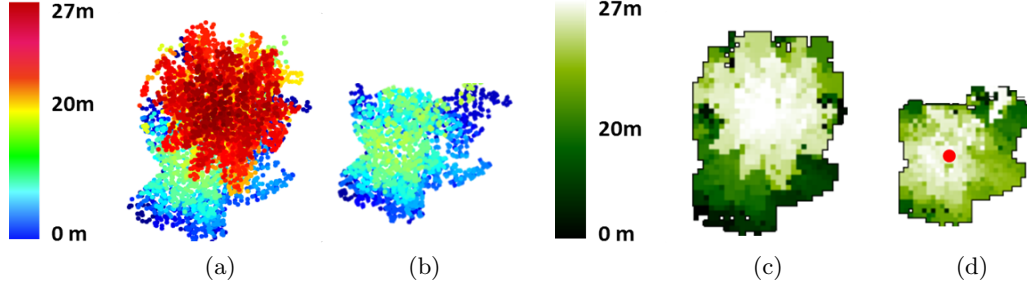
Figure 2.4: Example of sub-dominant tree detection: (a) top view of the dominant tree crown C_j in the PCS, (b) top view of the sub-dominant tree in the PCS obtained keeping the set of LiDAR point $\mathcal{P}_j^{\text{sub}} = \{\mathcal{P}_{j,\Theta_2}^{\text{sub}}, \mathcal{P}_{j,\Theta_3}^{\text{sub}}\}$, (c) CHM of the dominant tree crown, and (d) CHM of the sub-dominant tree crown, where the detected tree top is highlighted in red.

minimum which corresponds to the height of tree top of the sub-dominant crown $H_{j,\Theta_k}^{\text{sub}}$ located in the angular sector Θ_k, i.e.,:

$$H_{j,\Theta_k}^{\text{sub}} = V_{j,\Theta_k}(z_0), \text{ with } z_0 = \underset{z}{\operatorname{argmin}}\{V_{j,\Theta_k}(z)\} \tag{2.5}$$

Thus, if a local minimum is detected, we assume the presence of a sub-dominant tree in C_{j,Θ_k} (Fig. 2.3e), whereas if no local minima are identified we assume there is no understory vegetation in C_{j,Θ_k} (Fig. 2.3h). Let us define with $C_{j,\Theta_k}^{\text{sub}}$ the sectors where a sub-dominant crown has been identified. To detect the ground coordinates of the tree top $(x_j^{\text{sub}}, y_j^{\text{sub}})$ we consider only the set of LiDAR points $\mathcal{P}_{j,\Theta_k}^{\text{sub}}$ defined as:

$$\mathcal{P}_{j,\Theta_k}^{\text{sub}} = \{p_i \in C_{j,\Theta_k}^{\text{sub}} | z_i \leq H_{j,\Theta_k}^{\text{sub}}\} \tag{2.6}$$

Therefore, we generate the raster image of $\mathcal{P}_{j,\Theta_k}^{\text{sub}}$ and we detect the tree top of the sub-dominant tree by applying the LSM to the obtained CHM representing the understory vegetation (Fig. 2.4). In particular, adjacent angular sectors are rasterized in the same image to assess if they represent the same sub-dominant tree or different ones. In contrast, non-adjacent angular sectors are rasterized separately. Unlike the methods presented in the literature [115, 116, 119], by means of the angular analysis we are int he condition of detecting the presence of more than one sub-canopy below the same dominant tree. Moreover, the circular projection emphasizes the presence of the sub-dominant crowns, thus facilitating the detection. At the end of this step, we obtain the set of tree tops of the sub-dominant trees $\mathcal{T}^{\text{sub}} = \{t_1^{\text{sub}}, t_2^{\text{sub}}, .., t_G^{\text{sub}}\}$, where around each tree top t_j^{sub} we have the associated LiDAR point sectors, i.e., $\mathcal{P}_j^{\text{sub}} = \{\mathcal{P}_{j,\Theta_1}^{\text{sub}}, .., \mathcal{P}_{j,\Theta_S}^{\text{sub}}\}$, with $S \leq L$.

2.2.4 Sub-Dominant Trees Segmentation

In the final step of the proposed method, we extract the crowns of the detected sub-dominant trees directly in the PCS. For each tree top t_j^{sub} we consider the associated LiDAR point cloud $\mathcal{P}_j^{\text{sub}}$. Then, as in the dominant layer of the forest, we apply the angular analysis to automatically delineate the crown boundaries of the trees belonging to the sub-dominant layer of the forest. In particular, for each tree top t_j^{sub} we extract the crown C_j^{sub}, thus generating the set of sub-canopies $\mathcal{C}^{\text{sub}} = \{C_1^{\text{sub}}, C_2^{\text{sub}}, .., C_G^{\text{sub}}\}$.

2.3   Experimental Results

In this section we present the results obtained by the proposed method on two LiDAR data characterized by different laser point densities acquired in a complex mountainous scenario. First, we describe the dataset employed in the experiments. Then, an analysis of the parameters required by the proposed method is presented. Finally, the quantitative and qualitative results obtained are illustrated for both the dominant and the sub-dominant layers of the forest.

2.3.1   Dataset Description

To assess the performance of the proposed method we used two LiDAR data acquired in different geographical areas with different laser point density, hereafter referred to as the very high-density (i.e., average density of 15 pts/m^2) and the high-density dataset (i.e., average density of 5 pts/m^2). Both the study areas are coniferous forests located in the Southern Alps of the Trentino region (Italy). This mountainous scenario is characterized by a complex terrain's morphology due to the steep slopes and wide altitude range.

The very high-density LiDAR data were acquired between 7th and 9th of September 2012 with a Riegl LMS - Q680i sensor mounted on an airborne platform in the municipality of Pellizzano, Trentino region. The aircraft was flying at a speed of about 180 km/h at an altitude of approximately 660 m above the ground level. The pulse repetition frequency was 400 kHz and for each laser pulse 4 returns were recorded. The central point coordinates of the study area are 46°17′31,00″ N, 10°45′56,49″ E. The area extends approximately 3200 Ha and the altitude ranges from 900 to 2000 meters a.s.l.. The species composition of the forest is mainly Norway Spruce and European Larch. Field data were collected in 7 circular forest stands having radius 20 m (Fig. 2.5) characterized by different structure in terms of crown size and forest density. All of them are uneven-aged forest (i.e., inside the stand plot the trees have 3 or more distinct age classes), thus representing a complex test case.

Within the sample plot, for each tree the position (x, y coordinates), the height, the species were recorder, whereas we manually delineated the crown radius by means of an accurate visual interpretation (Tab. 2.1a). To this end trees were displayed in the 3-D LiDAR point cloud and the crown boundaries were manually drawn by an independent experienced operator. The crown segmentation was based on visual interpretation of the crown geometry both from the top and the side view of the considered tree. Because of the lack of sub-dominant trees in the sample plots, from the entire forest area a subset of 171 dominant trees were considered for validation purpose, 85 of which contain sub-dominant trees below, and 86 without sub-canopies. The presence of both the dominant and the sub-dominant trees was checked individually in the PCS to generate the reference data. The crown radii of the sub-dominant trees were manually delineated by visual interpretation.

The high-density LiDAR data were acquired on 4th September 2007 at Parco Naturale Paneveggio - Pale di San Martino, by means of an Optech ALTM 3100EA sensor. The LiDAR wavelength and the pulse repetition frequency are 1064 nm and 100 kHz, respectively. For each laser pulse four returns were recorded. The coordinates of the
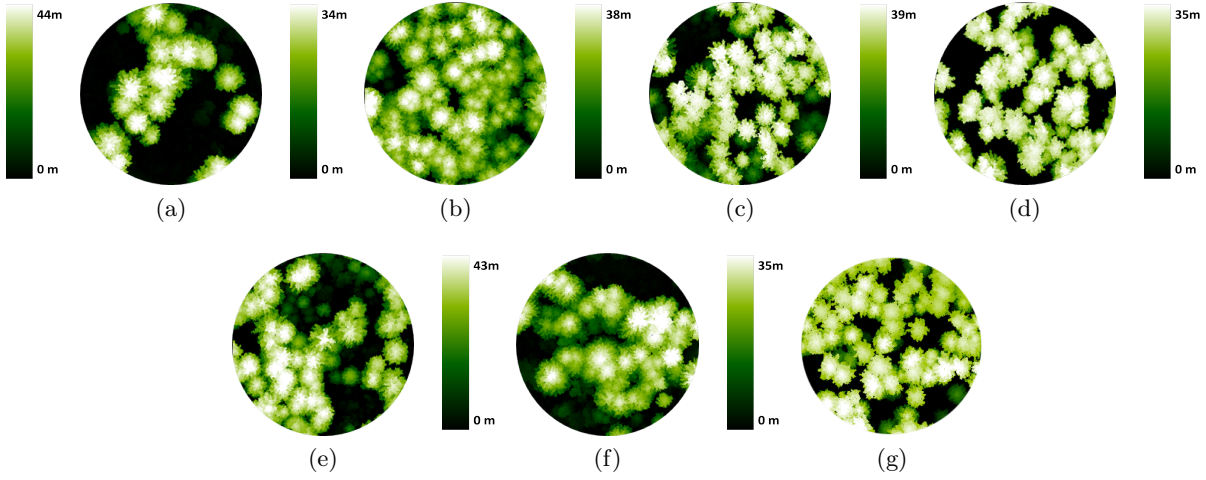
Figure 2.5:   False color representation of the CHMs representing the investigated stand plots for the very high-density LiDAR dataset. (a) Sample Plot H1, (b) Sample Plot H2, (c) Sample Plot H3, (d) Sample Plot H4, (e) Sample Plot H5, (f) Sample Plot H6, (g) Sample Plot H7. The rasterization has been performed with a spatial resolution of 25 cm.
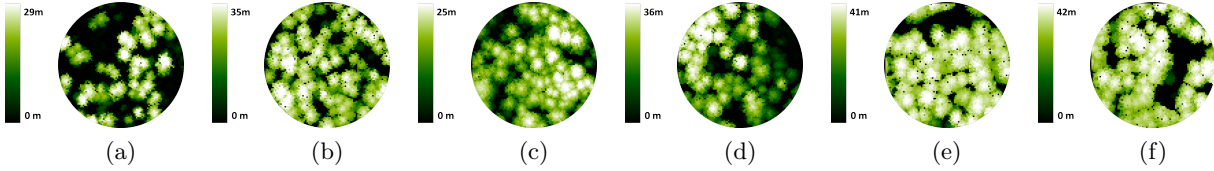
Figure 2.6:   False color representation of the CHMs representing the investigated stand plots for the high-density LiDAR dataset. (a) Sample Plot M1, (b) Sample Plot M2, (c) Sample Plot M3, (d) Sample Plot M4, (e) Sample Plot M5, (f) Sample Plot M6. The rasterization has been performed with a spatial resolution of 50 cm.

central point of this area are $46°17'47,60''$ N, $11°45'29,98''$ E. The area extends for 368 Ha and the altitude ranges between 1536 m and 2065 m. The dominant species are Norway Spruce and Silver Fir. Ground data are available in 6 circular stands plot of radius 20 m (Fig. 2.6). Within each stand plot, all the trees were measured. For each surveyed tree, the position (measured with respect to the center of the sample plot), the height, the species and the projected crown area were recorded. Also in this case the crown radii were manually delineated in the PCS for validation purpose (Tab. 2.1b).

To accurately match the surveyed trees to the segmented crowns, first the plot center coordinated were corrected by matching the dominant trees positions measured in situ with the tree tops visible in the CHM. Then, each detected tree has been associated to a field measured tree considering a maximum horizontal distance d_{xy} of 2 m and a maximum height difference d_h of 3 m.

Table 2.1: Number of trees, tree height (H) and crown radius (CR) presented divided per stands plot for the: (a) very high-density LIDAR data, (b) high-density LIDAR data. While the number and the height of the trees were measured in situ, the crown radii were manually delineated by visual interpretation.

Plot	Trees	H (m)		CR (m)	
		Range	Mean	Range	Mean
H1	14	34-44	38.4	2.9-5.5	4.4
H2	33	20.7-33.5	28.5	1.6-5.9	3.3
H3	37	24-37.4	33.2	2.1-4.1	3.1
H4	28	28.2-39.8	35.3	2.5-6.2	3.9
H5	31	3.6-35	23.6	1.2-5.2	2.8
H6	39	15-42.4	32.1	1.8-6.4	3.5
H7	36	27 - 35	31.3	1.6 - 4.5	3.1

(a)

Plot	Trees	H (m)		CR (m)	
		Range	Mean	Range	Mean
M1	33	4.4-28.3	21.4	1-3.6	2.3
M2	50	3.9-34.6	28.6	1-3.2	2.3
M3	24	16.6-24.4	20.6	1-3.6	2.4
M4	36	7.7-35.9	25	1-3.2	2.3
M5	45	34.6-40.5	38.1	2-3.2	4.1
M6	29	31.6-41.9	38.4	2-5	3.2

(b)

2.3.2 Sensitivity Analysis

Tab. 2.2 reports the values for the parameters used in all the experiments presented in this chapter for the very high- and the high- density LiDAR data. The tuning was carried out considering only the properties of the LiDAR data without the need of prior knowledge on the average crown size and forest density. The spatial resolution of the CHM was selected taking into account the density of the LiDAR data, whereas the 2-D Gaussian filtering was tuned considering the spatial resolution of the image to avoid commission errors. Accordingly, these values were the same for all the sample plots in the same dataset besides the average crown size.

The angular analysis was performed considering $N = 8$ sectors to have $\Theta = 45°$ for both the tree detection and segmentation regardless of the laser sampling density. Note that the value $\Theta = 45°$ allows the accurate representation of the different crown sides. The horizontal quantization step ξ was tuned considering the LiDAR point density to guarantee at least one LiDAR point per interval. In the considered dataset, ξ was equal to 0.3 m and to 0.6 m for the very high- and the high- density LiDAR dataset, respectively since the average point density was 15 pts/m^2 in the first case and 5 pts/m^2 in the second case. The Gaussian filtering applied to the 1-D discrete signal $S_{j,\Theta_k}(\rho)$ used for smoothing the crown profile and removing the outliers had a window size of 1×3, which can be used regardless of the LiDAR density and the crown size.

For the detection of the sub-dominant crowns the number of angular sectors L was 4. This conditions allows us to analyze the presence of the understory vegetation in 4 different portions of the dominant tree crown. From our experiments it turned out that in each sector an average of 20 LiDAR points for each quantization step δ is required to properly represent $V_{j,\Theta_k}(z)$. In our dataset, this condition was achieved setting $D = 29$, thus adapting the size of δ to the height of the crown. Accordingly, we fixed this value to perform all the experiments presented in this chapter. Fig. 2.7 depicts the behaviour of the number of detected trees and true negatives versus the value of D. Note that

Table 2.2: Recommended values for the parameters of the proposed method for the very high- and the high- density datasets. The tuning of the parameters is based only on the properties of the LiDAR data.

	Parameters	Values	
		Very High-Density	**High-Density**
Dominant	Spatial Resolution of the CHM	0.25 m	0.50 m
	2-D Filter Kernel Size	5×5	3×3
	2-D Filter Standard Deviation	10	5
	Search Radius R_s	20	20
	# of Angular Sectors N_θ	8	8
	Horizontal Quantization Step ξ	0.30 m	0.60 m
	1-D Filter Kernel Size (Horizontal Profile)	1×3	1×3
	1-D Filter Standard Deviation (Horizontal Profile)	4	4
Sub-Dom.	# of Angular Sectors L	4	-
	# of Vertical Quantization Step D	29	-
	1-D Filter Kernel Size (Vertical Profile)	1×7	-
	1-D Filter Standard Deviation (Vertical Profile)	4	-

the detection rate of sub-dominant trees increases as the value of D does. However, it leads to a lower detection of a true negative (i.e., high detection of false positive). Indeed, increasing the number of steps implies a better representation of the tree structure, but the number of LiDAR points per step δ decreases. Moreover, with too fine quantization scale some false trees can be detected because of the possible geometrical anomalies present in the vertical profile of the crown. Therefore, to obtain accurate detection results, it is necessary to have a reliable representation of the crown guaranteeing a minimum amount of LiDAR points per step.
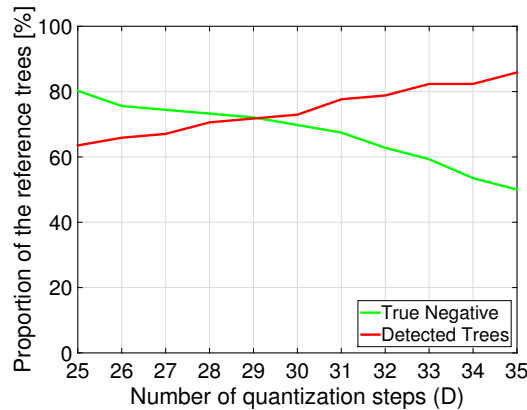
Figure 2.7: Behaviour of the vertical quantization step D vs the number of detected trees and true negatives for the sub-dominant layer of the forest.

2.3.3 Results on the Dominant Forest Layer

To evaluate the performance of the Proposed Method (PM), the detection results obtained were compared to the LSM [86] and the LMF [84]. In particular, the results were evaluated by considering the Detection Accuracy (DET), the Omission Error (OM) and the Commission Error (COM). The Detection Accuracy and the Omission Error represent the number of trees associated to the field data and the number of missed trees, respectively. The Commission Error represents the number of number of trees detected which are not associated to any field data. Tab. 2.3a and 2.3b show the detection results obtained with the PM, the LSM and the LMF on the very high- and the high- density dataset, respectively.

Both the state-of-the-art methods detect the trees only in the image domain. Therefore, the results are strongly affected by the degree of smoothing applied to the CHM. Moreover, while the LSM progressively slices the CHM to detect the tree top [86], the LMF exploit a sliding window to search the local peaks. Thus, the applied window size affects the detection results. Accordingly, a tuning of the state-of-the-art algorithms on a training set was necessary to ensure the best performance per forest type.

Even though the CHM provides the full representation of the dominant layer of the forest, the LSM and the LMF did not detect all the trees present in the scene due to the very high canopy density. In particular, the LMF achieved a lower detection rate compared to the LSM because of the window size, which was tuned to fit the larger crowns (to avoid too many false tree detected), thus penalizing the detection of the smaller crowns. This condition has less of an effect on the detection results for the high-density dataset (i.e., 183 trees detected compared to the 184 identified with the LSM) since the forest stands are characterized by homogeneous crown size (Fig. 2.6). In contrast, the choice of the window size strongly affects the detection in the very high-density dataset characterized by uneven-aged stands (i.e., 194 trees detected compared to the 204 identified with the LSM).

Differently from the state-of-the-art methods, the proposed approach exploits the information provided by the original LiDAR point cloud to refine the detection performance achieved in the CHM. Indeed, in the PCS the convex shape of the tree crowns is clearly visible and not affected by any interpolation process. Accordingly, the proposed approach is capable of handling the crown size variability within the same forest stand since it relies on the geometrical properties of the tree crowns. Thus, due to the further analysis in the PCS, the proposed method improved the detection rate regardless of the laser point density. This was achieved by keeping the commission errors under 7% and 2% for the very high- and the high- density dataset, respectively. In particular, in the very high-density dataset the PM identified 8 and 18 trees more than the LSM and the LMF, respectively, whereas it introduced only 3 and 4 commission errors more than the LSM and the LMF, respectively. In the high-density dataset the PM identified 16 trees more than the LSM and 17 more than the LMF, while incurring only 3 additional commission errors.

Note that on the very high-density dataset we obtained higher detection rate (i.e., 97.3%) than in the high-density dataset (i.e., 92.1%) because of the better characterization of the 3-D structure of the forest. However, while in the very high-density case the CHM provided enough information to detect the majority of the trees (the spatial resolution

Table 2.3: Tree detection results for the dominant layer of the forest obtained on: (a) the very high-density LiDAR dataset, (b) the high-density LiDAR dataset. The Detection Accuracy (DET), Commission (COM) and Omission (OM) Errors are presented divided per stand plot. The proposed method (PM) is compared with the standard LSM and LMF.

ID	#	PM			LSM			LMF		
Plot	Trees	DET	COM	OM	DET	COM	OM	DET	COM	OM
H1	14	13 (92.8%)	2 (14.2%)	1 (7.1%)	13 (92.8%)	2 (14.2%)	1 (7.1%)	11 (78.5%)	3 (21.4%)	3 (21.4%)
H2	33	30 (90.9%)	0 (0%)	3 (9.1%)	28 (84.9%)	0 (0%)	5 (15.2%)	26 (78.8%)	0 (0%)	7 (21.2%)
H3	37	36 (97.3%)	4 (10.8%)	1 (2.7%)	31 (86.4%)	4 (10.8%)	6 (13.5%)	31 (83.7%)	2 (5.4%)	6 (16.2%)
H4	28	28 (100%)	4 (14.2%)	0 (0%)	28 (100%)	2 (7.1%)	0 (0%)	27 (96.4%)	0 (0%)	1 (3.6%)
H5	31	31(100%)	1 (3.2%)	0 (0%)	31 (100%)	0 (0%)	0 (0%)	28 (90%)	3 (9.7%)	3 (9.,7%)
H6	39	38 (97.4%)	1 (2.6%)	1 (2.6%)	38 (97.4%)	1 (2.6%)	1 (2.6%)	36 (92.3%)	0 (0%)	3 (7.6%)
H7	36	36 (100%)	2 (5.6%)	0 (0%)	35 (97.2%)	2 (5.5%)	1 (2.78%)	35 (97.2%)	2 (5.5%)	1 (2.7%)
Tot.	218	212 (97.3%)	14 (6.6%)	6 (2.8%)	204 (93.6%)	11 (5.1%)	14 (6.6%)	194 (89.0%)	10 (4.6%)	24 (11%)

(a)

ID	#	PM			LSM			LMF		
Plot	Trees	DET	COM	OM	DET	COM	OM	DET	COM	OM
M1	33	31 (93.9%)	0 (0%)	2 (6.1%)	28 (84.8%)	0 (0%)	5 (15.2%)	26 (78.8%)	0 (0%)	7 (21.2%)
M2	50	46 (92%)	0 (0%)	4 (8%)	41 (82%)	0 (0%)	9 (18%)	43 (86%)	0 (0%)	7 (14%)
M3	24	22 (91.7%)	1 (4.1%)	2 (8.3%)	20 (83.3%)	0 (0%)	4 (16.7%)	20 (83.3%)	0 (0%)	4 (16.7%)
M4	36	34 (94.4%)	0 (0%)	2 (5.6%)	31 (86.1%)	0 (0%)	5 (13.9%)	29 (80.6%)	0 (0%)	7 (19.4%)
M5	45	41 (91.1%)	1 (2.2%)	4 (8.9%)	40 (88.9%)	0 (0%)	5 (11.1%)	38 (84.5%)	0 (0%)	7 (15.6%)
M6	29	26 (89.6%)	1 (3.4%)	3 (10.4%)	24 (82.7%)	0 (0%)	5 (17.3%)	27 (93.1%)	0 (0%)	2 (6.89%)
Tot.	217	200 (92.1%)	3 (1.3%)	17 (7.8%)	184 (84.8%)	0 (0%)	33 (15.2%)	183 (84.3%)	0 (0%)	34 (15.6%)

(b)

of the CHM is 0.25 m), in the high-density case the analysis of the PCS allowed us to halve the omission errors obtained with the LSM (i.e., from 33 to 16 missed trees). This reduction of the omissions strongly improves the estimation of forest parameters such as volume and structure, especially when dealing with trees characterized by an average height that ranges from 23.6 m to 38.4 m in Pellizzano (Tab. 2.1a) and from 20.6 m to 38.4 m in Paneveggio (Tab. 2.1b).

To quantitatively assess the crown delineation results, radii identified by visual interpretation were compared to the ones automatically detected by the proposed approach by considering: the statistical determination coefficient (R^2), the Mean Error (ME), the Mean Absolute Error (MAE), the Mean Square Error (MSE) and the Normalized Mean Square Error (NRMSE). Note that, the NRMSE is computed as the ratio between the RMSE and the range of the measured CR to facilitate the comparison between the dataset due to the different CR. Fig. 2.8a and Fig. 2.8b depict the scatterplots of the real versus the estimated crown radii of the correctly detected trees for the very high- and the high- dataset, respectively. The scatterplots show the capability of the angular analysis to properly delineate the single tree crowns regardless of the forest density and the laser sampling density.
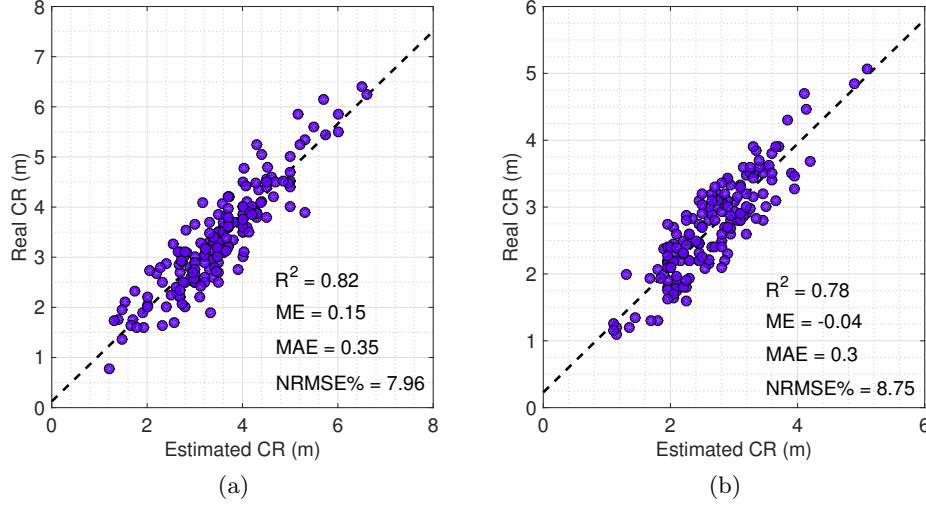
Figure 2.8: Real versus estimated (with the proposed method) crown radius (CR) of the dominant trees for: (a) the very high-density LiDAR dataset, (b) the high-density LiDAR dataset.

Due to the higher spatial resolution, the very high-density dataset resulted in a better delineation of the crown boundaries. However, the error metrics point out that we obtained accurate results in both of the dataset. Indeed, R^2 ranges between 0.78 to 0.82, whereas the NRMSE ranges from 7.96% and 8.75%. Because of the missed detection of some trees, there are few over-segmented crowns. For evaluating the overall method Tab. 2.4 reports ME, MAE, RMSE and NRMSE of the estimated crown radii divided per dataset. By taking into the omission errors we obtained a MAE of 0.52 m on an average crown radius of 3.4 m for the very high-density dataset (i.e., 15.3%), and a MAE of 0.51 m on an average crown radius of 2.6 m for the high-density dataset (i.e., 19.6%). A qualitative evaluation of the segmentation results confirms the effectiveness of the proposed method in detecting the crown boundaries. Fig. 2.9 shows some examples of crown delineation results by presenting the segmented trees in the forest area for the very high-density (Fig. 2.9a - Fig. 2.9f) and the high-density LiDAR dataset (Fig. 2.9g - Fig. 2.9l). As one can notice, the segmentation method was able to delineate the crowns of detected trees, despite the presence of overlapping and asymmetric crowns.

Table 2.4: ME, MAE, MSE and NRMSE of the estimated crown radius are presented divided per dataset. The error metrics include the over-segmentation error due to the omission errors.

Dataset	ME	MAE	MSE	NRMSE
Very High-Density	0.38 m	0.52 m	0.81	16.8%
High-Density	-0.26 m	0.51 m	0.59	15.1%
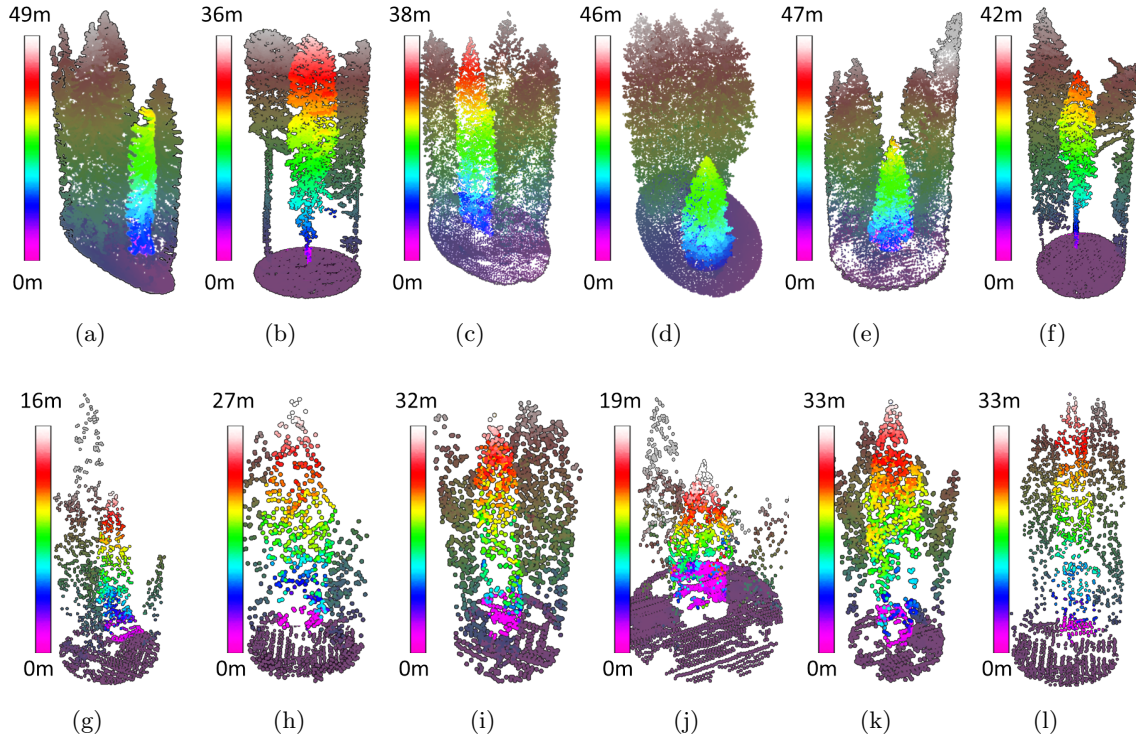
Figure 2.9: Qualitative example of tree crown segmentation obtained in the dominant layer of the forest for: (a)-(f) the very high-density LiDAR data, and (g)-(l) the high-density LiDAR data. The segmented crowns (represented in bright colors) are located in the original forest scenario. A visual analysis confirms that the proposed method is able to properly extract trees both in dense canopy scenario and when they are isolated regardless of the laser point density.

2.3.4   Results on the Sub-Dominant Forest Layer

To assess the effectiveness of the proposed method in the detection of the sub-dominant trees, the set of 171 trees selected in the very high-density LiDAR data was considered. The Detection Accuracy and the Omission Error represent the number of detected trees and the number of false negatives in proportion to the number of real sub-dominant trees (i.e., 85), respectively. The Commission Error represents the number of false positives in proportion to the number of dominant trees without sub-canopies (i.e., 86). Finally, the Overall Accuracy (OA) metric evaluates both the correct identification of the presence or absence of the sub-dominant trees in proportions to the total amount of trees (i.e., 171). The PM was compared with the Height Frequency Distribution method (HFD) presented in [115] and [108]. However, due to the assumption of double layer forest stands (not true for the considered dataset) in the latter case the technique resulted in both many commission errors and low detection rate. Thus, here we do not report the numerical results obtained. To have a fair detection comparison of the detection rate, the same set of dominant tree crowns extracted in the previous step was considered for both the HFD and the PM.

Tab. 2.5 shows the detection results obtained with the PM and the HFD [115]. Both

Table 2.5: Detection Accuracy (DET), Commission Errors (COM), Omission Errors (OM) and Overall Accuracy (OA) obtained for the sub-dominant layer of the forest with the Proposed Method (PM) and the Reference Method (HFD).

	DET	COM	OM	OA
PM	61 (71.8%)	24 (27.9%)	24 (28.3%)	123 (71.9%)
HFD	66 (77.6%)	43 (50%)	19 (22.3%)	109 (63.7%)

methods achieve similar performances in terms of number of detected trees (i.e., 61 with the PM and 66 with the HFD), whereas the proposed approach strongly reduced the number of commission errors (i.e., 24 compared to 43). This improvement is due to the analysis of the PM of the geometrical structure of the vertical profile, instead of considering the frequency height distribution. Indeed, when dealing with dense forest scenarios neighbouring trees are very close to each other and thus, the shape of the dominant crowns is no more symmetric. Accordingly, the presence of anomalies in the frequency height distribution is poorly correlated to the presence of understory vegetation as proved by the commission errors obtained by the HFD method. Moreover, the angular analysis allows us to address the issue of anisotropic crowns, while the projection of the laser points to the ρz plane (accomplished to represent the vertical profile of the tree) further reduces the influence of the asymmetry of the crown in the sub-dominant tree detection. Fig. 2.10 shows a qualitative example of the segmentation results obtained for the sub-dominant trees. As one can notice, the PM effectively extract the shape of the crown. Due to the angular analysis, the small trees can be extracted even though they are really close to the trunk of the dominant tree crown. The quantitative evaluation presented in Fig. 2.11 confirms the accuracy of the proposed approach in delineating the sub-canopies.
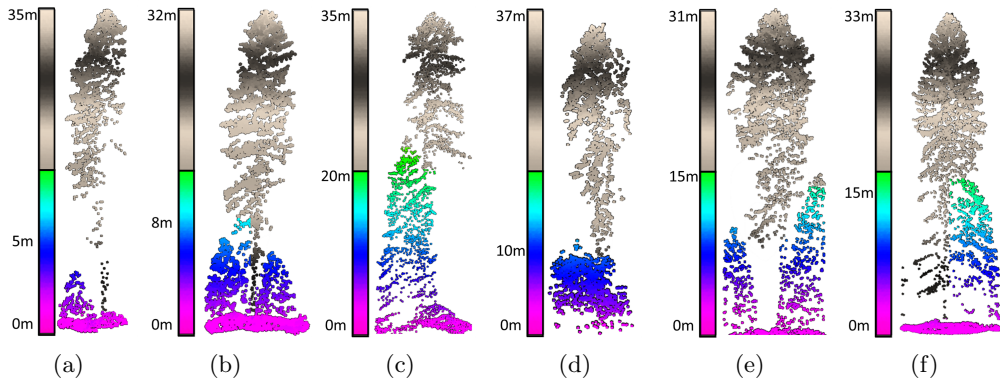
Figure 2.10: Qualitative example of tree crown segmentation obtained in the sub-dominant layer of the forest (very high-density LiDAR dataset). (a)-(f) the segmented crowns are represented in bright colors in the original forest scenario.
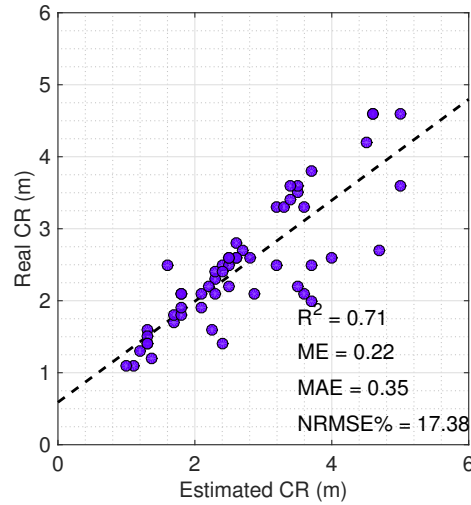
Figure 2.11: Real versus estimated (with the proposed method) crown radius (CR) of the sub-dominant trees.

2.4 Conclusion

In this chapter we presented a novel method to the 3-D segmentation of the individual tree crowns of both the dominant and the dominated layer of the forest. The obtained results demonstrate that the proposed method is able to improve the detection rate of the dominant trees with respect to the standard methods of the state-of-the-art. This is accomplished by refining the detection achieved in the CHM considering the information provided by the original LiDAR point cloud, which is not affected by the interpolation process and the smoothing filtering. Moreover, the method improves the detection accuracy while keeping the commission error rate under 7% for both datasets. Furthermore, the detection performed in the PCS proved to be robust with respect to the forest density and the average crown size since it relies on the geometrical properties of the tree crowns.

For the sub-dominant tree detection, the angular analysis of the vertical profile of the crown drastically reduced the commission errors while allowing the detection of multiple trees present below the same dominant crowns. Also in this case, the detection rate was better than the one obtained with the method presented in the literature. Finally, the proposed segmentation segmentation method is able to fit the shape of the trees for both the dominant and the sub-dominant trees besides the forest density. Indeed, the angular analysis performed in the PCS is able to adapt the crown delineation to the different portion of the crowns separately.

As future developments of this work, we aim at testing the proposed method on LiDAR data characterized by different point densities and in forests having properties different from the one used in the chapter. Moreover, we plan to test the effectiveness of the proposed approach on the full waveform LiDAR data. Finally, we aim to extend the method to the broadleaved forest, which represent a complex test case because of their crown umbrella shape difficult to delineate.

Chapter 3

Adaptive Tree Stem Diameter Estimation Method

The Diameter at Breast Height (DBH), together with the height of the tree, is one of the most important tree parameters for forest inventory. While the tree height is directly measured by the LiDAR sensor, DBH has to be estimated by means of regression models. To accurately retrieve the DBH of trees characterized by small and large stems, in this chapter we present a novel method for the adaptive estimation of the stem Diameter at Breast Height (DBH). The method is based on the identification of growth model classes. First, we aim to detect different tree growth model classes by means of a data-driven approach based on a clustering procedure. The clustering is performed considering all the environmental factors that can affect the growth of the trees (e.g., topography, forest density), modeled by a set of features extracted from the data. For each detected growth model class a tailored estimation model is trained to obtain accurate DBH estimation results. Experiments have been carried out in an Alpine mountainous scenario characterized by a complex topography and a wide range of soil fertility. The results obtained demonstrate the effectiveness of having multiple regression models adapted to the different tree classes.

3.1 Introduction

Diameter at Breast Height (DBH) is one of the most relevant tree parameter for the characterization of the structure of the forest. At single tree level DBH is fundamental to estimate the tree stem volume, the basal area as well as the carbon budget. At plot level, an accurate prediction of the tree diameter distribution is necessary to characterize the structure, the growth and the economic value of the forest stand (i.e., timber quality). However, while the height of the trees is directly measured by the laser scanner, DBH should be retrieved by means of regression models.

To address this issue, many papers in the literature estimate the DBH considering the height and the crown diameter measured by the LiDAR data ([95, 120, 121]). Although there is a correlation between the geometry of the crown and the stem diameter, these parameters are not sufficient to accurately model the variability of the DBH especially in heterogeneous forest scenario. To obtain a more detailed characterization of the canopy

structure, some papers extract LiDAR point cloud metrics calculated from the area of the segmented crowns ([28, 122, 123]). In [28] the variables extracted from the multireturn LiDAR data represent the distribution of the laser pulses within the crown, thus modeling the height of the tree, the horizontal and vertical shape of the crown, the crown internal structure and the forest species. However, despite the capability of these metrics to accurately represent the tree crowns, the characterization of the structure of the tree is not sufficient to obtain accurate DBH estimates. In this framework, some papers explored the possibility of extracting variables from the circular area around the tree in order to model the immediate forest neighbourhood ([29, 30, 31]). Indeed, the stand density plays a fundamental role in the expansion of the DBH in terms of availability of water and sunlight. In [31], the authors introduced a competition index to evaluate the influence of the surrounding trees (i.e., competitors) on the DBH growth in old-aged forest. The height and the distance of the competitors are evaluated to quantitatively estimate their pressure on the growth of the considered tree.

Much effort has focused on spatial statistical models ([124, 125, 126]) which take advantage from the spatial correlation for improving the accuracy of the predicted diameters. Indeed, it is reasonable to assume that the dendrometric variables of trees growing in the same forest area are more similar with respect to trees belonging to separate forest stands. In [124], the authors compared different statistical regression models and found that the linear mixed-effects model (LME) allows a better DBH estimation with respect to the geographically weighted regression (GWR), the ordinary least squares (OLS) and the generalized least squares (GLS) with a non-null correlation structure. Although LME does not directly incorporate the spatial information, the inclusion of random effects permit to focus on each individual tree by taking into account the lack of independence among trees belonging to same forest stand. Although these models improve the DBH estimation accuracy, in mountainous forest areas the properties of forest stands are not uniform due to the complex terrain morphology. Thus, the spatial distribution of the trees is not homogeneous and the terrain properties rapidly change when considering close trees due to the steep slopes.

From the analysis of the literature it turns out that even though height and DBH are correlated within the same forest area, there is a high variability in their relationship due to the terrain properties (e.g., fertility, soil class, altitude, slope) and the forest properties (e.g., stem density, management history of the stand). Accordingly, regression models based only on tree variables achieve good performances on medium size diameters but are highly sensitive to the outlayers, thus causing poor model fits at the tails of the distribution. In particular, these models tend to overestimate small diameters and underestimate large diameters. While the underestimation of the DBH strongly affects the tree (or stand) volume estimates, the overestimation of the small DBH is problematic for predicting the future growth of the stand plot. To solve these problems, in this chapter we propose a data-driven inference process to dynamically detect classes of trees characterized by different DBH growth rates. Instead of considering the spatial correlation, the proposed approach takes into account all the environmental factors that affect the DBH growth to detect classes of trees characterized by different growth models. Indeed, trees belonging to the same stand plot but affected by different environment conditions (e.g., stand density,
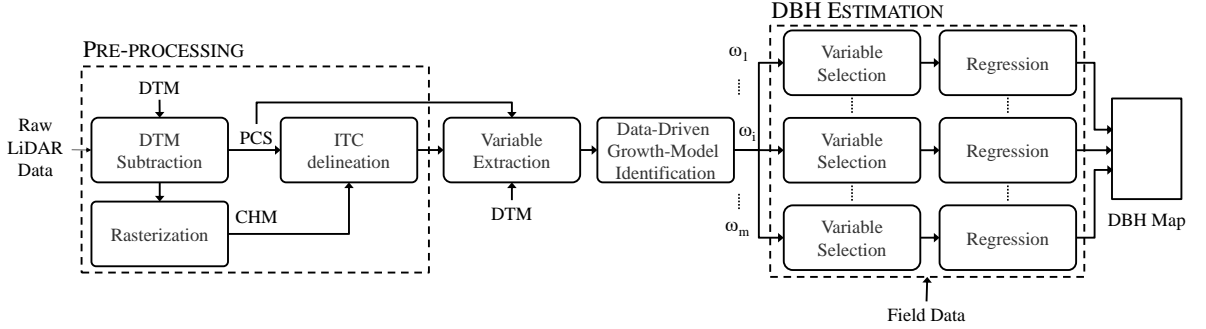
Figure 3.1: Architecture of the proposed method based on a data-driven identification of the tree growth models for an accurate DBH estimation.

terrain slopes) present different growth models. In contrast, trees located in different forest area but sharing similar forest condition are characterized by comparable stem expansion rates. Then, a growth model classes analysis based on a feature ranking method is used to identify the main variables characterizing the different growth models. Finally, a regression model is defined and adopted to each class, thus increasing the estimation accuracy. Results obtained demonstrate the effectiveness of having multiple regression model tailored on each growth model class, which allows a sharp improvement in the estimation accuracy of both small and large stem diameters.

The remaining of the chapter is organized as follows. Sec. 3.2 illustrates the architecture of the proposed and describes in detail each single step of the approach. Sec. 3.3 presents the experimental results. Finally, Sec. 3.4 draws the conclusion of the chapter.

3.2 Proposed Estimation Method

Fig. 3.1 presents the architecture of the proposed approach. The main steps of the method are: (i) pre-processing for the segmentation of the tree crowns, (ii) extraction of variables potentially correlated to the stem growth and the related mining, (iii) data-driven identification of the growth models, (iv) variable selection, and (v) data-driven DBH estimation.

3.2.1 Pre-processing

In the pre-processing step, first the DTM is subtracted to each point of the raw LiDAR data to obtain the absolute height value with respect to the ground (PCS). Then, from the normalized LiDAR point cloud we generate the CHM by assigning to each pixel the maximum height value of the first return measured in the considered area. A nearest neighbouring technique is employed to fill the empty pixels. Finally, the individual tree crowns (ITC) are delineated by means of the segmentation method presented in Chapter 2. At the end of this step, we obtain the set of tree tops $\mathcal{T} = \{\mathbf{t}_j\}_{j=1}^{H}$ and the set of related segmented crowns $\mathcal{C} = \{C_j\}_{j=1}^{H}$, with $\mathbf{t}_j = \{x_j^t, y_j^t, z_j^t\}$.
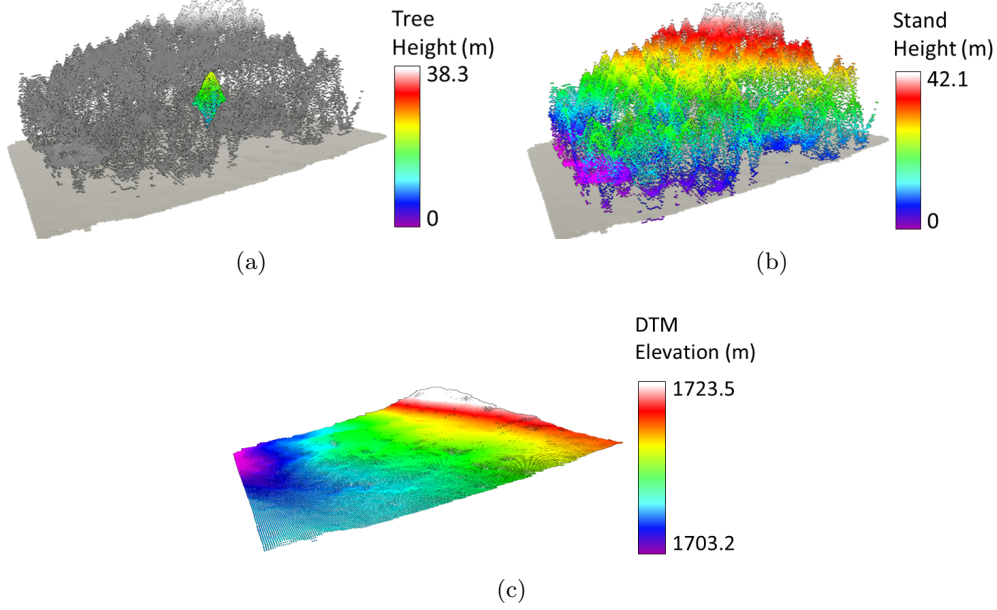
Figure 3.2: Visual representation of the variables extracted to model the growth of the tree stems in terms of: (a) the structure of the crown $\mathbf{x}^{\text{Tree}}$, (b) the forest stand $\mathbf{x}^{\text{Plot}}$, (c) the topography $\mathbf{x}^{\text{Dtm}}$.

3.2.2   Variable Extraction and Growth Model Analysis

In the proposed method we identify the growth model classes directly from the data. Thus, we need to properly model the environmental variables (in terms of stand density and topography) which may affect the stem growth. Moreover, there are variables necessary for the accurate estimation of the stem diameter growth model. Fig. 3.2 presents a visual representation of the main factors that affect the DBH. We extract variables from the LiDAR point cloud $\mathcal{P}$ and the DTM in order to model: (i) the structure of the tree $\mathbf{x}^{\text{Tree}}$, (ii) the local and global stand densities $\mathbf{x}^{\text{Plot}}$, and (iii) the topography $\mathbf{x}^{\text{Dtm}}$. Accordingly, the considered feature vector $\mathbf{x}_j \in \mathcal{R}^d$ associated to the C_j crown defined as follows:

$$\mathbf{x}_j = (\mathbf{x}_j^{\text{Dtm}} \cup \mathbf{x}_j^{\text{Plot}} \cup \mathbf{x}_j^{\text{Tree}}) \tag{3.1}$$

Tab. 3.1 reports the feature that we considered to represent the crown structure $\mathbf{x}^{\text{Tree}}$. Because of the availability of the multireturn LiDAR data, we extract both a set variables which represent the statistical distribution of the laser pulses within the crown (e.g., H_{max}^r, H_{range}^r, H_{av}^r) and a set of variables being able to model the crown geometry (e.g., C_a, r_1, r_2). The internal structure of the tree crowns is accurately characterized by the differences between the mean height values of different returns (e.g., H_{av}^1 - H_{av}^2), whereas the vertical profile is represented by the height percentiles H_p and the difference between the maximum height of the 1st return and the minimum height of the 3rd return, H_{max}^1-H_{max}^3. It is worth noting that this set of variables has been widely used for modelling the tree structure for both stem volume estimation ([127, 128, 129]) and forest species classification ([130, 131]).

To model the forest density, we extract features representing both the local and the

global stand density (Tab. 3.2). The Local Canopy Cover (LCC) allows us to model the immediate neighbourhood around the tree. The index is calculated as the ratio between canopy cover and ground area within a radius larger than 1m with respect to the crown radius (i.e., $r_1 + 1$m). For the stand density we calculate the Global Canopy Cover (GCC) as the ratio between canopy cover and ground area around the tree within a radius of 10m. In the same area we calculate the ratio between the number of 2nd and 1st pulses to evaluate the vertical density of the forest stand, p_2/p_1. Moreover, we extract the Canopy Reflection Sum (CRS) index, which has been proved to be an effective metric to model the forest density ([132, 133]).

Finally, a proper representation of the topography around each tree is obtained by extracting from the DTM the variables presented in Tab. 3.3. It is worth mentioning that even though the topography is not usually considered, the terrain properties play a fundamental role in the DBH growth (e.g., soil fertility, sunlight exposure). Let us define the partial derivatives of the DTM $z = g(x, y)$ along the orthogonal directions x and y in the horizontal plane and let us assume that the second-order partial derivative exist:

$$g_x = \frac{\partial z}{\partial x} \quad g_y = \frac{\partial z}{\partial y} \quad g_{xx} = \frac{\partial^2 z}{\partial x^2} \quad g_{yy} = \frac{\partial^2 z}{\partial y^2} \quad g_{xy} = \frac{\partial^2 z}{\partial x \partial y} \quad (3.2)$$

Let us also define:

$$p = (g_x^2 + g_y^2) \text{ and } q = (g_x^2 + g_y^2 + 1) \quad (3.3)$$

The standard topographic metrics usually employed in the DBH estimation (which are slope, altitude and aspect within a radius of 10m around the tree) are extracted, where the sun exposure γ has been calculated as follows:

$$\gamma = 180 - arctan\left(\frac{g_y}{g_x}\right) + 90\frac{g_x}{|g_x|} \quad (3.4)$$

Moreover, differently from the literature, an accurate characterization of the terrain morphology is performed by using approaches usually considered in the hydrological modeling of a terrain ([134], [135]). This is done to obtain a proper characterization of hydrological topographic attributes that allow a better estimation of the relation between stem diameter and tree height. As these variables are not usually considered to retrieve the DBH, in the following their mathematical definition is reported. We consider the profile curvature (φ), the plan curvature (ω) and the wetness index (w) which are defined as follows:

$$\varphi = \frac{g_{xx}g_x^2 + 2g_{xy}g_xg_y + g_yg_y^2}{pq^{3/2}} \quad (3.5)$$

$$\omega = \frac{g_{xx}g_x^2 - 2g_{xy}g_xg_y + g_yg_x^2}{q^{3/2}} \quad (3.6)$$

$$w = ln\left(\frac{A_s}{\sqrt{g_x^2 + g_y^2}}\right) \quad (3.7)$$

where A_s is the circular area around the tree having a radius of 10m.

Table 3.1: Set of variables modeling the crown structure.

Variable	Description
H^r_{max}	Maximum height per return, with $r = [1,4]$
H^r_{range}	Height range per return, with $r = [1,4]$
H^r_{av}	Average height per return, with $r = [1,4]$
H^r_{var}	Variance height per return, with $r = [1,2]$
H^r_{skw}	Skewness height per return, with $r = [1,2]$
H^r_{kurt}	Kurtosis height per return, with $r = [1,4]$
H^1_{max}-H^3_{max}	Max height 1st - Min height 3rd
H^1_{av} - H^2_{av}	Average height 1st - Average height 2nd
H^1_{av} - H^3_{av}	Average height 1st - Average height 3rd
H^1_{av} - H^4_{av}	Average height 1st - Average height 4th
H^2_{av} - H^3_{av}	Average height 2nd - Average height 3rd
H^2_{av} - H^4_{av}	Average height 2nd - Average height 4th
H^3_{av} - H^4_{av}	Average height 3rd - Average height 4th
H_p	pth height percentile, with $p = \{25,50,75,90,95\}$
C_a	Crown area
r_1	Radius of the circle circumscribed to the crown
r_2	Radius of the ellipse circumscribed to the crown

Table 3.2: Set of variables modeling the forest density.

Variable	Description
LCC	Local Canopy Cover (in a radius = $r_1 + 1$m)
GCC	Global Canopy Cover (in a radius = 10m)
p_2/p_1	Ratio of 2nd and 1st return pulses (in a radius = 10m)
CRS	Sum of intensity (in a radius = 10m)

Table 3.3: Set of variables modeling the topography.

Variable	Description
S_{west}	Slope between (x^t, y^t) and $(x^t - 10m , y^t)$
S_{east}	Slope between (x^t, y^t) and $(x^t + 10m , y^t)$
S_{south}	Slope between (x^t, y^t) and $(x^t, y^t - 10m)$
S_{nord}	Slope between (x^t, y^t) and $(x^t, y^t + 10m)$
γ	Aspect (degrees clockwise from north)
φ	Profile Curvature: direction of max slope
ϕ	Plan Curvature: transverse to the max slope
w	Wetness Index
A_{min}	Minimum Altitude
A_{max}	Maximum Altitude
A_{av}	Average Altitude

3.2.3   Data-Driven Identification of the Growth Models

In this step a data-driven inference process is performed to detect classes of trees characterized by the same growth model. Let us assume to have in the considered forest scenario M growth models classes $\Omega_M = \{\omega_i\}_{i=1}^M$. The first growth model to be detected is the one associated to the young trees, which present linear DBH/height relationship and relatively low height values. Indeed, while the growth model of the mature trees are affected by the environment, young trees are characterized by almost linear DBH/height growth rate. Accordingly, the detection of this class is performed in the $\mathbf{x}^{\text{Tree}}$ feature space considering the H_{max}^1 variable. Let us H_{th} be the height threshold that allows us to discriminate between young and mature trees in a reliable way. It is worth mentioning that the threshold can be selected by considering the average height of the forest stand. Let ω_1 be the growth model class associated to the young trees, and let $\Omega_K = \{\Omega_M - \omega_1\}$ be the remaining set of classes, with $K = M - 1$. The jth crown C_j is classified as ω_1 or Ω_K according to the following thresholding operation:

$$
\begin{aligned}
C_j \in \omega_1 \qquad &\text{if} \qquad (H_{max}^1 \in \mathbf{x}_j^{\text{Tree}}) \leq H_{\text{th}} \\
C_j \in \Omega_K \qquad &\text{if} \qquad (H_{max}^1 \in \mathbf{x}_j^{\text{Tree}}) > H_{\text{th}}
\end{aligned}
\tag{3.8}
$$

Even though the correct detection of the young trees is important to improve the DBH estimation of the small tree stem diameter, the main challenge is represented by the DBH estimation of mature trees. Thus, for a given tree height, the DBH considerably varies depending on the age of the tree. However, the stem growth of these trees is strictly related to the environmental condition. Therefore, by considering the feature space $\mathbf{x}^{Env} = (\mathbf{x}^{\text{Dtm}} \cup \mathbf{x}^{\text{Plot}})$, we can identify classes of mature trees characterized by different growth models. Accordingly, in the proposed method a data-driven approach is employed to automatically determine the remaining K growth models. An unsupervised clustering algorithm is applied to the feature space $\mathbf{x}^{Env}$ to partition the remaining set of trees into homogeneous growth model classes. Note that the clustering analysis is completely independent of the geographic location. Thus, trees widely separated in space can be associated to the same growth model class given the similarity of the environmental conditions. Moreover, the clustering result is completely driven by the employed variables (i.e., the considered feature space). Here, for simplicity we use the K-mean clustering algorithm. However, any other clustering techniques can be considered. In greater detail, the K-mean clustering algorithm initializes randomly the set of centroids and associates each features vector $\mathbf{x}_j^{Env} \in \Omega_K$ to the closest centroid considering the euclidean distance metric. By iteratively adjusting the centroid position with respect to the center of the obtained clusters $\{\upsilon_i\}_{i=1}^K$, the algorithm converges by minimizing the intra-cluster variance in the feature space, i.e.,:

$$
\underset{\Omega_K}{\arg\min} \sum_{i=1}^K \sum_{\mathbf{x}^{Env} \in \omega_i} ||\mathbf{x}^{Env} - \upsilon_i||^2
\tag{3.9}
$$

where υ_i is the cluster centroid of ω_i. At the end of the growth models identification, a growth model analysis is performed on the identified mature trees classes. Accordingly,

we analyze the separability of the set of K detected classes versus the considered variables to identify which are the variables that mainly influence the stem growth. To this end, we consider the Jeffreys-Matusita distance (JM) in order to evaluate the statistical separability of the growth model classes. By means of the Sequential Floating Feature Selection (SFFS) to identify the subset of features that maximizes the separability criterion. The considered algorithm has the capability of performing a fast selection reasonably close to the optimal one [136]. Let us consider the classes ω_h and ω_t, the JM_{ht} among their distributions can be defined according to the Bhattacharyya distance B_{ht}:

$$JM_{ht} = \sqrt{2\{1 - e^{-B_{ht}}\}} \tag{3.10}$$

Under the simplifying assumption that the distributions of the growth model classes can be modeled with Gaussian distributions, the Bhattacharyya distance can be defined as follows:

$$B_{ht} = \frac{1}{8}(\mu_h - \mu_t)^T \left(\frac{\Sigma_h + \Sigma_t}{2}\right)^{-1} (\mu_h - \mu_t) +$$
$$+ \frac{1}{2} ln \left(\frac{1}{2} \frac{|\Sigma_h + \Sigma_t|}{\sqrt{|\Sigma_h||\Sigma_t|}}\right) \tag{3.11}$$

where μ_h is the mean vector of class ω_h, and Σ_h is its covariance matrix. Therefore, we automatically detect both the most relevant set of variables and the number of variables to select due to the capability of the JM distance to saturate when the discriminability between the classes does not increases by increasing their distance. Thus, after the saturation point, any feature added does not increase the separability. This analysis allows us to: (i) determine which variables mostly affect the growth of mature stems, (ii) asses from the quantitative point of view the separability of the classes in the feature space where we perform the growth models classification.

3.2.4 Variable Selection

In the previous step a wide set of features has been extracted in order to model all the possible environmental factors that can affect the growth of the tree stems. Moreover, the analysis performed on the growth model classes allows us to detect the combinations of variables able to maximize the separability between the growth model classes. In contrast, the rationale of this step is the detection the combination of variables which results in better estimation than using the whole set of features. Indeed, from the methodological view point, the regression problem with high number of input variables represent a complex task because of: (i) the degradation of the generalization ability of the regression model due to the high number of parameters to estimate, (ii) the high computational cost of the regression analysis caused by a large number of input variables, (iii) the presence of noise and redundancy introduced by the variables. In this framework, the variable selection step becomes mandatory to avoid a model overfitting and to reduce the computational burden. Accordingly, the most relevant set of variables were selected by using an exhaustive feature selection method [137]. Unlike the SFFS algorithm, for this method is necessary to fix

the number of desired features. Even though it is computational demanding, the exhaustive feature selection method allows the detection of the overall best set of the features by testing all possible combinations of the input features $\mathbf{x} = (\mathbf{x}^{\text{Dtm}} \cup \mathbf{x}^{\text{Plot}} \cup \mathbf{x}^{\text{Tree}})$ and thus, guarantees the highest accuracy. In the considered implementation, the separability criterion employed is the MSE of the DBH estimation.

Let us assume to have a training set made up of q samples $T = (\mathbf{y}, \mathbf{X})$, where $\mathbf{X}$ is the $q \times d$ matrix of extracted variables and $\mathbf{y} \in \mathcal{R}^q$ is the vector of the observed values that needs to be estimated. According to the results of the growth model identification step, the considered training set is partitioned into M training set $T_i (i = 1, .., M)$, where the i_{th} training set $T_i = (\mathbf{y}_i, \mathbf{X}_i)$ is composed of the n_i training samples associated to the i_{th} growth model class ω_i, with $n_i \leq q$. For each growth model class we selected the set of $b_i \leq d$ features which minimizes the MSE.

3.2.5 Data-Driven DBH estimation

To accurately estimate the stem diameter regardless of the DBH growth model class, different regression models are defined and adopted for each class. Indeed, the dependence of he DBH from the extracted variables varies according to the different environmental conditions. Accordingly, having a regression model tailored to each class allows us to: (i) adapt the regression rule to the class of trees, (ii) to detect the set of most informative variables per regression model and (iii) increase the correlation between the predicted variables and the DBH.

Let us focus the attention on the i_{th} training set and let us considered to have $b_i \leq d$ features selected in the previous step. To retrieve the stem diameter a regression model is trained. For sake of simplicity in this study we employ a multilinear regression model. However, any other model can be used. The rationale of the multilinear regression is to derive the linear function $\mathbf{y}_i = f(\mathbf{X}_i)$ that models the relationship between the vector of dependent variables $\mathbf{y}_i$ and the matrix of variables $\mathbf{X}_i$. Accordingly, by focusing the attention on the i_{th} training set $T_i = (\mathbf{y}_i, \mathbf{X}_i)$, the multilinear regression model adopted is as follows:

$$\mathbf{y}_i = \mathbf{X}_i \boldsymbol{\beta}_i + \boldsymbol{\varepsilon}_i \tag{3.12}$$

where $\boldsymbol{\beta}_i$ is the vector of the model parameters estimated and $\boldsymbol{\varepsilon}_i$ the residual error. The considered equation can be rewritten as follows:

$$\begin{pmatrix} y_1 \\ y_2 \\ \vdots \\ y_{n_i} \end{pmatrix} = \begin{pmatrix} x_{11} & x_{12} & \ldots & x_{1b_i} \\ x_{21} & x_{22} & \ldots & x_{2b_i} \\ \vdots & \vdots & \ddots & \vdots \\ x_{n_i 1} & x_{n_i 2} & \ldots & x_{n_i b_i} \end{pmatrix} \begin{pmatrix} \beta_1 \\ \beta_2 \\ \vdots \\ \beta_{n_i} \end{pmatrix} + \begin{pmatrix} \varepsilon_1 \\ \varepsilon_2 \\ \vdots \\ \varepsilon_{n_i} \end{pmatrix} \tag{3.13}$$

At the end of this step, for each growth model ω_i a vector of parameters $\boldsymbol{\beta}_i$ is derived, thus adapting the regression rule to each growth model class.

3.3   Experimental Results

In this section we present the results obtained by applying the proposed method to a high-density LiDAR data acquired in a complex Alpine mountainous scenario characterized by a wide range of stem diameters. After a brief description of the used dataset, we show and analyze the results obtained in terms of identification of growth models. Moreover, the results of the growth model classes analysis performed on the identified mature growth model classes are presented and discussed. Then, we focus the attention on the estimation results by considering the accuracy obtained per growth model class and on the entire set of samples.

3.3.1   Dataset Description

Experiments were carried out considering a coniferous forest located at Parco Naturale Paneveggio – Pale di San Martino, in the Trento Province, Southern Alps, Italy. The area extends approximately 368 Ha and is characterized by a complex topography with hillsides having different inclinations and sun exposition (mainly north north-west aspect). The altitude ranges from 1536 to 2064 a.s.l., whereas the slopes are up to 30°. The main forest species are Norway Spruce (Picea Abies) and European Larch (Larix Decidua) with a small presence of Silver Fir (Abies Alba) and Swiss Pine (Pinus Cembra). High-density LiDAR data (5 pts/m²) were acquired with the Optech ALTM 3100EA sensor in September 2007. The number of returns acquired was as up to four, the laser pulse wavelength was 1064 nm and the laser repetition rate 100 kHz.

Reference data were collected on the ground within 2, 5 and 11 circular stand plots of radius of 7 m, 13 m and 25 m, respectively. Moreover, two additional square sample plots having on area of 1 Ha were surveyed. The plots were randomly distributed on the entire study area to obtain a statistical representation of the in terms of topography and forest density (Fig. 3.3). Within each sample plot, trees having Diameter at Breast Height (DBH) larger than 3 cm were surveyed. For each tree, the position with respect to the center of the sample plot, the species and the DBH were measured. To further reduce the uncertainty of the horizontal position, the samples plot were manually geo-referenced by visual interpretation with the LiDAR raster image. In our experiments we analyzed 1462 trees randomly divided into training, test and validation sets Tab. 3.4 shows the mean, variance, min and max value of DBH and tree height.

Table 3.4: Distribution of the reference data divided into training, test and validation set. For each set the mean, variance, min and max value of DBH, and the tree top height are reported.

Data set	Variable	Mean	Std	Min.	Max.
Training Set (380)	DBH (cm)	36.48	16.92	3.00	92.00
	Height (m)	24.17	9.60	2.26	42.91
Validation Set (200)	DBH (cm)	37.12	15.76	4.00	79.00
	Height (m)	24.25	9.16	2.31	41.56
Test Set (882)	DBH (cm)	36.29	16.95	3.00	92.00
	Height (m)	23.31	9.85	2.26	42.43
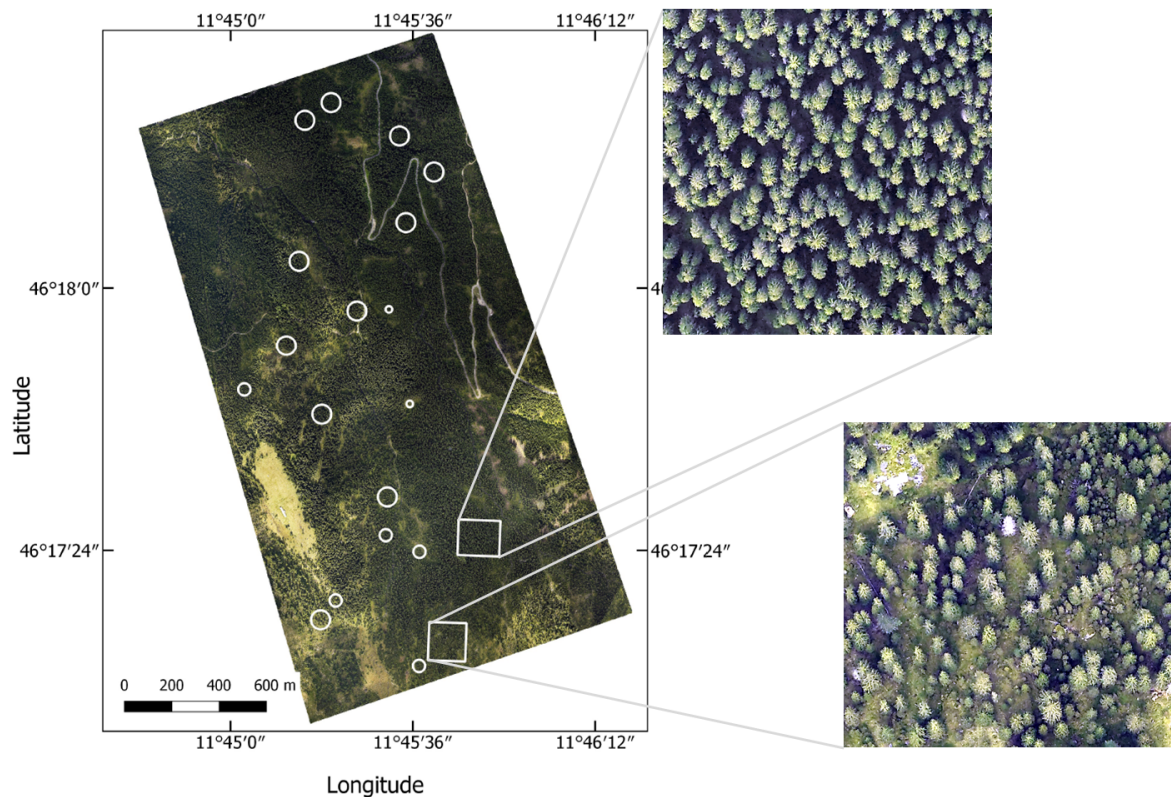
Figure 3.3: Study area, Trentino region, Italy. The stand plots are highlighted in white and a zoom of the two square stands points out the different forest density and structure conditions.

3.3.2 Results of Growth Models Identification

Fig. 3.4 shows the clustering results obtained by partitioning the set of detected trees into ω_1, ω_2 and ω_3. The DBH/height relationships are highlighted in black and overlapped on the sample distributions. As one can notice from the figure, the considered classes are described by different DBH/height growth rates due to the different tree structure, forest stand and topographic condition. While trees characterized by low height values present a linear relationship between height and DBH (Fig. 3.4b), tall trees present a non-linear dependence of the DBH from the tree top (Fig. 3.4c and Fig. 3.4d). Hence, for the same tree height, the DBH strongly varies due to the environmental conditions. In greater details, young trees ω_1 were correctly identified by a conservative height threshold $H_{th} = 15$ m, which is a reasonable threshold for young trees on an average forest height of 23 m (Tab. 3.4). In the considered forest two main mature growth models are dominant in the scene (Fig. 3.4). Accordingly, the clustering algorithm was able to accurately distinguish among different classes of mature trees ω_2 and ω_3 in an unsupervised way.

Let us focus the attention on the growth model classes analysis performed to identify which variables mainly affect the stem growth of the mature trees. Tab. 3.5 presents the variables selected by means of the SFFS in the ranking order. From this result it turns out that the altitude (i.e., A_{min} and A_{max}) plays a dominant role in the growth of
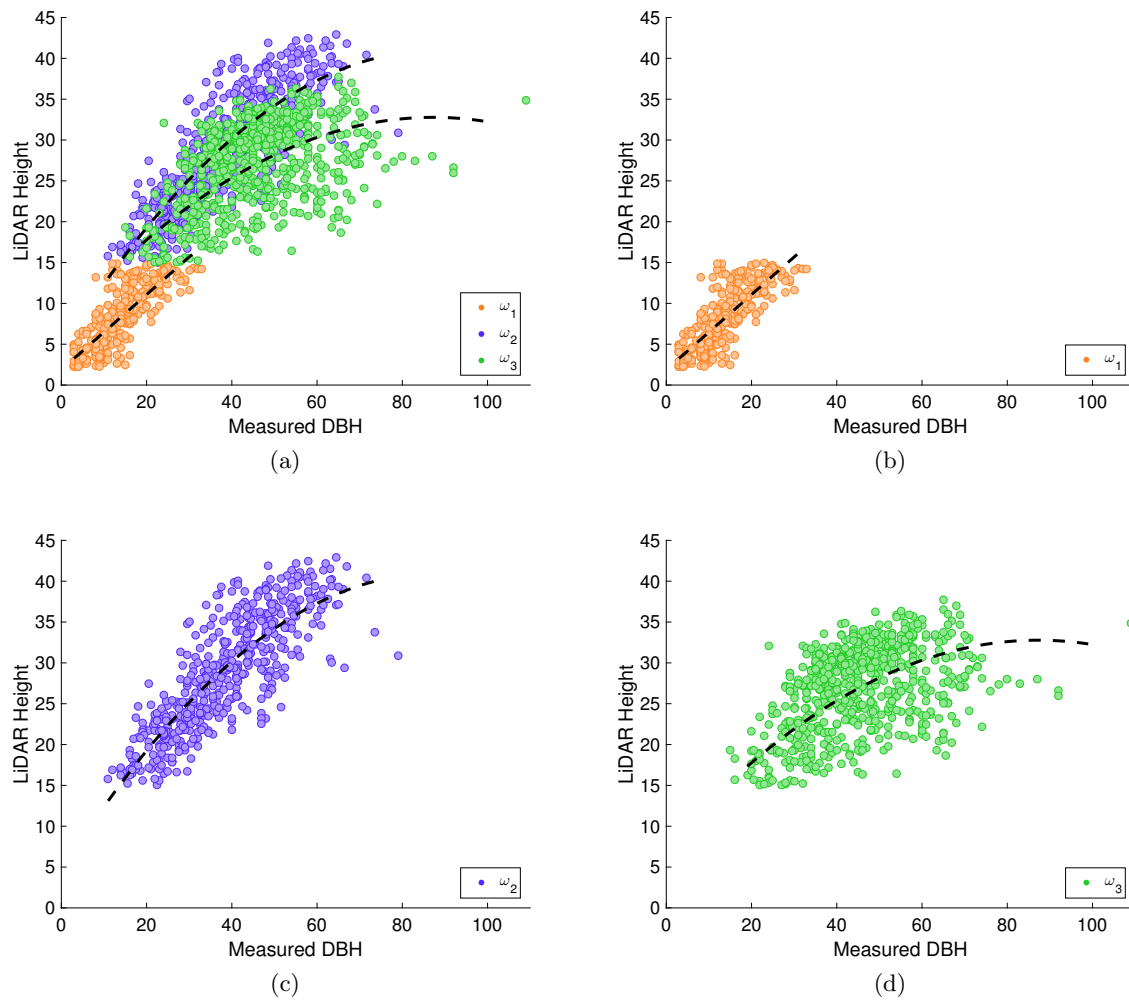
Figure 3.4: LiDAR tree heights vs DBH for: (a) all the considered trees, (b) the young trees classified as ω_1, (c) the mature trees classified as ω_2, (d) the mature trees classified as ω_3. For each class, the DBH/height relationship is presented in black and overlapped on the scatterplots to highlight the different growth rates.

the stem diameter. Indeed, the tree growth rate decreases when increasing the altitude because of the colder temperature, the increased exposure to wind, the shorter growing seasons and the reduced amount of soil nutrients [138]. The second variable selected is the plan curvature ϕ, which models the soil water drainage and thus is strongly correlated to the soil fertility, especially in mountainous and hilly terrain. Finally, the vertical density of the forest stand p_2/p_1 plays a fundamental role in the expansion of the stem in terms of availability of water, whereas the horizontal forest density metrics GCC models the impact of forest density in terms of surrounding trees. Thus, the stem growth of trees characterized by low height values is more sensitive to the presence of taller neighbouring trees because of the light reduction effect.

Table 3.5: The set of discriminative features between ω_2 and ω_3 are presented.

Mature Growth Models
A_{min}
A_{max}
ϕ
p_2/p_1
GCC

3.3.3 Stem Diameter Estimation

Fig. 3.5 shows the ranking of the features selected (divided per growth model class) by using the exhaustive search method. In these experiments, five variables were selected. For all the classes the crown radius r_2 was selected together with the tree top heights, i.e., H_{95} for ω_2 while H_{max}^1 for ω_1 and ω_3. Regardless of the growth model class, attributes modeling the topography were always selected, thus confirming the importance of a proper representation of the terrain morphology. In particular, for the young trees ω_1 the local forest density metric LCC and the terrain altitude A_{min} are selected together with the variance height value of the second return H_{var}^2. In contrast, the DBH growth of the mature trees is more influenced by the topographic metrics, φ and S_{est}. Finally, for the mature trees ω_3 the vertical forest density p_2/p_1 affects the stem expansion more than the terrain morphology ϕ and A_{max}.

At the end of the feature selection phase the regression analysis was performed. The results obtained with the PM were compared with a standard multilinear regression model trained on the entire set of trees (RM). Although in the literature the feature space $\mathbf{x}^{Tree}$ is usually employed, to have a fair comparison we considered the entire set of features $\mathbf{x}$ also for the RM. To quantitatively evaluate the estimation accuracy, we considered the R^2, the ME, the MAE, the MSE and the percentage Root Mean Square Error (RMSE(%)). Note that, the RMSE(%) is computed as the ratio between the RMSE and the average DBH value. Fig. 3.6a and 3.6b depict the DBH estimates obtained with the PM and the reference method (RM), respectively. These results demonstrate the importance of defining and adopting different regression models for each detected class. Thus, due to the clustering step, we can select the set of features which better fit the sample distribution
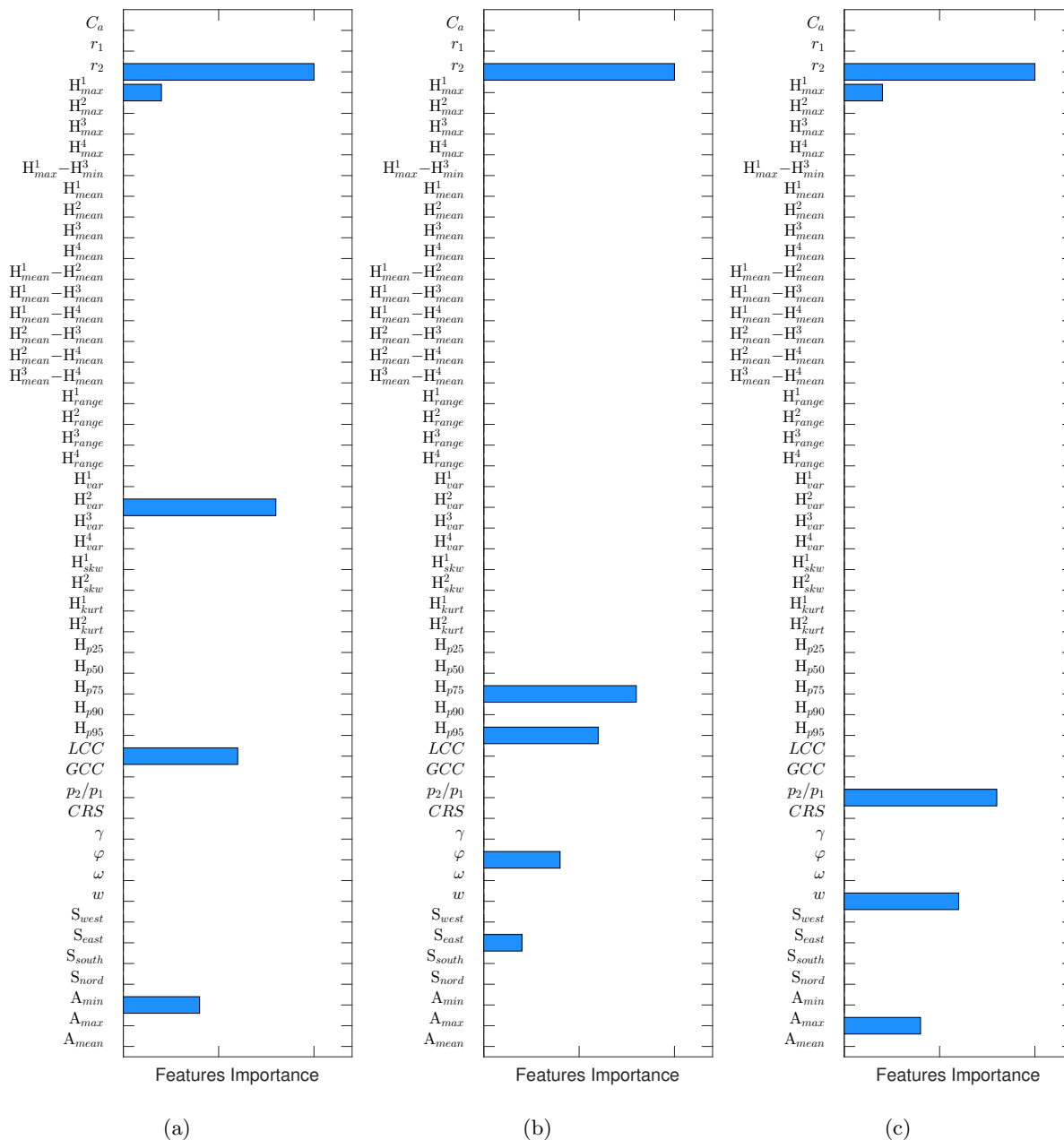
Figure 3.5: Features selected for the DBH estimation for: (a) the young trees ω_1, (b) the mature trees ω_2, (c) the mature trees ω_3. The features are represented in the ranking order normalized between [0,1].
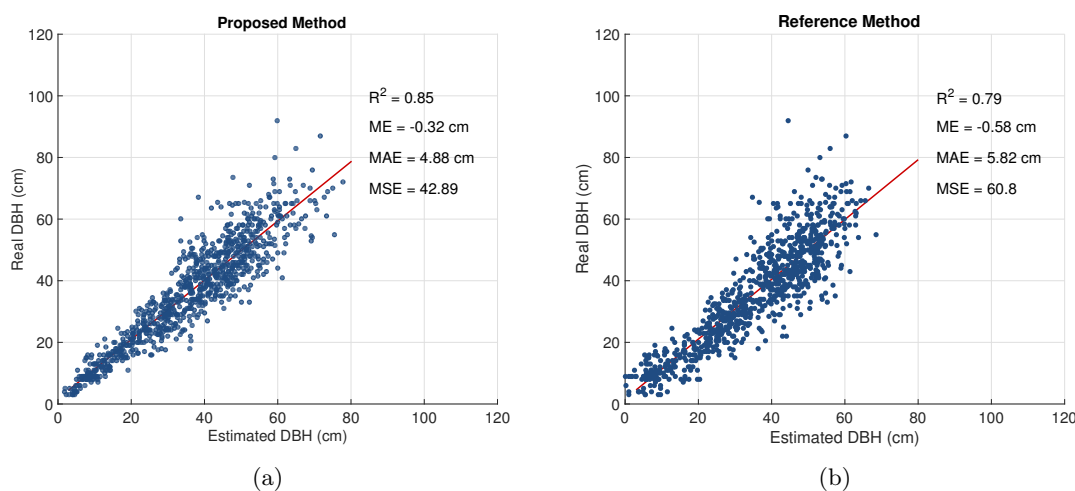
Figure 3.6: Estimated vs real DBH obtained by using the multilinear regression model with (a) the PM, (b) the RM.

of each class and to adapt the regression rule to the each tree growth model. As one can notice, the R^2 values show that the amount of variability within the estimates is sharply reduced by the PM with respect to the RM. Moreover, the ME values confirm that the PM allows to have unbiased estimates.

Tab. 3.6 shows the estimation results obtained with the PM and the RM applied to the entire set of trees and to the DBH classes applied for local forest inventories in the considered study area. The classification distinguish among pre-inventory trees (i.e., DBH $\leq$ 17.5 cm), small trees (i.e., 17.5 cm $<$ DBH $\leq$ 27.5 cm), medium trees (i.e., 27.5 cm $<$ DBH $\leq$ 47.5 cm), large trees (i.e., DBH $>$ 47.5 cm). In this framework, the RMSE(%) allows us to quantify the error on the DBH classes, by weighting the RMSE on the average stem diameter of each considered class. The results demonstrate the strong improvement obtained by the PM in estimating small and large stems. The RMSE was reduced of more than 2 cm for trees having DBH$<$17.5 cm and of more than 1 cm for DBH between 17.5 cm$-$27.5 cm. Moreover, it was reduced of almost 2 cm for large stems (DBH$>$47.5 cm). The percentage results point out the sharp increase of performance.

Table 3.6: MAE (cm), RMSE (cm) and RMSE(%) calculated on the entire set of trees and on 4 DBH classes obtained with the PM an the RM.

DBH class	PM			RM		
(cm)	MAE	RMSE	RMSE(%)	MAE	RMSE	RMSE(%)
<17.5	2.16	3.03	26.91%	4.29	5.38	47.83%
17.5−27.5	4.00	5.32	23.19%	4.88	6.56	28.62%
27.5−47.5	4.94	6.13	16.15%	5.51	6.93	18.26%
>47.5	6.98	8.92	20.27%	7.72	10.42	23.68%
All Trees	4.88	6.55	18.04%	5.82	7.80	21.48%

3.4   Conclusion

In this chapter we presented a data-driven method to the identification of growth model classes for the adaptive estimation of the DBH. Moreover, a growth model classes analysis which determines which variables mainly affect the stem growth of mature trees has been illustrated.

To accurately estimate the DBH regardless of the stem size, the PM in the first step extracts a large set of variables potentially correlated to the stem growth model. In particular, it considers variables modeling: (i) the crown structure, (ii) the terrain properties, and (iii) the forest density. In the second step, a data-driven unsupervised identification of the different tree growth models is performed. To this end a clustering is performed by in the feature space defined by all the environmental variables which may affect the stem expansion. Finally, a regression algorithm is trained for each detected growth model class. This allows us to adapt the regression rule to the different classes and to select the best set of features for each growth model class, thus improving the correlation between the predicted and the true DBH values.

The experimental results demonstrate that the method is able to properly model the environmental factors that influence the growth of the DBH. In particular, due to a the proper representation of the forest conditions, it accurately identifies the DBH growth models. Due to the growth model classes analysis it was then able to identify which variables mainly affect the stem expansion. In particular, it turned out that the terrain altitude together with the water drainage play a dominant role in the DBH growth of the mature trees. The proposed approach strongly improved the DBH estimation of the small and large stems with respect to the state-of-the-art methods. Regardless of the growth model classes, the crown radius and the tree top height were always selected as features in input to the regression models. The estimation results confirm that the terrain properties affect the stem expansion together with the forest density. Note that the PM is automatic and data-driven. Thus, it can be applied to different areas for identifying the specific growth-models to be used.

As future developments of this work, we aim to test the method on forest stands characterized by different ages and structures. Moreover, we plan to further analyze the growth model classes for a better comprehension of the environmental factor which affect the growth of the trees. In this context, experiments will be extended to LiDAR dataset characterize by higher laser point density and to forest having different environmental conditions. Moreover, we aim to automatically detect the number of growth models presented in the forest area by analyzing the distribution of the samples in the feature space.

Chapter 4

Tree Top Height Estimation Method

Typically, low-density LiDAR data are acquired in large forest areas for reducing the acquisition cost. However, due to the low laser sampling density, many trees are not hit by any LiDAR pulses and thus when working at single tree level the height of the trees is systematically underestimated. To solve this problem, in this chapter[1] we propose a 3-D model based approach to the reconstruction of the tree top height by fusing low-density LiDAR data and high resolution optical images. The joint use of the data sources is first employed to accurately detect and delineate the single tree crowns. For those trees where LiDAR measures are available, the vertical information together to the crown radius and the tree top position derived from a segmentation step are employed to reconstruct the real tree top height. A 3-D parametric model suited for conifers is considered. Finally, for the set of trees missed by the laser scanner, a novel k-NN trees technique is used to estimate their heights as the average of the k reconstructed height values of the trees having most similar crown properties. Experimental results confirmed the effectiveness of the proposed method.

4.1   Introduction

As anticipated in the previous chapters, the individual tree crown segmentation introduces to the estimation of the forest parameters at single tree level. One of the most important tree attribute that should be accurately retrieved is the tree top height, which is necessary for the estimation of other individual tree parameters (e.g., diameter at breast height (DBH), tree stem volume) [28, 19, 84, 139]. In this framework, LiDAR sensor represents an effective tool which directly measures the height of forest with high accuracy when acquired with high laser sampling density (i.e., larger than 5 pts/m^2) [140, 141, 142,

---

[1]Part of this chapter appears in:

C. Paris and L. Bruzzone, "A novel technique for tree stem height estimation by fusing low density LiDAR data and optical images," in *Geoscience and Remote Sensing Symposium (IGARSS), 2013 IEEE International.* IEEE, 2013, pp. 3022-3025.

C. Paris and L. Bruzzone, "A three-dimensional model-based approach to the estimation of the tree top height by fusing low-density lidar data and very high resolution optical images," *Geoscience and Remote Sensing, IEEE Transactions on*, vol. 53, no. 1, pp. 467-480, 2015.

143]. However, to guarantee a high number of points per m^2 it is necessary to increase the duration of the flight (or to decrease altitude/speed of the airborne platform), thus strongly increasing the acquisition cost. By decreasing the interval of the spacing of LiDAR hits from 1.5 m to 0.3 m the acquisition cost per km^2 may increase of about three times as pointed out in [144]. In this framework, the availability of low-density LiDAR data is more common on wide area coverage. However, the main problems related to the reduction of the LiDAR point density are: (i) the underestimation of the height of the trees due to the missed detection of the tree top positions by the LiDAR points, and (ii) the missed detection of some trees which are not hit by any laser pulse. In [145] the authors demonstrate that these effects, which happen when the altitude of the aircraft increases, are due to both the subsequently decrease of the pulse density and the increase of the footprint size. Moreover, there is a considerable underestimation of the tree top height when the platform altitude increases over a certain level (e.g., 1500 m). This considerable deterioration of the height estimation results is even more evident when dealing with mountainous scenarios due to the error associated to the generation of the DTM as presented in [146, 147]. Indeed, by increasing the flight altitude the penetration rate decreases, thus reducing the number of ground laser points used to model the topography of the scene [146]. The poor penetration rate of the laser pulses may miss crests and ridges, resulting in an inaccurate estimation of the DTM. Moreover, due to the terrain slope, the elevation obtained at the center of the footprint is higher than the one obtained at the last pulse [147]. Accordingly, when the tree leans towards upper side of slope, its height is underestimated.

For all reasons mentioned above, it is possible to conclude that the accuracy of the tree top height estimation suddenly declines when the laser sampling density is below 3-5 pts/m^2 leading to a heavy underestimation of both the tree height and the number of trees detected. In this framework, the complementary information provided by the optical images could be a possible solution for improving the performances of the low-density LiDAR data. Also when acquired with high laser sampling density, LiDAR data can take advantage from optical images for better describing the structure of the forest. The gaps among the laser pulses do not allow a comprehensive representation of the horizontal structure of the forest, which is provided by the optical data [148]. In [61] the complementary of LiDAR and optical sources for the individual tree crown segmentation is demonstrated. While the optical image allow a better segmentation results in dense forest area, LiDAR data are more effective in the delineation of isolated tree crowns. Thus, the vertical information measured by the LiDAR sensor allows the correct discrimination of ground and forest areas. In contrast, the radiance values of bare soil and forest are similar in the optical image, but the high level of detail allows a better representation of the crown structure in dense forest areas. By fusing the information brought by the data sources, the number of the false tree detected on the optical image was strongly reduced. A similar result is presented in [149], where an approach that aims at mapping the single tree location both on LiDAR data and high resolution aerial photo is presented. The results confirm that optical images are suited for describing dense forest, whereas LiDAR data allow higher accuracy in open woodland.

The importance of integrating the LiDAR data and optical images is even more evident

in the estimation of forest parameters mainly related to the vertical dimension. In [150] the authors compare the volume estimation results obtained by using only aerial images or integrating them with high-density LiDAR data. While the optical image is employed to delineate the single tree crown, LiDAR data provide the height information. As expected, the synergistic use of the data significantly improve the estimation results (R^2 from 0.14 to 0.54). In [63], the authors pointed out that for an accurate estimation of the tree stem volume, the height of the individual trees is the most important geometrical parameter. The crown segmentation was performed on high resolution optical image, while the height of trees was derived by high- and low- density LiDAR data. After having calculated the stem volume by means of allometric equation, they computed the error metrics of the entire stand plots. In the high-density case the RMSE ranges from 156.0 m^3/ha to 163.6 m^3/ha, whereas in the low-density case the RMSE ranges from 205.4 m^3/ha to 209.0 m^3/ha.

By focusing the attention on the fusion of low-density LiDAR data and optical images, few papers exploit the combination of these data source to improve the forest attribute estimation [64, 151, 65, 152]. In [151] the authors present an approach to derive the height of the forest at stand level by using multispectral images and low-density LiDAR data. First, they classify the multispectral image to distinguish broadleaves and conifers. For each species and for the two species combined, non-linear regression models are derived from field inventories to estimate the crown width from the tree height. The a priori information is employed to facilitate the tree top detection by using the species and the height of the pixel. By comparing the results obtained with and without considering the species information, there is an improvement only for the coniferous forest. In [64] the authors combine optical data acquired by SPOT5 satellite with tree height information provided by a laser scanner. The estimation of the forest stem volume at stand level was performed by using the single data source separately and by combining them. The joint use of the two sources improved the volume estimation of 49% compared to the use of the only optical image, reducing the RMSE on the average volume from 31% to 16%. In [65], aerial photo are employed to segment the single tree crowns while low-density LiDAR data provide the height values. Although the method achieves accurate segmentation results, the LiDAR derived height was underestimated due to the low-density LiDAR data acquisition. Similar problem is encountered in [152], where the authors define an automatic approach to the estimation of forest structural parameters based on aerial images and low-density LiDAR data. First, they perform an automatic registration step based on the intensity value of the LiDAR data and the RGB channels of the aerial images. At the end of the registration step, the tree height is estimated by fusing the remote sensing data. Although the registration properly integrates the two data, due to the low laser sampling density the height is not accurately estimated.

To solve these problems, in this chapter we propose a data fusion approach to integrate low-density LiDAR data and a single optical image. Unlike the methods described in the literature, we aim to address the height estimation from a real data fusion perspective to accurately estimate the height of the trees. In particular, the proposed approach first identifies the crowns of the trees present in the scene by applying a segmentation algorithm to the optical image with the integration of the height information provided
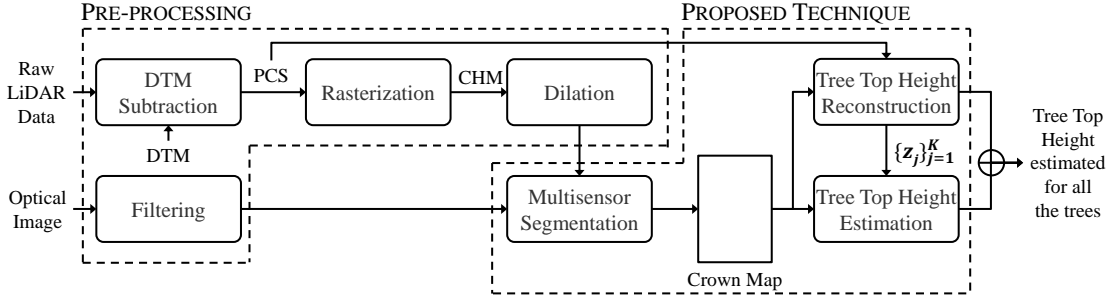
Figure 4.1: Architecture of the proposed Tree Top Height Estimation Approach.

by the LiDAR data. At the end of the crown detection phase, reconstructs the tree top height employing a 3-D parametric model for those trees hit by at least one laser point, while defines a *k-Nearest Neighbor* (*k*-NN) trees technique to reconstruct the height of those trees completely missed by the laser scanner.

The remainder of the chapter is organized as follows. Section 4.2 presents the proposed method illustrating in detail each single step of the proposed architecture. Section 4.3 describes the experimental results and finally Section 4.4 draws the conclusion.

4.2   Proposed Tree Top Height Estimation Method

Fig. 4.1 presents the architecture of the proposed method divided into two main parts, the pre-processing phase and the proposed technique. In the following the details of each part are presented.

4.2.1   Pre-processing Phase

In the first phase, we perform the pre-processing on both the LiDAR data and the optical image. In the LiDAR data pre-processing, first the DTM is subtracted to the original LiDAR point clous to obtain the PCS. Then, we generate the CHM image having the same spatial resolution of the optical data, where we assign at each pixel the height measured by the LiDAR pulses in the area correspondent to the pixel. Because of the low spatial density of the laser pulses, many pixels of the CHM do not include any height information. To solve this problem, we propagate the height information to the empty pixels by applying a dilation algorithm to the CHM (e.g., [153]). The structural element employed is a disk whose size depends on the tree crowns dimension. Thus, the aim of this procedure is to exploit the LiDAR height information to distinguish the forest area from the ground area. The accuracy of the result obtained depends on a trade-off between the laser sampling density of the LiDAR data and the density of the forest. However, since we aim at identifying flat ground areas or shrub vegetation, the sparse LiDAR information is sufficient to cope this purpose. Let $CHM(x, y)$ be the height value of the pixel at the position (x, y). Let Q be the structural element chosen for dilating the CHM image, and $Q(x', y')$ the value of the structural element at the position (x', y'). Let D_{CHM} and D_Q be

the domain of the image CHM and the domain of the structuring element Q, respectively. The dilation algorithm for the image CHM by Q is described by the following equation:

$$(\text{CHM} \oplus Q)(x,y) = max\{\text{CHM}(x-x', y-y') \,|\, (x',y') \in D_Q,$$
$$(x-x', y-y') \in D_{\text{CHM}}\} \quad (4.1)$$

Let th_{Height} be the height threshold value chosen to distinguish between forest and flat ground areas. The mask image M_{sk} is obtained by deleting all the pixels of the LiDAR image CHM having value smaller than the height threshold th_{Height}, [61]. We can write as follows:

$$M_{sk}(x,y) = \begin{cases} 1 & \text{if } \text{CHM}(x,y) \leq th_{Height} \\ 0 & \text{otherwise} \end{cases} \text{ with } (x,y) \in D_{\text{CHM}} \quad (4.2)$$

The goal of the optical image pre-processing is to emphasize the tree apexes and the crown boundaries, thus facilitating the segmentation of the individual tree crowns. Let G be the green band of the optical image, and $G(x,y)$ the radiance value of the pixel at the location (x,y). First, a $n \times n$ median convolution filter is applied to G for reducing the noise in the image. Then, the image is smoothed by means of a $n \times n$ Gaussian convolution filter in order to emphasize the local maxima and the crown contours. The filters size depends on the spatial resolution of the image and the average size of the tree crowns.

At the end of the pre-processing phase, the proposed tree top height estimation approach can be applied to the remotely sensed data. The approach is based on three steps: (i) multisensor segmentation of the crowns by using optical and LiDAR data, (ii) reconstruction of the tree top height for those crowns hit by laser points employing a 3-D parametric model of the tree based on the LiDAR height and the crown radius information, (iii) estimation of the height of those trees missed by any LiDAR points by using a similarity crown area criterion based on a k-NN trees algorithm.

4.2.2 Multisensor Segmentation

In this step we aim to accurately detect and delineate the single tree crowns present in the scene. Due to the low-laser sampling density, LiDAR data is not sufficient to describe the horizontal structure of the forest. In contrast the optical images allows a comprehensive representation of the crowns structure. In particular, we consider the green band of the optical image which is the most correlated band to the radiation intensity of the image [154]. Indeed, the radiance of the optical image, under nadir condition acquisition, can be considered a topographic surface which represents the structure of the forest (Fig. 4.2). However, where the forest is less dense the discrimination between bare soil and trees is a critical issue for the crown recognition in optical images. For this reason, we apply to the optical image the binary mask image M_{sk} generated by using LiDAR data. Let G be the green band of the optical image. Since the G image has the same dimension of the M_{sk} image, the masking procedure is accomplished as follows:

$$G_m(x,y) = M_{sk}(x,y) \cdot G(x,y),$$
$$\text{with } (x,y) \in D_{\text{CHM}} \quad (4.3)$$

(a)   (b)
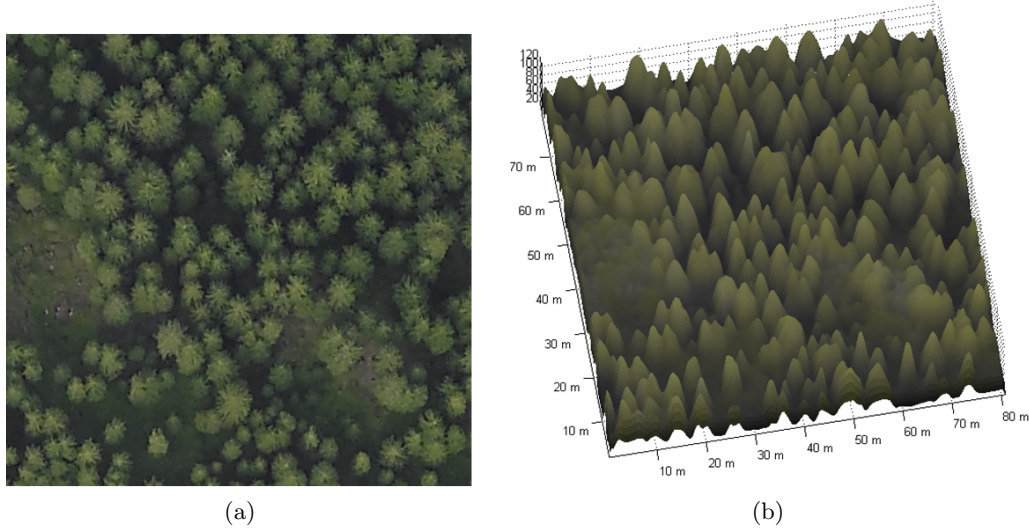
Figure 4.2: (a) RGB representation of the original ortophoto. (b) 3-D representation of the radiance value of the green band.

The obtained masked image G_m is processed to determine the center of the crown which corresponds to each tree top. Similarly to the valley following approach [155], we assume that on optical imagery the highest values of the radiation intensity are concentrated on the uppermost part of the tree, which is surrounded by lower intensity pixels (valleys) [61, 154]. The tree top positions are identified in the optical image G_m by applying the LSM to detect the local peaks of the optical data $\mathcal{T} = \{\mathbf{t}_j\}_{j=1}^K$, where $\mathbf{t}_j = \{x_j^t, y_j^t\}$. It is worth mentioning that the aim of the proposed method is the accurate estimation of the z_j^t coordinate by exploiting the sparse LiDAR vertical measures. The crown delineation is performed by assuming the crown surrounded by shadows, thus searching for the local minima along the four main directions ($0°$, $45°$, $90°$, $135°$) as presented in [156]. Then, the boundaries detected are processed to close possible gaps and to remove the pixels that have less than two minimum neighbours. This step provides a minima network which identifies the regions correspondent to the crown areas. Finally, we refine the segmentation result by removing the segmented areas having less than th_p pixels, which are too small for being a crown. The value of th_p depends on the resolution of the image.

For each labeled region we analyze the correspondence with the tree top locations. If the labeled region includes just one tree top $\mathbf{t}_j$, then this means that the region describes the tree crown belonging to that specific seed and thus it is associated with the tree crown C_j. If the region includes more than one tree top, then this means that two or more crowns are fused in a single connected region and should be separated. The remaining connected regions that include more tree tops are usually partially separated by the minimum network. For this reason, to separate them completely, we just follow the direction of the enclosure and split the remaining crowns. At the end of this process, we obtain the set of K detected crowns $\mathcal{C} = \{C_j\}_{j=1}^K$, where C_j identifies the region delineated around the tree top $\mathbf{t}_j$.
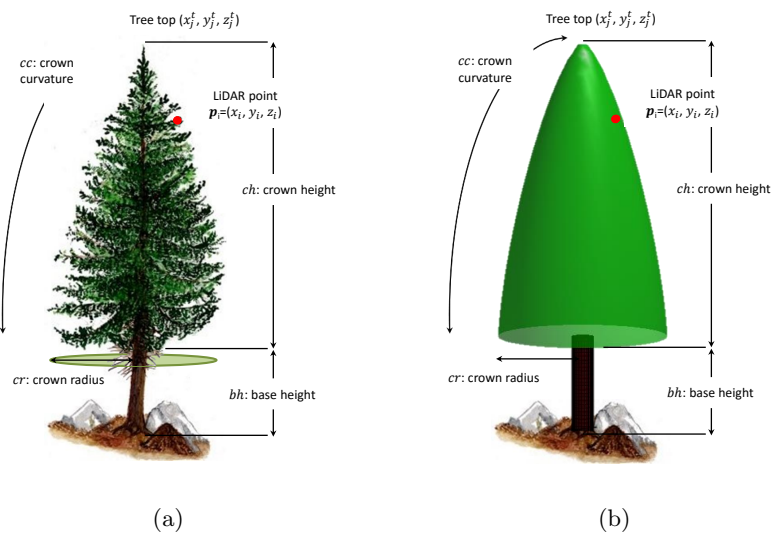
Figure 4.3: (a) Representation of the tree crown parameters of the defined 3-D reconstruction model. (b) Example of 3-D model of the tree.

4.2.3 Tree Top Height Reconstruction Method

The main idea of this step is to define a procedure that can accurately reconstruct the height of the tree top z_j^t exploiting the LiDAR elevation information associated to the crown. This is done starting from the assumption that: (i) the density of the considered LiDAR data is not sufficient to hit the top of each tree, (ii) only trees with at least 1 LiDAR measure are considered. The case in which some crowns are missed by laser pulses is addressed in the next section. Let $\mathcal{N} = \{n_j\}_{j=1}^{K}$ be the number of LiDAR pulses associated to the tree crowns, where n_j is the number of LiDAR pulses associated to the crown C_j. The K detected crowns can be split into three sets:

- the set of crowns hit by just one laser point $\{C_j \in \mathcal{C} | \ n_j = 1, j \in [1, K]\}$;

- the set of crowns hit by more than one laser point $\{C_j \in \mathcal{C} | \ n_j > 1, j \in [1, K]\}$;

- the set of crowns missed by the laser scanner $\{C_j \in \mathcal{C} | \ n_j = 0, j \in [1, K]\}$.

In Fig. 4.4, an example of the classification of the tree crowns is reported. The crowns hit by more than one laser pulse are represented in white, the crowns hit by just one laser pulse are represented in blue, whereas the crowns missed by the laser scanner are represented in red. It is worth nothing that the low laser sampling density limits the number of pulses acquired inside each crown to few sparse measures (at the limit of 1 point per crown). Moreover, when low-density LiDAR signals are acquired with a narrow laser beam, there is a systematic underestimation of the height due to the missed tree top location. To solve these problems, the proposed technique defines a proper 3-D parametric model of the crown surface for reconstructing the real height of the tree by using the altitude information of the LiDAR points associated with the tree crown and the segmentation results from the optical image.

(a)   (b)   (c)

□ crowns hit by more than one laser pulse $\{C_j \in \boldsymbol{C} | n_j > 1, j \in [1, K]\}$

■ crowns hit by just one laser pulse $\{C_j \in \boldsymbol{C} | n_j = 1, j \in [1, K]\}$

■ crowns missed by the laser scanner $\{C_j \in \boldsymbol{C} | n_j = 0, j \in [1, K]\}$
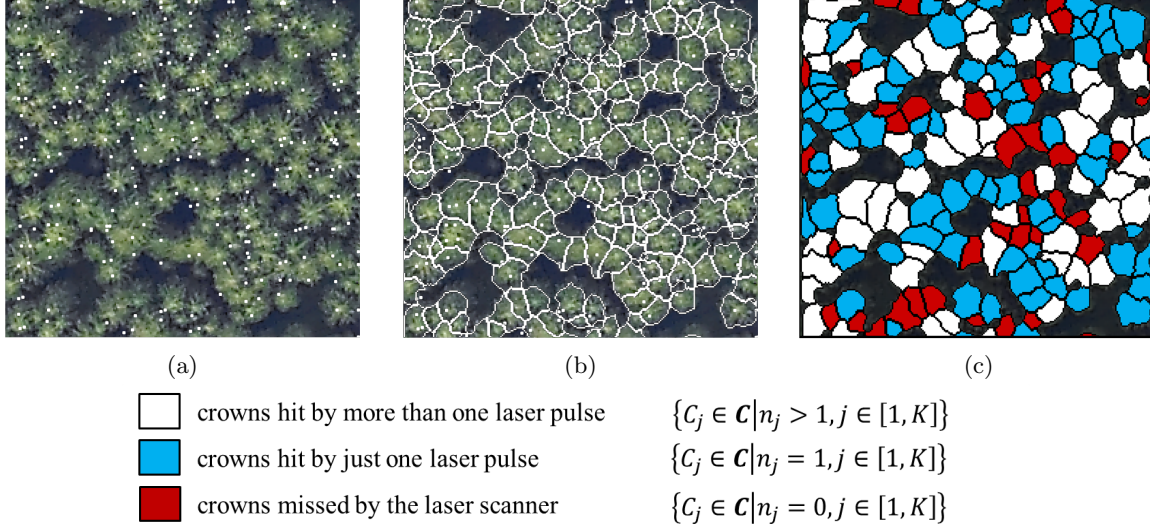
Figure 4.4: Example of classification based on the number of LiDAR points associated to the crown. (a) LiDAR points shown in white and overlapped on the ortophoto, (b) both LiDAR pulses and crown boundaries represented in white overlapped on the ortophoto, and (c) crowns hit by more than one laser pulse (white), crowns hit by just one laser pulse (blue) and crowns missed by the laser scanner (red).

In the proposed approach, we address the issue of reconstructing the tree apex for coniferous forests. Indeed, broadleaves are characterized by a round canopy almost flat on the uppermost part. Thus, due to this umbrella shaped crown morphology, the tree height is not heavily underestimated when the LiDAR pulses do not center the tree apex. In contrast, the steep morphology of the crown surface of the conifer strongly affects the height estimates depending on the distance of the laser pulse from the tree top. The 3-D geometric model of the tree used in this chapter is derived from the synthetic template presented in [157], which was employed to describe the crown envelope of conifers for delineating the single tree crown on high resolution optical images. In greater detail, by focusing the attention on the generic jth tree the authors proposed a generalized ellipsoid described by the tree top coordinates (x_j^t, y_j^t, z_j^t), the adjusting coefficient of the crown surface curvature cc, the crown height ch and the crown radius cr (Fig. 4.3). The same mathematical representation has been adopted in [140] for delineating the single tree crowns on LiDAR images, and in [104] to visually reconstruct the forest after having estimated all the tree attributes by using a high-density LiDAR data (≤ 10 pts/m^2). The mathematical representation of the crown envelope is as follows:

$$\frac{(z + ch - z_j^t)^{cc}}{ch^{cc}} + \frac{[(x - x_j^t)^2 + (y - y_j^t)^2]^{cc/2}}{cr^{cc}} = 1$$

$$\text{where } z_j^t - ch < z < z_j^t$$

(4.4)

From the segmentation results we can derive the tree top location (x_j^t, y_j^t) and the crown radius cr. Then, after having associated to each tree the related laser pulses, the ground coordinates of the each LiDAR point $\mathbf{p}_i = (x_i, y_i, z_i)$ are known. Accordingly, fixed the

parameters cc and ch, z_j^t represents the only unknown variable to retrieve by employing the height information z_i provided by the LiDAR data. It is worth mentioning that z_i is constrained among $z_j^t - ch$ and z_j^t for ensuring that the considered LiDAR measure is inside the vertical structure of the crown.

Let us address the case of having $n_j > 1$, thus having one equation per point $\mathbf{p}_i$ and a single unknown variable z_j^t. Once the value of the parameters ch and cc are defined, in order to find the z_j^t we can solve the estimation problem with a least square method, i.e.,

$$
\begin{aligned}
z_j^t &= \arg\min_{\bar{z}_j^t} \left\| \bar{z}_j^t \right\|_2^2 \\
&= \min_{\bar{z}_j^t} \left[r_1(\bar{z}_j^t)^2 + .. + r_i(\bar{z}_j^t)^2 + .. + r_{n_j}(\bar{z}_j^t)^2 \right]
\end{aligned}
\tag{4.5}
$$

where $r_i(\bar{z}_j^t)$ is the residual of the ith LiDAR point $\mathbf{p}_i$ described by the ground coordinates (x_i, y_i, z_i) and calculated as follows:

$$
r_i(\bar{z}_j^t) = \frac{(z_i + ch - \bar{z}_j^t)^{cc}}{ch^{cc}} + \frac{[(x_i - x_j^t)^2 + (y_i - y_j^t)^2]^{cc/2}}{cr^{cc}} - 1
\tag{4.6}
$$

Under the assumption that $n_j > 1$, instead of imposing a couple of parameters cc and ch for all the trees, we automatically determine the optimal tree model representation for each tree. In particular, we aim to fit as close as possible the 3-D structure of the tree to the LiDAR points acquired inside the crown. The residual metric can be used to identify the combination of parameters that minimizes the distance between the 3-D parametric model and the LiDAR points associated to the crown. The lower is the sum of the residual values the better the crown surface fits the LiDAR points.

This method cannot be applied to the set of crowns hit by just one LiDAR point since the residual metric remains zero for all the possible crown surfaces (i.e., combination of parameters). For this reason, for each crown we refine the search of the optimal tree model among N_m possible models. Afterwards, we select the model that returns the z_j^t equal to the median value of the N_m different z_j^t obtained. Since the ith LiDAR point associated to the crown is described by the height value z_i and the distance from the center of the tree given by $d_{ref} = \sqrt{(x_i - x_j^t)^2 + (y_i - y_j^t)^2}$ to choose the N_m combinations of parameters cc and ch to analyze, we consider the distance from the center. We compute the absolute difference between d_{ref} and the distance from the center of the LiDAR points associated to the crowns hit by more than one laser point. Finally, we select the models of the N_m crowns having the minimum absolute difference. Fig. 4.5 shows an example of the described procedure with $N = 3$.

4.2.4 k-Nearest Neighbors Trees k-NN trees

Low-density LiDAR measures do not affect only the accuracy of the tree top height estimates, but also tree detection rate. Although we are dealing with dense forest, by decreasing the laser sampling density the number of crowns hit by LiDAR points decreases as well. As the tree top reconstruction method described in the previous subsection requires at least one LiDAR measure for estimating the tree top height, a strategy for
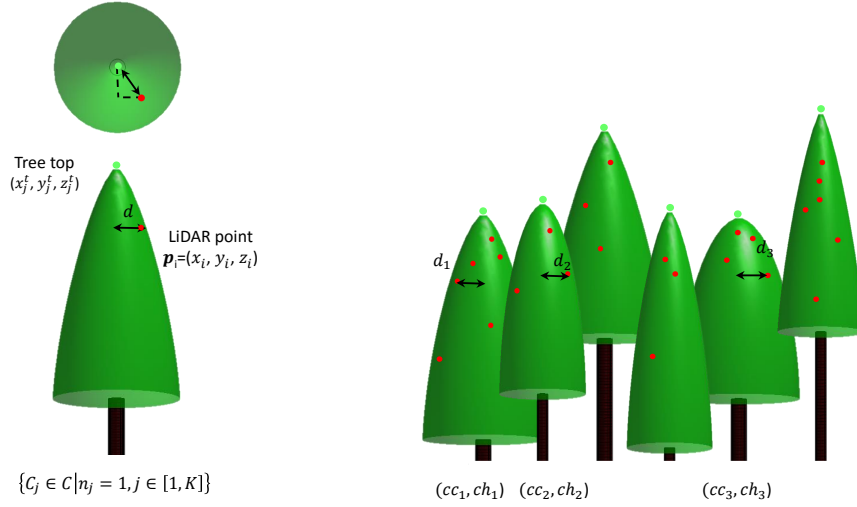
Figure 4.5: Example of the Tree Top reconstruction method for those crowns hit by just one LiDAR point, with $N = 3$. For the generic tree, the 3 trees having similar point distances (d_1, d_2 and d_3) and thus the 3 associated models (i.e., (cc_1, ch_1), (cc_2, ch_2) and (cc_3, ch_3)) are tested. The chosen model is the one that returns the z_j^t equal to the median value of the 3 resulting z_j^t.

estimating the heights of the missed crowns is developed. To this purpose we define a k-Nearest Neighbors Trees (k-NN trees) algorithm. Note that due to the segmentation, we are in the condition of detecting crowns missed by the laser scanner. Assuming that the tree properties can be considered in average homogeneous at local level in the studied area, the defined k-NN trees estimation method is based on the correlation among crown area and tree top height. Indeed, as demonstrated in [158, 159], there is a strong correlation between these two tree parameters. Accordingly, it is reasonable to exploit the crown area information to detect trees with similar tree top height by considering the same forest scenario. Let us focus the attention on the jth crown C_j and let us assume to have $n_j = 0$ laser points associated to it. To estimate the missed z_j^t, we identify the k trees that:

- belong to a predefined sparse neighborhood of the forest of C_j;

- are hit by at least 1 LiDAR pulse;

- are the most similar in terms of crown area.

The similarity measure defined is the absolute difference between the missed crown area of C_j and the area of all the crowns hit by at least one laser points $\{C_j \in \mathcal{C} | \ n_j \leq 1, j \in [1, K]\}$. Then, we estimate the tree height z_j^t as the average of the tree top reconstructed heights of the k trees having the minimum distance measure to the C_j crown. It is worth noting that here we considered all the trees belonging to the same coniferous forest to detect the k-NN trees. However, one can define more refined rules restricting the search to trees belonging to areas having similar terrain properties (e.g., same slope and/or same aspect of the terrain).
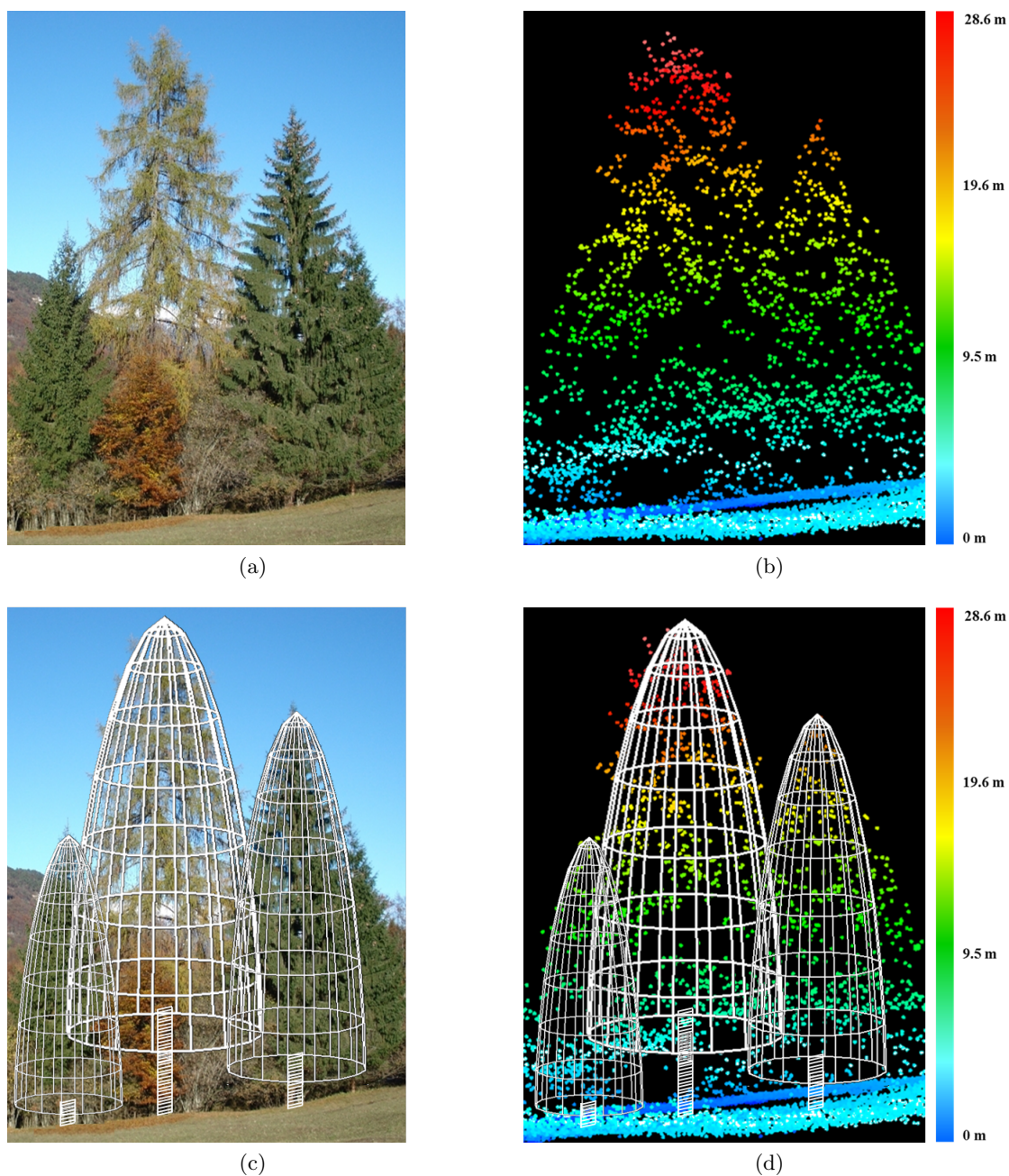
Figure 4.6: Examples of the considered 3-D parametric model: (a) real scene, (b) LiDAR points cloud of the trees, (c) 3-D parametric models of the trees automatically detected by the proposed method superimposed on the real scene, and (d) 3-D parametric models of the trees automatically detected by the proposed method superimposed on the LiDAR points cloud.

4.3   Experimental results

In this section we present the results obtained by the proposed technique on 4 low-density LiDAR dataset generated undersampling the original high-density LiDAR data. To assess the effectiveness of the proposed method from the quantitative view point the tree top height estimation results were evaluated on 3 circular stand plots where ground reference data were available. In particular, we analyze the results obtained considering: (i) the multisensor segmetnation, (ii) the 3-D reconstruction model for those crowns hit by more than one LiDAR pulse, and (iii) the overall method. Moreover, we applied the proposed technique on a wide test forest even though ground data were not available. Due to the availability of high-density LiDAR data, the heights measured by the sensor were used as reference data.

4.3.1   Dataset Description

The study area is a coniferous forest located in the Southern Italian Alps at Parco Naturale Paneveggio - Pale di San Martino in the Trentino province (Fig. 4.7). The predominant specie are the Norway Spruce (*Picea Abies*) and Silver Fir (*Abies Alba*). The optical image and the LiDAR data considered in the experiments were acquired simultaneously on September 4, 2007. The optical data are very high spatial resolution ortophotos (20 cm) characterizes my limited spectral resolution (RGB). LiDAR data have been acquired by an Optech ALTM 3100EA sensor, with an average point density > 5 pts/m^2. The laser scanner is characterized by a pulse wavelength of 1064 nm and a pulse repetition frequency of 100 Khz. To assess the effectiveness of the proposed technique, we undersampled the original LiDAR data for generating four low-density LiDAR datasets. The undersampling process has been realized by overlapping a uniform grid over the high-density LiDAR data and randomly selecting just one LiDAR point belonging to the first return within each grid cell. In greater details, we generated datasets having:

- 1 pt/m^2;

- 0.75 pts/m^2;

- 0.5 pts/m^2;

- 0.25 pts/m^2.

For the quantitative evaluation we considered 3 circular stands plot of radius 20 m and area 400 m^2 (Fig. 4.7a, Fig. 4.7b and Fig. 4.7c), where field data were collected during the summer 2007. The considered stand plots area characterized by different topography and different forest densities (Tab. 4.1) to test the method in different forest conditions. Within each stand plot all the trees were surveyed by measuring the tree position, the height, the crown diameter, the DBH and the forest species. Moreover, we considered a wide area (for which ground data are not available) located in the same coniferous forest (Fig. 4.7d) characterized by an extension of approximately 1.9 hectares and an altitude that ranges between 1565 m and 1604 m a.s.l.. Although the sensors were mounted on the same airborne platform during the simultaneous acquisition, we registered the
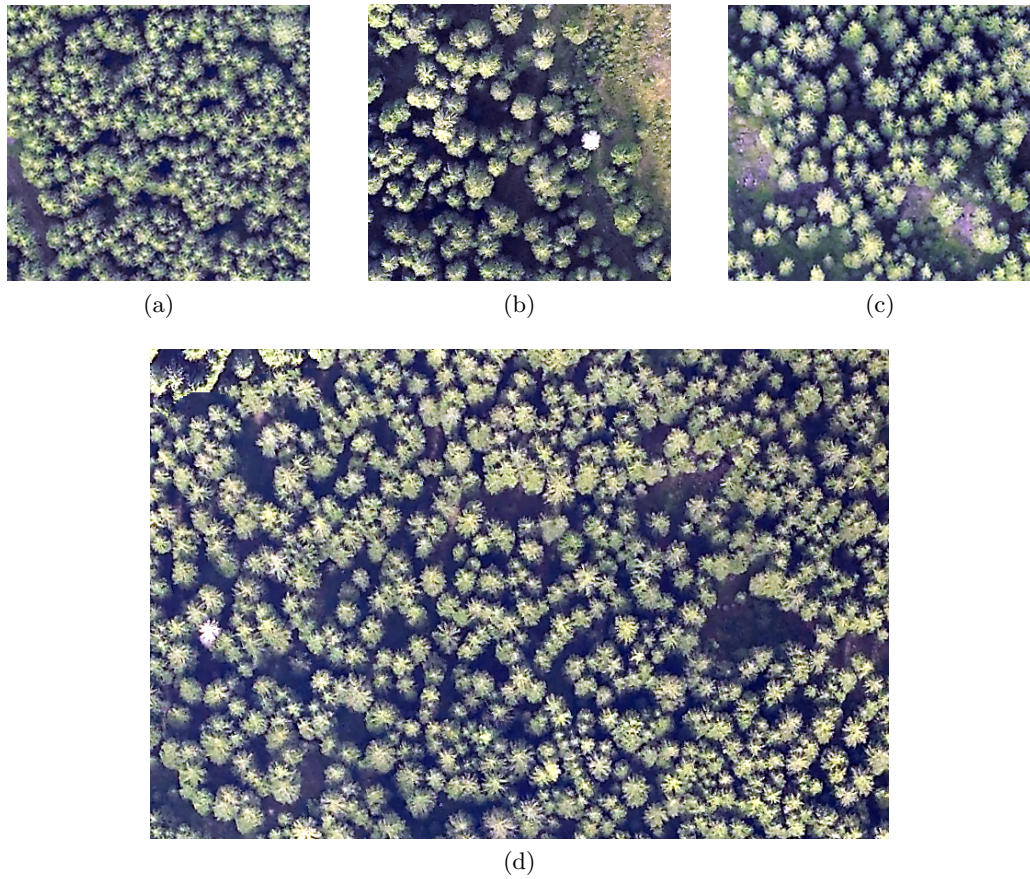
Figure 4.7: Optical images of the investigated area. (a) Stand plot P1, (b) Stand plot P2, (c) Stand plot P1, (d) extended test area.

Table 4.1: Number of trees, average value of altitude, slope and aspect, mean and range of the tree heights for each sample plot.

Plot	# Trees	Altitude	Slope	Aspect	Mean H (m)	Range H (m)
P1	71	1401 m	6°	264°	23.3	19.3 - 29.2
P2	32	1550 m	13°	131°	26.6	15.4 - 35.9
P3	48	1554 m	9°	253°	26.9	15.2 - 34.2

data by using Ground Control Points (GCP). The warped image has been obtained with a polynomial transformation of first order and a nearest-neighbour resampling of the pixels. The RMSE after the registration phase was 0.92 for Stand P1, 0.97 for Stand P2, 1.13 for Stand P3 and 1.22 for the wide area.

4.3.2 Experimental Setup

For the pre-processing of the optical images, the parameters were tuned considering the spatial resolution of the optical image and the expected minimum dimension of the tree crowns. Accordingly, the Gaussian and the Median filters window size was 5×5, while the standard deviation of the Gaussian filter was 10. The minimum number of pixels th_p of a segmented region to be considered a crown has been set to 5. Regarding the tree top reconstruction model, the ranges of parameters tested are as follows:

- The crown curvature $cc \in [1.7, 1.9]$ with a step of 0.1.

- The crown height $ch \in [10, 25]$ with a step of 1.

Please note that we tested a wide set of combinations of parameter values because of the high variability of the tree height which ranges from 15.2 m to 35.9 m (Tab. 4.1). For those crown hit by one LiDAR point, we set the number of models to test N_m equal to 3. Similarly, the value of the k trees selected for reconstructing the tree top height of the missed crowns has been set to 3 to evaluate just the most similar crowns.

4.3.3 Segmentation Results

An example of segmentation results is presented in Fig. 4.8 and Fig. 4.9 for the stand plot P2 and wide test forest area, respectively. In Fig. 4.8 the comparison between the result obtained using only the optical image and integrating the LiDAR data having the lowest density (i.e., 0.25 pts/m^2, the worst case for the considered dataset) is presented.

As discusses in Sec. 4.1, while in dense forest scenario the optical image allows a comprehensive representation of the horizontal structure of the forest, in wide open areas it is difficult to discriminate forest areas and bare soil. In this framework, the complementary information provided by the LiDAR data by means of the binary mask is fundamental to improve the segmentation result (Fig. 4.8d). Indeed, the fusion between the LiDAR height information and the optical image increased the crown delineation accuracy by avoiding that ground pixels were merged inside the tree crowns. This is confirmed by the results obtained on the wide area forest, where the segmentation identified 740 trees. Fig. 4.9 shows in white crown boundaries overlapped on the ortophoto. A qualitative visual analysis of the results confirms that the multisensor segmentation algorithm obtained a reliable delineation of the tree crowns.

To have a quantitative evaluation of the crown delineation results, for the three stand plots we compared the crown radius derived from the segmentation phase with crown radius measured in situ (Tab. 4.2). The results obtained demonstrate that the multisensor segmentation algorithm is able to detect the dominant trees present in the scene and to properly estimate the crown radius with a MAE of 0.78 m. It is worth noting that the
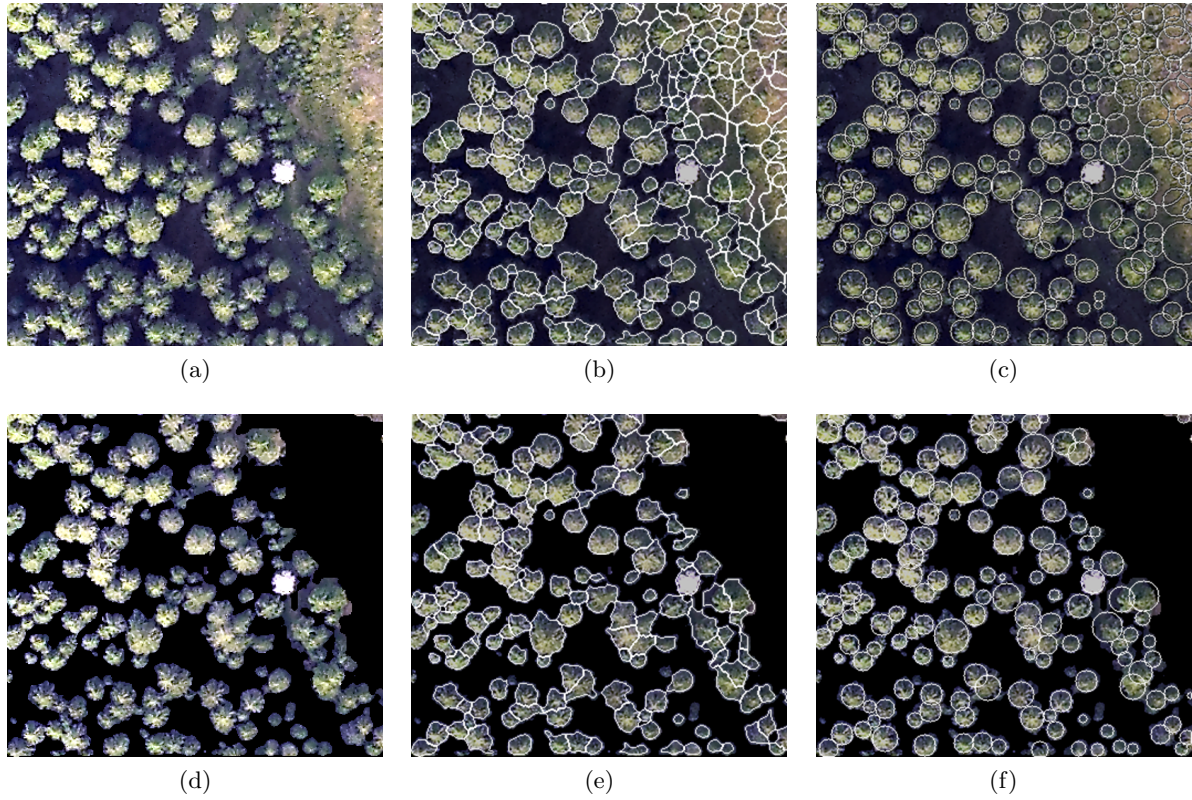
Figure 4.8: Masking procedure process. (a) Ortophoto of the Stand P2, (b) segmentation result obtained on the ortophoto, (c) circular representation of the segmentation result, (d) masking process result using the lowest sampling density dataset (i.e., 0.25 pts/m^2), (e) multisensor segmentation result, and (f) circular representation of the multisensor segmentation result.

Table 4.2: Number of trees detected by the multisensor segmentation algorithm compared to the number of dominant trees associated to ground data and ME, MAE and MSE of the Estimated Crown Radius.

Plot	N. Dominant Trees	N.Detected Trees	Percentage of Detected Trees	Estimated CR		
				ME	MAE	MSE
P1	72	71	99 %	-0.36	0.57	0.74
P2	33	32	97 %	-1.04	1.10	1.44
P3	50	48	96 %	-0.82	-0.89	1.09
All Stands	155	151	97 %	-0.65	0.78	1.04
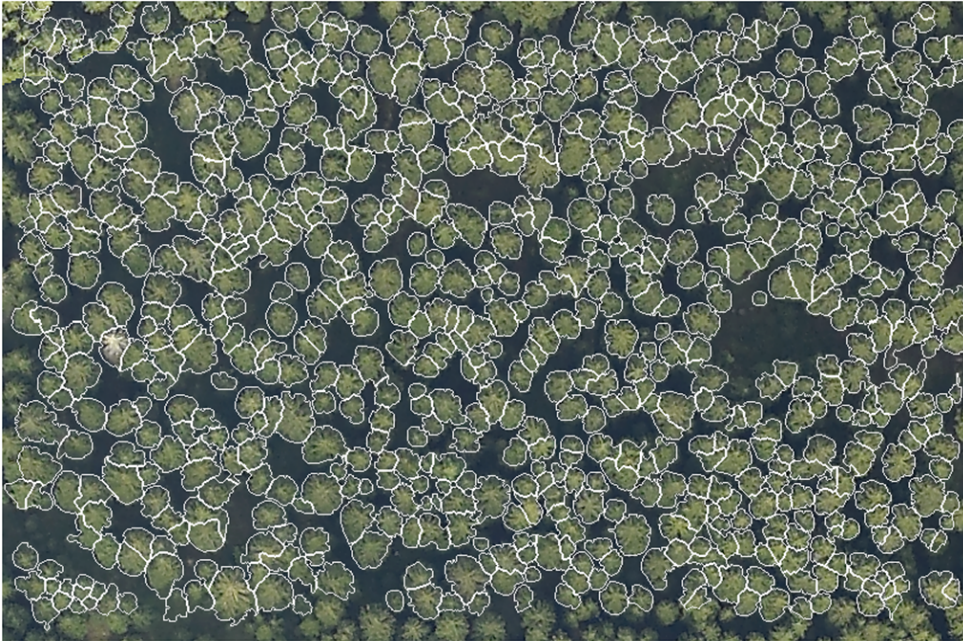
Figure 4.9: Segmentation result obtained on the wide coniferous forest. The crown boundaries are highlighted in white and overlapped on the ortophoto.

quality of the segmentation results affects the accuracy of the height estimation, since the derived crown radius and area are employed in tree top reconstruction step and in the k-NN trees criterion, respectively.

4.3.4   Tree Top Height Estimation Results

Let us now focus the attention on the tree top height estimation results, by first considering the results obtained on the three sample plots for those trees hit at least by one LiDAR points. Fig. 4.10 depicts the scatterplots of the Measured versus the Reconstructed Tree Top Height for the trees hit by more than one laser pulse, divided per laser sampling density. The results shows that the geometric representation of the shape of the crown effectively reconstruct the real height of the trees. By decreasing the laser sampling density the number of laser pulses associated to each crown decreases. However, for all the datasets the coefficient of variation R^2 ranges between 0.77 to 0.88.

Tab. 4.3 shows the tree top height estimates versus the number of hits associated to the crowns for the three stand plots. As expected the most accurate results are obtained when the tree crowns are hit by more than one LiDAR point. For those crowns, we obtained a MAE error of 1.41 m. Moreover, the ME demonstrates that the use of the 3-D parametric model resulted in almost unbiased estimates regardless of the laser sampling density (i.e. 1.02 m).

By reducing the number of points associated to the crown to one, the error values slightly increased. This is due to the suboptimal choice of the parameters ch and cc, which affected the performance of the tree top height estimation. Indeed, with more than
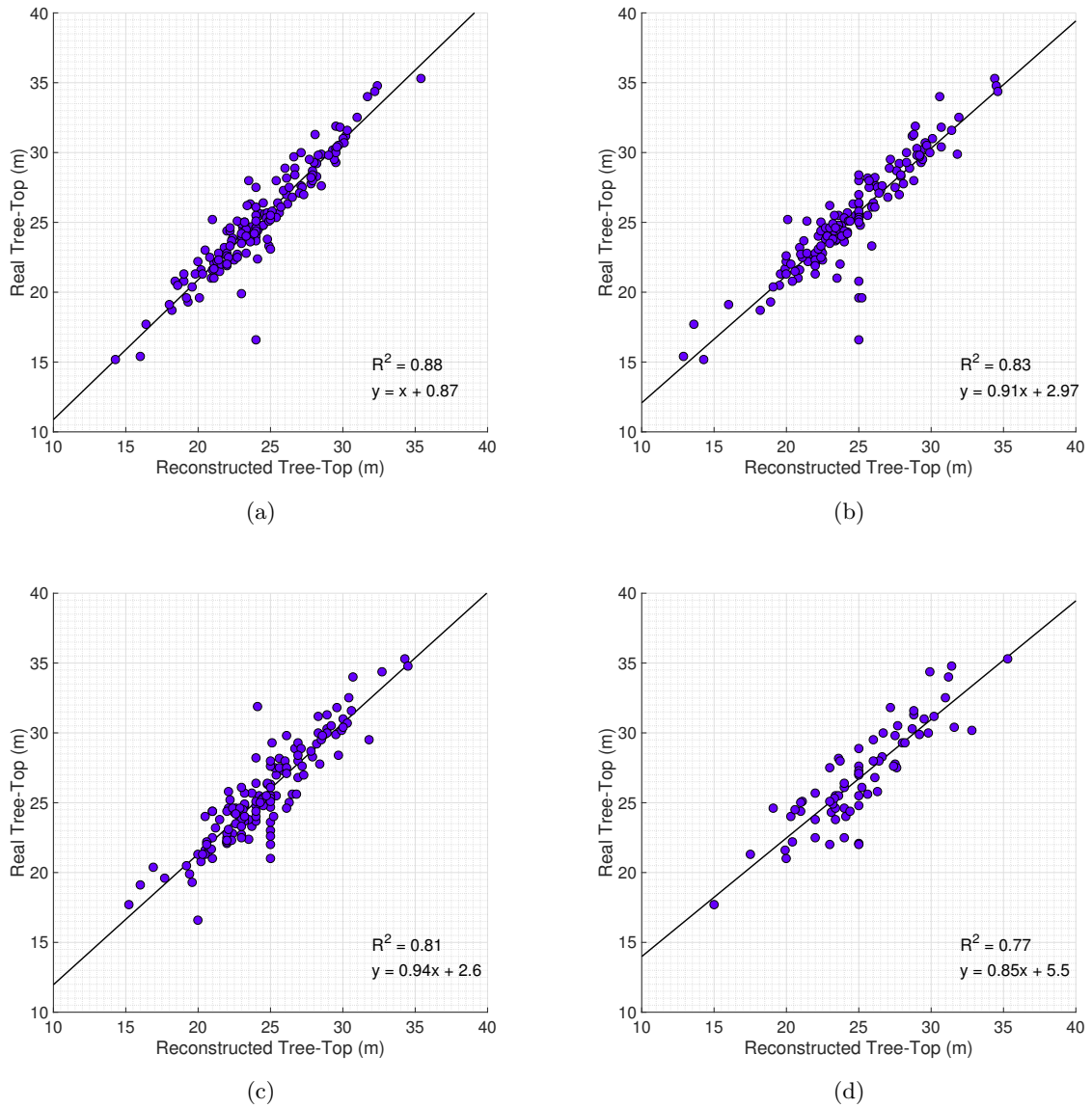
Figure 4.10: Reconstructed versus Observed Tree Top height for the trees hit by more than 1 LiDAR point. The height estimation results of all the Stand Plots is presented for the dataset having density of: (a) 1 pt/m^2, (b) 0.75 pts/m^2, (c) 0.5 pts/m^2, and (d) 0.25 pts/m^2.

one LiDAR point per crown it was possible to choose the model parameters more suited to the real shape of the considered tree crown. In contrast, with just one LiDAR point the model was selected only on the basis of the distance of the LiDAR point from the crown center and thus the accuracy of the height estimation decreased. Regarding those crowns that were not hit by any LiDAR point, the MAE is 3.97 m, while the low-density LiDAR could not obtain any measure for these trees.

Table 4.3: ME, MAE and MSE of the Estimated Tree Top and the Measured Tree Top. The average height estimation results are presented divided per number of hits associated to the crowns.

LiDAR points		All Datasets					
		Measured Tree Top			Estimated Tree Top		
	N. Trees	ME	MAE	MSE	ME	MAE	MSE
> 1 Point	510	2.15	2.15	7.12	1.02	1.41	3.47
1 Point	59	4.98	4.98	33.53	-0.08	2.25	9.28
k-NN Trees	35	22.83	22.83	532.59	-2.32	3.79	26.86

4.3.5 Overall Method Results

By focusing the attention on the overall method, the results obtained demonstrate the effectiveness of the proposed approach. Tab. 4.4a and Tab. 4.4b presents the comparison between the height measured by the low-density LiDAR data (Measured Tree Top) and the height estimated with the proposed method (Estimated Tree Top) for the all the stand plots and the entire test area, respectively. While for the stand plot the grountruth was used as reference data, for the entire forest area the error metrics were calculated considering the height measured by the high-density LiDAR data.

The proposed technique always reduced the error with respect to the low-density LiDAR data. Considering the stand plots, for the LiDAR datasets having 1 pt/m^2 the ME was reduced of 0.71 m and the MAE of 0.44 m, while for dataset having 0.75 pts/m^2 there was an improvement of the ME of 0.99 m and of the MAE of 0.43 m. By decreasing the laser sampling density the difference increases. In the case of 0.5 pts/m^2 the ME decreased of 2.01 m and the MAE of 1.38 m, while with 0.25 pts/m^2 the ME decreased of 7.93 m and the MAE of 5.72 m. Accordingly, we obtained a small MAE which ranges from 1.17 m (datasets of 1 pt/m^2) to 2.48 m (datasets of 0.25 pts/m^2) on an average height value of 25 m (approximately the 10% of average tree height value). These results contain all the sources of errors (included the segmentation errors).

For the entire forest area, the results obtained (Tab. 4.4b) confirmed the analysis performed on the stand plots. Also in this case, the proposed technique reduced all the error metrics with respect to the low-density LiDAR measures for all the considered datasets. Moreover, also in this case we can observe that by decreasing the laser sampling density the accuracy of the height estimation of the low-density LiDAR data decreases, whereas the accuracy of the proposed technique is not heavily affected. In greater detail, the ME of the Estimated Tree Top ranged from 0.31 m to 1.36 m and the MAE ranged

Table 4.4: ME, MAE and MSE of the heights estimated (Estimated Tree Top) and the heights measure by the low-density LiDAR data (Measured Tree Top) divided per laser sampling density on : (a) the three stand plots; (b) the wide area forest

LiDAR	All Stands Plot					
	Measured Tree Top			Estimated Tree Top		
	ME	MAE	MSE	ME	MAE	MSE
1 pt/m^2	1.61	1.61	3.70	0.90	1.17	2.45
0.75 pts/m^2	1.74	1.74	4.78	0.75	1.31	3.32
0.50 pts/m^2	2.95	2.95	17.89	0.94	1.57	4.03
0.25 pts/m^2	8.20	8.20	134.23	0.27	2.48	11.77

(a)

LiDAR	Entire Test Area					
	Measured Tree Top			Estimated Tree Top		
	ME	MAE	MSE	ME	MAE	MSE
1 pt/m^2	1.15	1.15	2.50	0.31	0.97	2.13
0.75 pts/m^2	1.46	1.46	3.92	0.33	1.19	3.13
0.50 pts/m^2	2.79	2.79	16.16	1.20	1.96	7.08
0.25 pts/m^2	4.33	4.33	41.22	1.36	2.39	9.86

(b)

from 0.97 m to 2.39 m for all the low-density LiDAR datasets, whereas the ME and the MAE of the Measured Tree Top ranged from 1.15 m to 4.33 m. Furthermore, we can again observe that the proposed method mitigated the systematic underestimation of the tree height.

By analyzing the MAE of the Measured Tree Top, one can observe that, as expected, it is equal to the ME since the LiDAR data systematically underestimate the Tree Top Height. In contrast, the ME obtained with the proposed method was close to zero (almost unbiased estimate) for all the stands (i.e., 0.90 for the datasets of 1 pt/m^2, 0.75 for the datasets of 0.75 pts/m^2, 0.94 for the datasets of 0.5 pts/m^2 and 0.27 for the datasets of 0.25 pts/m^2). Furthermore, while the Measured Tree Top estimates were strongly affected by the decreasing of laser sampling density, the proposed method achieved similar accuracies for all the LiDAR density considered. Indeed, by halving the laser sampling density the error metrics of the Measured Tree Top were almost doubled, whereas the proposed method slightly increased the error metrics.

4.4 Conclusion

In this chapter we presented a method for the accurate reconstruction of the tree top height by fusing low-density LiDAR data and optical images. The proposed method is

tailored on coniferous forest when the density of the LiDAR data available is not sufficient for an accurate estimation of the individual tree height.

To accurately estimate the height of the trees present in the scene, the method exploits the synergistic use of the two data sources in a data fusion perspective. First, a multisensor segmentation method is applied to the optical image by integrating the height information provided by the LiDAR data to obtain accurate crown delineation results. Starting from the segmentation results, we propose a height reconstruction method for those trees hit by at least one laser point and a k-NN trees technique for those trees completely missed by the laser scanner. In the first case, a 3-D parametric model of the conifers is employed to address the reconstruction of the true height of the tree. The model is adapted to the shape of the tree both in the horizontal and vertical directions. The horizontal crown structure is modelled by the crown radius and the tree top location derived from the segmentation phase, while the vertical structure is obtained by fitting the LiDAR points associated to the crown. For those crowns missed by the laser scanner, the k-NN trees technique estimates the missed tree height as the average of the k reconstructed height of the trees having similar crown area and belonging to a sparse neighbourhood.

The experimental results obtained demonstrate the effectiveness of the proposed technique. The quantitative results obtained on the three stand plots confirm that the 3-D parametric model is able to accurately reconstruct the structure of the trees. As expected, the higher is the number of LiDAR points associated to the tree crowns the better is the choice of the values of the model parameters and thus, the tree top height estimation. Accordingly, reducing the number of points associated to the tree crown to one, the accuracy of the height estimation decreases. Regarding the results obtained on those crowns that are not hit by any LiDAR point, the error metrics only slightly increased with respect to those obtained by applying the reconstruction model. However, the k-NN trees technique allows the estimation of the height for those crowns which are not measured by LiDAR. Therefore, the height estimate of the entire stand plot is strongly improved by the introduction of the proposed method.

The robustness of the proposed technique is confirmed by the results obtained on a dataset characterized by a wide area coverage. The significant reduction of the estimation errors becomes more evident when we deal with very low-density LiDAR data (i.e., 0.5 pts/m^2 and 0.25 pts/m^2). Moreover, the height estimation results are almost unbiased and thus do not systematically underestimate or overestimate the tree height. On the contrary the laser sampling density results in strongly underestimated height values due to both the missed tree top by the laser pulses and the missed detection of tree crowns.

As future developments, we aim to investigate other strategies for selecting the 3-D parametric model for those crowns hit by just one LiDAR point, in order to better adapt the model to the real shape of those tree. Moreover, we plan to improve the performance of the k-NN trees technique by investigating the forest environment in order to select trees similar to the missed ones in terms of crown structure, topography and forest density.

Chapter 5

A Method for Crown Structure Estimation based on the fusion of Airborne and Terrestrial LiDAR data

In this chapter[1] we present a method for the accurate estimation of the 3-D structure of a tree crown, which is based on the fusion of low-density airborne and high resolution terrestrial LiDAR data. By exploiting the joint LiDAR data coverage acquired from different viewpoints it is possible to accurately characterize the 3-D structure of the single tree crowns to perform localized forest analysis. The method is made up of: (i) the Li-DAR data pre-processing, (ii) the registration of airborne and terrestrial LiDAR scans, (iii) the fusion of the segmented tree point clouds, and (iv) the automatic crown parameter estimation. After the pre-processing, an automatic registration module allows us to accurately match the LiDAR point clouds obtained by airborne and terrestrial acquisition. In particular, the spatial pattern of the forest is used to adapt the segmentation result obtained on the airborne data to the terrestrial one, to accurately extract the crowns in both the data types. Second, a refined registration analysis accurately fuses the LiDAR point clouds at single tree level. Finally, the crown parameters are estimated from these fused point clouds and compared with the ones obtained by a separate processing of airborne and terrestrial data. Experimental results obtained on data acquired in an open woodland forest area confirm the effectiveness of the proposed approach.

5.1 Introduction

Tree crowns have important implications to wildland fire dynamics [160], avian habitat provision [161], microclimates [161] and estimation of the fractal dimension of trees [162].

---

[1]Part of this chapter appears in:
C. Paris, D. Kelbe, J. van Aardt, and L. Bruzzone, "A precise estimation of the 3d structure of the forest based on the fusion of airborne and terrestrial LiDAR data," in *Geoscience and Remote Sensing Symposium (IGARSS), 2015 IEEE International.* IEEE, 2015, pp. 49-52.

Within a tree crown, the net leaf surface area drives the size of the plant-atmosphere interface, which affects the rate and balance of biotic exchanges through photosynthesis and transpiration [163]. Likewise, the distribution of elements governs radiation penetration through to lower-canopy strata [164, 165], with implications to growth and productivity [166, 167]. Accurate and precise measurement of crown structure is therefore an enviable goal for systematic characterization and measurement. However, explicit measurement of tree crowns using conventional techniques is not trivial, due to the complex structure of irregular, natural surfaces. Despite a long history of forest mensuration, traditional methods for quantifying canopy structure remain limited in their ability to make detailed, quantitative, and spatially-explicit measurements [161]. Moreover, tree-level parameters are often restricted to coarse metrics, such as crown height, crown base height, and crown width, while more informative metrics are modeled based on lower-level parameters [168]. Crown volume, in particular, has been reported as one of the more difficult parameters to obtain [169]. Traditional techniques rely on allometric equations to parameterize geometric primitives (e.g., cones and ellipsoids) and require species information and certain field-measured variables [168].

In contrast, laser scanning records range data based on an emitted laser pulse [170], thus providing non-destructive, high-resolution, and repeatable 3-D surveys of individual trees crowns. Laser scanning has a demonstrated capability to address the limitations of traditional measurement approaches [32], both from airborne and terrestrial platforms. ALS provides wide-area coverage by coupling an across-track scanning mechanism to along-track aircraft movement [171], while large-footprint sensors have focused on stand-scale parameters, e.g., mean canopy height, increasingly fine footprints (sub-meter) and point densities (>15 hits/m^2) [172], have allowed the detection and measurement of individual tree canopy parameters, including volume. As was done with typical forestry techniques, a common approach is to fit assumed geometric shapes to LiDAR point clouds, in order to derive basic tree crown parameters [173, 95, 174, 175, 176]. In this approach, tree canopy height and stem location are obtained by detecting convex shapes in a CHM (e.g., [85]), thus allowing extraction of crown width and ultimately crown volume. However, these methods relied on a priori species identification for parametrizing the appropriate geometric crown shape, information which is often unavailable from remote sensing data [169]. This is especially challenging for heterogeneous, non-managed forest environments. Moreover, these simple geometric models are coarse compared to the fidelity of ALS measurement. With the recent trend towards higher point density LiDAR collection, direct measurement of tree crowns should be considered [169].

Several alternative approaches therefore have been pursued, based on either graph-based segmentation or direct measurement. In [108] the authors employed normalized cut segmentation to detect individual trees, including those below canopy, theoretically allowing for direct computation of volume (although quantitative results were not presented). Similarly, in [177] authors employed a graph-based segmentation algorithm with potential for volume assessment based on existing techniques. In [169], on the other hand, authors developed a direct, wrapped surface reconstruction technique based on radial basis functions. Irregular tree crown shapes were validated with respect to survey-grade equipment to assess goodness of fit. Among other reported metrics, the authors achieved

measurement of crown volume with $R^2 = 0.84/0.89$ for coniferous/deciduous trees. Finally, computational geometry to measure explicit crown volume using 3-D alpha shapes and convex hulls can be used. These estimates were validated against field-measured values and modelled ellipsoids, with $R^2 = 0.83$ (best), but significant underestimation (-24%, on average), attributed to insufficient LiDAR returns from the lower crown regions. The observed challenges in crown volume assessment with ALS [178] underscore several fundamental system limitations. A first limitation is the reduced capability to sample sub-canopy structure. Discrete-return ALS, for example, records only the first and last, or perhaps, a few, e.g., up to 5, backscattered returns from each emitted laser pulse. As a result, limited information from the inner or lower canopy is obtained [32, 77]. While waveform-digitizing LiDAR [179] offers potential to rectify this gap, the systems are still poorly understood, and there remains a measurement gap due to dead time in the digitization of the return pulse. A second limitation is related to measurement characteristics: as a result of limited incidence angles constrained to predominantly nadir, and finite footprint sizes on the order of 0.1–0.5 m, ALS may be unable to detect small canopy gaps [161, 180, 181], or other fine-scale structures. Finally, when acquired with low laser sampling density, these data do not allow a comprehensive representation of the crown structure.

Recent studies have suggested the potential to address these concerns via fusion with a complementary, upward-looking laser ranging system, i.e., TLS [182]. TLS provides hemispherical scanning from a ground-based platform, and thus samples different parts of the forest structure. In [77] the authors examined the voxel column percentile distributions of point returns for both ALS and TLS and demonstrated that a higher percentage of laser pulses intercept the top of the canopy for ALS, with limited returns within the canopy and understory. Likewise, TLS exhibited a higher number of returns from the lower-canopy, but had fewer returns in the upper canopy. In light of this, there is a growing interest in utilizing TLS to complement the strengths of ALS ([79, 78]), and thus link ground-level structural measurement with the synoptic perspective of ALS. However, there has been limited research in this area, in part due to the difficult prerequisite of registration [80]. Indeed, the main limitation of TLS acquisition is the need of positioning reference targets to register the multi-angular scans, which often requires time-consuming manual refinements. To solve these problems, in this chapter we propose a method for fusion of ALS and TLS based on an automatic registration module. In greater detail, we aim to take advantage from the spatial pattern of the forest to register the terrestrial scan to the airborne data without the need for reference targets. This condition allows us to adapt the crown segmentation performed on the ALS data to the terrestrial scans. By fusing for each crown the LiDAR point clouds a extremely high resolution 3-D crown profile is obtained. Therefore, the main objectives of this work are to: (i) utilize the airborne LiDAR data to automatically register the multiple terrestrial scans (without the need for reference targets), (ii) analyze the spatial pattern of observed forest structure to perform co-registration, (iii) use of the airborne segmentation results to delineate the crown in the TLS scans, and (iv) integrate the 3-D LiDAR point clouds of both the ALS and TLS data for quantitative measurements of both forest and tree crown structure.

The following chapter is organized as follows. Sec. 5.2 illustrates the considered
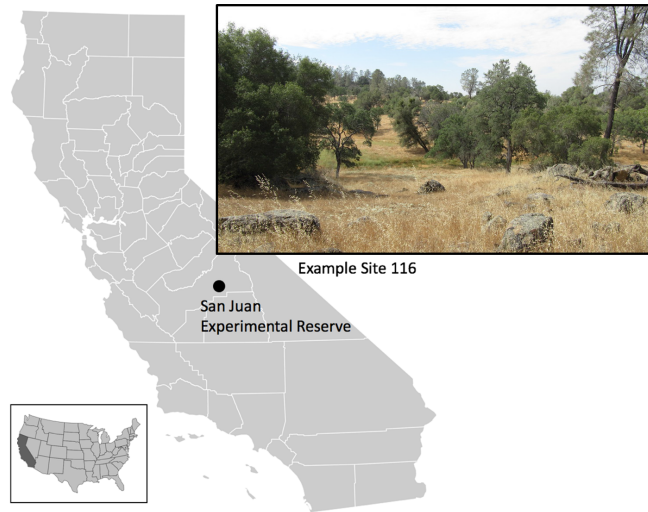
Figure 5.1: The NEON Pacific Southwest domain (D17) is located in central California. It contains one core site and two relocatable sites. The core site, San Joaquin Experiment Range (SJER), is an oak savanna.

dataset by presenting in detail the study area, the terrestrial measurement setup and the airborne data available. Sec. 5.3 describes the proposed data fusion approach and 5.4 presents the obtained experimental results. Finally Sec. 5.5 draws the conclusion of the chapter.

5.2   Dataset Description

The considered study area is the National Ecological Observatory Network (NEON) Pacific Southwest (PWS) Domain 17 (D17) core site, located in the San Joaquin Experimental Range (SJER; 37°6′43,77″ N, 119°44′11,85″). The SJER is an oak savanna woodland. An example of the study area is presented in Fig. 5.1. The dominant species are blue oak (Quercus Douglasii), interior live oak (Quercus Wislizeni), and grey pine (Pinus Sabiniana). Reference data were collected in June 2013 (14 trees) for the considered site area. For each sample plot the height, species and crown width were measured.

ALS data were obtained from the National Ecological Observatory Network (NEON) Airborne Observation Platform (AOP), which operates an Optech ALTM Gemini LiDAR system. The 1064nm, four-return-per-pulse system was operated at a 100kHz pulse repetition rate and 1000m above-ground-level (AGL), for an average point density of 2 hits/m2. The ALS overflight was performed coincident with the TLS field measurement campaign performed during the period of June 9-21, 2013. Terrestrial data were acquired using a portable laser system created by Rochester Institute of Technology [183]. The TLS sensor head is a SICK LMS-151 laser scanner, which is compact and weather-resistant. A 905 nm laser is pulsed at 27 kHz with range measurement recorded based on time-of-flight. The laser pulse is deflected by a rotating mirror to sample a 270 arc, swept out in elevation angle. This sensor head is coupled to an azimuthal rotation stage, which provides cover-
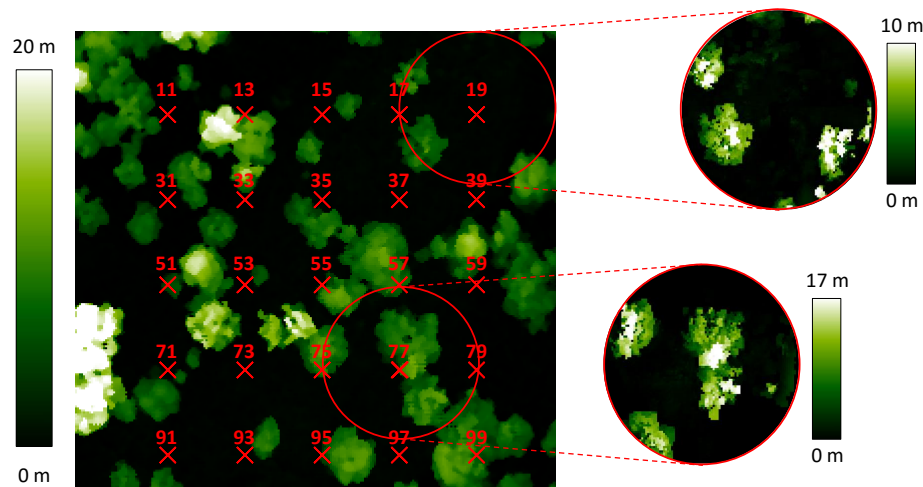
Figure 5.2: False color representation of the airborne CHM. The ideal TLS measurement setup is in red and overlapped on the image, where for each position the acquisition number of the TLS scan is reported. Two example of TLS data are presented.

age of the full hemisphere above the instrument and a portion of the hemisphere below (270 V x 360 H coverage). Up to two returns per outgoing pulse are digitized. Mounted to the unit are a BeagleBone computer and power tool battery. Sensor control is achieved via a wireless mobile application. The main properties of the system are the light weight (1.1 kg) and fast scanning speed (less than a minute per scanning location), which allow practical acquisition campaigns. To this end, at plots of 40 m × 40 m, 25 scans per plot were collected along an equally spaced grid at 10 m increments (Fig. 5.2). No artificial tie points were placed to drive the terrestrial data acquisition and registration. After having measured the center of the stands with the GPS, the plots were laid out by means of the traditional tape-and-compass method. This regular sampling acquisition setup allows us to acquire fast, but consistent data coverage.

5.3 Proposed Method

The aim of the proposed method is the accurate characterization of the structure forest exploiting the joint LiDAR data coverage acquired from different viewpoint perspectives. In particular, we aim to accurately reconstruct the 3-D structure of the crowns. To this end, the proposed method is made up of four main phases: (i) the LiDAR data pre-processing, (ii) the registration of airborne and terrestrial LiDAR scans, (iii) the fusion of the segmented tree point clouds, and (iv) the automatic crown parameter estimation. In greater detail, in the registration module we first exploit the forest spatial pattern to register the airborne data to each LiDAR scan separately. This condition allows us to apply the segmentation result obtained on the airborne image to the terrestrial LiDAR point cloud. Finally, a registration at single tree level is performed by registering the terrestrial data to the airborne one. Fig. 5.3 shows the block-scheme of the proposed
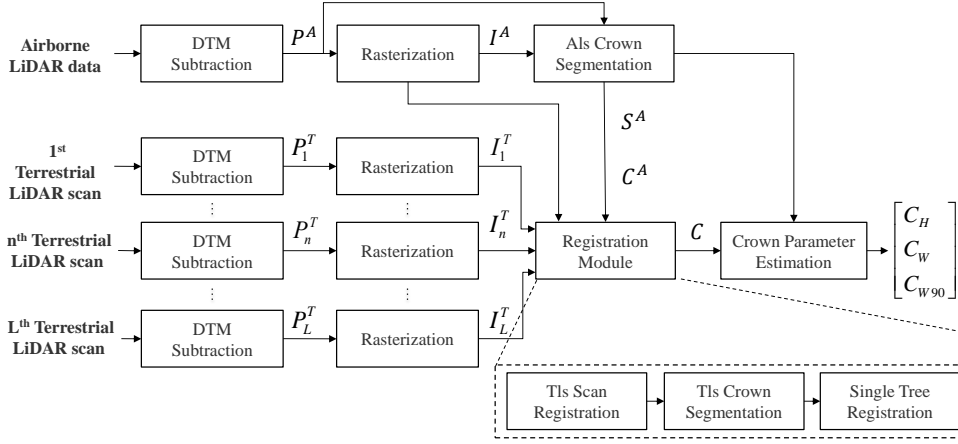
Figure 5.3: Block scheme of the proposed data fusion approach to the accurate reconstruction of the 3-D structure of the crown.

data fusion method. In the following we describe in detail each phase of the proposed method.

5.3.1 Pre-processing

Let us assume to have L evenly-spaced terrestrial scans and one airborne LiDAR data acquired in the same forest area. In the pre-processing phase, in the first step we perform the subtraction of the Digital Terrain Model (DTM) from the airborne and the terrestrial LiDAR data. Accordingly, we generate a series of normalized point clouds where each point's z coordinate represents the height above ground. Let $\mathcal{P}^A$ be the normalized airborne LiDAR point cloud and let $\mathcal{P}_n^T$ be the nth normalized terrestrial LiDAR scan, with $n = 1, .., L$. In the second step, we rasterize the data to generate a series of Canopy Height Models (CHMs). Let I^A be the CHM of the airborne LiDAR data and I_n^T the CHM of the nth terrestrial LiDAR scan, with $n = 1, .., L$. Because of the comprehensive representation of the horizontal structure of the forest provided by the airborne acquisition, the detection and the delineation of the individual tree crowns is performed considering only the airborne LiDAR data. Therefore, at the end of the pre-processing phase, the ALS data are employed to segment the trees with the method presented in Chapter 2. The single trees are first detected in the CHM by means of an LSM that identifies the tree tops. Then, the analysis is refined in the LiDAR point cloud to detect possible missed crowns. Finally, an angular analysis is performed to adapt the delineation of the border to the different sides of the crown. At the end of this phase we obtained the segmented image S^A representing the set of crowns $\mathcal{C}^A$.

5.3.2 Registration Module

Because of the different acquisition perspective, the terrestrial and the airborne point clouds are not comparable and thus cannot be automatically registered (Fig. 5.4). However, the spatial pattern of the forest structure is the same regardless of the acquisition
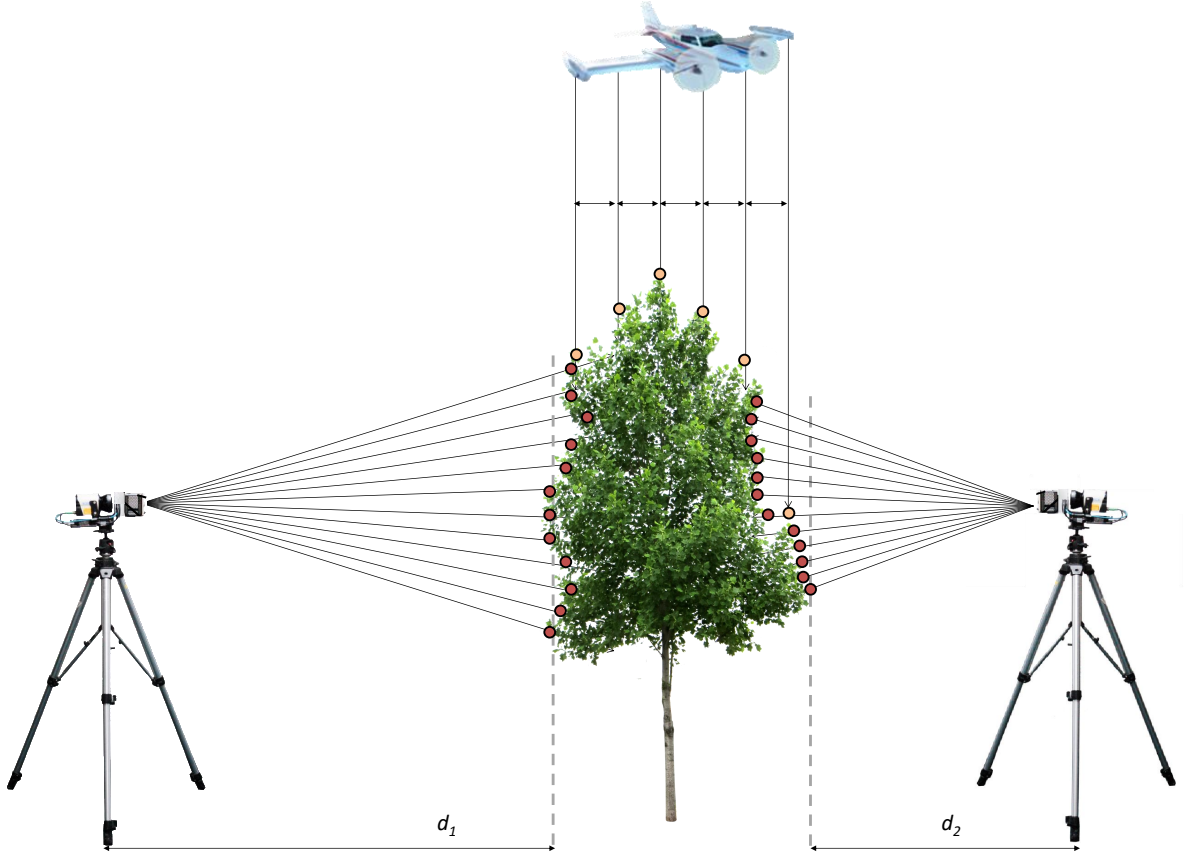
Figure 5.4: Visual representation of the different LiDAR point sampling obtained by using ALS and multi-angular TLS scans when considering the same tree. Due to the different view point, the LiDAR point cloud obtain are not comparable.

view point. For this reason, the first step of the registration module takes advantage from the correlation between the forest structure represented in the airborne and the terrestrial CHMs to determine the registration parameters. For sake of simplicity, in the following we focus the attention on the nth terrestrial scan.

Step 1 - Tls Scan Registration: The goal of this step is registering the airborne data I^A to the terrestrial scan I_n^T in order to adapt the segmentation image S^A to the terrestrial point cloud $\mathcal{P}_n^T$. Indeed, even though TLS provides a high resolution point cloud, the segmentation of the crowns is usually addressed manually due to the lateral scanning pattern. To solve this problem, we adapt the airborne segmentation results to the terrestrial data, thus accurately delineating the single tree crowns present in $\mathcal{P}_n^T$. In particular, we aim to determine a linear affine transformation that allows the best image alignment since these linear models apply a shape-preserving mapping because of their capability of preserving angles and curvatures of the original image [184]. Thus, the shape of the tree crowns is preserved. The starting registration point is given by the GPS coordinates on the ter-

restrial scanner that are measured in situ. However, these coordinates are not precise enough to guarantee no shift in terms of translation or rotation. Moreover, even tough the forest pattern represented by the two CHMs is the same, the geometry of the scene acquired from the ground does not perfectly match the one acquired from the airborne platform because of the different acquisition perspective. Thus, a scale factor should be considered. For all these reasons, a geometric affine transformation ζ_n should be applied to I^A to accurately match the forest recorded by the terrestrial scan. Let $N \times M$ be the size of I_n^T. First, the CHM of the airborne data I^A is cropped in order to keep the portion of the airborne CHM I^A representing the same forest area present in I_n^T. Let us define with I_n^A the considered portion of the airborne image having corresponding to I_n^T. Second, the parameters of the affine transformation ζ_n applied to I_n^A are estimated. The affine transformation is defined as follows, i.e.,:

$$\zeta_n(x,y) = \begin{pmatrix} s_x \cdot cos\phi & -s_y \cdot sin\phi \\ s_x \cdot cos\phi & +s_y \cdot sin\phi \end{pmatrix} \begin{pmatrix} x \\ y \end{pmatrix} + \begin{pmatrix} t_x \\ t_y \end{pmatrix} \tag{5.1}$$

where ϕ is the rotation angle, $[t_x, t_y]$ the translation vector and $[s_x, s_y]$ is the scaling factor. The estimation of the five unknown parameters is performed by minimizing an objective criterion function. Here we select as criterion function the Sum of Squared intensity Differences (SSD) between the terrestrial CHM I_n^T and the registered airborne CHM $I_n^{A'}$ as follows:

$$\begin{aligned} \text{SSD}_{min} &= \min_{[\phi,t_x,t_y,s_x,s_y]} \sum_{i=1}^{M} \sum_{j=1}^{N} [I_n^T(x_i,y_j) - I_n^A(\zeta_n(x_i,y_i))]^2 \\ &= \min_{[\phi,t_x,t_y,s_x,s_y]} \sum_{i=1}^{M} \sum_{j=1}^{N} [I_n^T(x_i,y_j) - I_n^{A'}(x_i,y_j)]^2 \end{aligned} \tag{5.2}$$

In particular, a gradient descent step optimization algorithm was adopted to estimate the transformation parameters [185, 186]. To evaluate the effectiveness of the registration process, we compute the normalized cross correlation similarity measure between I_n^T and $I_n^{A'}$. Accordingly, the value of the correlation matrix Υ at the position (w,l) is computed as follows:

$$\Upsilon(w,l) = \frac{\sum_{x,y} [I_n^T(x,y) - \mu_n^T][I_n^{A'}(x-w,y-l) - \mu_n^A]}{\sqrt{\sum_{x,y} [I_n^T(x,y) - \mu_n^T]^2 \sum_{x,y} [I_n^{A'}(x-w,y-l) - \mu_n^A]^2}} \tag{5.3}$$

where μ_n^T and μ_n^A are the mean value of I_n^T and $I_n^{A'}$, respectively. By checking in the normalized correlation matrix Υ, if the position of the peak (X_p, Y_p) is the image center and the value of the peak $\in [-1,1]$ is higher than a positive threshold we can automatically confirm the registration result.

Step 2 - Tls Crown Segmentation: At the end of the first registration step, for each nth terrestrial scan we have the affine transformation ζ_n which allows us to register I_n^A to the I_n^T. To accurately detect and delineate the single tree crowns present in the terrestrial

scans, we exploit the segmentation result obtained on the airborne image. Indeed, because of the comprehensive representation of the horizontal structure of the forest provided by the airborne acquisition, the airborne segmentation result is more accurate than the one obtained on a terrestrial data. First, we crop the segmented image S^A to represent the portion of the forest area present in I_n^T. Let S_n^A be the portion of the segmented image corresponding to I_n^T. Second, we apply the affine transformation ζ_n, thus adapting the segmented crowns to the shape of the terrestrial data. Let $S_n^{A'}$ be the portion of the segmented image S_n^A registered to I_n^T. Finally, we delineate the crowns directly in $\mathcal{P}_n^T$, thus generating the set of segmented LiDAR point clouds $\mathcal{C}_n^T$ visible in I_n^T.

Step 3 - Single Tree Registration: in the last step of the registration module we address the registration of the single tree crowns delineated in the LiDAR point clouds. For each crown $C_k^A \in \mathcal{C}^A$ we consider the set of associated terrestrial crowns. In this step, the airborne data drive the registration process, due to the whole representation of the forest structure. The crown boundaries of the terrestrial segmented point cloud are matched to the to the boundaries of C_k^A. In particular, we consider only the portion of the terrestrial crown that was facing the laser scanner during the acquisitions. Accordingly, different LiDAR acquisition of the same crown are registered into a single reference coordinate system, i.e., the airborne coordinate system.

5.3.3 Point Cloud Fusion

At the end of the registration phase, the proposed method performs the fusion of the ALS and TLS point clouds per crown to generate the set of final segmented point clouds. Although airborne LiDAR data represent the horizontal structure of the entire stand plot, an over-segmentation problem usually arises due to both the crown overlapping and the low density of the LiDAR point cloud. However, due to the fusion we have a high resolution crown profile. Therefore, to detected the possible over-segmentation errors, we analyze the obtained set of fused LiDAR point clouds. In particular, each crown is first rasterized and then the tree tops are detected. If the LiDAR point cloud represents a single tree crown, the tree top identification result coincides with the result obtained from the airborne data. In contrast, if the LiDAR point cloud represents two or more trees, thanks to the contribution from the terrestrial data, we separate the crowns.

5.3.4 Crown Parameter Estimation

Finally, we address the automatic estimation of the tree parameter by considering the height of the tree, the crown width and the 90° crown width. Accordingly, the height is measured as the highest LiDAR point belonging to the crown. To determine the two crown widths we considered the length of the major and the minor axis of the ellipse having the same normalized second central moments of the crown region.

Table 5.1: Normalized cross correlation similarity results. For each terrestrial scan the obtained correlation coefficient $\Upsilon \in [-1, 1]$ and the position (X_p, Y_p) of the correlation peak after the automatic registration are presented.

								TLS Scan Number									
	11	**13**	**17**	**19**	**31**	**33**	**37**	**39**	**53**	**55**	**59**	**73**	**75**	**77**	**79**	**91**	**95**
Υ	0.78	0.85	0.83	0.78	0.66	0.71	0.67	0.60	0.74	0.78	0.65	0.81	0.56	0.63	0.70	0.66	0.75
$\mathbf{X}_p$	0	0	0	0	0	0	0	0	0	0	0	0	0	0	0	0	0
$\mathbf{Y}_p$	1	0	0	0	0	0	0	0	0	0	0	0	0	0	1	1	0

5.4 Experimental Results and Discussion

In this section we show the results obtained by applying the proposed method to the considered dataset. In the following, we analyze the registration and the point cloud fusion results from the quantitative and the qualitative view point.

5.4.1 Results on TLS and ALS Point Clouds Registration

Among the 25 terrestrial scans collected in the considered study area, eight were discarded due to acquisition problem. Accordingly, the results presented consider the remaining 17 scans. No parameter were tuned to perform the registration, which was completely driven by the spatial pattern of the forest. Tab. 5.1 shows the accuracy of the TLS scan registration phase. Although the proposed method is fully automatic, to asses the reliability of the registration phase, the normalized cross-correlation similarity among the registered airborne data and the terrestrial scan is computed. Both the values of the correlation peak ($\Upsilon \in [-1, 1]$) and of its position (X_p and Y_p) are presented per TLS scan. As one can notice, all the terrestrial scans obtained high values of the correlation coefficient which range between 0.56 and 0.85, with an average value of 0.71. Moreover, the position of the correlation peak, which is always almost [0,0], confirms the accuracy of the registration results obtained. Thus, the affine transformation applied to the airborne image is able to accurately register the data to each terrestrial scan regardless of the spatial pattern of the forest. These results are confirmed by those presented in Fig. 5.6 - Fig. 5.10, where each TLS scan is represented before and after the registration step. The crown boundaries of the airborne image are highlighted in grey and superimposed to the TLS CHM to show the effectiveness of the registration procedure. The images demonstrate the importance of performing the registration step since the original TLS scan is shifted with respect to the ALS data due to the inaccurate GPS position and the different acquisition point of view. This misalignment is clearly visible when overlapping S^A directly on the terrestrial scan. Due to the registration performed we are in the condition of accurately adapting the airborne segmented image to the TLS data.

It is worth noting that the registration phase is not affected by the accuracy of the

airborne segmentation result since it is performed by considering the original CHMs. In contrast, the TLS segmentation is affected by the accuracy of the ALS crown delineation result. However, the proposed method allows us to extract in an automatic way the TLS crown without performing any manual refinement of the segmentation results. Moreover, due to the top view perspective, the ALS allows a better segmentation result with respect to the TLS even though the terrestrial data provide a higher resolution point cloud.

5.4.2 Results on Point Cloud Fusion

(a) *Pinus Sabiniana*   (b) *Quercus Douglasii*   (c) *Quercus Wislizeni*
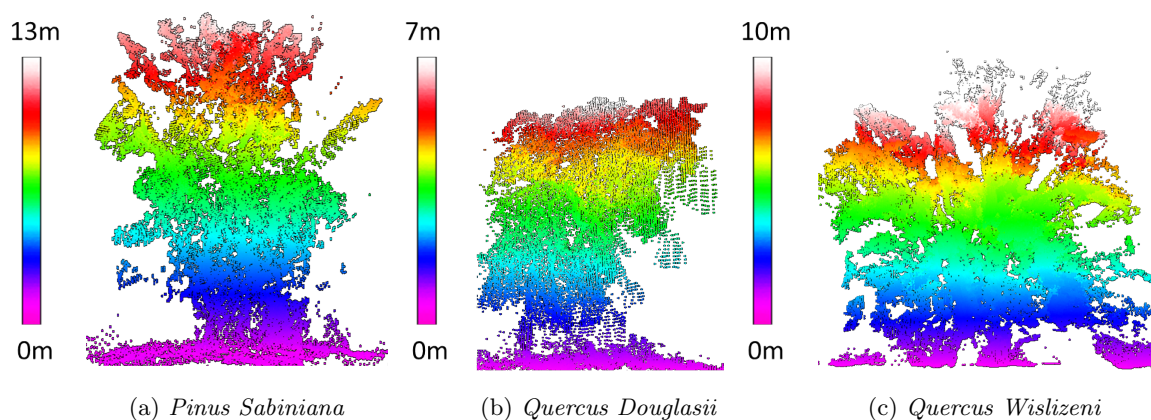
Figure 5.5: Example of point cloud fusion results. Due to the high resolution data obtained, the three main species of the considered study area can be recognized by considering the different crown structures.

At the end of the proposed processing chain we perform the fusion of the LiDAR point clouds associated to the same crowns. Fig. 5.5 shows some qualitative examples of the data fusion result. The three main species of the study area were selected in order to highlight the capability of the fused point clouds obtained by the proposed method to accurately describe the shape of the crowns. The presented results confirm the complementarity of airborne and terrestrial LiDAR data, which leads to a more comprehensive 3-D crown reconstruction. The airborne data allow us to drive the registration of the TLS scans in an automatic way and to perform the crown delineation. However, due to the low laser sampling density and the top view acquisition perspective, ALS data alone do not describe the below canopy structure. In contrast, TLS provides very high resolution profile of sub canopy tree-crown structure. It is worth noting that the resolution of the obtained crowns varies depending on the number of associated TLS scan and their distance from the crown during the acquisition. Moreover, due to the topography (i.e., on steep slopes occlusion problems arise), the TLS acquisitions are not performed in homogeneous conditions for all the scans, thus influencing the quality of the obtained crowns. However, the airborne acquisition guarantees a minimum laser sampling density for each crown. Moreover, the number of terrestrial scans can be increased to obtain a more accurate result due to the possibility of processing the TLS data in an automatic way. Furthermore, we would like to point out that the considered TLS setup was defined to have a regular sampling on the study area. However, by measuring multiple TLS scans

Table 5.2: Mean error (ME), mean absolute error (MAE), root mean square error (RMSE), and coefficient of determination (R^2) of the crown parameters estimation results obtained by using only the TLS data, only the ALS data, and by fusing the two data sets with the proposed method.

	Tree Top Height (m)			Crown Width (m)			90° Crown Width (m)		
	TLS	ALS	Fusion	TLS	ALS	Fusion	TLS	ALS	Fusion
ME	0.07	0.14	0.41	-1.02	1.69	0.28	-2.74	-0.01	-0.94
MAE	0.47	0.41	0.48	2.64	2.62	1.58	3.49	2.07	1.79
RMSE	0.53	0.54	0.57	3.87	3.03	1.84	4.47	2.47	2.41
R^2	0.97	0.96	0.98	0.59	0.54	0.71	0.47	0.45	0.55

around the trees, it is possible to strongly improve the reconstruction of the 3-D crowns.

Tab. 5.2 presents the quantitative results of the crown parameter estimation obtained by using the ALS data, one singular TLS data, and the fused data. To have a fair comparison, the best singular TLS scan was considered. In particular, the height of the tree, the crown width and the 90° crown width results are compared with ground reference data. From the results obtained it turns out that the fusion always improves the crown parameter estimation by taking advantage from the combination of the complementary acquisition view point. TLS allows a better tree top height estimation with respect to ALS due to the fact that the considered dataset is characterized by relatively small height values. Therefore, the laser scanner is able to acquire samples over the entire crown even though it is mounted on a tripod. Moreover, the ALS acquisition is low-density and thus underestimates the real height of the trees. By combining the two information sources, the proposed method improves the estimation results with a coefficient of correlation R^2 of 0.98. However, the impact of the improvement is more visible in the crown width estimates. Regarding the maximum crown width, the ALS data allow a better estimation with respect to the TLS data since a singular scan is not sufficient to represent the entire crown shape. By fusing the data the proposed method sharply improves the estimates of the maximum crown width obtaining a MAE of 1.58 m compared to a MAE of 2.62 m and 2.64 m obtained with ALS and TLS, respectively. Similar results are obtained for the estimation of the 90° crown width, where the fused data show a MAE of 1.79 m compared to 2.07 m and 3.49 m obtained with ALS and TLS, respectively.

5.5 Conclusion

In this chapter we have presented an automatic method for the fusion of airborne and terrestrial LiDAR data for an accurate reconstruction of the forest structure. The fusion of these data leads to a more comprehensive representation of the tree crowns. In particular, the proposed method is suited for a localized forest analysis that aims to accurately measure the forest structure. Little research has been done on the joint use of these two data sources mainly due to the registration problems. The main novelties of the presented work are: (i) the use of the ALS data for the automatic registration of the multiple

terrestrial scans, (ii) the analysis of the spatial pattern of forest to drive the registration, (iii) the TLS crown delineation performed using the ALS segmentation results, and (iv) the fusion of the LiDAR point clouds.

The registration results demonstrate that the proposed method is able to accurately match the TLS and ALS data by using the spatial pattern of the forest. Accordingly, the method does not require any reference targets during the acquisition of the TLS scan. This condition leads to a fast and practical TLS acquisition campaign. Moreover, by registering the airborne segmented image to the TLS scan, we accurately delineate the single tree crowns present in the terrestrial data without requiring manual analysis or refinements. The registration validation strategy based on the normalized correlation matrix allows the automatic detection of possible residual misregistration, due to problems related to the TLS scan acquisition. We would like to remark that due to the different acquisition perspective it is not possible to address the registration directly in the point cloud domain.

The data fusion results further confirm the effectiveness of the proposed approach. From the qualitative and the quantitative point view, we assessed that the 3-D structure of the crown is accurately reconstructed. The resolution of the obtained fused data varies depends on the number of terrestrial scans and the distance of the terrestrial data acquisitions. However, the fusion always improves the estimation results due to the joint use of the two data sources. As future developments, we aim to extend the method to forest characterized by different tree densities and different spatial patterns. Moreover, we aim to extend the method to the estimation of a larger set of parameters than those considered in this thesis.
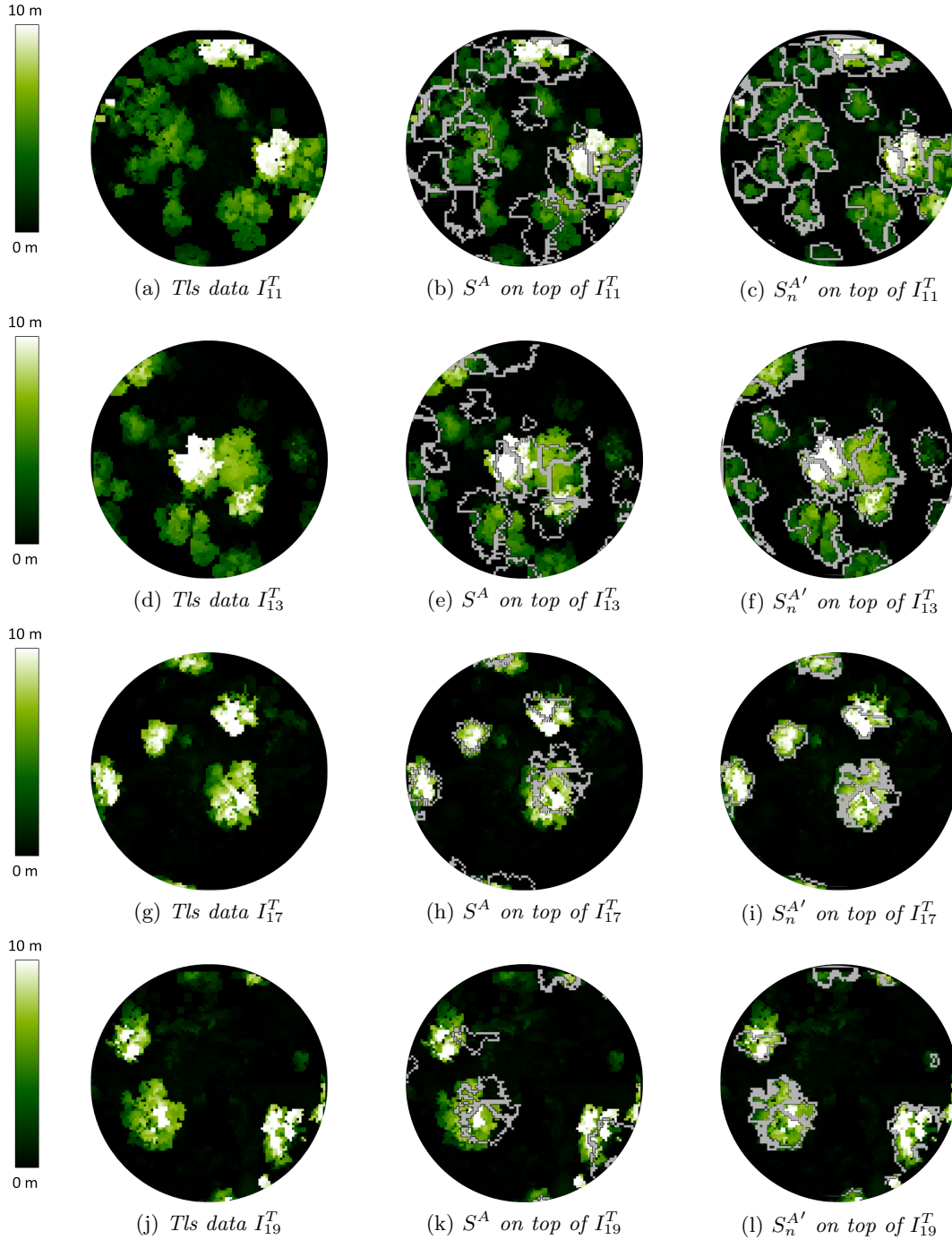
Figure 5.6: TLS scan registration results: (a),(d),(g),(j) original terrestrial data, (b),(c),(h),(k) crown boundaries of the original airborne segmented image S^A are highlighted in gray and superimposed on the nth terrestrial scan, (c),(f),(i),(l) crown boundaries of the registered airborne segmented image $S_n^{A'}$ are superimposed on the nth terrestrial scan.
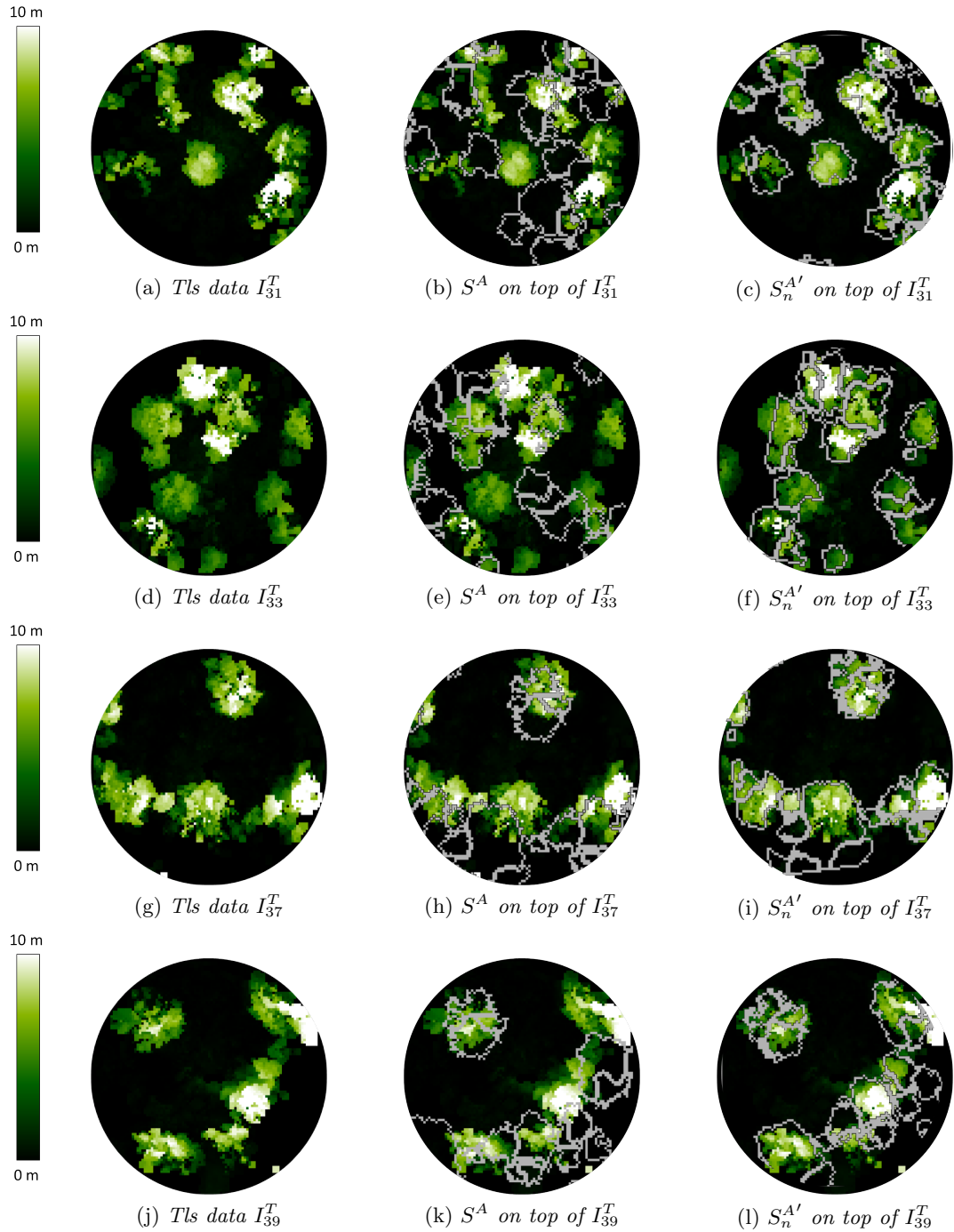
Figure 5.7: TLS scan registration results: (a),(d),(g),(j) original terrestrial data, (b),(c),(h),(k) crown boundaries of the original airborne segmented image S^A are highlighted in gray and superimposed on the nth terrestrial scan, (c),(f),(i),(l) crown boundaries of the registered airborne segmented image $S_n^{A'}$ are superimposed on the nth terrestrial scan.
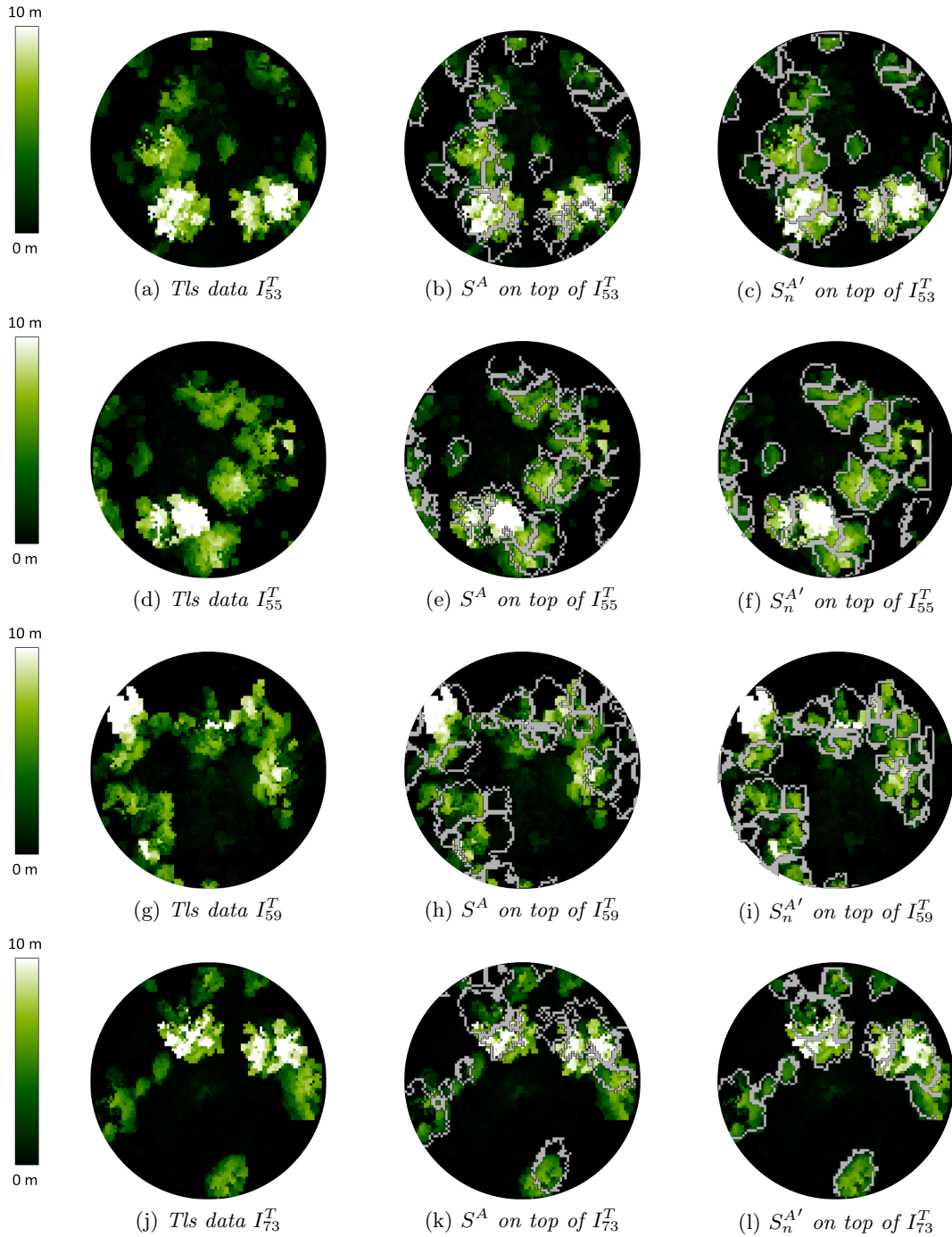
Figure 5.8: TLS scan registration results: (a),(d),(g),(j) original terrestrial data, (b),(c),(h),(k) crown boundaries of the original airborne segmented image S^A are highlighted in gray and superimposed on the nth terrestrial scan, (c),(f),(i),(l) crown boundaries of the registered airborne segmented image $S_n^{A'}$ are superimposed on the nth terrestrial scan.
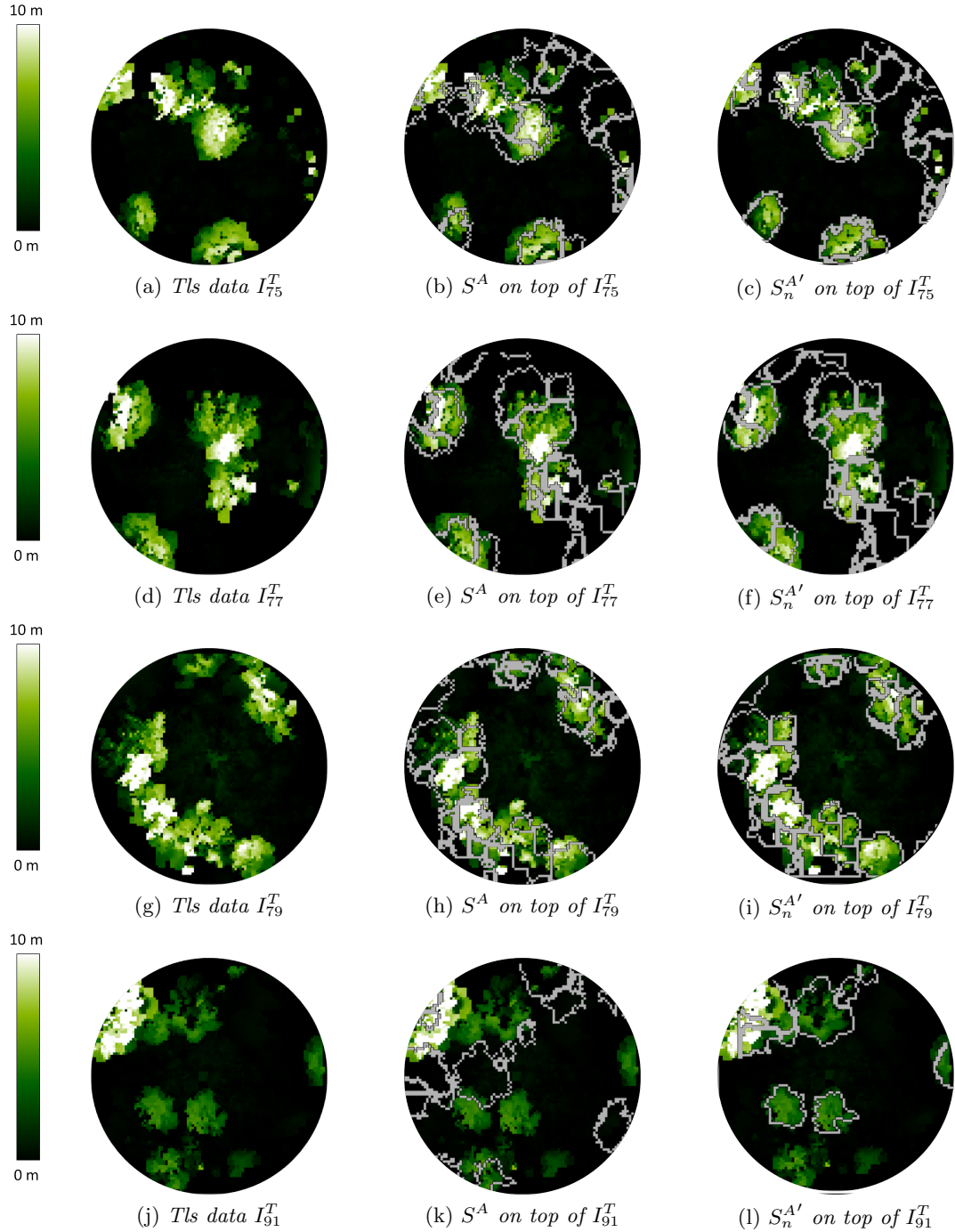
Figure 5.9: TLS scan registration results: (a),(d),(g),(j) original terrestrial data, (b),(c),(h),(k) crown boundaries of the original airborne segmented image S^A are highlighted in gray and superimposed on the nth terrestrial scan, (c),(f),(i),(l) crown boundaries of the registered airborne segmented image $S_n^{A'}$ are superimposed on the nth terrestrial scan.

(a) *Tls data I_{95}^T*   (b) *S^A on top of I_{95}^T*   (c) *$S_n^{A'}$ on top of I_{95}^T*
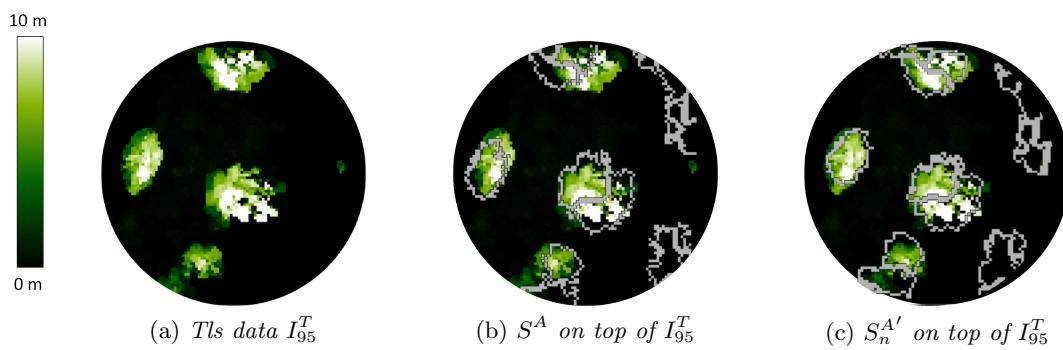
Figure 5.10: TLS scan registration results: (a) original terrestrial data, (b) crown boundaries of the original airborne segmented image S^A are highlighted in gray and superimposed on the nth terrestrial scan, (c) crown boundaries of the registered airborne segmented image $S_n^{A'}$ are superimposed on the nth terrestrial scan.

Chapter 6

Classification of Large Forest Areas by a Sensor-Driven Domain Adaptation Method

In this chapter[1] a method to the transferring of knowledge between remote sensing data acquired on different geographical area but sharing the same set of land-cover classes is presented. Due the different acquisition scenario a shift in the spectral response of the land-cover classes is expected to be addressed. To solve this problem, we aim to take advantage from a multisensor data acquisition to detect features subspaces where data manifolds are partially (or completely) aligned. In particular, the capability of each sensor of measuring different physical properties of the scene can be employed to identify one sensor (or a combination of sensors) being able to measure spatial-invariant properties for a subset of classes. The detection of these invariant feature subspaces allows us to infer labels of the target samples that result more aligned (i.e., more reliable) to the source data for the considered subset of classes. Then, the labeled target samples are re-projected into the full feature space to classify the remaining target samples of the same classes. Finally, for those classes for which none of the sensors can measure invariant features we perform the adaptation via a standard AL technique. The sensor-driven inference method allows us to: (i) accurately model the distribution of the subset of classes for which invariant feature subspaces have been detected, and (ii) introduce constraints on the general structure of the adaptation problem, thus simplifying the adaptation procedure. Experimental results confirm the effectiveness of the proposed method.

6.1 Introduction

The possibility of generating accurate land-cover maps by applying supervised classification approaches to remote sensing data has been extensively analyzed in the literature.

---

[1]Part of this chapter appears in:
C. Paris, and L. Bruzzone, "A sensor-driven domain adaptation method for the classification of remote sensing images," in *Geoscience and Remote Sensing Symposium (IGARSS), 2014 IEEE International*. IEEE, 2014, pp. 185-188.

The main drawback of these methods is the need of reference data for training the classification algorithm, which requires expensive and labour intensive field data collection. Therefore, in a real application scenario it is not reasonable to assume to have ground reference data available each time that a new remote sensing data is acquired. To mitigate the need of labeled samples, the new remote sensing image can be classified by exploiting the ground reference data associated with an image acquired by the same sensor in a region with comparable properties (i.e., same set of land-cover classes). However, when transferring the knowledge among pairs of remote sensing images, even tough they are similar to each other, it is necessary to face many problems. The different acquisition conditions of the two data (i.e., illumination, atmosphere, look/view angles, sensor parameters) affect the radiometry of the scene. Moreover, the phenological state of the vegetation or the differences in the soil moisture can lead to crucial variations in the spectral response of the same land-cover classes (e.g., bare soil, crops). From the statistical view point, all these factors result in a shift of the probability distribution of the classes between the images. Hence, the direct application of the classifier trained on the source domain (remote sensing data where reference data are available) to the target domain (remote sensing data where no reference data are initially available) results in a low classification accuracy of the obtained land-cover map.

In machine learning and pattern recognition literature, the issue mentioned above is addressed by using DA methods in the framework of transfer learning. The main idea is to transfer the knowledge learned on the source domain to a target domain by modelling the differences among the areas [187, 188]. Several methods have been presented in the framework of change detection, where the source and the target domains are acquired in the same geographical area but at different times. Few approaches have been developed to normalize the images if they have been taken under identical acquisition condition [189, 190], while others adopt image processing for matching as more as possible the statistical distributions of the images [191]. More sophisticated techniques aim at adapting the classification model estimated on the source domain to the target domain [192, 193, 194]. In [192, 193] the main idea is to use in an unsupervised way the samples of the target image to tune the classifier in order to update the land-cover map generated on the source domain. In [194] the authors first apply an unsupervised change-detection method to the source and the target domains, then they exploit the unchanged pixels associated with the groundtruth samples of the source domain to generate the reference data of the target domain. However, all these methods can address the case of classification of time-series images acquired on the same area.

In the case of images acquired on different regions, it is not possible to use the change information or the temporal correlation between areas for addressing the DA issue. To solve this problem, a common DA strategy consists in weighting the samples of the source domain in order to use them in the classification of the target domain. In [195] the authors address the DA problem from a distribution point of view by weighting the training samples of the source domain to model the target distribution, while in [196, 197] the re-weighting technique of the source samples is combined with an AL method to evaluate the similarity between source and target domains. Note that AL methods aim at iteratively expanding the original training set by selecting the most informative unlabeled samples

of the target domain. Typically, an interactive process with a supervisor is required to manually label the selected samples, thus strongly improving the classification accuracy [198].

Many DA problems have been also addressed by semisupervised learning (SSL) methods [199, 200, 201, 202] when the reference data are not sufficient to represent the real distributions of the land-cover classes. Indeed, often ground data are acquired over contiguous sites easily to access, thus resulting in a unrepresentative pool of samples that affect the training of the classifier. SSL methods aim to solve this problem by taking advantage from the unlabeled samples of the image to better model the distributions of the classes and thus train the classifier. In [199] the authors present an iterative algorithm which exploits a weighting strategy based on a time-dependent criterion to include in the training set the unlabeled samples of the image. At each iteration a Support Vector Machine (SVM) classifier is trained with the enlarged set of labeled samples, thus gradually searching the optimal classification function. In particular, they observe that the most informative unlabeled samples are the ones close to the margin boundaries of the SVM. Recently, graph-based methods brought a great contribution in solving semisupervised classification problems due to their solid mathematical background [203, 204, 205]. Typically, both the labeled and unlabeled samples are considered as nodes of the graph, while the weights between the nodes represent the similarity among pairs of samples. This condition allows one to drive the labeling process in a natural way among samples of the same classes under the assumption of consistency (i.e., nearby points should belong to the same class) [203]. In [206], the graph represents the structure of the land-cover classes to highlight possible changes between the domains. Thus, the method does not require to have the same set of land-cover classes between source and target domains. First, the number of classes of the target domain is detected by means of a clustering algorithm. Second, a sub-graph matching algorithm is proposed to detect the common classes and to identify possible changes among pairs of land-cover classes. To match the classes of the different domains, the data are projected into a higher dimensional kernel induced feature space which allows a linear class separation.

Although all these methods address the adaptation between different domains, recently some papers focused the attention on feature extraction and/or feature-selection methods to detect the feature space where the data are more aligned to perform the adaptation [207, 208, 209, 210]. In [207] the authors propose a method which aims to select a subset of features that are characterized by both invariant spatial behaviour and discrimination ability among the set of land-cover classes. The feature selection is performed considering a novel criterion function based on a standard measure of distance between the classes and a novel metric that evaluates the stationary behaviour of features between the domains. Due to this feature-selection phase, the generalization capability of the classification method is strongly improved with respect to the standard techniques. In [208] a nonlinear deformation based on vector quantization and graph matching is presented to adapt the source domain to the target domain. The data manifolds of the images are locally deformed to facilitate the statistical alignment. Therefore, by maximizing the similarity of the graphs representing the two domains it is possible to transfer the knowledge from the source to the target domain in an unsupervised way. In [211, 210, 212, 209] the

authors address the adaptation from a local perspective, trying to adapt locally the samples of the images while preserving the geometrical structure of the entire distribution. In [209] the authors propose an alignment method which works directly on the manifolds of the images, thus addressing the cases of having multiangular, multitemporal, and multisource image classification problems. In greater details, the method aims to pull close samples of the same classes while preserving the geometry of each manifold along the transformation. However, to detect possible spaces where the manifolds are aligned the presented method requires a set of labeled data from the target image. Indeed, the alignment transformation is defined by using both labeled and unlabeled samples. Similarly, in [210] the authors focus on the feature extraction phase to statistically align the distributions of the source and the target domains either in a semisupervised or in an unsupervised way. In particular, they present a Transfer Component Analysis, which allows the preservation of the local geometry (data manifold) while minimizing the distance between the domains, thus improving the classification accuracy of the target domain regardless of the classifier.

From this brief analysis of the literature, one can notice that the choice of the feature space strongly affects the DA result. In this framework, the possibility of acquiring multisensor data results in the collection of complementary measurements (features) of the classes. By exploiting the capability of each sensor of measuring different physical properties of the scene, we aim to detect feature subspaces where subset of classes results almost aligned between the domains. Instead of using data-driven feature-extraction methods, in the proposed approach such a detection is driven by the physical properties of the classes. This condition allows us to infer knowledge from the source to the target domain in an unsupervised yet reliable way. However, even though these feature subspaces guarantee a better alignment of the data with respect to the original space, they are not sufficient to model the entire distribution of the target domain. Thus, the main idea of the proposed method is to exploit the invariant feature subspaces to infer the labels of the target samples having the highest probability of being properly aligned to the source data. The labeled target samples are then re-projected in the full feature space to properly represent the Probability Density Function (PDF) of the target domain for the considered subset of classes. Note that the method presented in this chapter significantly extends and enhances the work described in [213]. The proposed approach is based on three main steps. First, we decompose the DA problem defining a hierarchical-tree structure of the land-cover classes. By analyzing the source domain (both the reference ground data and the remote sensing data) the set of land-cover classes is divided into two groups: (i) a subset of classes for which we have one sensor (or a combination of sensors) being able to acquire almost invariant features (physical properties) between the domains, and (ii) a subset of classes for which none of the sensors available can measure invariant features. In the second step, we aim to define an initial training set for the invariant classes selecting the more reliable target samples by means of a sensor-driven inference method. The condition of data alignment allows us to propagate in an unsupervised way the labels from the source to the target domain rather than adapting the classification parameters. Then the labeled target samples are re-projected into the full feature space to classify the remaining samples for the considered subset of classes. This inference process results in:

(i) modelling the distribution of the subset of classes for which invariant features have been measured in the target domain (thus handling possible shift in the statistical distributions in the whole feature space between the domains for that subset of classes), (ii) introducing constraints on the general structure of the DA method, and (iii) simplifying the global adaptation process. In the third step, we aim to address the adaptation of those classes characterized by a variant feature behaviour by means of an AL procedure which takes advantage from the adaptation performed in the previous step. Thus, the AL strategy focuses only on the variant land-cover classes for the entire procedure. This strategy allows us to rapidly increase the classification accuracy of the target domain while requiring a small amount of target samples. Experiments conducted on two real multisensor datasets confirm the effectiveness of the proposed method.

The following chapter is organized as follow. Sec. 6.2 introduces the problem formulation and the notation used in the chapter. Sec. 6.3 presents the proposed DA method, while Sec. 6.4 describes the considered dataset. Sec. 6.5 illustrates and discusses the experimental results. Finally, Section VI draws the conclusion of this chapter.

6.2 Problem Formulation

In this section we formalize the sensor-driven DA problem and define the notation used in the chapter. Let us assume to have N sensors Ψ_n, with $n = 1, .., N$, which can acquire data on two different geographical areas. The feature vector extracted by the nth sensor Ψ_n is defined as $\mathbf{x}^{\Psi_n} = (x_1^{\Psi_n}, x_2^{\Psi_n}, .., x_{z_n}^{\Psi_n})$, with $\mathbf{x}^{\Psi_n} \in \mathbb{R}^{z_n}$. Accordingly, the vector $\mathbf{x} \in \mathcal{R}^d$ of features extracted by all the available N sensors is as follows:

$$
\begin{aligned}
\mathbf{x} &= (\mathbf{x}^{\Psi_1} \cup \mathbf{x}^{\Psi_2} \cup .. \cup \mathbf{x}^{\Psi_N}) \\
&= (x_1^{\Psi_1}, .., x_{z_1}^{\Psi_1}, x_1^{\Psi_2}, .., x_{z_2}^{\Psi_2}, x_1^{\Psi_N}, .., x_{z_N}^{\Psi_N})
\end{aligned}
\tag{6.1}
$$

Let $\mathcal{D}_S$ be the source domain and $\mathcal{D}_T$ the target domain that we assume share the same set of M land-cover classes $\Omega = \{\omega_m\}_{m=1}^M$. The source domain $\mathcal{D}_S = \{\mathcal{X}_S, \mathcal{Y}_S\}$ is characterized by a set of ns labeled samples $\mathcal{X}_S = \{\mathbf{x}_i^s\}_{i=1}^{ns}$ with $\mathcal{Y}_S = \{y_i^s\}_{i=1}^{ns}$, where $\mathbf{x}_i^s \in \mathcal{R}^d$, $y_i^s \in \Omega$. The target domain is characterized by a set of nt unlabeled samples $\mathcal{D}_T = \{\mathcal{X}_T\} = \{\mathbf{x}_i^t\}_{i=1}^{nt}$, where $\mathbf{x}_i^t \in \mathcal{R}^d$. In this framework, the main goal of DA methods is to predict the target labels $\{\mathcal{Y}_T\} = \{y_i^t\}_{i=1}^{nt} \in \Omega$ by taking advantage from the labeled samples of the source domain. This can be done under the assumption that the distributions of $\mathcal{D}_S$ and $\mathcal{D}_T$ are sufficiently correlated. From the statistical view point, each class $\omega_m \in \Omega$ is characterized by the prior probability $P(\omega_m)$ and the class conditional probability $p(\mathbf{x}|\omega_m)$. Accordingly, the distribution of the source domain can be written as:

$$
p^S(\mathbf{x}) = \sum_{\omega_m \in \Omega} P^S(\omega_m) p^S(\mathbf{x}|\omega_m)
\tag{6.2}
$$

and the distribution of the target domain:

$$
p^T(\mathbf{x}) = \sum_{\omega_m \in \Omega} P^T(\omega_m) p^T(\mathbf{x}|\omega_m)
\tag{6.3}
$$
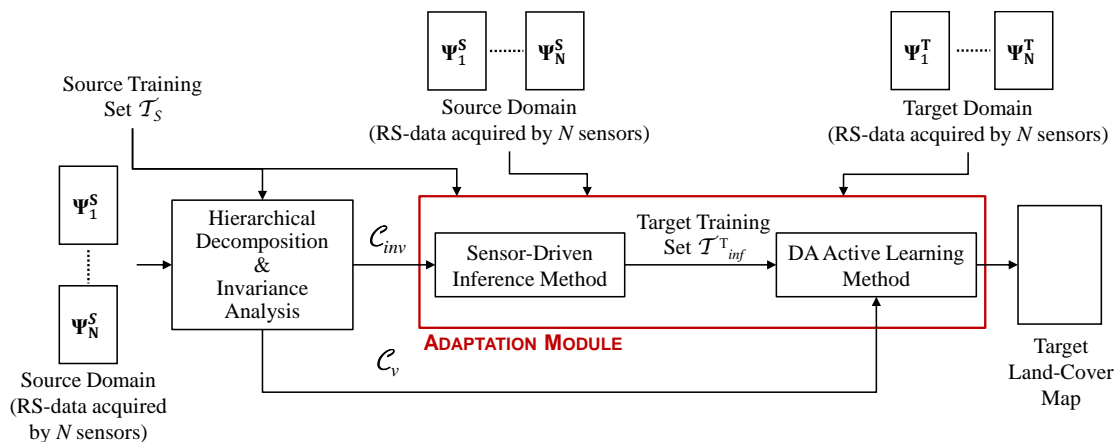
Figure 6.1: Block scheme of the proposed sensor-driven DA approach.

Due to the different scenes represented by $\mathcal{D}_S$ and $\mathcal{D}_T$ (e.g., different acquisition condition, different ground condition, different geographical locations), usually a shift in the probability distributions of the classes is observed (i.e., $p^S(\mathbf{x}) \neq p^T(\mathbf{x})$). Typically, DA methods overcome this shift by searching feature spaces where the data are more aligned from the global view point [214] or by matching local deformations [215, 216]. Differently from the literature, in the proposed method the detection of these features subspaces is driven by the physical meaning of the properties measured by the sensors. The main assumptions of the proposed method are: (i) the availability of multisensor data acquired on $\mathcal{D}_S$ and $\mathcal{D}_T$, and (ii) the same set of land-cover classes is shared between the domains.

6.3 Proposed Method

The acquisition of multisensor data results in the collection of complementary measurements on the scene, thus increasing the probability of obtaining features characterized by invariant behaviour between the domains. By focusing the attention on the capability of each sensor of measuring different physical properties of the land-cover classes, we aim at identifying those physical properties which are reasonably invariant between $\mathcal{D}_S$ and $\mathcal{D}_T$ for some specific classes. The detection of these feature subspaces allows us to bridge the gap between the distributions according to a sensor-driven strategy. Fig. 6.1 shows the block-scheme of the proposed DA approach, which is based on three main steps: (i) hierarchical decomposition of the land-cover classes on the basis of an invariance analysis of the adaptation problem, (ii) sensor driven inference on the classes for which invariant features have been measured by one or more sensors, and (iii) adaptation of the classes for which none of the available sensors can measure invariant features by means of an AL strategy.

6.3.1 Hierarchical Decomposition

A class hierarchical structure can be obtained by iteratively partitioning the multiclass problem into meta-class problems. In the literature, Binary Hierarchical Classifiers (BHC) are constructed in order simplify the classification problem such that the adaptation can be performed solving binary problems [217, 218, 219]. The similarity of the classes is evaluated in the feature space to keep similar classes in the same partition until the leaf nodes of the tree represent the data classes. In the proposed method we aim to keep in the same partition the classes for which one sensor (or a set of sensors) has measured the same invariant properties. While in the entire feature space the distributions of classes in the two domains can significantly change, by focusing the attention on the physical properties of the scene we can derive a class hierarchy where some classes in a feature subspace result statistically aligned. Therefore, to derive the hierarchical decomposition of the classes we perform an invariance analysis considering both the labeled samples of the source domain and the available sensors. Differently from the BHC, at each level of the hierarchy there can be more than two classes, relaxing the constraint of the binary tree construction. Note that this class decomposition is not realized to solve the classification problem but to facilitate the detection of invariant feature subspaces.

Let us consider a hierarchical tree structure made up of the set of classes $\mathcal{C}_{all} = \{c_k\}_{k=1}^{N_k}$, where c_k can be a meta- or a data- class (i.e., ω_m). The first meta-class c_1 includes the whole set of land-cover classes Ω. For all the hierarchy levels starting from two, each class c_k is connected to a unique parent-class $M(c_k)$ and a set of child-classes $F(c_k) = \{c_{k_1}, c_{k_2}, .., c_{k_{f_k}}\}$, where f_k is the number of classes included in the meta-class c_k (Fig. 6.2). The key idea of the proposed method is to divide at each level of the hierarchy the set of classes into two groups: (i) a subset of classes $\mathcal{C}_{inv} \subseteq \mathcal{C}_{all}$ for which we have at least one sensor being able to measure spatial invariant features, and (ii) a subset of classes $\mathcal{C}_v \subseteq \mathcal{C}_{all}$ for which none of the sensors available can measure invariant features. Accordingly, for each level of the tree the PDFs of $\mathcal{D}_\mathcal{S}$ and $\mathcal{D}_\mathcal{T}$ can be rewritten as follows:

$$
\begin{aligned}
p^S(\mathbf{x}) &= \sum_{c_k \in \mathcal{C}_{all}} P^S(c_k) p^S(\mathbf{x}|c_k) \\
&= \sum_{c_k \in \mathcal{C}_v} P^S(c_k) p^S(\mathbf{x}|c_k) + \sum_{c_k \in \mathcal{C}_{inv}} P^S(c_k) p^S(\mathbf{x}|c_k)
\end{aligned}
\tag{6.4}
$$

and

$$
\begin{aligned}
p^T(\mathbf{x}) &= \sum_{c_k \in \mathcal{C}_{all}} P^T(c_k) p^T(\mathbf{x}|c_k) \\
&= \sum_{c_k \in \mathcal{C}_v} P^T(c_k) p^T(\mathbf{x}|c_k) + \sum_{c_k \in \mathcal{C}_{inv}} P^T(c_k) p^T(\mathbf{x}|c_k)
\end{aligned}
\tag{6.5}
$$

Note that the sets $\mathcal{C}_v$ and $\mathcal{C}_{inv}$ are different for different levels of the tree (for simplifying the notation we do not include explicitly the dependence). The goal of the hierarchical structure is to decompose the adaptation problem in order to identify and separate from the others the classes $\mathcal{C}_{inv}$, which result statistically aligned between the domains in some feature subspaces. This allows us to adapt first the classes $\mathcal{C}_{inv}$ by means of a sensor-driven inference method and then to address the adaptation of classes characterized by variant

behaviour $\mathcal{C}_v$. In the latter case, the adaptation is based on a standard AL technique. The adaptation process is driven by a sensor Ψ_n (or a combination of sensors if more than one sensor provides invariant features) that measures spatial invariant features $\mathbf{x}^{\Psi_n}$ for the class $c_k \in \mathcal{C}_{inv}$.
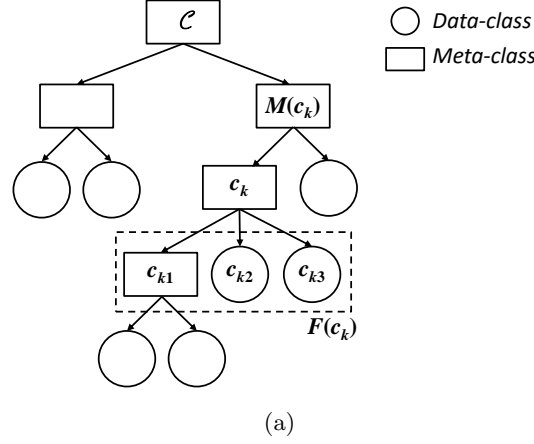
(a)

Figure 6.2: Example of hierarchical partitioning of the land-cover classes where the generic class c_k is represented connected to its parent class $M(c_k)$ and its child-classes $F(c_k)$. In the considered example f_k is equal to three.

6.3.2   Sensor-driven Inference Method

The goal of this step is to propagate the labels of the classes $\mathcal{C}_{inv}$ from the source to the target domains, thus generating a training set adopted to $\mathcal{D}_T$ for those classes. This is accomplished by means of two main steps. First, we exploit the detection of invariant features subspaces to infer class labels of the target samples that result more aligned to the source samples (i.e., that have the highest probability of being correctly labeled). Then, we re-project the labeled target samples in the full feature space to accurately model the target distribution of the considered classes and thus to label the remaining samples of that classes. Let us focus the attention on the generic meta-class c_k which includes 2 child-classes $F(c_k) = \{c_{k_1}, c_{k_2}\}$. Without loosing generality, let us assume that one sensor Ψ_n, among the N available ones, provides an invariant features subspace $\mathbf{x}^{\Psi_n}$ where the classes $F(c_k)$ can be discriminated. Even tough the prior probabilities in the two domains are not influenced by the features measured by the sensor Ψ_n, the conditional PDFs result almost aligned in that feature subspace $\mathbf{x}^{\Psi_n}$, i.e.,

$$
\begin{aligned}
p^T(\mathbf{x}^{\Psi_n}|c_{k_1}) \approx{}& p^S(\mathbf{x}^{\Psi_n}|c_{k_1}), \text{ and} \\
p^T(\mathbf{x}^{\Psi_n}|c_{k_2}) \approx{}& p^S(\mathbf{x}^{\Psi_n}|c_{k_2})
\end{aligned}
\tag{6.6}
$$

whereas they are not aligned for all other feature subspaces:

$$
\begin{aligned}
p^T(\mathbf{x}^{\Psi_v}|c_{k_1}) \neq{}& p^S(\mathbf{x}^{\Psi_v}|c_{k_1}), \text{ and} \\
p^T(\mathbf{x}^{\Psi_v}|c_{k_2}) \neq{}& p^S(\mathbf{x}^{\Psi_v}|c_{k_2}) \quad \forall v \in [1, N], \text{ with } v \neq n
\end{aligned}
\tag{6.7}
$$

This alignment condition of the data allows us to transfer the knowledge from $\mathcal{D}_S$ to $\mathcal{D}_T$ in an unsupervised but reliable way. In greater details, the proposed label propagation strategy exploits the classifier trained on $\mathcal{D}_S$ in the feature subspace $\mathbf{x}^{\Psi_n}$ to predict the labels of $\mathcal{D}_T$ for the invariant classes c_{k_1} and c_{k_2}. Note that, due to the hierarchical tree structure, we are in the condition of focusing the attention on the unlabeled samples of the target domain $\mathcal{X}_{c_k}^T$ belonging to the meta-class c_k. Indeed, while at the first level of the hierarchy the entire set of unlabeled samples is considered, for all the levels starting from two the samples belonging to the meta-class c_k have been already identified at the previous level (i.e., classification map representing the classes $\{c_k, \mathcal{C} - c_k\}$). In our study we consider SVMs classifiers, which have been extensively employed in remote sensing because of their high generalization capability [220, 221], high classification accuracy when compared with other classifiers and effectiveness in handling ill-posed problems (i.e., low ratio between the number of training samples and the number of features) [222, 223]. It is worth mentioning that since the data results almost aligned because of the invariance of the feature space, any classifier can be employed.

For sake of simplicity, let us present the binary classification problem for the classes $\{c_{k_1}, c_{k_2}\}$, which can be extended to the multiclass case by means of the One Against All (OAA) multiclass strategy [199]. Let $\mathcal{T}_{c_k}^S = \{(\mathbf{x}_i^s, y_i^s)\}_{i=1}^{ns_{c_k}}$, where $\mathbf{x}_i^s \in \mathcal{R}^{z_n}$ and $y_i^s \in [c_{k_1}, c_{k_2}]$ be the training set of $\mathcal{D}_S$ for the considered invariant classes. First, the standard SVM classifier is trained using the labeled samples of the source domain $\mathcal{T}_{c_k}^S$ by solving the following constrained optimization problem:

$$\min_{\mathbf{w}, \xi^s} \quad \frac{1}{2}\|\mathbf{w}\|^2 + C \sum_{i=1}^{ns_{c_k}} \xi_i^s \tag{6.8}$$
$$\text{subject to: } y_i^s(\mathbf{x}_i^s \cdot \mathbf{w} + b) \geq 1 - \xi_i^s, \quad \xi_i^s \geq 0 \ \forall i \in [1, ns_{c_k}]$$

where $\mathbf{w}$ is a vector normal to the separating hyperplane; b is a bias term such that $b/\|\mathbf{w}\|$ represents the distance of the hyperplane from the origin; C is the regularization parameter; ξ_i^s are the slack variable associated with the ns_{c_k} labeled samples of the source domain for the classes c_{k_1} and c_{k_2}. By using the Lagrangian formulation, the aforementioned convex optimization problem can be reformulated into the following dual representation:

$$\max_{\alpha^s} \quad \sum_{i=1}^{ns_{c_k}} \alpha_i^s - \frac{1}{2} \sum_{i,j=1}^{ns_{c_k}} \alpha_i^s \alpha_j^s y_i^s y_j^s \left\langle \mathbf{x}_i^s \cdot \mathbf{x}_j^s \right\rangle \tag{6.9}$$
$$\text{subject to: } 0 \leq \alpha_i^s \leq C \ \ \forall i \in [1, ns_{c_k}], \quad \sum_{i=1}^{ns_{c_k}} \alpha_i^s y_i^s = 0$$

where α_i^s with $i = 1, .., ns_{c_k}$ are the Lagrange multipliers and $\left\langle \mathbf{x}_i^s \cdot \mathbf{x}_j^s \right\rangle$ is the inner product between the two feature vectors. If the data cannot be linearly separated in the original input space, it is possible to project them into a higher dimensional feature space. Hence, by means of the nonlinear mapping function $\Phi(\mathbf{x})$, the inner product between the two mapped feature vectors $\left\langle \mathbf{x}_i^s \cdot \mathbf{x}_j^s \right\rangle$ is replaced by the inner product in the transformed

space $\langle \Phi(\mathbf{x}_i^s) \cdot \Phi(\mathbf{x}_j^s) \rangle$. Note that there is no need of explicitly compute $\Phi(\mathbf{x})$ because of the possibility of employing a kernel function that satisfies the Mercer's condition $K(\mathbf{x}_i^s, \mathbf{x}_j^s) = \Phi(\mathbf{x}_i^s) \cdot \Phi(\mathbf{x}_j^s)$. Thus, the final discriminant function associated to the hyperplane can be represented as a function of the data (conveniently in the original dimensional feature space) as follows:

$$f(\mathbf{x}) = \sum_{i \in \mathcal{G}} \alpha_i^s y_i^s K(\mathbf{x}_i^s, \mathbf{x}_j^s) + b \qquad (6.10)$$

where $K(\mathbf{x}_i^s, \mathbf{x}_j^s)$ is a kernel function, and $\mathcal{G}$ is the subset of training samples corresponding to the nonzero Lagrange multipliers (i.e., support vectors). By applying the classifier to the target samples $\mathcal{X}_{c_k}^T$, their labels are predicted according to the $\text{sign}[f(\mathbf{x})]$, where $f(\mathbf{x})$ represents the hyperplane.

Although the considered feature subspace Ψ_n guarantees a better alignment of the data with respect to the original space (and thus a more reliable classification of the target samples), this subspace is not sufficient to properly model the entire target PDFs of c_{k_1} and c_{k_2}. For this reason, we generate a reliable training set for the target domain, by considering only the samples that fall outside the margin (i.e., $|f(\mathbf{x})| > 1$) because they are the ones having the highest probability of being correctly classified. Let $\mathcal{T}_{c_k(0)}^T = \{(\mathbf{x}_i^t, y_i^t) | \mathbf{x}_i^t \in \mathcal{X}_{c_k}^T, |f(\mathbf{x}_i^t)| > 1\}$ be the initial training set of $\mathcal{D}_{\mathcal{T}}$ generated by transferring the knowledge in $\mathbf{x}^{\Psi_n}$ for the invariant classes c_{k_1} and c_{k_2}. Then, we re-project the target labeled samples $\mathcal{T}_{c_k(0)}^T$ into the full feature space to represent the PDFs of the considered classes on all the available features (i.e., $p^T(\mathbf{x}|c_{k_1})$ and $p^T(\mathbf{x}|c_{k_2})$). This condition allows us to use all the available information to select a subset of features where the considered classes are more discriminable in order to ensure an accurate classification of the remaining unlabeled samples. To this end a feature-selection technique is applied to the training samples $\mathcal{T}_{c_k(0)}^T$ to select the most discriminative subset of features. In our study, we exploited a Sequential Forward Floating Selection (SFFS) considering the Jeffreys-Matusita distance as separability criterion [224, 225]. Then, the classifier is trained on the initial training set $\mathcal{T}_{c_k(0)}^T$ in the obtained feature subspace, thus generating the training set $\mathcal{T}_{c_k(1)}^T$ which includes all the originally unlabeled samples $\mathcal{X}_{c_k}^T$. Therefore, we can update the initial classification map $\{c_k, \mathcal{C} - c_k\}$ with the classification map $\{c_{k_1}, c_{k_2}, \mathcal{C} - c_k\}$. Moreover, we distinguish among the child classes $F(c_{k_1})$ and $F(c_{k_2})$ which can further classified on the basis of the invariance analysis if they belong to the invariant classes $\mathcal{C}_{inv}$ or by means of an AL method (Section 6.3.3). It is worth mentioning that depending on the complexity of the adaptation problem, more restrictive criteria on the value $|f(\mathbf{x})|$ can be adopted for increasing the probability of selecting reliable target samples to generate the initial training set.

By applying the label inference method to all the classes $\mathcal{C}_{inv}$, at the end of this step we generate an initial training set for the target domain $\mathcal{T}_{inf}^T = \{(\mathbf{x}_j^t, y_j^t)\}$, with $\mathbf{x}_j^t \in \mathcal{R}^d$ and $y_j^t \in \mathcal{C}_{inv}$ and a classification map representing all the invariant data-classes $\omega_m \in \mathcal{C}_{inv}$ and the meta-classes $c_k \in \mathcal{C}_v$. It is worth mentioning that by inferring the knowledge on the classes $\mathcal{C}_{inv}$, we simplify the adaptation problem by: (i) reducing the number of classes that should be adapted in the next step, and (ii) introducing constraints in the adaptation of the remaining classes $\mathcal{C}_v$ that increase the reliability of adaptation based

on AL method. The amount of simplification depends on the number of classes $\mathcal{C}_{inv}$ on which we can detect invariant feature subspaces between $\mathcal{D}_S$ and $\mathcal{D}_T$.

6.3.3 Adaptation based on Machine Learning

The last step of the proposed method aims to complete the land-cover map of $\mathcal{D}_T$ generated at the previous step, by integrating the classes $\omega_m \in \mathcal{C}_v$. According to the constraints on the additional labeling cost for the user, the goal of this step is to minimize the number of training samples of the target domain required to achieve a predefined classification accuracy. This is obtain by using AL methods in order to rapidly increase the classification accuracy of the target land-cover map. Usually AL methods are employed in the supervised classification of remote sensing data to optimize the definition of the training set by selecting the most informative samples. The initial training set is iteratively expanded by means of an interactive procedure which involves a supervisor (i.e., a human expert) who correctly assigns the labels to the selected uncertain samples [226, 227, 228]. The labeling process can be either based on photointerpretation or on the collection of ground reference data.

The AL strategy employed in the proposed method focuses the attention only on the $\mathcal{C}_v$ classes by taking advantage from: (i) the hierarchical decomposition of the DA problem, and (ii) the adaptation performed in the previous step on the classes $\mathcal{C}_{inv}$. Due to the hierarchical decomposition of the classes, we are in the condition of identifying the target samples belonging to the variant classes $\mathcal{X}_{\mathcal{C}_v}^T$. This condition allows us to refine the initial training set $\mathcal{T}_{inf}^T = \{(\mathbf{x}_j^t, y_j^t)\}$ generated in the previous step by integrating only unlabeled target samples belonging to the classes $\omega_m \in \mathcal{C}_v$. Indeed, the sensor-driven inference method already provided the labels for the classes $\omega_m \in \mathcal{C}_{inv}$. In this framework, the iterative AL procedure minimizes the number of target samples to label by directly selecting the most informative samples of the $\omega_m \in \mathcal{C}_v$ classes. It is worth mentioning that the proposed method can use any kind of AL strategy. Here we consider the MCLU-ECBD (i.e., *MultiClass Level Uncertainty - Enhanced Clustering Based Diversity*) batch mode AL technique presented in [198]. This technique has been developed in order to improve the classification accuracy of remote sensing data with SVMs classifiers. The method is based on a clustering technique performed in the kernel space which aims to select at each iteration more samples that are both uncertain and diverse (distant one another). While the diversity criterion avoids redundancy in the selection of the samples, the uncertainty criterion guarantees the selection of the most informative ones. In greater detail, first m uncertain samples are selected considering their distance from the hyperplane of the binary SVM classifiers according to the OAA architecture. Then, the m samples are refined by applying a kernel k-means clustering [229] to define h different clusters (with $h \leq m$) and select the most uncertain sample from each cluster (i.e., diverse samples).

At the end of the step, we generate the land-cover map of the target domain by means of the training set obtained with the inference method integrated to the AL approach.
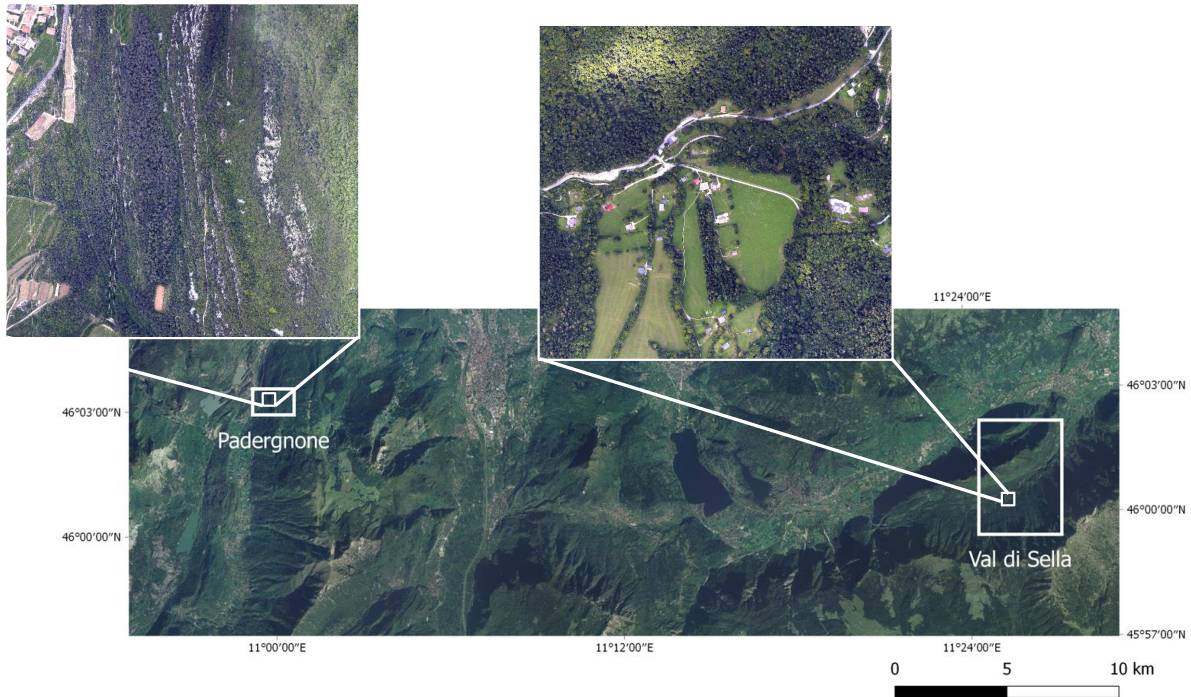
Figure 6.3: Color composition of the orthophoto acquired on a portion of the Trentino region. The study areas are highlighted in the white rectangles overlapped on the optical image. A small portion of the high resolution optical images of the dataset is represented for both the study areas.

6.4   Experimental Results

In this Section the experimental results obtained on a wide forest area are presented. In particularity, to assess the effectiveness of the proposed method we carried out two experiments. In the first experiment we focused the attention on the set of classes $\mathcal{C}_{inv}$ for which the adaptation can be addressed by means of the sensor-driven inference method SVM^{inf}, without requiring any labeled sample from $\mathcal{D}_{\mathcal{T}}$.

6.4.1   Dataset Description

For our analysis we considered two spatially disjoint forest areas located in the Southern Italian Alps, in the Trentino region, (Fig. 6.3). The first study area is located in Val di Sella (1090 Ha), whereas the second one is located in Padergnone (175 Ha), hereafter referred as *Vds* and *Pad*, respectively.

The sensors available were a hyperspectral scanner, a LiDAR system and a color camera. The hyperspectral images were acquired by the AISA Eagle sensor mounted on an airborne platform with a spectral range between 402.9 nm and 989.1 nm and a spatial resolution (GIFOV) of 1 m. In *Vds*, the acquisition was performed on 16th July 2008 with a spectral resolution of 4.6 nm (126 spectral bands), whereas in *Pad* the data were taken on 4th September 2007 with a spectral resolution of 9.2 nm (63

Table 6.1: Number of available labeled samples of the land-cover classes in the source and the target domains.

| Class Name | Number of samples | | | | | |
| | Vds | | | Pad | | |
	TR	TS	Pool	TR	TS	Pool
Norway Spruce (ω_1)	478	238	239	43	21	21
Silver Fir (ω_2)	378	189	189	105	52	53
European Larch (ω_3)	373	186	187	388	194	194
European Beech (ω_4)	512	255	256	815	407	408
Hop Hornbeam (ω_5)	83	41	41	145	72	72
Grass (ω_6)	178	89	89	172	86	86
Building (ω_7)	143	71	71	137	68	68
Roads (ω_8)	148	73	74	137	68	68
Bare Soil (ω_9)	190	94	95	200	99	100

spectral bands). For each spectral channel of the *Pad* image there are two spectral channels of the *Vds* image acquired in the same wavelength range. Thus, to perform the adaptation, the *Vds* image was resampled by applying a Gaussian model with a Full Width at Half Maximum (FWHM) equal to the band spacings (i.e., 9.2 nm) by matching the corresponding wavelength ranges.

LiDAR data were acquired jointly with the hyperspectral image by the Optech ALTM 3100EA sensor mounted on the same aircraft of the hyperspectral sensor for both the areas. The average point density is 5 points per m^2, with up to four returns acquired. The laser pulse wavelength was 1064 nm whereas the laser repetition rate was 100 kHz. The digital terrain model (DTM) was produced and subtracted from the LiDAR data to obtain the relative height of the targets with respect to the terrain. The obtained LiDAR point cloud was rasterized to generate the canopy height model (CHM) image.

The high resolution optical image has 3 spectral bands acquired in the visible range (RGB) with a spatial resolution of 0.2 m. The spatial resolution of the optical image was degraded to 1 m to be coherent with the hyperspectral image and the CHM, using the nearest neighbour resampling. The multi-sensor data were manually registered by guaranteeing a data shift up to 1 m. To this end, we used as reference targets the buildings present in the scene

To assess the performance of the proposed approach, both the areas were considered as $\mathcal{D}_\mathcal{S}$ and $\mathcal{D}_\mathcal{T}$. Tab. 6.1 reports the number of samples available per area divided in Training (TR) and Test (TS) and Pool sets. When an area is considered as $\mathcal{D}_\mathcal{S}$, the training set is exploited to infer the knowledge on the unlabeled samples of $\mathcal{D}_\mathcal{T}$. The test set of the other area (i.e., $\mathcal{D}_\mathcal{T}$) is used for the accuracy assessment and the pool set is the unlabeled set of samples used by the AL technique. Five random datasets per area have been generated and the average results obtained on the test set of the $\mathcal{D}_\mathcal{T}$ for the 5 trials are reported.
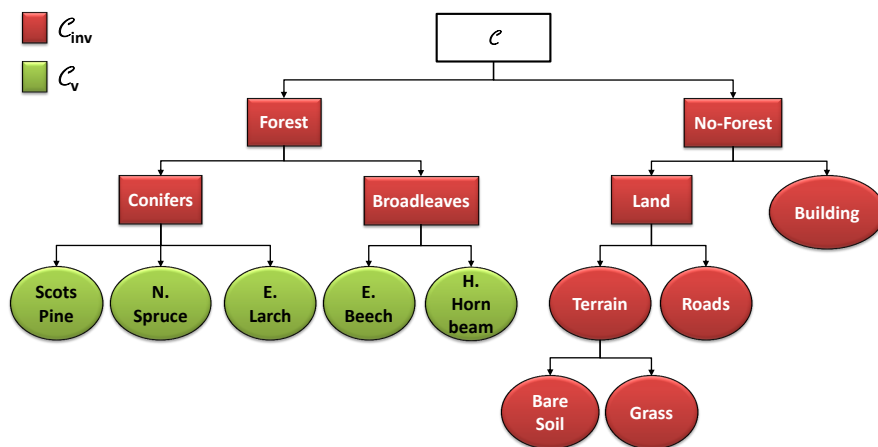
Figure 6.4: Hierarchical tree structure derived at the end of the invariance analysis for the considered DA problem.

In all the experiments carried out, a radial basis function (RBF) kernel was adopted in the SVM classifier. In the experiments with AL methods, at the first iteration the model selection phase was performed using a grid strategy on the validation set of $\mathcal{D}_S$, thus tuning the RBF kernel width and the regularization parameter of the SVM classifier. The same grid strategy was used to tune the model parameters for the standard supervised SVM. For the P³SVM we considered the best parameters obtained for the supervised classifier. Then, we applied a grid strategy to tune the parameters of the semisupervised method, thus selecting the ones that resulted in the highest classification accuracy on the samples of the test set of $\mathcal{D}_T$.

6.4.2 Hierarchical Decomposition

Let us focus the attention on the hierarchical decomposition of the considered set of land-cover classes. Fig. 6.4 shows the hierarchical representation of the land-cover classes for the considered DA problem. Accordingly, the two domains share 9 land-cover classes: 3 species of Conifers Trees (i.e., Norway Spruce, European Larch, Scots Pine), 2 species of Broadleaves Trees (i.e., European Beech, Hop Hornbeam), Grass, Buildings, Roads and Bare Soil. Even tough the considered areas are characterized by similar forest composition, the different properties of the terrain (altitude, slope and aspect) and the different phenological state of the various type of vegetation present in the scene result in a remarkable shift of the class distributions in the full feature space. At the first level of the hierarchy, the adaptation problem is represented by the Forest and No-Forest classes. By analyzing the source training samples (and their physical meaning) we observed that it is possible to infer knowledge from the $\mathcal{D}_S$ to $\mathcal{D}_T$ in the feature subspace defined by a simple Normalized Difference Vegetation Index (NDVI) extracted from the hyperspectral sensor and the height measured by the LiDAR sensor. In particular, the NDVI was calculated by considering the red and the infra-red channels acquired at the wavelengths of 623.13 nm and 863.13 nm, respectively, whereas the height was the maximum height value measured by the laser scanner. Accordingly, it is reasonable to assume that the
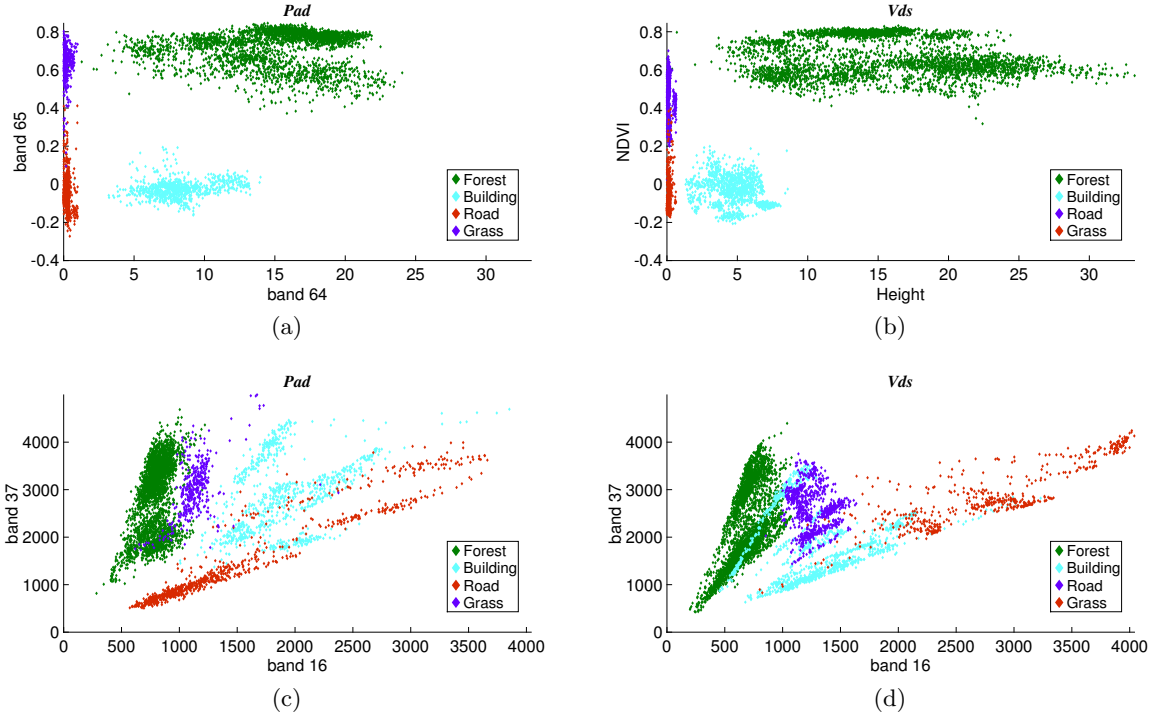
Figure 6.5: Distributions of the labeled samples of *Pad* (left) and *Vds* (right) represented in: (a-b) the invariant feature subspace defined by the NDVI (hyperspectral scanner) and the height (LiDAR sensor), and (c-d) the feature subspace defined by the 16 and 37 spectral channels at the wavelength of 538 nm and 737 nm, respectively.

forest samples are characterized by positive NDVI (because of the chlorophyll response in the infra-red band) and relatively high values of the measured height. In contrast, by analyzing the No-Forest class, it includes the Land and the Building classes. Therefore, all the samples belonging to the Land are characterized by relatively low height values, whereas the target samples of the Buildings present negative NDVI values. Therefore, the considered simple feature space is both invariant and discriminative for the Forest and No-Forest classes. Accordingly, we expect that $\mathcal{D}_\mathcal{T}$ and $\mathcal{D}_\mathcal{S}$ are approximatively aligned in this space.

A representation of the DA problem is presented in Fig. 6.5. The two scatterplots in Fig. 6.5a and Fig. 6.5b show the distribution of the Forest, Roads, Buildings and Grass classes in the invariant feature subspace defined by the hyperspectral and the LiDAR sensors. Due to the physical properties of the NDVI and the Height features, the distributions result statistically aligned on the considered classes besides the samples belongs to different domains. In contrast, if we consider other features (e.g., the other spectral channels) we can observe a relevant shift in the class distributions. An example of this shift is presented in Fig. 6.5c and Fig. 6.5d, where the same set of classes is represented in the subspace defined by bands 16 and 37 of the hyperspectral data (i.e., 538 nm and 737 nm).

At the second level of the hierarchy, the Forest samples can be classified into Conifers

and Broadleaves, which are characterized by different spectral response in the infra-red spectral band. In our study, the infra-red channel considered was the one centered in 863 nm. Moreover, typically conifers are higher than broadleaves. Therefore, the feature subspace defined by the NDVI and the LiDAR height is employed due to its discriminative and almost stationary behaviour for those classes. Note that the NDVI is preferable to the infra-red bands of the hyperspectral data because the ratio of the spectral bands (infra-red and red spectral channels) performed to generate the normalization index compensates possible differences in acquisition condition between the $\mathcal{D}_{\mathcal{S}}$ and $\mathcal{D}_{\mathcal{T}}$.

To discriminate between Buildings and Land, the height feature is sufficient to guarantee the samples distribution alignment, whereas for discriminating the Terrain from the Roads the inference can be applied in the feature subspace defined by the homogeneity textural feature derived by processing the green band of the high resolution optical image [230] and the NDVI values. Indeed, by analzying the samples of the source domain it turned out that the spectral signature of the Grass is affected by the presence of chlorophyll, thus generating higher reflectance responses in the infra-red band with respect to the Roads and the Bare Soil. Moreover, the textural behaviour of the Roads samples is different from the one of the Bare Soil samples. Finally, the Bare Soil and the Grass classes were discriminated by means of the NDVI response and the color textural features (i.e., mean and variance of the Red, Green and Blue spectral channels) derived by processing the high resolution optical image [231].

6.4.3   Adaptation of Invariant Classes

In the first experiment we analyze the results obtained by means of the sensor-driven inference method, thus focusing the attention on the $\mathcal{C}_{inv}$ classes. As a baseline for our comparison, we considered both the standard supervised SVM classifier trained on $\mathcal{D}_{\mathcal{S}}$ and directly applied to $\mathcal{D}_{\mathcal{T}}$, and the DA Progressive Semisupervised Support Vector Machine (P^{3}SVM) presented in [199]. In this context, the adaptation results in a 6 land-cover classes problem: Conifers, Broadleaves, Bare Soil, Roads, Grass and Building. Tab. 6.2a and Tab. 6.2b show the Overall Accuracy (OA%), the Producer Accuracy (PA%) and the User Accuracy (UA%) obtained on $\mathcal{D}_{\mathcal{T}}$ for each class by using: (1) the SVM classifier trained on $\mathcal{D}_{\mathcal{S}}$, (2) the semisupervised P^{3}SVM method, and (3) the proposed sensor-driven DA method SVM^{inf}. In Tab. 6.2a *Pad* was the source domain, whereas in Tab. 6.2b the source domain was *Vds*.

By directly applying the SVM trained on $\mathcal{D}_{\mathcal{S}}$ to $\mathcal{D}_{\mathcal{T}}$, it turned out that the shift in the sample distributions strongly affects the classification accuracies of the Grass and Bare Soil classes. This effect is encountered in both the adaptation problems, thus generating a PA and a UA lower than 50% for the Bare Soil class. By focusing the attention on the other classes, one can notice that the labeled samples of *Pad* properly represent the unlabeled samples of *Vds*. In contrast, by considering *Vds* as source domain, the sample distributions of Building and Roads are not effective in representing the distributions that characterize the *Pad* samples for the same classes.

By exploiting the considered semi-supervised classifier we slightly increase the OA with respect to the use of the supervised SVM classifier, by reaching 82.18% instead of 81.73% and 82.40% instead of 76.59% when *Pad* and *Vds* are considered source domain,

Table 6.2: Average classification results (over five trials): (a) *Pad* is the source domain, (b) *Vds* is the source domain. OA%, PA% and UA% obtained by applying: (1) the supervised SVM classifier trained on the source domain, (2) the semisupervised P³SVM method, (3) the proposed sensor-driven DA method SVM^{inf}.

Classes	Baselines				PM	
	SVM		**P³SVM**		**SVM**^{inf}	
	PA%	**UA%**	**PA%**	**UA%**	**PA%**	**UA%**
Conifers	94.09	91.53	95.5	90.1	93.44	94.99
Broadleaves	82.64	88.05	79.87	89.06	90.07	87.01
Grass	86.29	45.02	75.06	43.66	99.10	99.32
Building	62.25	91	67.46	99.79	98.03	100
Roads	90.96	73.78	99.73	77.65	100	99.46
Bare Soil	1.48	7.53	6.98	25.00	98.94	98.10
OA %	81.73		82.18		94.11	

(a)

Classes	Baselines				PM	
	SVM		**P³SVM**		**SVM**^{inf}	
	PA%	**UA%**	**PA%**	**UA%**	**PA%**	**UA%**
Conifers	92.21	77.42	95.66	86.31	94.01	95.08
Broadleaves	84.68	92.65	90.82	94.72	97.58	96.69
Grass	78.14	87.27	79.65	92.82	98.37	99.30
Building	70.00	53.13	87.35	60.12	100	100
Roads	66.76	33.83	66.47	37.92	100	99.71
Bare Soil	5.25	50	16.08	78.43	99.19	100
OA %	76.59		82.40		97.21	

(b)

respectively. However, the P³SVM method is not able to handle the adaptation of the classes Grass and Bare Soil as proven by the accuracy obtained on the target domain. As expected the sharp differences in the PDFs of the classes decrease the effectiveness of the semi-supervised approach. In contrast, the proposed method is not affected by the statistical misalignment of those classes because of the selected simple feature subspace which is based on spatial-invariant physical properties of the scene. In particular, by means of the invariant feature subspace we correctly transfer the knowledge to the more aligned unlabeled samples of the target domain. Then, by re-projecting these samples in the full feature space we are able to accurately model the PDFs of the target domain for the invariant classes as proven by the obtained PA and UA (all higher than 87% for both the adaptation problems). Therefore, we always improve the OA yielded by both the SVM and the P³SVM methods. Moreover, we sharply increase the PA and UA of the Grass and Bare Soil classes, thus generating a reliable classification map for the target domain without requiring any labeled sample for it. Note that we achieve similar OA

results for both the DA problems (i.e., 94.11% and 97.21%), regardless of the accuracies obtained by directly applying the classifier (i.e., 81.73% and 76.59%). Thus, although the samples of *Vds* are not appropriate to represent the target ones in the entire feature space, by generating an unsupervised training set of the target domain $\mathcal{T}_{inf}^{T}$, we are in the condition to properly represent the statistical distribution of the target samples and then to model them in the full feature space.

6.4.4   Adaptation of Variant Classes

To increase the level of detail of the obtained classification map, in the second experiment the AL procedure was integrated to the inference method to adapt the remaining $\mathcal{C}_v$ classes, i.e., SVM_{AL}^{infer}. Due to the significant changes in the distribution of the classes, no comparison with semisupervised techniques are provided since they resulted in poor classification accuracy. Thus, the proposed method was compared to a standard DA method based on AL. The considered DA-AL approach is composed of two steps: (i) direct application of the supervised classifier trained on $\mathcal{D}_{\mathcal{S}}$ to $\mathcal{D}_{\mathcal{T}}$, and (ii) AL procedure to select the most informative unlabeled samples of $\mathcal{D}_{\mathcal{T}}$. In particular, the AL query considered in the standard DA-AL approach was the same exploited by the proposed AL method, i.e., the MCLU-ECBD. At each iteration of the AL process, 5 most informative samples of $\mathcal{D}_{\mathcal{T}}$ were added to the initial training set.

Even though the adaptation performed in the previous step allows us to obtain an accurate classification map of the target domain for the invariant classes without any labeling cost, the AL technique is integrated in the inference method for addressing the adaptation of the remaining forest species (i.e., $\mathcal{C}_v$ classes). Indeed, for the specific adaptation problem a strong shift in the sample distribution occurred both for the Conifers and the Broadleaves. This shift cannot be recovered by working in simple subspaces defined on the basis of physical measures since the discriminability of these classes require an accurate modeling of the spectral signature. Tab. 6.3a and Tab. 6.3b show the Overall Accuracy (OA%), the Producer Accuracy (PA%) and the User Accuracy (UA%) obtained on the target domain for each class by applying: (1) the supervised SVM classifier trained on $\mathcal{D}_{\mathcal{S}}$, (2) the standard MCLU-ECBD AL method for DA, (3) the proposed inference method SVM_{AL}^{inf} integrated with the AL step for adapting the $\mathcal{C}_v$ classes. In the first case the source domain was *Pad* and 20 samples were added by means of the AL method, whereas in the latter case Vds was the source domain and the number of samples added was 25.

Due to the adaptation performed by means of the sensor-driven inference method, we are in the condition of focusing the attention only on the $\mathcal{C}_v$ classes, thus reducing the number of needed target samples to achieve accurate classification map. Indeed, while the standard DA-AL technique selects the most informative samples of all the land-cover classes, with the proposed method we require only the labels of samples belonging to the $\mathcal{C}_v$ classes (i.e., the forest species). This condition allows us to rapidly increase both the accuracy of the $\mathcal{C}_v$ classes and of the entire DA problem. This effect is more evident when we select few samples from $\mathcal{D}_{\mathcal{T}}$.

Let us focus the attention on the results obtained when *Pad* is the source domain (Tab. 6.3a). By requiring the labels of only 20 samples of the target domain, the PM

Table 6.3: Average classification results (over five trials) considering: (a) *Pad* as the source domain and the number of target samples added is 20, (b) *Vds* as the source domain and the number of target samples added is 25. OA%, PA% and UA% obtained by applying: (1) the supervised SVM classifier trained on the source domain, (2) the MCLU-ECBD, (3) the proposed adaptation method SVM_{AL}^{inf} integrated with the AL step for adapting the $\mathcal{C}_v$ classes.

| | Classes | Baselines | | | | PM | |
| | | SVM | | SVM_{AL} | | SVM_{AL}^{inf} | |
		PA%	UA%	PA%	UA%	PA%	UA%
Forest	N. Spruce	88.32	64.16	86.30	65.83	78.40	71.28
	E. Larch	1.80	38.64	26.67	77.06	48.04	72.18
	S. Pine	80.97	49.64	82.37	58.25	86.56	67.14
	E. Beech	70.35	83.36	72.86	86.34	77.41	85.38
	Hornbeam	55.61	40.71	55.61	42.86	59.51	48.03
No Forest	Grass	88.54	50.32	100	99.55	99.10	99.32
	Building	66.48	100	92.68	98.21	98.03	100
	Roads	98.08	74.90	98.36	96.51	100	99.46
	Bare Soil	17.87	65.63	100	97.51	98.94	98.10
	OA %	63.17		75.90		79.61	

(a)

| | Classes | Baselines | | | | PM | |
| | | SVM | | SVM_{AL} | | SVM_{AL}^{inf} | |
		PA%	UA%	PA%	UA%	PA%	UA%
Forest	N. Spruce	31.43	15.42	35.24	43.53	48.57	46.79
	E. Larch	1.15	0.86	0.38	0.93	9.23	33.80
	S. Pine	74.54	46.20	87.94	68.73	89.90	70.27
	E. Beech	41.87	93.52	85.11	96.49	91.40	97.03
	Hornbeam	50.28	23.66	64.72	45.96	69.72	62.91
No Forest	Grass	81.40	92.59	89.07	87.64	98.37	99.30
	Building	65.59	65.40	95.00	87.77	100	100
	Roads	68.53	38.58	80.00	68.00	100	99.71
	Bare Soil	37.37	88.10	77.37	97.21	99.19	100
	OA %	52.16		79.04		87.20	

(b)

Table 6.4: Average (over five trials) Overall accuracy (%) versus the number of target labeled samples annotated by AL with the proposed method (SVM_{AL}^{infer}) and the standard DA AL method (SVM_{AL}) considering: (a) *Pad* as source domain, (b) *Vds* as source domain.

(a)   (b)
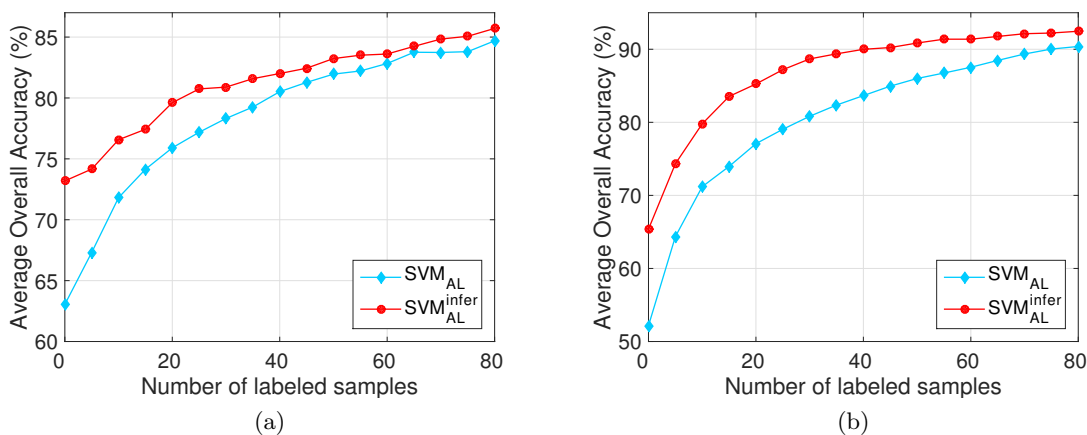
improves the OA accuracy of approximatively a 4% with respect to the standard SVM_{AL} and of a 17% with respect to the SVM. Moreover, the PA and the UA of the forest species sharply increased compared to the ones obtained with the SVM_{AL}. Therefore, due to the accurate adaptation performed in the previous step for the classes Grass, Building, Roads and Bare Soil, by requiring the labels of few samples for the remaining classes we obtained an accurate land-cover map of the target domain. Tab. 6.3b shows similar results when *Vds* is the source domain. By labeling 25 samples of the target domain, the PM improves the OA accuracy of a 8% with respect to the SVM_{AL} and of a 35% with respect to the SVM.

Fig. 6.4a and Fig. 6.4b depict the average (on five trials) classification accuracies obtained on $\mathcal{D}_T$ versus the number of new labeled samples with the proposed method SVM_{AL}^{inf} and the standard AL method SVM_{AL} considering *Pad* and *Vds* as source domains, respectively. The results obtained confirm that the proposed approach allows a significant reduction of the number of labeled samples of the target domain required for obtaining a given classification accuracy, and thus the labelling cost. As an example, when *Pad* is the source domain, to reach an OA of 80% our method requires 20 samples whereas the SVM_{AL} needs twice the number of samples (Fig. 6.4a). Similarly, when *Vds* is the source domain, with the PM by adding 25 samples the OA obtained is 87%, whereas the standard SVM_{AL} requires 35 samples more than the PM to reach the same OA (Fig. 6.4b). Furthermore, even tough the AL exploited in the PM selects samples only from the variant set of classes $\mathcal{C}_v$, by adding a high number of labeled samples from the $\mathcal{D}_T$ the standard AL method still achieves comparable OA. Thus, the results obtained confirm the effectiveness of the inference method in adaptation the invariant set of classes $\mathcal{C}_{inv}$.

6.5   Conclusion

In this chapter a sensor-driven DA method based on invariant features for the classification of remote sensing data has been presented. The proposed method allows the transferring of knowledge between remote sensing data acquired on different geographical areas which share the same set of classes. In particular, it takes advantage from a multisensor data scenario to overcome the shift in the PDFs of the classes due to the different acquisition condition. By exploiting the peculiarity of each sensor of measuring different physical properties of the scene, it is possible to detect feature subspaces where subsets of classes result statistically aligned. Accordingly, instead of using data-driven feature extraction methods, the detection of invariant features is driven by the physical properties of the land-cover classes.

The proposed approach is based on three main steps. In the first step we analyze the labeled samples of the source domain and the set of sensors available to perform an invariance analysis of the land-cover classes. Thus, the adaptation problem can be decomposed by dividing the classes into two groups: (i) a subset of classes for which invariant features are measured, and (ii) a subset of classes for which none of the sensor available can measure invariant properties. To facilitate the identification of the subset of invariant classes, we perform a hierarchical decomposition of the land-cover classes by focusing the attention on the physical properties of the scene. In the second step, we bridge the gap between the distributions according to a sensor-driven DA strategy, which infers labels from the source to the target domain for the invariant classes. By taking advantage from the statistical alignment of the domain distributions in the detected features subspaces, we generate an initial training set for the target domain selecting the target samples more aligned to the source data. This training set is re-projected in the full-feature to properly model the PDF of the target domain for the considered subset of classes. Indeed, even though the invariant feature subspaces guarantee a reliable data alignment between the domains, they may be not sufficient to accurately manage the complex classification problem of the target domain. Finally, the proposed method addresses the adaptation of the remaining land-cover classes characterized by variant features behaviour using an AL method.

Experimental results obtained show that the sensor-driven inference method can generate a reliable training set for the target domain. Thus, without any additional labeling cost, we are in the condition of properly model the distribution of the target domain for the subset of invariant classes and, thus to generate an accurate land-cover map of them. Moreover, the adaptation of the invariant classes introduces constraints to the general structure of the entire problem facilitating the adaptation of the remaining variant classes. Accordingly, by integrating the AL technique with the inference method we increase the level of detail in the adaptation process by strongly reducing the number of labeled samples required with respect to DA methods based on standard AL.

As future developments, we plan to further analyze the sensor-driven inference strategy by testing the proposed technique on datasets where a different combination of sensors is available. Moreover, we aim to replace the AL technique with an unsupervised DA method in order to adapt the set of variant classes without any labeling cost. Thus, it can be achieved by exploiting the constraints introduced on the set of invariant classes to

drive the unsupervised adaptation of the remaining land-cover classes. As a final remark, we point out that due to the increasing availability of multisensor data, the proposed sensor-driven domain adaptation method is promising from the operational view point. Indeed, the possibility of acquiring complementary measures of the scene makes it possible to take advantage from the physical properties of the classes to drive the adaptation, thus increasing the reliability of the adaptation process.

Conclusions

This chapter concludes the thesis by presenting a general discussion of the work described and by providing a summary of the novel contributions illustrated in the document. Finally, possible future developments of the proposed methods are presented.

Summary and Discussion

In this thesis we have presented novel methods for the accurate estimation of forest parameters based both on the fusion of multisensor remote sensing data and the use of high resolution LiDAR data. In particular, we focused the attention on data acquired by active LiDAR sensors, mounted on both airborne and terrestrial platform, and passive high spatial/spectral optical sensors. The proposed methods represent a valuable contribution for the automatic estimation of forest parameters in the framework of the precision forestry. Indeed, to obtain a more comprehensive representation of the forest structure and to cope with the huge amount of data collected over wide forest areas, automatic methods capable of taking advantage from the specific properties of the different data sources are essential for modern forestry inventories.

Five main novel contributions to the state-of-the-art have been presented in the dissertation. As a first step, we presented a method for the individual tree crowns delineation in multilayered forests by using very high-density LiDAR data. The proposed 3-D segmentation method is able to accurately detect and delineate both the dominant trees and the understory vegetation. The obtained results demonstrate the importance of integrating the analysis carried out in the original LiDAR point cloud with the one performed in the rasterized image domain, which leads to a higher detection accuracy of the dominant trees. Moreover, by taking advantage from the capability of the new LiDAR sensors of deeply penetrating the vegetation, it is possible to accurately detect the sub-dominant trees. In particular, the angular analysis of the vertical profile allows the detection of multiple trees located under different portions of the crown and drastically reduces the commission errors. Moreover, from the results obtained, we can conclude that the proposed crown delineation performed directly in the LiDAR point cloud accurately fits the shape of the trees of both the dominant and the sub-dominant vegetation with a low computational load.

In the second contribution of the thesis, we addressed the estimation of the DBH at single tree level by fully exploiting the information provided by the high-density LiDAR data to model the main environmental factors that can affect the stem growth. The proposed novel method for the adaptive estimation of the DBH demonstrates the importance

of modelling the forest environment in order to accurately retrieve the forest parameters. Moreover, it highlights the need of developing methods being able to fully exploit the potential of the high resolution LiDAR data. After the unsupervised detection of the growth model classes based on a data-driven inference process, for each detected growth model class a regression rule is defined and adopted. The experimental results pointed out that the method is able to identify the environmental factors that affect the growth expansion and to identify groups of trees characterized by different growth conditions. In particular, we assessed that the topography plays a dominant role in the growth of the trees and affects the stem expansion in different ways in mature and old-growth trees. Moreover, the proposed approach sharply improves the estimation accuracy of small and large stems with respect to the state-of-the-art methods due to tailored regression models defined for each growth model class. Furthermore, it is automatic and data-driven and thus can be applied to different areas for identifying the specific growth-models to be used.

In the third contribution of the thesis, we addressed the fusion of low-density LiDAR data and high resolution optical images for an accurate estimation of the individual tree top height. The synergistic use of the two data sources performed in a data fusion perspective mitigates the lack of height information when data with low laser sampling density are available. Indeed, the proposed multisensor segmentation method allows an accurate delineation of the single tree crowns due to the joint use of the information provided by the optical image and the LiDAR data. The proposed 3-D parametric model is able to accurately reconstruct the real tree top height, whereas the k-NN trees technique allows the estimation of the height of those trees completely missed by the laser scanner. The sharp improvement of the estimation accuracy becomes more evident when we deal with very low-density LiDAR data (i.e., 0.5 pts/m^2 and 0.25 pts/m^2). Moreover, the robustness of the method is confirmed by the fact that the accuracy is not affected by the decrease of number of laser samples.

Towards the direction of the precision forestry, the fourth contribution of the thesis consists in a method for the integration of low-density airborne LiDAR data with high resolution terrestrial LiDAR data for the accurate reconstruction of the 3-D structure of the crowns. The fusion of the two LiDAR point clouds acquired by different view points results in extremely high resolution crown profiles. Moreover, limited research has been done in this area because of the difficult prerequisite of registration. The experimental results obtained demonstrate that the proposed method is able to register the LiDAR point clouds in an automatic way by taking advantage from the spatial pattern of the forest. These results are accurate and thus promising for operational applications. Moreover, the fusion of the LiDAR point clouds allows a more comprehensive representation of the scene, thus mapping the forest structure at high level of detail. This is confirmed by the crown parameter estimation improvement obtained by the proposed method with respect to the results obtained by using the singular LiDAR data sources.

Finally, the availability of multiple remote sensing data was employed to define a sensor-driven DA method based on invariant features for the classification of remote sensing data. The main idea is to model the differences among forest areas (domains) sharing the same set of land-cover classes by transferring the knowledge from a source domain (forest area where reference data are available) to a target domain (forest area where no

reference data are initially available). The proposed method demonstrates the importance of exploiting the peculiarity of each sensor of measuring different physical properties of the scene, which allows the detection of feature subspaces where subsets of classes result statistically aligned. Accordingly, instead of using data-driven feature extraction methods, the detection of invariant features is driven by the physical properties of the land-cover classes. Then, for the remaining set of variant classes we perform the adaptation by using an AL method. Experimental results obtained show that the sensor-driven inference method can accurately classify the target domain. Moreover, from the results obtained we can conclude that the adaptation of classes characterized by invariant feature behaviour introduces constraints to the general structure of the entire problem, thus facilitating the adaptation of the remaining variant classes. Thus, the proposed approach strongly reduces the number of labeled samples required to achieve a predefined classification accuracy with respect to DA methods based on standard AL.

Future Developments

In this research activities we defined and developed methods that can significantly improve the capability of automatically estimating forest parameters at individual tree level by using high resolution LiDAR data and by integrating multiple remote sensing data. On the basis of the developed methods, the analysis and the experimental results carried out in the framework of this thesis, we identified some interesting directions of research as future developments of the presented work.

First, we aim to test the proposed methods on forest areas characterized by different ages and structures to confirm the robustness of the developed approaches. Moreover, future developments should be devoted to extend the proposed methods to the broadleaved trees, which represent a complex test case because of their crown umbrella shape difficult to delineate. Thus, even though the classification of these species has been widely addressed, little research has been done in the estimation of the individual tree parameters for broadleaved forest.

In the direction of the precision forestry we aim to develop automatic methods for the analysis and the extraction of the high amount of information contained in the full waveform LiDAR data. These scanners provide a higher spatial point density as well as additional information on the reflecting properties of crown structure. Moreover, the cross section calculated from the waveforms gives important information on the type of vegetation, whereas the calibration and the decomposition of full waveform data are still open tasks in the literature that need to be further analyzed.

By focusing the attention on the fusion of multiple remote sensing data, we aim to further investigate the combination of different data sources by including synthetic aperture radar (SAR) systems. Indeed, SAR data represent an important source of information for studies on forest environments, but their use is still limited since the forest parameter estimates are affected by the tree structure, incidence angle, and environmental conditions. In this framework, the integration of these data with optical images represents an interesting research topic.

Finally, attention will be devoted to the update of the forest parameter estimation. In

particular, we aim to develop 3-D change detection methods based on the comparison of multi-temporal LiDAR point clouds to monitor the forest changes. Even though, multi-temporal analysis has been extensively analyzed for optical and SAR data, few works have done considering LiDAR data because of the challenges introduced by the point cloud domain. The point density may be significantly different between two LiDAR data acquisition and the laser may penetrate different parts of the canopy in the two acquisitions. Moreover, the tree canopies are natural structures with highly irregular properties difficult to compare. Accordingly, novel reliable approaches to change detection in multi-temporal LiDAR data for forestry application should be studied and developed.

List of Publications

Journal Papers

[**1**] C. Paris, L. Bruzzone, "A 3D Model-Based Approach to the Estimation of the Tree Top Height by fusing Low-Density LiDAR data and Very High Resolution Optical Images", IEEE Transactions on Geoscience and Remote Sensing, Vol. 53, pp. 467-480, 2015.

[**2**] C. Paris, D. Valduga, L. Bruzzone, "A Hierarchical Approach to 3D Segmentation of LiDAR Data at Single Trees Level in Multi-Layered Forest," IEEE Transactions on Geoscience and Remote Sensing, in Press.

[**3**] C. Paris, L. Bruzzone, "A Sensor-Driven Domain Adaptation Method Based on Spatial Invariant Features for Remote Sensing Data Classification," IEEE Transactions on Geoscience and Remote Sensing, Submitted for publication in October 2015.

[**4**] C. Paris, D. Kelbe, J. van Aardt, L. Bruzzone, "Towards Fusion of Airborne and Terrestrial LiDAR data for robust assessment of tree crown structure," IEEE Geoscience and Remote Sensing Letters, in Preparation.

[**5**] C. Paris, L. Bruzzone, "A Diameter Class Based Approach to Tree Stem Volume Estimation in the Southern Alps by using Airborne LiDAR data," IEEE Transactions on Geoscience and Remote Sensing, in Preparation.

International Conferences

[**1**] C. Paris, L. Bruzzone, "A novel technique for tree stem height estimation by fusing low density LiDAR data and optical images," IEEE International Geoscience and Remote Sensing Symposium (IGARSS '13), Melbourne, Australia, 21-26 July 2013.

[**2**] C. Paris, L. Bruzzone, "A sensor-driven domain adaptation method for the classification of remote sensing images," IEEE International Geoscience and Remote Sensing Symposium (IGARSS '14), Quebec City, Quebec, 13-18 July 2014.

[**3**] C. Paris, D. Valduga, L. Bruzzone, "A hierarchical approach to the segmentation of single dominant and dominated trees in forest areas by using high-density LiDAR data," IEEE International Geoscience and Remote Sensing Symposium (IGARSS '15), Milan, Italy, 27-31 July 2015.

[4] C. Paris, D. Kelbe, J. v. Aardt, L. Bruzzone, "A precise estimation of the 3d structure of the forest based on the fusion of airborne and terrestrial LiDAR data," IEEE International Geoscience and Remote Sensing Symposium (IGARSS '15), Milan, Italy, 27-31 July 2015.

[5] D. Marinelli, C. Paris, L. Bruzzone, "Fusion of high and very high density LiDAR data for 3d forest change detection," IEEE International Geoscience and Remote Sensing Symposium (IGARSS '16), Beijing, China, Submitted for publication in December 2015.

[6] C. Paris, L. Bruzzone, "A data-driven identification of growth-model classes for the adaptive estimation of single-tree stem diameter in LiDAR data," IEEE International Geoscience and Remote Sensing Symposium (IGARSS '16), Beijing, China, Submitted for publication in December 2015.

Bibliography

[1] U. Stilla and B. Jutzi, "Waveform analysis for small-footprint pulsed laser systems," *Topographic laser ranging and scanning: Principles and processing*, pp. 215–234, 2008.

[2] J. Reitberger, C. Schnörr, M. Heurich, P. Krzystek, and U. Stilla, "Towards 3d mapping of forests: A comparative study with first/last pulse and full waveform lidar data," *Int. Atch. Photogrammetry, Remote Sensing, and Spatial Information Sciences*, vol. 37, pp. 1397–1403, 2008.

[3] J. Reitberger, P. Krzystek, and U. Stilla, "Analysis of full waveform lidar data for the classification of deciduous and coniferous trees," *International journal of remote sensing*, vol. 29, no. 5, pp. 1407–1431, 2008.

[4] E. Næsset, "Effects of different sensors, flying altitudes, and pulse repetition frequencies on forest canopy metrics and biophysical stand properties derived from small-footprint airborne laser data," *Remote Sensing of Environment*, vol. 113, no. 1, pp. 148–159, 2009.

[5] J. Holmgren, M. Nilsson, and H. Olsson, "Simulating the effects of lidar scanning angle for estimation of mean tree height and canopy closure," *Canadian Journal of Remote Sensing*, vol. 29, no. 5, pp. 623–632, 2003.

[6] U. Stilla, M. Schmitt, O. Maksymiuk, and S. Auer, "Towards the recognition of individual trees in decimeter-resolution airborne millimeterwave sar," in *Pattern Recognition in Remote Sensing (PRRS), 2014 8th IAPR Workshop on*. IEEE, 2014, pp. 1–4.

[7] M. Schmitt and U. Stilla, "Maximum-likelihood estimation for multi-aspect multi-baseline sar interferometry of urban areas," *ISPRS Journal of Photogrammetry and Remote Sensing*, vol. 87, pp. 68–77, 2014.

[8] M. Lefsky, W. Cohen, and T. Spies, "An evaluation of alternate remote sensing products for forest inventory, monitoring, and mapping of douglas-fir forests in western oregon," *Canadian Journal of Forest Research*, vol. 31, no. 1, pp. 78–87, 2001.

[9] N. C. Coops, M. A. Wulder, D. S. Culvenor, and B. St-Onge, "Comparison of forest attributes extracted from fine spatial resolution multispectral and lidar data," *Canadian Journal of Remote Sensing*, vol. 30, no. 6, pp. 855–866, 2004.

[10] E. Næsset, "Airborne laser scanning as a method in operational forest inventory: status of accuracy assessments accomplished in scandinavia," *Scandinavian Journal of Forest Research*, vol. 22, no. 5, pp. 433–442, 2007.

[11] M. Woods, D. Pitt, M. Penner, K. Lim, D. Nesbitt, D. Etheridge, and P. Treitz, "Operational implementation of a lidar inventory in boreal ontario," *The Forestry Chronicle*, vol. 87, no. 4, pp. 512–528, 2011.

[12] M. Maltamo, P. Packalén, E. Kallio, J. Kangas, J. Uuttera, J. Heikkilä *et al.*, "Airborne laser scanning based stand level management inventory in finland." in *Proceedings of SilviLaser 2011, 11th International Conference on LiDAR Applications for Assessing Forest Ecosystems, University of Tasmania, Australia, 16-20 October 2011*. Conference Secretariat, 2011, pp. 1–10.

[13] D. Mongus and B. Zalik, "Computationally efficient method for the generation of a digital terrain model from airborne lidar data using connected operators," *Selected Topics in Applied Earth Observations and Remote Sensing, IEEE Journal of*, vol. 7, no. 1, pp. 340–351, 2014.

[14] E. Ahokas, H. Kaartinen, and J. Hyyppä, "On the quality checking of the airborne laser scanningbased nationwide elevation model in finland," *Int. Arch. Photogramm. Remote Sens. Spat. Inf. Sci*, vol. 37, pp. 267–270, 2008.

[15] E. Næsset, "Predicting forest stand characteristics with airborne scanning laser using a practical two-stage procedure and field data," *Remote Sensing of Environment*, vol. 80, no. 1, pp. 88–99, 2002.

[16] M. Hollaus, W. Wagner, B. Maier, and K. Schadauer, "Airborne laser scanning of forest stem volume in a mountainous environment," *Sensors*, vol. 7, no. 8, pp. 1559–1577, 2007.

[17] J. Holmgren, "Prediction of tree height, basal area and stem volume in forest stands using airborne laser scanning," *Scandinavian Journal of Forest Research*, vol. 19, no. 6, pp. 543–553, 2004.

[18] M. Villikka, P. Packalén, and M. Maltamo, "The suitability of leaf-off airborne laser scanning data in an area-based forest inventory of coniferous and deciduous trees," *Silva Fenn*, vol. 46, no. 1, pp. 99–110, 2012.

[19] M. Dalponte, N. Coops, L. Bruzzone, and D. Gianelle, "Analysis on the use of multiple returns lidar data for the estimation of tree stems volume," *Selected Topics in Applied Earth Observations and Remote Sensing, IEEE Journal of*, vol. 2, no. 4, pp. 310–318, Dec. 2009.

[20] S. C. Popescu, R. H. Wynne, and R. F. Nelson, "Measuring individual tree crown diameter with lidar and assessing its influence on estimating forest volume and biomass," *Canadian journal of remote sensing*, vol. 29, no. 5, pp. 564–577, 2003.

[21] M. Schardt, M. Ziegler, A. Wimmer, R. Wack, and J. Hyyppa, "Assessment of forest parameters by means of laser scanning," *International archives of photogrammetry remote sensing and spatial information sciences*, vol. 34, no. 3/A, pp. 302–309, 2002.

[22] M. Heurich, "Automatic recognition and measurement of single trees based on data from airborne laser scanning over the richly structured natural forests of the bavarian forest national park," *Forest Ecology and Management*, vol. 255, no. 7, pp. 2416–2433, 2008.

[23] M. J. Falkowski, A. M. Smith, A. T. Hudak, P. E. Gessler, L. A. Vierling, and N. L. Crookston, "Automated estimation of individual conifer tree height and crown diameter via two-dimensional spatial wavelet analysis of lidar data," *Canadian Journal of Remote Sensing*, vol. 32, no. 2, pp. 153–161, 2006.

[24] A. Bucksch, R. Lindenbergh, M. Menenti, and M. Z. Rahman, "Skeleton-based botanic tree diameter estimation from dense lidar data," in *SPIE Optical Engineering+ Applications*. International Society for Optics and Photonics, 2009, pp. 746 007–746 007.

[25] Q. Chen, D. B. Peng Gong, and Y. Q. Tian, "Estimating basal area and stem volume for individual trees from lidar data," *Photogrammetric Engineering & Remote Sensing*, vol. 73, no. 12, pp. 1355–1365, Dec. 2007.

[26] J. Vauhkonen, L. Ene, S. Gupta, J. Heinzel, J. Holmgren, J. Pitkänen, S. Solberg, Y. Wang, H. Weinacker, K. M. Hauglin *et al.*, "Comparative testing of single-tree detection algorithms under different types of forest," *Forestry*, p. cpr051, 2011.

[27] H. Kaartinen, J. Hyyppä, X. Yu, M. Vastaranta, H. Hyyppä, A. Kukko, M. Holopainen, C. Heipke, M. Hirschmugl, F. Morsdorf *et al.*, "An international comparison of individual tree detection and extraction using airborne laser scanning," *Remote Sensing*, vol. 4, no. 4, pp. 950–974, 2012.

[28] M. Dalponte, L. Bruzzone, and D. Gianelle, "A system for the estimation of single-tree stem diameter and volume using multireturn lidar data," *Geoscience and Remote Sensing, IEEE Transactions on*, vol. 49, no. 7, pp. 2479–2490, 2011.

[29] M. Vastaranta, V. Kankare, M. Holopainen, X. Yu, J. Hyyppä, and H. Hyyppä, "Combination of individual tree detection and area-based approach in imputation of forest variables using airborne laser data," *ISPRS Journal of Photogrammetry and Remote Sensing*, vol. 67, pp. 73–79, 2012.

[30] J. Vauhkonen, I. Korpela, M. Maltamo, and T. Tokola, "Imputation of single-tree attributes using airborne laser scanning-based height, intensity, and alpha shape metrics," *Remote Sensing of Environment*, vol. 114, no. 6, pp. 1263–1276, 2010.

[31] C.-S. Lo and C. Lin, "Growth-competition-based stem diameter and volume modeling for tree-level forest inventory using airborne lidar data," *Geoscience and Remote Sensing, IEEE Transactions on*, vol. 51, no. 4, pp. 2216–2226, 2013.

[32] J. Lovell, D. L. Jupp, D. Culvenor, and N. Coops, "Using airborne and ground-based ranging lidar to measure canopy structure in australian forests," *Canadian Journal of Remote Sensing*, vol. 29, no. 5, pp. 607–622, 2003.

[33] I. Moorthy, J. R. Miller, J. A. J. Berni, P. Zarco-Tejada, B. Hu, and J. Chen, "Field characterization of olive (olea europaea l.) tree crown architecture using terrestrial laser scanning data," *Agricultural and Forest Meteorology*, vol. 151, no. 2, pp. 204–214, 2011.

[34] N. Pfeifer, B. Gorte, D. Winterhalder *et al.*, "Automatic reconstruction of single trees from terrestrial laser scanner data," in *Proceedings of 20th ISPRS Congress*, 2004, pp. 114–119.

[35] M. Thies*, N. Pfeifer, D. Winterhalder, and B. G. Gorte, "Three-dimensional reconstruction of stems for assessment of taper, sweep and lean based on laser scanning of standing trees," *Scandinavian Journal of Forest Research*, vol. 19, no. 6, pp. 571–581, 2004.

[36] Z.-L. Cheng, X.-P. Zhang, and B.-Q. Chen, "Simple reconstruction of tree branches from a single range image," *Journal of computer science and technology*, vol. 22, no. 6, pp. 846–858, 2007.

[37] J. G. Henning and P. J. Radtke, "Detailed stem measurements of standing trees from ground-based scanning lidar," *Forest Science*, vol. 52, no. 1, pp. 67–80, 2006. [Online]. Available: http://www.ingentaconnect.com/content/saf/fs/2006/00000052/00000001/art00007

[38] H.-G. Maas, A. Bienert, S. Scheller, and E. Keane, "Automatic forest inventory parameter determination from terrestrial laser scanner data," *International journal of remote sensing*, vol. 29, no. 5, pp. 1579–1593, 2008.

[39] E. Tomppo, "Designing a satellite image-aided national forest survey in finland [nfi]," *Rapport-Sveriges Lantbruksuniversitet, Institutionen foer Biometri och Skogsindelning, Avdelningen foer Skoglig Fjaerranalys*, 1990.

[40] F. Sedano, P. Gong, and M. Ferrao, "Land cover assessment with modis imagery in southern african miombo ecosystems," *Remote sensing of environment*, vol. 98, no. 4, pp. 429–441, 2005.

[41] D. G. Goodenough, A. Dyk, K. O. Niemann, J. S. Pearlman, H. Chen, T. Han, M. Murdoch, and C. West, "Processing hyperion and ali for forest classification," *Geoscience and Remote Sensing, IEEE Transactions on*, vol. 41, no. 6, pp. 1321–1331, 2003.

[42] N. Kosaka, T. Akiyama, B. Tsai, and T. Kojima, "Forest type classification using data fusion of multispectral and panchromatic high-resolution satellite imageries," in *Geoscience and Remote Sensing Symposium, 2005. IGARSS'05. Proceedings. 2005 IEEE International*, vol. 4. IEEE, 2005, pp. 2980–2983.

[43] L. Wang, W. P. Sousa, P. Gong, and G. S. Biging, "Comparison of ikonos and quickbird images for mapping mangrove species on the caribbean coast of panama," *Remote Sensing of Environment*, vol. 91, no. 3, pp. 432–440, 2004.

[44] Y. Dian, Z. Li, and Y. Pang, "Spectral and texture features combined for forest tree species classification with airborne hyperspectral imagery," *Journal of the Indian Society of Remote Sensing*, vol. 43, no. 1, pp. 101–107, 2015.

[45] M. Martin, S. Newman, J. Aber, and R. Congalton, "Determining forest species composition using high spectral resolution remote sensing data," *Remote Sensing of Environment*, vol. 65, no. 3, pp. 249–254, 1998.

[46] D. G. Goodenough, A. Dyk, K. O. Niemann, J. S. Pearlman, H. Chen, T. Han, M. Murdoch, and C. West, "Processing hyperion and ali for forest classification," *Geoscience and Remote Sensing, IEEE Transactions on*, vol. 41, no. 6, pp. 1321–1331, 2003.

[47] D. G. Leckie, S. Tinis, T. Nelson, C. Burnett, F. A. Gougeon, E. Cloney, and D. Paradine, "Issues in species classification of trees in old growth conifer stands," *Canadian Journal of Remote Sensing*, vol. 31, no. 2, pp. 175–190, 2005.

[48] D. M. Gates, H. J. Keegan, J. C. Schleter, and V. R. Weidner, "Spectral properties of plants," *Applied optics*, vol. 4, no. 1, pp. 11–20, 1965.

[49] P. J. Zarco-Tejada, J. R. Miller, J. Harron, B. Hu, T. L. Noland, N. Goel, G. H. Mohammed, and P. Sampson, "Needle chlorophyll content estimation through model inversion using hyperspectral data from boreal conifer forest canopies," *Remote sensing of environment*, vol. 89, no. 2, pp. 189–199, 2004.

[50] E. B. Knipling, "Physical and physiological basis for the reflectance of visible and near-infrared radiation from vegetation," *Remote Sensing of Environment*, vol. 1, no. 3, pp. 155–159, 1970.

[51] C. Trotter, J. Dymond, and C. Goulding, "Estimation of timber volume in a coniferous plantation forest using landsat tm," *International Journal of Remote Sensing*, vol. 18, no. 10, pp. 2209–2223, 1997.

[52] M. Steininger, "Satellite estimation of tropical secondary forest above-ground biomass: data from brazil and bolivia," *International Journal of Remote Sensing*, vol. 21, no. 6-7, pp. 1139–1157, 2000.

[53] A. Leboeuf, A. Beaudoin, R. Fournier, L. Guindon, J. Luther, and M.-C. Lambert, "A shadow fraction method for mapping biomass of northern boreal black spruce forests using quickbird imagery," *Remote Sensing of Environment*, vol. 110, no. 4, pp. 488–500, 2007.

[54] D. Lu, "The potential and challenge of remote sensing based biomass estimation," *International Journal of Remote Sensing*, vol. 27, no. 7, pp. 1297–1328, 2006.

[55] E. Baltsavias, A. Gruen, H. Eisenbeiss, L. Zhang, and L. Waser, "High-quality image matching and automated generation of 3d tree models," *International Journal of Remote Sensing*, vol. 29, no. 5, pp. 1243–1259, 2008.

[56] K. Nurminen, M. Karjalainen, X. Yu, J. Hyyppä, and E. Honkavaara, "Performance of dense digital surface models based on image matching in the estimation of plot-level forest variables," *ISPRS Journal of Photogrammetry and Remote Sensing*, vol. 83, pp. 104–115, 2013.

[57] E. Honkavaara, J. Hyyppä, A. Kukko, H. Luukkonen, P. Savolainen, and X. Yu, "Method for determination of stand attributes and a computer program for performing the method," Jun. 26 2012, uS Patent 8,208,689.

[58] B. St-Onge, Y. Hu, and C. Vega, "Mapping the height and above-ground biomass of a mixed forest using lidar and stereo ikonos images," *International Journal of Remote Sensing*, vol. 29, no. 5, pp. 1277–1294, 2008.

[59] J. Bohlin, J. Wallerman, and J. E. Fransson, "Forest variable estimation using photogrammetric matching of digital aerial images in combination with a high-resolution dem," *Scandinavian Journal of Forest Research*, vol. 27, no. 7, pp. 692–699, 2012.

[60] J. Poon, C. S. Fraser, Z. Chunsun, Z. Li, and A. Gruen, "Quality assessment of digital surface models generated from ikonos imagery," *The Photogrammetric Record*, vol. 20, no. 110, pp. 162–171, 2005.

[61] D. Leckie, F. Gougeon, D. Hill, R. Quinn, L. Armstrong, and R. Shreenan, "Combined high-density lidar and multispectral imagery for individual tree crown analysis," *Canadian Journal of Remote Sensing*, vol. 29, no. 5, pp. 633–649, 2003.

[62] S. Koukoulas and G. A. Blackburn, "Mapping individual tree location, height and species in broadleaved deciduous forest using airborne lidar and multi-spectral remotely sensed data," *International Journal of Remote Sensing*, vol. 26, no. 3, pp. 431–455, 2005.

[63] T. Takahashi, Y. Awaya, Y. Hirata, N. Furuya, T. Sakai, and A. Sakai, "Stand volume estimation by combining low laser-sampling density lidar data with quickbird panchromatic imagery in closed-canopy japanese cedar (cryptomeria japonica) plantations," *International Journal of Remote Sensing*, vol. 31, no. 5, pp. 1281–1301, 2010.

[64] J. Fransson, M. Magnusson, and J. Holmgren, "Estimation of forest stem volume using optical spot-5 satellite and laser data in combination," in *Geoscience and Remote Sensing Symposium, 2004. IGARSS '04. Proceedings. 2004 IEEE International*, vol. 4, Sept. 2004, pp. 2318–2322 vol.4.

[65] Z. Abd Latif, S. Aman, and R. Ghazali, "Delineation of tree crown and canopy height using airborne lidar and aerial photo," in *Signal Processing and its Applications (CSPA), 2011 IEEE 7th International Colloquium on*, March 2011, pp. 354–358.

[66] M. Dalponte, L. Bruzzone, and D. Gianelle, "Tree species classification in the southern alps based on the fusion of very high geometrical resolution multispectral/hyperspectral images and lidar data," *Remote sensing of environment*, vol. 123, pp. 258–270, 2012.

[67] S. Ali, P. Dare, and S. Jones, "Fusion of remotely sensed multispectral imagery and lidar data for forest structure assessment at the tree level," *ISPRS Proceedings, Beijing*, 2008.

[68] J. Li, B. Hu, G. Sohn, and L. Jing, "Individual tree species classification using structure features from high density airborne lidar data," in *Geoscience and Remote Sensing Symposium (IGARSS), 2010 IEEE International*, 2010, pp. 2099–2102.

[69] M. Dalponte, L. Bruzzone, and D. Gianelle, "Fusion of hyperspectral and lidar remote sensing data for classification of complex forest areas," *Geoscience and Remote Sensing, IEEE Transactions on*, vol. 46, no. 5, pp. 1416–1427, 2008.

[70] J. Holmgren, Å. Persson, and U. Söderman, "Species identification of individual trees by combining high resolution lidar data with multi-spectral images," *International Journal of Remote Sensing*, vol. 29, no. 5, pp. 1537–1552, 2008.

[71] H. O. Ørka, T. Gobakken, E. Næsset, L. Ene, and V. Lien, "Simultaneously acquired airborne laser scanning and multispectral imagery for individual tree species identification," *Canadian Journal of Remote Sensing*, vol. 38, no. 2, pp. 125–138, 2012.

[72] T. G. Jones, N. C. Coops, and T. Sharma, "Assessing the utility of airborne hyperspectral and lidar data for species distribution mapping in the coastal pacific northwest, canada," *Remote Sensing of Environment*, vol. 114, no. 12, pp. 2841–2852, 2010.

[73] M. Dalponte, H. O. Ørka, L. T. Ene, T. Gobakken, and E. Næsset, "Tree crown delineation and tree species classification in boreal forests using hyperspectral and als data," *Remote sensing of environment*, vol. 140, pp. 306–317, 2014.

[74] K. Olofsson, J. Wallerman, J. Holmgren, and H. Olsson, "Tree species discrimination using z/i dmc imagery and template matching of single trees," *Scandinavian Journal of Forest Research*, vol. 21, no. S7, pp. 106–110, 2006.

[75] H. O. Ørka, M. Dalponte, T. Gobakken, E. Næsset, and L. T. Ene, "Characterizing forest species composition using multiple remote sensing data sources and inventory approaches," *Scandinavian journal of forest research*, vol. 28, no. 7, pp. 677–688, 2013.

[76] E. Lindberg, J. Holmgren, K. Olofsson, and H. Olsson, "Estimation of stem attributes using a combination of terrestrial and airborne laser scanning," *European Journal of Forest Research*, vol. 131, no. 6, pp. 1917–1931, 2012.

[77] L. Chasmer, C. Hopkinson, and P. Treitz, "Assessing the three-dimensional frequency distribution of airborne and ground-based lidar data for red pine and mixed deciduous forest plots," *Int Arch Photogramm Remote Sens Spat Inf Sci*, vol. 36, p. 8W, 2004.

[78] F. Hosoi and K. Omasa, "Voxel-based 3-d modeling of individual trees for estimating leaf area density using high-resolution portable scanning lidar," *Geoscience and Remote Sensing, IEEE Transactions on*, vol. 44, no. 12, pp. 3610–3618, 2006.

[79] M. Hauglin, V. Lien, E. Næsset, and T. Gobakken, "Geo-referencing forest field plots by co-registration of terrestrial and airborne laser scanning data," *International Journal of Remote Sensing*, vol. 35, no. 9, pp. 3135–3149, 2014.

[80] D. Kelbe, J. van Aardt, P. Romanczyk, and M. van Leeuwen, "Marker-free registration of forest terrestrial laser scanner data pairs with embedded confidence metrics," *Geoscience and Remote Sensing, IEEE Transactions on., submitted*, 2015.

[81] T. Brandtberg, T. A. Warner, R. E. Landenberger, and J. B. McGraw, "Detection and analysis of individual leaf-off tree crowns in small footprint, high sampling density lidar data from the eastern deciduous forest in north america," *Remote sensing of Environment*, vol. 85, no. 3, pp. 290–303, 2003.

[82] M. Maltamo, K. Mustonen, J. Hyyppä, J. Pitkänen, and X. Yu, "The accuracy of estimating individual tree variables with airborne laser scanning in a boreal nature reserve," *Canadian Journal of Forest Research*, vol. 34, no. 9, pp. 1791–1801, 2004.

[83] S. C. Popescu, R. H. Wynne, and R. F. Nelson, "Measuring individual tree crown diameter with lidar and assessing its influence on estimating forest volume and biomass," *Canadian journal of remote sensing*, vol. 29, no. 5, pp. 564–577, 2003.

[84] J. Hyyppä, O. Kelle, M. Lehikoinen, and M. Inkinen, "A segmentation-based method to retrieve stem volume estimates from 3-d tree height models produced by laser scanners," *Geoscience and Remote Sensing, IEEE Transactions on*, vol. 39, no. 5, pp. 969–975, May 2001.

[85] J. Hyyppä, M. Schardt, H. Haggrén, B. Koch, U. Lohr, R. Paananen, H. Scherrer, H. Luukkonen, M. Ziegler, H. Hyyppä *et al.*, "High-scan: The first european-wide attempt to derive single-tree information from laserscanner data," *The Photogrammetric Journal of Finland*, 2001.

[86] A. Kato, L. M. Moskal, P. Schiess, M. E. Swanson, D. Calhoun, and W. Stuetzle, "Capturing tree crown formation through implicit surface reconstruction using airborne lidar data," *Remote Sensing of Environment*, vol. 113, no. 6, pp. 1148 – 1162, 2009.

[87] S. Solberg, E. Næsset, and O. Bollandsas, "Single-tree segmentation using airborne laser scanner data in a structurally heterogeneous spruce forest," *Photogrammetric Engineering and Remote Sensing*, vol. 72, pp. 1369–1378, 2006.

[88] D. Tiede, G. Hochleitner, and T. Blaschke, "A full gis-based workflow for tree identification and tree crown delineation using laser scanning," in *ISPRS Workshop CMRT*, vol. 5, 2005, pp. 29–30.

[89] D.-A. Kwak, W.-K. Lee, J.-H. Lee, G. S. Biging, and P. Gong, "Detection of individual trees and estimation of tree height using lidar data," *Journal of Forest Research*, vol. 12, no. 6, pp. 425–434, 2007.

[90] U. Pyysalo and H. Hyyppä, "Reconstructing tree crowns from laser scanner data for feature extraction," *International Archives Of Photogrammetry Remote Sensing And Spatial Information Sciences*, vol. 34, no. 3/B, pp. 218–221, 2002.

[91] L. Ene, E. Næsset, and T. Gobakken, "Single tree detection in heterogeneous boreal forests using airborne laser scanning and area-based stem number estimates," *International journal of remote sensing*, vol. 33, no. 16, pp. 5171–5193, 2012.

[92] K. Barbara, H. Ursula, and W. Holger, "Detection of individual tree crowns in airborne lidar data," *Photogrammetric Engineering and Remote Sensing*, vol. 72, no. 4, pp. 357—363, 2006.

[93] X. Yu, J. Hyyppä, M. Vastaranta, M. Holopainen, and R. Viitala, "Predicting individual tree attributes from airborne laser point clouds based on the random forests technique," {*ISPRS*} *Journal of Photogrammetry and Remote Sensing*, vol. 66, no. 1, pp. 28 – 37, 2011.

[94] J. N. Heinzel, H. Weinacker, and B. Koch, "Prior-knowledge-based single-tree extraction," *International journal of remote sensing*, vol. 32, no. 17, pp. 4999–5020, 2011.

[95] A. Persson, J. Holmgren, and U. Söderman, "Detecting and measuring individual trees using an airborne laser scanner," *Photogrammetric Engineering and Remote Sensing*, vol. 68, no. 9, pp. 925–932, 2002.

[96] J. Holmgren, A. Barth, H. Larsson, and H. Olsson, "Prediction of stem attributes by combining airborne laser scanning and measurements from harvesters," *Silva Fenn*, vol. 46, no. 2, pp. 227–239, 2012.

[97] T. Lahivaara, A. Seppanen, J. P. Kaipio, J. Vauhkonen, L. Korhonen, T. Tokola, and M. Maltamo, "Bayesian approach to tree detection based on airborne laser scanning data," *Geoscience and Remote Sensing, IEEE Transactions on*, vol. 52, no. 5, pp. 2690–2699, 2014.

[98] M. Vastaranta, M. Holopainen, X. Yu, J. Hyyppä, A. Mäkinen, J. Rasinmäki, T. Melkas, H. Kaartinen, and H. Hyyppä, "Effects of individual tree detection error sources on forest management planning calculations," *Remote Sensing*, vol. 3, no. 8, pp. 1614–1626, 2011. [Online]. Available: http://www.mdpi.com/2072-4292/3/8/1614

[99] T. Hengl, "Finding the right pixel size," *Computers and Geosciences*, vol. 32, no. 9, pp. 1283 – 1298, 2006.

[100] L. Wallace, A. Lucieer, and C. S. Watson, "Evaluating tree detection and segmentation routines on very high resolution uav lidar data," *Geoscience and Remote Sensing, IEEE Transactions on*, 2014.

[101] C. Alexander, "Delineating tree crowns from airborne laser scanning point cloud data using delaunay triangulation," *International Journal of Remote Sensing*, vol. 30, no. 14, pp. 3843–3848, 2009.

[102] W. Li, Q. Guo, M. Jakubowski, and M. Kelly, "A new method for segmenting individual trees from the lidar point cloud." *Photogrammetric Engineering and Remote Sensing*, vol. 78, pp. 75—-84, 2012.

[103] S. Gupta, H. Weinacker, and B. Koch, "Comparative analysis of clustering-based approaches for 3-d single tree detection using airborne fullwave lidar data," *Remote Sensing*, vol. 2, no. 4, pp. 968–989, 2010.

[104] F. Morsdorf, E. Meier, B. Kötz, K. I. Itten, M. Dobbertin, and B. Allgöwer, "Lidar-based geometric reconstruction of boreal type forest stands at single tree level for forest and wildland fire management," *Remote Sensing of Environment*, vol. 92, no. 3, pp. 353–362, 2004.

[105] H. Lee, K. C. Slatton, B. Roth, and W. Cropper Jr, "Adaptive clustering of airborne lidar data to segment individual tree crowns in managed pine forests," *International Journal of Remote Sensing*, vol. 31, no. 1, pp. 117–139, 2010.

[106] M. Maltamo, K. Eerikäinen, J. Pitkänen, J. Hyyppä, and M. Vehmas, "Estimation of timber volume and stem density based on scanning laser altimetry and expected tree size distribution functions," *Remote Sensing of Environment*, vol. 90, no. 3, pp. 319 – 330, 2004.

[107] D. Riano, E. Meier, B. Allgöwer, E. Chuvieco, and S. L. Ustin, "Modeling airborne laser scanning data for the spatial generation of critical forest parameters in fire behavior modeling," *Remote Sensing of Environment*, vol. 86, no. 2, pp. 177–186, 2003.

[108] J. Reitberger, C. Schnörr, P. Krzystek, and U. Stilla, "3d segmentation of single trees exploiting full waveform lidar data," *ISPRS Journal of Photogrammetry and Remote Sensing*, vol. 64, no. 6, pp. 561–574, 2009.

[109] J. Shi and J. Malik, "Normalized cuts and image segmentation," *Pattern Analysis and Machine Intelligence, IEEE Transactions on*, vol. 22, no. 8, pp. 888–905, 2000.

[110] E. Lindberg, L. Eysn, M. Hollaus, J. Holmgren, and N. Pfeifer, "Delineation of tree crowns and tree species classification from full-waveform airborne laser scanning data using 3-d ellipsoidal clustering," *Selected Topics in Applied Earth Observations and Remote Sensing, IEEE Journal of*, vol. 7, no. 7, pp. 3174–3181, July 2014.

[111] J. J. Richardson and L. M. Moskal, "Strengths and limitations of assessing forest density and spatial configuration with aerial lidar," *Remote Sensing of Environment*, vol. 115, no. 10, pp. 2640–2651, 2011.

[112] A. Ferraz, F. Bretar, S. Jacquemoud, G. Gonçalves, L. Pereira, M. Tomé, and P. Soares, "3-d mapping of a multi-layered mediterranean forest using als data," *Remote Sensing of Environment*, vol. 121, pp. 210–223, 2012.

[113] J. Lopatin, M. Galleguillos, F. E. Fassnacht, A. Ceballos, and J. Hernandez, "Using a multistructural object-based lidar approach to estimate vascular plant richness in mediterranean forests with complex structure," *Geoscience and Remote Sensing, IEEE Transactions on*, 2015.

[114] M. Maltamo, P. Packalén, X. Yu, K. Eerikäinen, J. Hyyppä, and J. Pitkänen, "Identifying and quantifying structural characteristics of heterogeneous boreal forests using laser scanner data," *Forest Ecology and Management*, vol. 216, no. 1–3, pp. 41 – 50, 2005.

[115] A. Barilotti, F. Sepic, E. Abramo, and F. Crosilla, "Assessing the 3d structure of the single crowns in mixed alpine forests," *International Archives of Photogrammetry, Remote Sensing and Spatial Information Sciences*, vol. 36, no. 3/W49A, 2007.

[116] Y. Wang, H. Weinacker, and B. Koch, "A lidar point cloud based procedure for vertical canopy structure analysis and 3d single tree modelling in forest," *Sensors*, vol. 8, no. 6, pp. 3938–3951, 2008.

[117] S. Kim, R. J. McGaughey, H.-E. Andersen, and G. Schreuder, "Tree species differentiation using intensity data derived from leaf-on and leaf-off airborne laser scanner data," *Remote Sensing of Environment*, vol. 113, no. 8, pp. 1575–1586, 2009.

[118] B. Hu, J. Li, L. Jing, and A. Judah, "Improving the efficiency and accuracy of individual tree crown delineation from high-density lidar data," *International Journal of Applied Earth Observation and Geoinformation*, vol. 26, pp. 145–155, 2014.

[119] L. Duncanson, B. Cook, G. Hurtt, and R. Dubayah, "An efficient, multi-layered crown delineation algorithm for mapping individual tree structure across multiple ecosystems," *Remote Sensing of Environment*, vol. 154, pp. 378–386, 2014.

[120] M. Heurich, "Automatic recognition and measurement of single trees based on data from airborne laser scanning over the richly structured natural forests of the bavarian forest national park," *Forest Ecology and Management*, vol. 255, no. 7, pp. 2416–2433, 2008.

[121] S. C. Popescu, "Estimating biomass of individual pine trees using airborne lidar," *Biomass and Bioenergy*, vol. 31, no. 9, pp. 646–655, 2007.

[122] X. Yu, J. Hyyppä, M. Vastaranta, M. Holopainen, and R. Viitala, "Predicting individual tree attributes from airborne laser point clouds based on the random forests technique," *ISPRS Journal of Photogrammetry and Remote Sensing*, vol. 66, no. 1, pp. 28–37, 2011.

[123] X. Yu, J. Hyyppä, M. Holopainen, and M. Vastaranta, "Comparison of area-based and individual tree-based methods for predicting plot-level forest attributes," *Remote Sensing*, vol. 2, no. 6, pp. 1481–1495, 2010.

[124] C. Salas, L. Ene, T. G. Gregoire, E. Næsset, and T. Gobakken, "Modelling tree diameter from airborne laser scanning derived variables: a comparison of spatial statistical models," *Remote Sensing of Environment*, vol. 114, no. 6, pp. 1277–1285, 2010.

[125] L. Zhang, H. Bi, P. Cheng, and C. J. Davis, "Modeling spatial variation in tree diameter–height relationships," *Forest Ecology and Management*, vol. 189, no. 1, pp. 317–329, 2004.

[126] L. Zhang, J. H. Gove, and L. S. Heath, "Spatial residual analysis of six modeling techniques," *Ecological Modelling*, vol. 186, no. 2, pp. 154–177, 2005.

[127] E. Naesset, "Estimating timber volume of forest stands using airborne laser scanner data," *Remote Sensing of Environment*, vol. 61, no. 2, pp. 246–253, 1997.

[128] M. García, D. Riaño, E. Chuvieco, and F. M. Danson, "Estimating biomass carbon stocks for a mediterranean forest in central spain using lidar height and intensity data," *Remote Sensing of Environment*, vol. 114, no. 4, pp. 816–830, 2010.

[129] Q. Chen, P. Gong, D. Baldocchi, and Y. Q. Tian, "Estimating basal area and stem volume for individual trees from lidar data," *Photogrammetric Engineering & Remote Sensing*, vol. 73, no. 12, pp. 1355–1365, 2007.

[130] H. O. Ørka, E. Næsset, and O. M. Bollandsås, "Effects of different sensors and leaf-on and leaf-off canopy conditions on echo distributions and individual tree properties derived from airborne laser scanning," *Remote Sensing of Environment*, vol. 114, no. 7, pp. 1445–1461, 2010.

[131] M. Dalponte, L. Bruzzone, and D. Gianelle, "Fusion of hyperspectral and lidar remote sensing data for classification of complex forest areas," *Geoscience and Remote Sensing, IEEE Transactions on*, vol. 46, no. 5, pp. 1416–1427, 2008.

[132] J. E. Means, S. A. Acker, D. J. Harding, J. B. Blair, M. A. Lefsky, W. B. Cohen, M. E. Harmon, and W. A. McKee, "Use of large-footprint scanning airborne lidar to estimate forest stand characteristics in the western cascades of oregon," *Remote Sensing of Environment*, vol. 67, no. 3, pp. 298–308, 1999.

[133] A. T. Hudak, J. S. Evans, M. J. Falkowski, N. L. Crookston, P. E. Gessler, P. Morgan, and A. Smith, "Predicting plot basal area and tree density in mixed-conifer forest from lidar and advanced land imager (ali) data," *Proceedings of the 26th Canadian Symposium on Remote Sensing*, 2005.

[134] I. D. Moore, P. Gessler, G. Nielsen, and G. Peterson, "Soil attribute prediction using terrain analysis," *Soil Science Society of America Journal*, vol. 57, no. 2, pp. 443–452, 1993.

[135] G. Jordan, "Morphometric analysis and tectonic interpretation of digital terrain data: a case study," *Earth Surface Processes and Landforms*, vol. 28, no. 8, pp. 807–822, 2003.

[136] P. Pudil, J. Novovičová, and J. Kittler, "Floating search methods in feature selection," *Pattern recognition letters*, vol. 15, no. 11, pp. 1119–1125, 1994.

[137] K. Kira and L. A. Rendell, "A practical approach to feature selection," in *Proceedings of the ninth international workshop on Machine learning*, 1992, pp. 249–256.

[138] D. A. Coomes and R. B. Allen, "Effects of size, competition and altitude on tree growth," *Journal of Ecology*, vol. 95, no. 5, pp. 1084–1097, 2007.

[139] I. Korpela, B. Dahlin, H. Schäfer, E. Bruun, F. Haapaniemi, J. Honkasalo, S. Ilvesniemi, V. Kuutti, M. Linkosalmi, J. Mustonen *et al.*, "Single-tree forest inventory using lidar and aerial images for 3d treetop positioning, species recognition, height and crown width estimation," in *Proceedings of ISPRS workshop on laser scanning*, 2007, pp. 227–233.

[140] J. Persson, Å. Holmgren and U. Söderman, "Detecting and measuring individual trees using an airborne laser scanner," *Photogrammetric Engineering and Remote Sensing*, vol. 68, pp. 925–932, 2002.

[141] J. Hyyppä and M. Inkinen, "Detecting and estimating attributes for single trees using laser scanner," *Photogrammetric Journal of Finland*, vol. 16, pp. 27–42, 1999.

[142] S. Magnussen, P. Eggermont, and V. N. LaRiccia, "Recovering tree heights from airborne laser scanner data," *Forest science*, vol. 45, no. 3, pp. 407–422, 1999.

[143] P. Rönnholm, J. Hyyppä, H. Hyyppä, H. Haggrén, X. Yu, and H. Kaartinen, "Calibration of laser-derived tree height estimates by means of photogrammetric techniques," *Scandinavian journal of forest research*, vol. 19, no. 6, pp. 524–528, 2004.

[144] M. A. Wulder, C. W. Bater, N. C. Coops, T. Hilker, and J. C. White, "The role of lidar in sustainable forest management," *The Forestry Chronicle*, vol. 84, no. 6, pp. 807–826, 2008.

[145] X. Yu, J. Hyyppä, H. Hyyppä, and M. Maltamo, "Effects of flight altitude on tree height estimation using airborne laser scanning," *Proceedings of the Laser Scanners for Forest and Landscape Assessment–Instruments, Processing Methods and Applications*, pp. 02–06, 2004.

[146] T. Takahashi, Y. Awaya, Y. Hirata, N. Furuya, T. Sakai, and A. Sakai, "Effects of flight altitude on lidar-derived tree heights in mountainous forests with poor laser penetration rates," *Photogrammetric Journal of Finland*, vol. 21, no. 1, pp. 86–96, 2008.

[147] Y. Hirata, "The effects of footprint size and sampling density in airborne laser scanning to extract individual trees in mountainous terrain," *International Archives of Photogrammetry, Remote Sensing and Spatial Information Sciences*, vol. 36, no. 8/W2, pp. 102–107, 2004.

[148] E. P. Baltsavias, "A comparison between photogrammetry and laser scanning," *ISPRS Journal of photogrammetry and Remote Sensing*, vol. 54, no. 2, pp. 83–94, 1999.

[149] S. Koukoulas and G. A. Blackburn, "Mapping individual tree location, height and species in broadleaved deciduous forest using airborne lidar and multi-spectral remotely sensed data," *International Journal of Remote Sensing*, vol. 26, no. 3, pp. 431–455, 2005.

[150] J. Hyyppä, T. Mielonen, H. Hyyppä, M. Maltamo, X. Yu, E. Honkavaara, and H. Kaartinen, "Using individual tree crown approach for forest volume extraction with aerial images and laser point clouds," in *Proceedings of The ISPRS Workshop Laser Scanning 2005*. Citeseer, 2005, pp. 144–149.

[151] P. Sorin C. and R. H. Wynne, "Seeing the trees in the forest: Using lidar and multispectral data fusion with local filtering and variable window size for estimating tree height." *Photogrammetric Engineering & Remote Sensing*, vol. 70, no. 5, pp. 589–604, May 2004.

[152] H. Huang, P. Gong, X. Cheng, N. Clinton, and Z. Li, "Improving measurement of forest structural parameters by co-registering of high resolution aerial imagery and low density lidar data," *Sensors*, vol. 9, no. 3, pp. 1541–1558, 2009.

[153] R. Van Den Boomgaard and R. Van Balen, "Methods for fast morphological image transforms using bitmapped binary images," *CVGIP: Graphical Models and Image Processing*, vol. 54, no. 3, pp. 252–258, 1992.

[154] L. Wang, P. Gong, and G. S. Biging, "Individual tree-crown delineation and treetop detection in high-spatial-resolution aerial imagery," *Photogrammetric Engineering and Remote Sensing*, vol. 70, no. 3, pp. 351–358, 2004.

[155] F. A. Gougeon, "A crown-following approach to the automatic delineation of individual tree crowns in high spatial resolution aerial images," *Canadian journal of remote sensing*, vol. 21, no. 3, pp. 274–284, 1995.

[156] D. S. Culvenor, "Tida: an algorithm for the delineation of tree crowns in high spatial resolution remotely sensed imagery," *Computers & Geosciences*, vol. 28, no. 1, pp. 33–44, 2002.

[157] R. J. Pollock, "The automatic recognition of individual trees in aerial images of forests based on a synthetic tree crown image model," Ph.D. dissertation, The University of British Columbia (Canada), 1996.

[158] A. Barbati, G. Chirici, P. Corona, A. Montaghi, and D. Travaglini, "Area-based assessment of forest standing volume by field measurements and airborne laser scanner data," *International Journal of Remote Sensing*, vol. 30, no. 19, pp. 5177–5194, 2009.

[159] M. Schardt, M. Ziegler, A. Wimmer, R. Wack, and J. Hyyppä, "Assessment of forest parameters by means of laser scanning," *International archives of photogrammetry remote sensing and spatial information sciences*, vol. 34, no. 3/A, pp. 302–309, 2002.

[160] M. A. Finney *et al.*, *FARSITE: Fire area simulator: model development and evaluation.* US Department of Agriculture, Forest Service, Rocky Mountain Research Station Ogden, UT, 2004.

[161] G. G. Parker, D. J. Harding, and M. L. Berger, "A portable lidar system for rapid determination of forest canopy structure," *Journal of Applied Ecology*, vol. 41, no. 4, pp. 755–767, 2004.

[162] B. Zeide and P. Pfeifer, "Fractal dimension is used to characterized tree crown," *Forest Science*, vol. 37, no. 5, pp. 1253–1265, 1991.

[163] D. Ellsworth and P. Reich, "Canopy structure and vertical patterns of photosynthesis and related leaf traits in a deciduous forest," *Oecologia*, vol. 96, no. 2, pp. 169–178, 1993.

[164] P. Oker-Blom, "influence of penumbra on the distribution of direct solar radiation in a canopy of scots pine," *Photosynthetica*, 1985.

[165] P. Stenberg, "Penumbra in within-shoot and between-shoot shading in conifers and its significance for photosynthesis," *Ecological Modelling*, vol. 77, no. 2, pp. 215–231, 1995.

[166] C. Field, "Allocating leaf nitrogen for the maximization of carbon gain: leaf age as a control on the allocation program," *Oecologia*, vol. 56, no. 2-3, pp. 341–347, 1983.

[167] T. J. Givnish, "Adaptation to sun and shade: a whole-plant perspective," *Functional Plant Biology*, vol. 15, no. 2, pp. 63–92, 1988.

[168] A. Kangas and M. Maltamo, *Forest inventory: methodology and applications*. Springer Science & Business Media, 2006, vol. 10.

[169] A. Kato, L. M. Moskal, P. Schiess, M. E. Swanson, D. Calhoun, and W. Stuetzle, "Capturing tree crown formation through implicit surface reconstruction using airborne lidar data," *Remote Sensing of Environment*, vol. 113, no. 6, pp. 1148–1162, 2009.

[170] C. G. Bachman, "Laser radar systems and techniques," *Dedham, Mass., Artech House, Inc., 1979. 203 p.*, vol. 1, 1979.

[171] A. Wehr and U. Lohr, "Airborne laser scanning—an introduction and overview," *ISPRS Journal of Photogrammetry and Remote Sensing*, vol. 54, no. 2, pp. 68–82, 1999.

[172] T. U. Kampe, B. R. Johnson, M. Kuester, and M. Keller, "Neon: the first continental-scale ecological observatory with airborne remote sensing of vegetation canopy biochemistry and structure," *Journal of Applied Remote Sensing*, vol. 4, no. 1, pp. 043 510–043 510, 2010.

[173] H.-E. Andersen, S. E. Reutebuch, and G. F. Schreuder, "Bayesian object recognition for the analysis of complex forest scenes in airborne laser scanner data," *International archives of photogrammetry remote sensing and spatial information sciences*, vol. 34, no. 3/A, pp. 35–41, 2002.

[174] D. Riaño, E. Chuvieco, S. Condés, J. González-Matesanz, and S. L. Ustin, "Generation of crown bulk density for pinus sylvestris l. from lidar," *Remote Sensing of Environment*, vol. 92, no. 3, pp. 345–352, 2004.

[175] M. J. Falkowski, A. M. Smith, A. T. Hudak, P. E. Gessler, L. A. Vierling, and N. L. Crookston, "Automated estimation of individual conifer tree height and crown diameter via two-dimensional spatial wavelet analysis of lidar data," *Canadian Journal of Remote Sensing*, vol. 32, no. 2, pp. 153–161, 2006.

[176] B. Koch, U. Heyder, and H. Weinacker, "Detection of individual tree crowns in airborne lidar data," *Photogrammetric Engineering & Remote Sensing*, vol. 72, no. 4, pp. 357–363, 2006.

[177] V. F. Strîmbu and B. M. Strîmbu, "A graph-based segmentation algorithm for tree crown extraction using airborne lidar data," *ISPRS Journal of Photogrammetry and Remote Sensing*, vol. 104, pp. 30–43, 2015.

[178] J. Breidenbach, E. Næsset, V. Lien, T. Gobakken, and S. Solberg, "Prediction of species specific forest inventory attributes using a nonparametric semi-individual tree crown approach based on fused airborne laser scanning and multispectral data," *Remote Sensing of Environment*, vol. 114, no. 4, pp. 911–924, 2010.

[179] C. Mallet and F. Bretar, "Full-waveform topographic lidar: State-of-the-art," *ISPRS Journal of photogrammetry and remote sensing*, vol. 64, no. 1, pp. 1–16, 2009.

[180] J. G. Henning and P. J. Radtke, "Ground-based laser imaging for assessing three-dimensional forest canopy structure," *Photogrammetric Engineering & Remote Sensing*, vol. 72, no. 12, pp. 1349–1358, 2006.

[181] P. Tickle, A. Lee, R. Lucas, J. Austin, and C. Witte, "Quantifying australian forest floristics and structure using small footprint lidar and large scale aerial photography," *Forest Ecology and Management*, vol. 223, no. 1, pp. 379–394, 2006.

[182] T. Hilker, M. van Leeuwen, N. C. Coops, M. A. Wulder, G. J. Newnham, D. L. Jupp, and D. S. Culvenor, "Comparing canopy metrics derived from terrestrial and airborne laser scanning in a douglas-fir dominated forest stand," *Trees*, vol. 24, no. 5, pp. 819–832, 2010.

[183] D. Kelbe, P. Romanczyk, J. van Aardt, K. Cawse-Nicholson, and K. Krause, "Automatic extraction of tree stem models from single terrestrial lidar scans in structurally heterogeneous forest environments," in *12th International conference on LiDAR applications for assessing forest ecosystems, SilviLaser*, 2012, pp. 16–19.

[184] B. Zitova and J. Flusser, "Image registration methods: a survey," *Image and vision computing*, vol. 21, no. 11, pp. 977–1000, 2003.

[185] G. E. Christensen and H. J. Johnson, "Consistent image registration," *Medical Imaging, IEEE Transactions on*, vol. 20, no. 7, pp. 568–582, 2001.

[186] P. Thévenaz and M. Unser, "Optimization of mutual information for multiresolution image registration," *Image Processing, IEEE Transactions on*, vol. 9, no. 12, pp. 2083–2099, 2000.

[187] L. Bruzzone and M. Marconcini, "Domain adaptation problems: A dasvm classification technique and a circular validation strategy," *Pattern Analysis and Machine Intelligence, IEEE Transactions on*, vol. 32, no. 5, pp. 770 –787, May 2010.

[188] S. J. Pan and Q. Yang, "A survey on transfer learning," *Knowledge and Data Engineering, IEEE Transactions on*, vol. 22, no. 10, pp. 1345–1359, 2010.

[189] J. R. Schott, C. Salvaggio, and W. J. Volchok, "Radiometric scene normalization using pseudoinvariant features," *Remote Sensing of Environment*, vol. 26, no. 1, pp. 1–16, 1988.

[190] C. E. Woodcock, S. A. Macomber, M. Pax-Lenney, and W. B. Cohen, "Monitoring large areas for forest change using landsat: Generalization across space, time and landsat sensors," *Remote Sensing of Environment*, vol. 78, no. 1, pp. 194–203, 2001.

[191] J. Heo and T. W. FitzHugh, "A standardized radiometric normalization method for change detection using remotely sensed imagery," *Photogrammetric Engineering and Remote Sensing*, vol. 66, no. 2, pp. 173–181, 2000.

[192] L. Bruzzone and D. F. Prieto, "Unsupervised retraining of a maximum likelihood classifier for the analysis of multitemporal remote sensing images," *Geoscience and Remote Sensing, IEEE Transactions on*, vol. 39, no. 2, pp. 456–460, 2001.

[193] L. Bruzzone and R. Cossu, "A multiple-cascade-classifier system for a robust and partially unsupervised updating of land-cover maps," *Geoscience and Remote Sensing, IEEE Transactions on*, vol. 40, no. 9, pp. 1984–1996, 2002.

[194] B. Demir, F. Bovolo, and L. Bruzzone, "Updating land-cover maps by classification of image time series: A novel change-detection-driven transfer learning approach," *Geoscience and Remote Sensing, IEEE Transactions on*, vol. 51, no. 1, pp. 300–312, 2013.

[195] J. Jiang and C. Zhai, "Instance weighting for domain adaptation in nlp," in *ACL*, vol. 7, 2007, pp. 264–271.

[196] C. Persello, "Interactive domain adaptation for the classification of remote sensing images using active learning," *Geoscience and Remote Sensing Letters, IEEE*, vol. 10, no. 4, pp. 736–740, 2013.

[197] G. Matasci, D. Tuia, and M. Kanevski, "Svm-based boosting of active learning strategies for efficient domain adaptation," *Selected Topics in Applied Earth Observations and Remote Sensing, IEEE Journal of*, vol. 5, no. 5, pp. 1335–1343, 2012.

[198] B. Demir, C. Persello, and L. Bruzzone, "Batch-mode active-learning methods for the interactive classification of remote sensing images," *Geoscience and Remote Sensing, IEEE Transactions on*, vol. 49, no. 3, pp. 1014–1031, 2011.

[199] L. Bruzzone, M. Chi, and M. Marconcini, "A novel transductive svm for semisupervised classification of remote-sensing images," *Geoscience and Remote Sensing, IEEE Transactions on*, vol. 44, no. 11, pp. 3363–3373, 2006.

[200] S. Bickel, M. Brückner, and T. Scheffer, "Discriminative learning for differing training and test distributions," in *Proceedings of the 24th international conference on Machine learning*. ACM, 2007, pp. 81–88.

[201] J. Huang, A. Gretton, K. M. Borgwardt, B. Schölkopf, and A. J. Smola, "Correcting sample selection bias by unlabeled data," in *Advances in neural information processing systems*, 2006, pp. 601–608.

[202] G. Jun and J. Ghosh, "Spatially adaptive classification of land cover with remote sensing data," *Geoscience and Remote Sensing, IEEE Transactions on*, vol. 49, no. 7, pp. 2662–2673, 2011.

[203] G. Camps-Valls, T. Bandos Marsheva, and D. Zhou, "Semi-supervised graph-based hyperspectral image classification," *Geoscience and Remote Sensing, IEEE Transactions on*, vol. 45, no. 10, pp. 3044–3054, 2007.

[204] M. Belkin, P. Niyogi, and V. Sindhwani, "Manifold regularization: A geometric framework for learning from labeled and unlabeled examples," *The Journal of Machine Learning Research*, vol. 7, pp. 2399–2434, 2006.

[205] L. Gómez-Chova, G. Camps-Valls, J. Munoz-Mari, and J. Calpe, "Semisupervised image classification with laplacian support vector machines," *Geoscience and Remote Sensing Letters, IEEE*, vol. 5, no. 3, pp. 336–340, 2008.

[206] B. Banerjee, F. Bovolo, A. Bhattacharya, L. Bruzzone, S. Chaudhuri, and K. M. Buddhiraju, "A novel graph-matching-based approach for domain adaptation in classification of remote sensing image pair," *Geoscience and Remote Sensing, IEEE Transactions on*, vol. 53, no. 7, pp. 4045–4062, 2015.

[207] L. Bruzzone and C. Persello, "A novel approach to the selection of spatially invariant features for the classification of hyperspectral images with improved generalization capability," *Geoscience and Remote Sensing, IEEE Transactions on*, vol. 47, no. 9, pp. 3180–3191, 2009.

[208] D. Tuia, J. Munoz-Mari, L. Gomez-Chova, and J. Malo, "Graph matching for adaptation in remote sensing," *Geoscience and Remote Sensing, IEEE Transactions on*, vol. 51, no. 1, pp. 329–341, 2013.

[209] D. Tuia, M. Volpi, M. Trolliet, and G. Camps-Valls, "Semisupervised manifold alignment of multimodal remote sensing images," *Geoscience and Remote Sensing, IEEE Transactions on*, 2014.

[210] G. Matasci, M. Volpi, M. Kanevski, L. Bruzzone, and D. Tuia, "Semisupervised transfer component analysis for domain adaptation in remote sensing image classification," *Geoscience and Remote Sensing, IEEE Transactions on*, vol. 53, no. 7, pp. 3550–3564, 2015.

[211] C. Wang and S. Mahadevan, "Heterogeneous domain adaptation using manifold alignment," in *IJCAI Proceedings-International Joint Conference on Artificial Intelligence*, vol. 22, no. 1, 2011, p. 1541.

[212] J. Ham, D. Lee, and L. Saul, "Semisupervised alignment of manifolds," in *Proceedings of the Annual Conference on Uncertainty in Artificial Intelligence*, vol. 10, 2005, pp. 120–127.

[213] C. Paris and L. Bruzzone, "A sensor-driven domain adaptation method for the classification of remote sensing images," in *Geoscience and Remote Sensing Symposium (IGARSS), 2014 IEEE International*. IEEE, 2014, pp. 185–188.

[214] J. Arenas-García, K. Petersen, G. Camps-Valls, and L. K. Hansen, "Kernel multivariate analysis framework for supervised subspace learning: A tutorial on linear and kernel multivariate methods," *Signal Processing Magazine, IEEE*, vol. 30, no. 4, pp. 16–29, 2013.

[215] M. Brand, "Charting a manifold," in *Advances in neural information processing systems*, 2002, pp. 961–968.

[216] Y. W. Teh and S. T. Roweis, "Automatic alignment of local representations," in *Advances in neural information processing systems*, 2002, pp. 841–848.

[217] W. Kim and M. M. Crawford, "Adaptive classification for hyperspectral image data using manifold regularization kernel machines," *IEEE transactions on geoscience and remote sensing*, vol. 48, no. 11, pp. 4110–4121, 2010.

[218] S. Rajan, J. Ghosh, and M. M. Crawford, "Exploiting class hierarchies for knowledge transfer in hyperspectral data," *Geoscience and Remote Sensing, IEEE Transactions on*, vol. 44, no. 11, pp. 3408–3417, 2006.

[219] S. Kumar, J. Ghosh, and M. M. Crawford, "Hierarchical fusion of multiple classifiers for hyperspectral data analysis," *Pattern Analysis & Applications*, vol. 5, no. 2, pp. 210–220, 2002.

[220] J. Gualtieri, S. R. Chettri, R. Cromp, and L. Johnson, "Support vector machine classifiers as applied to aviris data," in *Proc. Eighth JPL Airborne Geoscience Workshop*. Citeseer, 1999.

[221] F. Melgani and L. Bruzzone, "Classification of hyperspectral remote sensing images with support vector machines," *Geoscience and Remote Sensing, IEEE Transactions on*, vol. 42, no. 8, pp. 1778 – 1790, Aug. 2004.

[222] M. Chi and L. Bruzzone, "A semilabeled-sample-driven bagging technique for ill-posed classification problems," *Geoscience and Remote Sensing Letters, IEEE*, vol. 2, no. 1, pp. 69–73, 2005.

[223] G. Camps-Valls and L. Bruzzone, "Kernel-based methods for hyperspectral image classification," *Geoscience and Remote Sensing, IEEE Transactions on*, vol. 43, no. 6, pp. 1351–1362, 2005.

[224] S. B. Serpico and L. Bruzzone, "A new search algorithm for feature selection in hyperspectral remote sensing images," *Geoscience and Remote Sensing, IEEE Transactions on*, vol. 39, no. 7, pp. 1360–1367, 2001.

[225] L. Bruzzone, F. Roli, and S. B. Serpico, "An extension of the jeffreys-matusita distance to multiclass cases for feature selection," *Geoscience and Remote Sensing, IEEE Transactions on*, vol. 33, no. 6, pp. 1318–1321, 1995.

[226] S. Patra and L. Bruzzone, "A fast cluster-assumption based active-learning technique for classification of remote sensing images," *Geoscience and Remote Sensing, IEEE Transactions on*, vol. 49, no. 5, pp. 1617–1626, 2011.

[227] S. Rajan, J. Ghosh, and M. M. Crawford, "An active learning approach to hyperspectral data classification," *Geoscience and Remote Sensing, IEEE Transactions on*, vol. 46, no. 4, pp. 1231–1242, 2008.

[228] C. Persello and L. Bruzzone, "A novel active learning strategy for domain adaptation in the classification of remote sensing images," in *Geoscience and Remote Sensing Symposium (IGARSS), 2011 IEEE International*. IEEE, 2011, pp. 3720–3723.

[229] R. Zhang, A. Rudnicky *et al.*, "A large scale clustering scheme for kernel k-means," in *Pattern Recognition, 2002. Proceedings. 16th International Conference on*, vol. 4. IEEE, 2002, pp. 289–292.

[230] M. Herold, X. Liu, and K. C. Clarke, "Spatial metrics and image texture for mapping urban land use," *Photogrammetric Engineering & Remote Sensing*, vol. 69, no. 9, pp. 991–1001, 2003.

[231] H. Permuter, J. Francos, and I. Jermyn, "A study of gaussian mixture models of color and texture features for image classification and segmentation," *Pattern Recognition*, vol. 39, no. 4, pp. 695–706, 2006.